On the voltage gated ion channels involved in action potential generation and back propagation in layer 5 pyramidal neurons

Laila Blomer

To cite this version:

Laila Blomer. On the voltage gated ion channels involved in action potential generation and back propagation in layer 5 pyramidal neurons. Physics [physics]. Université Grenoble Alpes [2020-..], 2022. English. NNT : 2022GRALY077 . tel-04077615

HAL Id: tel-04077615
https://theses.hal.science/tel-04077615
Submitted on 21 Apr 2023

THÈSE

Pour obtenir le grade de

DOCTEUR DE L'UNIVERSITÉ GRENOBLE ALPES

École doctorale : PHYS - Physique
Spécialité : Physique pour les Sciences du Vivant
Unité de recherche : Laboratoire Interdisciplinaire de Physique

Sur les canaux ioniques potentiel-dépendant impliqués dans la génération du potentiel d'action et la rétropropagation dans les neurones pyramidaux de la couche 5

On the voltage gated ion channels involved in action potential generation and back propagation in layer 5 pyramidal neurons

Présentée par :

Laila BLOMER

Direction de thèse :

Marco CANEPARI Directeur de thèse
Chargé de recherche hors classe, Université Grenoble Alpes

Rapporteurs :

ANITA LÜTHI
Professeur associé, Université de Lausanne
EMMANUEL BOURINET
Directeur de recherche, CNRS DELEGATION OCCITANIE EST

Thèse soutenue publiquement le **12 décembre 2022**, devant le jury composé de :

ANITA LÜTHI Rapporteure
Professeur associé, Université de Lausanne
EMMANUEL BOURINET Rapporteur
Directeur de recherche, CNRS DELEGATION OCCITANIE EST
NICOLA KUCZEWSKI Examinateur
Maître de conférences HDR, UNIVERSITE LYON 1 - CLAUDE BERNARD
DELPHINE DEBARRE Examinatrice
Chargé de recherche HDR, CNRS DELEGATION ALPES
GIOVANNI CAPPELLO Examinateur
Directeur de recherche, CNRS DELEGATION ALPES
BERTRAND FOURCADE Président
Professeur des Universités, UNIVERSITE GRENOBLE ALPES

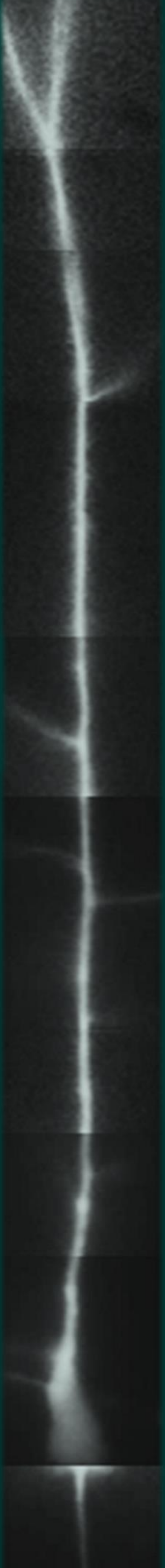

On the voltage gated ion channels involved in action potential generation and back propagation in layer 5 pyramidal neurons

Laila Ananda Blömer

Laboratoire Interdisciplinaire de Physique

CNRS – Université Grenoble Alpes

Dissertation submitted in partial satisfaction of the requirements for the degree

Doctor of Philosophy

December 12, 2022

Advisor Dr Marco Canepari
Rapporteur Prof Anita Lüthi
Rapporteur Dr Emmanuel Bourinet
Jury president Prof Bertrand Fourcade
Jury member Dr Nicola Kuczewski
Jury member Dr Delphine Debarre
Jury member Dr Giovanni Cappello

This thesis was funded by the Centre National de la Recherche Scientifique (CNRS) and the LabEx Ion Channel Science and Therapeutics, completed at Laboratoire Interdiplinaire de Physique (LIPhy) and Université Grenoble Alpes.

Acknowledgements

Before thanking all the people involved in this thesis, I want to emphasise the ethical use of laboratory animals. Animals are used in scientific research to help us understand our own physiology, which is also the case in this manuscript. Therefore, I would like to acknowledge the involuntary sacrifice of the 230 mice that were euthanised for the experiments described in this thesis.

Then, I would like to thank the following people, without whom I would not have been able to complete this research project. First of all, my gratitude goes out to Dr Marco Canepari, my supervisor, for your enthusiasm for this project and for sharing your extensive knowledge. I am especially grateful for your guidance during the writing process and hands-off support, giving me the opportunity to learn independently. Although this thesis has been so frustrating at times, I have always felt supported by your trust.

I am grateful to the members of my jury, Prof. Anita Lüthi, Dr. Emmanuel Bourinnet, Asst. Prof. Nikola Kuczewski, Dr. Delphine Debarre, Dr. Giovanni Cappello and Prof. Bertrand Fourcade, for taking the time to read my manuscript and be present to discuss my work as a scientist.

Next, I thank our collaborators, without whom this thesis would have been considerably smaller. Many thanks to Prof. Michele Migliore and Elisabetta Giacalone, for you guidance on the NEURON modelling; and Dr. Michel de Waard and his team for our collaborations on developing highly selective toxins. Lastly I give my thanks to the members of Laboratoire d'Excellence Canaux Ioniques d'Intérêt Thérapeutique, especially Dr. Massimo Mantegazza and Dr. Philippe Lory for many interesting discussions.

Besides my scientific relationships aiding my development as a scientist, I owe a great deal of gratitude to the people in my personal life. A special thanks to Dr Luiza Filipis; you were my example and your presence made all the difference to me especially during my first year. I also want to thank my fellow PhD students (and post-docs) at the laboratory, for it is always better to struggle together than alone; Saranath, Andrea, Gautier, Windried, Wanda, Maaike, Markus, Raj, Dandara, Edouardo, Adrien, Cécile, William, Artur, Gautier and particularly Fatima, without whom this thesis would have been a lonely road. In addition, I express my gratitude to my friends outside of the lab, who joined me in hours of outdoor sports and

activities, keeping me sane; especially Alexo, Chiara, Nachi, Renata, Line, Ariana & all crossfit members. Thank you! Anna, we spent most of the COVID confinements together in isolation, a special thanks to you for your never ending energy and enthusiasm, always ready for new adventures ('that is impossible' does not exist in your vocabulary)! Tarah, thank you for all your faith and your unwavering friendship these last ten years. Although I have been the most unreliable friend (I really never call and for that I am sorry), you have always stayed by my side. Duru, you have been my conscience on many occasions and I thank you for keeping me on the right track (I would surely have become a professional bike thief if you had not turned me around). Georges, you are so special to me and I am so thankful for your encouragement, support and adopting Tompoes with me.

Last but not least(!), wil ik mijn familie bedanken. In het bijzonder papa, altijd sta je klaar met kalme woorden en het juiste advies; mam, nooit schuw om de pittigste vragen te stellen, ik ben je dankbaar voor je spiegel; Mayra, de beste, liefste en creatiefste zus die ik had kunnen wensen; en de allerbeste omas Adriana & Anja, dank voor jullie luisterend oor, zorgzaamheid en aanmoedigingen om een betere versie van mijzelf te zijn. Dank voor jullie liefde.

Abstract

In the mammalian brain the shape of neuronal potentials is the result of the sequential activation, inactivation and de-activation of several voltage gated (VG) ion channels, belonging to different families. Indeed, ion channel expression and distribution make up an essential part of a cells machinery, and mutations in these channels can lead to severe diseases and disorders. Therefore, the biophysical properties of ion channels are an important field of research, and the subject of this thesis. Specifically, I investigated the contribution of VG Ca^{2+} channels (VGCC), VG Na^{+} channels (VGNC), VG K^{+} channels (VGKC) and Ca^{2+} activated K^{+} channels (CAKC) to action potential (AP) initiation at the axon initial segment (AIS) and AP back propagation (bAP) into the apical dendrite of layer 5 pyramidal neurons (L5PN).

The methodology, described in the second chapter, consists of electrophysiological recordings of L5PNs in acute mouse brain slices, combined with ultrafast imaging to record the membrane potential (V_m), Ca^{2+} and Na^{+} transients and pharmacological analyses using selective channel blockers. To confirm our experimental results we develop computational models using the NEURON software. We show that analysing VG channels in synergy is essential to understand their interactions and their individual contributions to the AP.

The results of my work are reported in two chapters. Chapter 3 reports on a study on AP generation in the AIS, driven by VGNCs. $Na_v1.2$ and $Na_v1.6$ are the two expressed isoforms of VGNCs, and their role is crucial to the AP shape. Studying these VGNCs has been limited by a lack of pharmacological tools to distinguish between the two. Here, we used the novel peptide G^1G^4-huwentoxin-IV and show its partial selectivity for $Na_v1.2$ over $Na_v1.6$. Exploiting this inhibitor to partially block $Na_v1.2$, we recorded the effect on Na^{+} currents, V_m waveforms and Ca^{2+} currents associated with the AP. We demonstrate that the exclusive permeability of $Na_v1.2$ to Ca^{2+} allows activation of large conductance (BK) CAKCs in the AIS. The interplay between $Na_v1.2$, mediating the AP rise, and BK CAKCs, regulating the peak and the early phase of the AP repolarisation, shapes the AP waveform. To confirm our findings, we created a NEURON model of the AIS. This allowed simulating the interaction between $Na_v1.2$ and BK channels and mimic the experimental results obtained by blocking $Na_v1.2$ with G^1G^4-huwentoxin-IV.

Chapter 4 reports on the AP that back propagates into the dendrite after its generation at the AIS. This bAP is associated with a large Ca^{2+} influx, which we recorded ∼100 µm from the soma. We show that all neuronal VGCCs contribute to the Ca^{2+} current. We show that a VGCC subtype, N-type VGCCs, mediate activation of BK CAKCs through close functional coupling. Using V_m imaging we show the effect of their interplay occurs in the 500 µs after the bAP peak but before the expected Ca^{2+} current peak. This result suggests a physical interaction between BK and N-type channels. We confirm these results with a preliminary NEURON model, connecting the AIS and apical dendrite.

Taken together, we propose a dual, spatially restricted role of BK CAKCs. Firstly by shaping the generating AP in the AIS through its interaction with $Na_v1.2$. Secondly by driving fast repolarisation through functional coupling with N-type VGCCs during a bAP in the apical dendrite, in this way controlling the activation of the other VGCCs.

The synergistic approach of analysing the contributions of the various VG ion channels to the AP generation and back propagation allowed for the discovery of the close functional coupling between BK CAKCs and $Na_v1.2$ and N-type VGCCs in the AIS and apical dendrite, respectively. Together with our modelling efforts, these experiments provide a basis to study the dysfunction of VG ion channels in neuropathologies, such as autism and epilepsy.

Résumé en français

Dans le cerveau des mammifères, la forme des potentiels neuronaux est le résultat de l'activation, de l'inactivation et de la désactivation séquentielles de plusieurs canaux ioniques potentiel-dépendants (PD), appartenant à différentes familles. L'expression et la distribution des canaux ioniques constituent une partie essentielle de la machinerie cellulaire, et les mutations de ces canaux peuvent entraîner des maladies et des troubles graves. Par conséquent, les propriétés biophysiques des canaux ioniques constituent un domaine de recherche important, dans lequel s'inscrit cette thèse. Plus précisément, j'ai étudié la contribution des canaux PD Ca^{2+} (CDPC), des canaux PD Na^{+} (CPDN), des canaux PD K^{+} (CPDK) et des canaux K^{+} activés par le Ca^{2+} (CKAC) à l'initiation du potentiel d'action (PA) au segment initial de l'axone (SIA) et à la rétro-propagation du PA (rPA) dans la dendrite apicale.

Chapitre 1 - Introduction

Les neurones, et en fait toutes les cellules, ont un potentiel de membrane (V_m) au repos dû à l'existence d'un potentiel électrique à travers la membrane (Nicholls 2012). Ce potentiel membranaire résulte de concentrations ioniques différentes dans les espaces intra- et extracellulaire, que le membrane plasmique délimite. Plus précisément, de faibles concentrations intracellulaires de Na^{+} et Ca^{2+} et de fortes concentrations de K^{+}, par rapport à l'espace extracellulaire, entraînent un V_m de $\sim$-70 mV.

Les canaux ioniques potentiel-dépendants dans les neurones pyramidaux

Incorporés à la membrane, de grands complexes protéiques agissent comme des portes entre l'extérieur des cellules et le cytoplasme. Ces canaux ioniques PD permettent la circulation d'espèces ioniques sélectionnées, de la même manière que les fils métalliques permettent la circulation des électrons. L'activation, l'inactivation et la désactivation séquentielles des canaux ioniques PD, entraînées par des changements du V_m, génèrent et façonnent les PA. Les PA sont caractérisés par une forte augmentation du potentiel membranaire médiée par les CPDN après le dépassement d'un certain seuil (dépolarisation), suite à laquelle le potentiel atteint un pic puis diminue vers le potentiel de repos (-70 mV) (repolarisation) sous l'effet de l'activation des CPDK et des CKAC, puis peu s'ensuivre d'une post-hyperpolarisation (PHP) au cours de laquelle le potentiel membranaire tombe en dessous du potentiel membranaire de repos avant de revenir lentement au V_m.

L'expression des canaux ioniques varie entre les types de cellules neuronales, et entre les compartiments d'une même cellule. Par exemple, les courants entrants par les CPDC peuvent augmenter et prolonger la dépolarisation. Dans le même temps, l'entrée de calcium dans la cellule peut générer des courants potassiques sortants par les CKAC et ainsi raccourcir le potentiel d'action. Ainsi, les caractéristiques de tout potentiel d'action donné dépendent des types de canaux ioniques présents dans la membrane et de la manière dont les courants passant par ces canaux interagissent (Nicholls 2012).

Dans cette thèse, je concentre mes recherches sur les neurones pyramidaux de la couche 5 (NPC5). Les cellules pyramidales sont l'un des neurones les plus abondants dans le cortex cérébral des mammifères (Elston 2003). Ces grandes cellules sont la principale source de sortie corticale et sont donc des intégrateurs cruciaux dans les circuits corticaux (Hoffman 2013).

Génération du potentiel d'action au segment initial de l'axone

Le site de génération des PA dans les NPC5, et dans la plupart des neurones, est le segment initial de l'axone (SIA). La forme de l'onde du PA dans le SIA est le résultat d'une cascade d'événements, dont le premier est l'activation des CPDN, permettant au Na^+ d'entrer dans la cellule et provoquant une dépolarisation rapide. Dans le SIA des neurones pyramidaux excitateurs, $Na_v1.2$ et $Na_v1.6$ sont les deux isoformes de CPDN présentes (Tian et al. 2014), et la compréhension du rôle fonctionnel de ces deux canaux est donc fondamentale pour relier la forme du PA à la séquence ultérieure d'étapes d'activation et de désactivation des canaux ioniques. Plus précisément, dans les NPC5 néocorticaux, ces deux canaux ont des distributions axonales (Hu et al. 2009) et des propriétés biophysiques (Rush et al. 2005) différentes. Jusqu'à récemment, l'étude de l'activation et de la signalisation d'une isoforme spécifique du CPDN a été limitée par une série d'obstacles expérimentaux. Premièrement, bien que partiellement sélectifs, les bloqueurs de CPDN agissent sur plusieurs isoformes, et une sélectivité acceptable entre $Na_v1.2$ et $Na_v1.6$ n'a pu être obtenue jusqu'à présent. Deuxièmement, la distribution inhomogène des CPDN, ainsi que la dépendance du site de la forme de l'onde PA, nécessitent l'enregistrement des concentrations d'ions et des variations de V_m à hautes résolutions spatiale et temporelle pour une bonne compréhension du rôle de chaque sous-type de canal. Enfin, la modification des transitoires V_m induite par l'inhibition du CPDN affecte l'activation des autres canaux ioniques PD impliqués dans la formation du PA. Cette importante synergie de divers canaux ioniques, qui sous-tend la génération du PA, rend nécessaire l'analyse combinée de tous ces canaux. Le chapitre 3 s'attache à aborder ces questions, sur la base du développement récent d'un peptide muté à partir d'une toxine animale de type sauvage, qui bloque partiellement mais sélectivement $\mathrm{Na}_v1.2$ par rapport à $\mathrm{Na}_v1.6$.

Rétro-propagation du potentiel d'action dans la dendrite apicale

Un PA déclenché au SIA ne se déplace pas seulement le long de l'axone, mais se propage également dans la dendrite : on parle de la rétro-propagation du potentiel d'action (Stuart and Sakmann 1994). Le rPA est associé à une augmentation rapide de la concentration de Ca^{2+} dans la dendrite. Cette augmentation est associée à plusieurs événements neuronaux, tels que l'intégration et la plasticité synaptiques (Bereshpolova et al. 2007), la génération de pointes de calcium (Larkum et al. 1999a), la libération dendritique de neurotransmetteurs (Kaiser et al. 2004) et la mise en forme des signaux synaptiques entrants (Bloodgood and Sabatini 2007; Waters et al. 2005). Des analyses pharmacologiques effectuées sur des neurones pyramidaux dissociés (Stewart and Foehring 2000) et sur des NPC5 provenant de tranches de cerveau (Almog and Korngreen 2009; Markram et al. 1995) ont montré que tous les CCPD activés par haute tension (HVA), à savoir les types L, P/Q, N et R, contribuent au courant dendritique de Ca^{2+} médié par la rPA, mais que les CCPD activés par basse tension (LVA) (type T) peuvent également y contribuer puisque l'expression de ces canaux dans ce type de neurones a été observée (Talley et al. 1999). Après le courant de Ca^{2+}, les protéines de liaison au Ca^{2+} peuvent être activées par une élévation non-sélective du Ca^{2+} cytosolique (Ghosh and Greenberg 1995), et dans ce cas, ces protéines peuvent également être activées par des ions Ca^{2+} provenant de toute source contribuant au signal. Par ailleurs, les protéines de liaison au Ca^{2+} peuvent être activées de manière plus sélective par une source de Ca^{2+} physiquement couplée. Dans ce cas, la protéine peut subir une élévation de Ca^{2+} plus importante dans un nanodomaine restreint adjacent à la source de Ca^{2+} spécifique, alors que les ions Ca^{2+} provenant d'autres sources sont moins efficaces.

Les CPDC dans les dendrites des neurones pyramidaux ciblent, entre autres protéines, les canaux K^{+} activés par le Ca^{2+} (CKAC), en particulier les CKAC SK et BK (Sah and Davies 2000). Ces deux canaux peuvent être couplés physiquement à une source de Ca^{2+} (Vierra and Trimmer 2022), mais il a été suggéré que les CKAC BK doivent être localisés plus près de la source de Ca^{2+} pour assurer une activation dépendante et fiable du Ca^{2+}, car ils ont une affinité plus faible pour le Ca^{2+} par rapport aux CKAC SK (Fakler and Adelman 2008). Dans des patchs fixés sur les cellules de neurones pyramidaux isolés de l'hippocampe CA1, il a été démontré que les CPDC de type L activent exclusivement les CKAC SK, tandis que les CPDC de type N activent exclusivement les CKAC BK (Marrion and Tavalin 1998). En revanche, des enregistrements par *patch-clamp* de cellules entières de neurones pyramidaux néocorticaux fraîchement dissociés ont montré que les BK CKAC sont activés à la fois par les CPDC de type L et de type N dans cette préparation (Sun et al. 2003), ce qui est cohérent avec les résultats selon lesquels les CPDC de type L (Grunnet and Kaufmann 2004) et les CPDC de type N (Loane et al. 2007) peuvent s'associer moléculairement aux BK CKAC. Enfin, il a été rapporté que les canaux SK sont sélectivement activés par les CPDC de type R dans les dendrites basales adjacentes aux épines dendritiques (Jones and Stuart 2013). D'un point de vue fonctionnel, les rôles des CKAC SK et BK semblent différents (Sah and Davies 2000). Plus précisément, les CKAC SK régulent la forme de l'onde du PA pendant la phase moyenne et tardive de la repolarisation du PA avec une variabilité qui dépend de la source de Ca^{2+} et des types de neurones (Bond et al. 2004; Pedarzani and Stocker 2008). En revanche, les CKAC BK, fonctionnellement exprimés dans les dendrites des NPC5 (Benhassine and Berger 2005; Kang et al. 2000), régulent le PA dans la phase précoce de repolarisation (Sun et al. 2003), lorsque le potentiel de membrane (V_m) est dépolarisé, ce qui est cohérent avec la dépendance en tension du canal (Cui 2010). L'interaction étroite entre la source de Ca^{2+} et le CPDC BK implique non seulement un couplage sélectif, mais aussi une capacité d'activation du canal K^+ à une échelle de temps inférieure à la milliseconde (Berkefeld et al. 2006). La cinétique d'activation et de désactivation des CPDC, cependant, est de l'ordre de 1 ms (Kay and Wong 1987), ce qui soulève l'hypothèse d'une cinétique d'activation plus rapide pour les CKACs BK. Le chapitre 4 rapporte l'investigation de cette hypothèse et le rôle du couplage spécifique entre les CPDCs et les CKACs pendant les rPAs dans la dendrite apicale des NPC5s.

Chapitre 2 - La méthodologie

La méthodologie, décrite au chapitre 2, consiste en des enregistrements électrophysiologiques des NPC5s dans des tranches fines de cerveau de souris, combinés à (i) une imagerie ultrarapide pour enregistrer le potentiel membranaire (V_m) et les courants des Ca^{2+} et Na^+, et (ii) à des analyses pharmacologiques utilisant des bloqueurs sélectifs de canaux. Pour confirmer nos résultats expérimentaux, nous développons des modèles computationnels en utilisant le logiciel NEURON. Nous montrons que l'analyse du système de canaux PD ensemble est essentielle pour comprendre leurs interactions et leurs contributions individuelles au PA.

Chapitre 3 - Etude des canaux ioniques potentiel-dépendants impliqués dans la génération du potentiel d'action

Le courant de Na^+ associé au PA est caractérisé par une composante inactivante rapide et par une composante non-inactivante (Astman 2006). Les souris déficientes en $Na_v1.6$ sont caractérisées par une réduction du courant Na^+ non-inactivant (Katz et al. 2018), tandis que les souris déficientes en $Na_v1.2$ sont caractérisées par une réduction de l'excitabilité dendritique et de la fonction synaptique (Spratt et al. 2019). Enfin, il a été récemment découvert que les canaux $Na_v1.2$ sont non seulement perméables au Na^+, mais aussi au Ca^{2+}, et qu'un influx de Ca^{2+} médié par les CPDN se produit pendant le PA dans le SIA (Hanemaaijer et al. 2020). Le rôle précis de $Na_v1.2$ et $Na_v1.6$, cependant, et leurs contributions à la génération du PA restent à comprendre. Les dysfonctionnements de ces canaux sont à l'origine de troubles neuronaux chez les patients porteurs de mutations critiques dans leurs gènes codants. Dans le cas de $Na_v1.2$, plusieurs versions du gène provoquent divers syndromes neuropsychiatriques, notamment des épilepsies avec différents degrés de gravité, une déficience intellectuelle et un autisme avec ou sans crises d'épilepsie (Hedrich et al. 2019). De même, les canalopathies de $Na_v1.6$ sont associées à des cas rares mais graves d'encéphalopathie épileptique (Mantegazza et al. 2021). Il est clair que comprendre les processus de signalisation déclenchés par les CPDN est une étape importante pour le développement de stratégies thérapeutiques innovantes visant ces pathologies génétiques, mais cet objectif nécessite d'abord une compréhension approfondie de la contribution de chaque sous-type de canal à l'excitabilité neuronale.

Dans ce chapitre, nous démontrons que la perméabilité exclusive de $Na_v1.2$ au Ca^{2+} permet l'activation des CKACs BK dans le SIA. De cette façon, l'interaction entre $Na_v1.2$, médiateur de la montée du PA, et les canaux BK, qui régulent le pic et la phase précoce de la repolarisation du PA, façonne la forme de l'onde du PA au site de génération. Pour parvenir à cette importante conclusion, nous avons combiné des techniques d'imagerie ultrarapide avec des analyses pharmacologiques utilisant des bloqueurs de canaux sélectifs. Le plus importante des molécules utilisées cette étude est la G^1G^4-huwentoxin-IV, mutée à partir du huwentoxin-IV, un peptide de l'araignée-oiseau chinoise Haplopelma schmidti (Xiao et al. 2011). En utilisant ce puissant inhibiteur de $Na_v1.2$, suffisamment sélectif contre $Na_v1.6$, nous avons pu bloquer, de manière fiable, 30-40% de $Na_v1.2$ dans le SIA des NPC5. Ceci a permis l'étude détaillée des courants Na^+, des formes de l'onde V_m et des courants Ca^{2+}, associés à la génération du PA, dans le SIA. Nous avons ensuite analysé le changement de la forme de l'onde du PA produit par le blocage sélectif de différents types de CKAC, qui établit finalement l'interaction entre les canaux $Na_v1.2$ et BK. En particulier, plusieurs autres canaux contribuent au processus précoce de génération et de propagation du PA. Nous avons alors créé un modèle NEURON qui s'ajoute aux modèles précédemment développés pour le SIA des neurones pyramidaux L5 (Fleidervish et al. 2010; Hallermann et al. 2012; Hu et al. 2009; Kole et al. 2008) et qui reproduit nos résultats expérimentaux. Grâce à ce modèle, nous avons pu simuler l'interaction fonctionnelle entre $Na_v1.2$ et les canaux BK, et imiter les résultats expérimentaux obtenus en bloquant $Na_v1.2$ avec G^1G^4-huwentoxin-IV.

Chapitre 4 - Etude des canaux ioniques potentiel-dépendants impliqués dans la rétro-propagation du potentiel d'action dans la dendrite apicale

Dans le chapitre suivant, nous fournissons des preuves cinétiques d'une interaction physique et fonctionnelle entre les CPDC de type N et les CKAC de type BK qui proviennent à nouveau de l'analyse d'expériences d'imagerie ultrarapide du V_m et du Ca^{2+}. Plus précisément, nous avons analysé le rPA et le courant de Ca^{2+} associé à une résolution temporelle de 50 µs dans la dendrite apicale des neurones pyramidaux L5, et nous avons corrélé la cinétique de la forme de l'onde du rPA avec celle du courant Ca^{2+}. Les CKACs BK contribuent à la repolarisation du rPA avant le pic du courant Ca^{2+}. En particulier, cette contribution est exclusive de la partie proximale de la dendrite apicale (∼100 µm du soma), alors qu'il a été montré que ce phénomène est absent dans la partie distale des NPC5 (Bock and Stuart 2016). Nous avons ensuite construit un modèle NEURON qui a confirmé que nous pouvons expliquer un phénomène déclenché par le Ca^{2+}, se produisant avant le pic de courant de Ca^{2+} attendu, que si la source de Ca^{2+} et sa cible interagissent physiquement. Par conséquence, l'activation complète de la cible se produit avant l'équilibrage du Ca^{2+} dans le cytosol, finalement régi par la pente du courant Ca^{2+}. La première conséquence biophysique importante de cette découverte est que seule une fraction de l'influx initial de Ca^{2+} provenant d'une source particulière peut déclencher un processus, alors que le reste du Ca^{2+} contribue à l'augmentation de la concentration intracellulaire de Ca^{2+}. La deuxième conséquence importante est que, de cette façon, un CPDC peut réguler à la baisse l'influx global de Ca^{2+}, car il peut changer le profil du V_m pendant la phase d'ouverture des autres CPDC.

Chapitre 5 - Discussion et conclusions

Dans l'ensemble, nous proposons un rôle double et spatialement restreint des CKACs BK. Premièrement, en façonnant le PA générateur dans le SIA par son interaction avec $\mathrm{Na}_v1.2$. Ceci est dû à l'observation confirmée que les canaux $\mathrm{Na}_v1.2$ médient l'influx de Ca^{2+}. Il est important de noter que ce courant Ca^{2+} précoce, dont la cinétique est similaire à celle du courant Na^{+}, permet la liaison du Ca^{2+} à ses cibles avant que le PA n'atteigne son pic. Ceci est crucial puisque les CKACs BK nécessitent une liaison Ca^{2+} et une dépolarisation simultanées pour s'ouvrir (Cui et al. 2009). Au pic du PA, les canaux BK contribuent au courant K^{+} total qui contrebalance le courant Na^{+} non activé, avec les divers canaux K^{+} PD exprimés dans le SIA (Trimmer 2015). Ainsi, une diminution du courant $\mathrm{Na}_v1.2$ est contrebalancée par une diminution du courant BK, ce qui entraîne un élargissement de la phase précoce de la repolarisation du PA avec un changement modeste du pic du PA. L'interaction entre les canaux $\mathrm{Na}_v1.2$ et BK est donc un elément majeur du pic du PA et un régulateur clé de la forme du PA.

Deuxièmement, les canaux BK CKACs entraînent la repolarisation rapide au moyen d'un couplage fonctionnel avec les CPDCs de type N, pendant les rPAs dans la dendrite apicale. Comme les canaux BK peuvent s'activer à une échelle de temps inférieure à la milliseconde, la forme du rPA à proximité de son pic est régulé et, par conséquent, les autres conductances PD modulée, y compris les CPDC, ce qui se traduit finalement par une régulation du courant du Ca^{2+} cytosolique. La signification fonctionnelle de l'activation sub-milliseconde des CKACs BK menant à une régulation du courant de Ca^{2+} cytosolique reste uncompris. Il a été montré, dans les neurones pyramidaux de l'hippocampe CA1, que les BK CKACs facilitent le déclenchement à haute fréquence (Gu et al. 2007), mais dans ce cas, une grande contribution de ces canaux est observée dans la phase ultérieure de la repolarisation du rPA. En revanche, dans les neurones pyramidaux L5, les CPDC BK n'affectent pas les schémas de déclenchement mesurés dans le soma, mais les canaux BK dans les épines à faible volume de tête sont également activés localement par le Ca^{2+} synaptique, et leur rôle est de réguler à la baisse l'amplitude des potentiels synaptiques excitateurs (Tazerart et al. 2022). Par conséquent, si l'activation des canaux BK CKAC par les CPDC de type N est maintenue dans ces épines et se produit avant l'activité synaptique, cela pourrait empêcher la poursuite de l'activation des canaux BK par le Ca^{2+} synaptique, conduisant à une modulation de l'entrée synaptique. En ce qui concerne la régulation de l'élévation du Ca^{2+} cytosolique dans la masse dendritique, qui est observée dans cette étude, elle pourrait jouer un rôle dans la modulation du Ca^{2+} des protéines qui interviennent pendant l'activité de déclenchement.

L'analyse des contributions du système des différents canaux ioniques PD à la génération et à la rétro-propagation du PA a permis de découvrir le couplage fonctionnel entre les CKAC BK et les CPDC $\mathrm{Na}_v1.2$ et de type N, dans le SIA et la dendrite apicale, respectivement. Associées à nos résultats de modélisation, ces expériences fournissent une base pour étudier le dysfonctionnement des canaux ioniques PD dans les neuropathologies, telles que l'autisme et l'épilepsie.

Contents

List of Figures **xvii**

List of Tables **xix**

List of Abbreviations **xx**

1 Introduction **1**

1.1 Voltage gated ion channels: a brief overview 5

1.1.1 Voltage gated sodium channels 5

1.1.2 Voltage gated calcium channels 7

1.1.3 Potassium channels 9

1.2 The excitable brain 12

1.2.1 The membrane potential and passive electrical properties of neurons 12

1.2.2 Active properties of neurons: the action potential 13

1.3 Action potentials in layer 5 pyramidal neurons 16

1.3.1 Action potential generation in the axon initial segment . . . 18

1.3.2 Action potential back propagation into the apical dendrite . 21

1.4 Open research questions addressed in this thesis 26

1.4.1 Challenges when studying voltage gated sodium channels in the axon initial segment 26

1.4.2 Understanding voltage gated ion channel interaction and functional coupling in the apical dendrite 27

2 Methodology **29**

2.1 Cortical slice preparations 30

2.2 Electrophysiology 32

2.2.1 Choosing a brain slice 32

2.2.2 Identifying healthy pyramidal neurons 32

2.2.3 Establishing a patch 33

2.2.4 Electrophysiology recordings 34

2.3 Imaging 34

2.3.1 The imaging system 34

- 2.3.2 Fluorescent Indicators 37
- 2.4 Pharmacology 38
- 2.5 Experimental protocols 39
  - 2.5.1 Protocols used for the AIS 39
  - 2.5.2 Protocols used for the apical dendrite 40
- 2.6 Optical data analysis 40
  - 2.6.1 Calcium imaging 40
  - 2.6.2 Voltage imaging 42
  - 2.6.3 Sodium imaging 44
- 2.7 Statistical data analysis 45
  - 2.7.1 The Lilliefors test 45
- 2.8 Computational modelling 46
  - 2.8.1 In the axon initial segment 46
  - 2.8.2 In the apical dendrite 47
- 2.9 Methods extensions 48
  - 2.9.1 Cal520FF - a new calcium indicator 48
  - 2.9.2 Toxins to distinguish between Na$_v$1.2 and Na$_v$1.6 51
  - 2.9.3 Photosensitive G^{1}G^{4}K^{36}Huwentoxin-IV 54

3 Study of the ion channels involved in generating the action potential in the axon initial segment 60
- 3.1 The effect of blocking Na$_v$1.2 channels and VGCCs in the AIS . . . 61
  - 3.1.1 The selective block of Na$_v$1.2 reduces the Na$^+$ current associated with the AP waveform in the AIS 61
  - 3.1.2 The selective block of Na$_v$1.2 widens the generating AP waveform in the AIS 63
  - 3.1.3 The distal I$_{Ca}$ precedes the proximal I$_{Ca}$ in the AIS 65
  - 3.1.4 VGCCs mediate part of the Ca^{2+} influx in the AIS 67
  - 3.1.5 Na$_v$1.2 mediates Ca^{2+} influx associated with the AP in the AIS 68
- 3.2 The effect of blocking CAKCs in the AIS 70
  - 3.2.1 The block of CAKCs widens the AP in the AIS after blocking VGCCs 70
  - 3.2.2 The block of BK CAKCs widens the AP in the AIS preventing the widening caused by blocking Na$_v$1.2 73
- 3.3 The effect of blocking Na$_v$1.6 channels in the AIS 73
  - 3.3.1 Na$_v$1.6 does not mediate Ca^{2+} influx associated with the AP in the AIS 74
- 3.4 The Na$_v$1.2-BK channels interaction is mimicked by simulations in a NEURON model 76
- 3.5 Summary and significance 79

4 Study of the ion channels involved in action potenial back propagation in the apical dendrite 82

4.1 The effect of blocking VGCCs and CAKCs on the Ca^{2+} currents during a bAP . . . 83

4.1.1 The dendritic Ca^{2+} influx associated with the bAP is exclusively mediated by diverse VGCCs . . . 83

4.1.2 Blocking N-type VGCCs increases Ca^{2+} influx in the apical dendrite during a bAP . . . 86

4.1.3 BK CAKCs are activated by Ca^{2+} influx through N-type VGCCs during the bAP . . . 87

4.2 The effect of blocking VGCCs and CAKCs on the shape of the bAP 89

4.2.1 The peak of the inward I_{Ca} is delayed compared to the peak of the bAP . . . 90

4.2.2 The effect of N-type VGCC and BK CAKC coupling occurs in the first 500 µs after the AP peak . . . 90

4.2.3 The effect of blocking L-type VGCCs on the bAP waveform mimics the effect of SK CAKC block . . . 94

4.2.4 The block of T-type VGCCs decreases the bAP peak . . . 96

4.3 Simulations with a NEURON model reproduce the experimental results 97

4.3.1 The NEURON model reproduces the AP waveforms and changes in Ca^{2+} transients . . . 98

4.3.2 N-type VGCC and BK CAKC interaction is mimicked by simulations in the NEURON model . . . 101

4.4 Summary and significance . . . 104

5 Discussion 105

5.1 Challenges of working with brain slices . . . 106

5.2 A synergistic approach to understanding VG ion channel functioning 108

5.3 Voltage gated Na^+ channels in the AIS . . . 109

5.3.1 Channelopathies caused by $Na_v1.2$ mutations . . . 111

5.4 On the properties of BK CAKCs . . . 113

5.4.1 BK CAKC and $Na_v1.2$ interaction . . . 115

5.4.2 BK CAKC and N-type VGCC interaction . . . 116

5.5 VGCCs in the apical dendrite during AP back propagation . . . 117

5.5.1 Ca^{2+} electrogenesis and plasticity at the tuft of the apical dendrite . . . 119

5.6 Anterograde action potential propagation and neuronal firing . . . 122

5.7 Importance of sub-microsecond activation of Ca^{2+} binding proteins 123

5.8 Future perspectives . . . 124

List of Figures

1.1 Drawing from cortical cells by Ramón y Cajal 2
1.2 The ion channel super family 4
1.3 Amino acid sequence similarity and phylogenetic relationships of voltage-gated sodium channel α subunits 6
1.4 Sequence similarity of voltage-gated calcium channel $\alpha 1$ subunits . . 7
1.5 Classification of potassium ion channels 9
1.6 Phylogenetic tree for the K_v1–9 families 11
1.7 Electrical circuit representing a membrane 14
1.8 Recordings from a pyramidal cell 17

2.1 Dissection and slicing preparation 31
2.2 Patching a Layer 5 pyramidal neuron 33
2.3 Imaging setup and example recordings 35
2.4 Experimental protocols 41
2.5 Calcium imaging in L5PNs 42
2.6 Voltage imaging in the AIS 43
2.7 Calibration of the dendritic AP 44
2.8 Statistical assessment of the AP widening following pharmacological manipulation 47
2.9 Evaluation of the three low-affinity indicators Fluo4FF, OG5N and Cal520FF 49
2.10 Performance of Fluo4FF, OG5N and Cal520FF for ultrafast Ca^{2+} imaging and optical recording of Ca^{2+} currents 52
2.11 Selectivity of G^1G^4-Huwentoxin-IV (G^1G^4hwtx) 53
2.12 Selectivity of 4,9-Anhydrotetrodotoxin (attx) 55
2.13 Selectivity of $G^1G^4K^{36}$Huwentoxin-Nvoc 55
2.14 $G^1G^4K^{36}$hwtx-Nvoc assessments in L5 pyramidal neurons from mouse brain slices 57
2.15 Recovery from $G^1G^4K^{36}$hwtx-Nvoc 58
2.16 Sodium imaging with $G^1G^4K^{36}$hwtx-Nvoc 59

3.1 Effect of G^1G^4hwtx (block of Na_v1.2) on the Na^+ influx in the AIS 62

3.2 Effect of G^1G^4hwtx (block of $Na_v1.2$) on the AP waveform in the AIS 64
3.3 Calcium transients in the AIS 65
3.4 Analysis of the Ca^{2+} current (I_{Ca}) components mediated by individual VGCC types in the AIS 66
3.5 Effect of G^1G^4hwtx (block of $Na_v1.2$) on the Ca^{2+} influx in the AIS 68
3.6 Effect of blocking SK CAKCs, BK CAKCs or IK CAKCs on the AP waveform in the AIS 70
3.7 Effect of blocking SK CAKCs or BK CAKCs on the AP waveform in the AIS, after blocking VGCCs 72
3.8 Effect of G^1G^4hwtx on the AP waveform in the AIS after blocking BK channels 74
3.9 Analysis of the effect of 4,9-anhydrotetrodotoxin (attx) on the Na^+ influx in the AIS 75
3.10 Analysis of the effect of attx on the AP waveform in the AIS 77
3.11 Analysis of the effect of attx on the Ca^{2+} influx in the AIS 78
3.12 NEURON simulations of the AP generation in the AIS 80

4.1 Analysis of the diverse VGCCs mediating the Ca^{2+} transient associated with the bAP 84
4.2 Analysis of the blockade of N-type VGCCs using pd173212 86
4.3 Analysis of the blockade of N-type VGCCs after blocking BK CAKCs 87
4.4 Delay between the calcium current and the peak of the back-propagating action potential 91
4.5 Examples of the effects of the diverse VGCC and CAKC blockades on the bAP shape 92
4.6 Analysis of the effect of the diverse VGCCs on the bAP shape . . . 95
4.7 Analysis of the effect of the diverse CAKCs on the bAP shape . . . 97
4.8 Morphology of the layer 5 pyramidal neuron model in NEURON . . 98
4.9 Simulation of a bAP and Ca^{2+} current ~100 µm from the soma . . 100
4.10 Simulations on the effect of blocking VGCCs on the Ca^{2+} currents . 101
4.11 Simulations on the effect of blocking VGCCs and CAKCs on the bAP waveform 102
4.12 The functional coupling of BK CAKCs and N-type VGCCs simulated with the NEURON model 103

5.1 Schematic of voltage gated ion channel distributions in the AIS of L5PNs 111
5.2 Spectrum of mutations and phenotypes for *SCN2a*/$Na_v1.2$ 113
5.3 Schematic of voltage gated ion channel distributions in the apical dendrite of L5PNs 118
5.4 The effect of blocking N-type or T-type VGCCs on Ca^{2+} electrogenesis 120

List of Tables

1.1 Standard example of intracellular and extracellular concentrations of ions in neurons at a resting membrane potential around -70 mV . . 13

2.1 Excitation and emission of fluorescent indicators 36
2.2 List of chemicals used to block ion channels 38
2.3 List of toxins used to block ion channels 39

4.1 Wilcoxon rank non-parametric tests performed on the effects on Ca^{2+} transient produced by blocking N-type VGCCs and BK CAKCs . . 89
4.2 Lilliefors test to assess whether a set of values is consistent with a normal distribution performed on sample differences in V_m imaging experiments after blocking a channel and in control conditions . . . 94
4.3 Channel distribution in the apical dendrite in the computational model 99

List of Abbreviations

agatx	ω-Agatoxin IVA, a specific P/Q-type VGCC blocker derived from spider venom.
AIS	Axon initial segment
AP	Action potential
ASD	Autism spectrum disorder
attx	4,9-Anhydrotetrodotoxin, derived from tetrodotoxin and a partically selective blocker of Na$_v$1.6 channels
bAP	Back propagating action potential
BK	Large conductance calcium-activated potassium channel, also voltage gated.
BNIFS	Benign neonatal-infantile familial seizures
Ca^{2+}	Calcium ion
CAKC	Calcium-activated potassium channels, including BK, IK and SK.
Ca$_v$1	Group of voltage gated calcium channels encoded by CACNA1C, CACNA1D, CACNA1S and CACNA1F giving rise to the L-type calcium current
Ca$_v$2.1	Voltage gated calcium channels encoded by the CACNA1A giving rise to the P/Q-type calcium current
Ca$_v$2.2	Voltage gated calcium channels encoded by the CACNA1B giving rise to the N-type calcium current
Ca$_v$2.3	Voltage gated calcium channels encoded by the CACNA1E giving rise to the R-type calcium current
Ca$_v$3	Group of voltage gated calcium channels encoded by CACNA1G, CACNA1H and CACNA1I giving rise to the T-type calcium current
Cl$^-$	Chloride ion

cntx	ω-conotoxin-GVIA, a specific N-type VGCC blocker, isolated from the venom of the marine cone snail Conus geographus
g	Conductance
$\mathbf{g}_m$	Membrane conductance
G	Glycine
$\mathbf{G^1G^4hwtx}$	G^1G^4Huwentoxin-IV, derived from the venom of the Chinese bird spider Haplopelma schmidti is a potent blocker of VGNCs with a selectivity for $Na_v1.2$ over $Na_v1.6$ channels
$\mathbf{G^1G^4K^{36}hwtx}$	$G^1G^4K^{36}$Huwentoxin-IV, a mutated version of Huwentoxin-IV (two glycines (G) at positions 1 and 4, and a lysine (K) added to the protein at position 36), is a potent VGNC blocker
GOF	Gain of function
HCN	Hyperpolarization-activated cyclic nucleotide-gated cation channels.
hwtx	Huwentoxin-IV
I	Current
$\mathbf{I}_A$	A-type potassium current
$\mathbf{I}_{Ca}$	Calcium current
$\mathbf{I}_h$	Inward hyperpolarization-activated current generated by HCN channels
$\mathbf{I}_K$	Potassium current
$\mathbf{I}_{KDR}$	Delayed rectifier potassium current
$\mathbf{I}_M$	M-type potassium current
$\mathbf{I}_{Na}$	Sodium current
ibtx	Iberiotoxin, a specific blocker of BK channels originally isolated from Buthus tamulus scorpion venom
ICDEE	Infantile-childhood developmental and epileptic encephalopathies
ID	Intellectual disability
IK	Intermediate conductance calcium-activated potassium channel
ING-2	Na^+ indicator Ion Natrium Green-2
K	Lysine
$\mathbf{K^+}$	Potassium ion

KCNMA1	Gene encoding the α subunit of human BK CAKC
Kcnma1	Gene encoding the α subunit of mouse BK CAKC
KI	Knock-in
KO	Knock-out
L5PN	Layer 5 pyramidal neuron
LOF	Loss of function
LTP	Long-term potentiation
LTD	Long-term depression
Lys	Lysine
Na$^+$	Sodium ion
Na$_v$1.2	Voltage gated sodium channel type II, encoded by the SCN2A gene
Na$_v$1.6	Voltage gated sodium channel type VI, encoded by the SCN8A gene
NEIDEE	Neonatal early-infantile developmental and epileptic encephalopathies
NMDA	N-methyl-D-aspartate. NMDA receptors are ligant-gated glutamate receptors that mediate a Ca^{2+} flux
OG5N	Fluorescent calcium indicator Oregon-Green-BAPTA-5N
PN	Pyramidal neuron
PSP	Postsynaptic potential
R	Resistance
R$_m$	Membrane resistance
V	Voltage
V$_m$	Membrane voltage
VG	Voltage gated
VGCC	Voltage gated calcium channel
VGKC	Voltage gated potassium channel
VGNC	Voltage gated sodium channel
VSD	Voltage sensitive dye
S/N	Signal to noise ratio
SCN2a	Gene encoding the α subunit of human Na$_v$1.2

Scn2a	Gene encoding the α subunit of mouse $\mathrm{Na}_v1.2$
SK	Small conductance calcium-activated potassium channel
STDP	Spike time dependent plasticity

The brain is a world consisting of a number of unexplored continents and great stretches of unknown territory.

— Santiago Ramón y Cajal

1

Introduction

Contents

1.1 Voltage gated ion channels: a brief overview 5
- 1.1.1 Voltage gated sodium channels 5
- 1.1.2 Voltage gated calcium channels 7
- 1.1.3 Potassium channels 9

1.2 The excitable brain 12
- 1.2.1 The membrane potential and passive electrical properties of neurons 12
- 1.2.2 Active properties of neurons: the action potential 13

1.3 Action potentials in layer 5 pyramidal neurons 16
- 1.3.1 Action potential generation in the axon initial segment . 18
- 1.3.2 Action potential back propagation into the apical dendrite 21

1.4 Open research questions addressed in this thesis . . . 26
- 1.4.1 Challenges when studying voltage gated sodium channels in the axon initial segment 26
- 1.4.2 Understanding voltage gated ion channel interaction and functional coupling in the apical dendrite 27

The first recognition of individual brain cells, or neurons was driven by the pioneering work of Ramón y Cajal. His neuroanatomical studies (see figure 1.1), thanks to the Golgi staining method named after its inventor, showed the first evidence of the existence of axonal growth cones. Contrary to popular opinion at the time, he demonstrated that the relationship between neurons was not continuous, but that brain cells are individual cells (Finger 2000). His neuron doctrine laid the foundation for cable theory, which observes neural structures as circuits and uses mathematical models to calculate the electric current along passive membranes

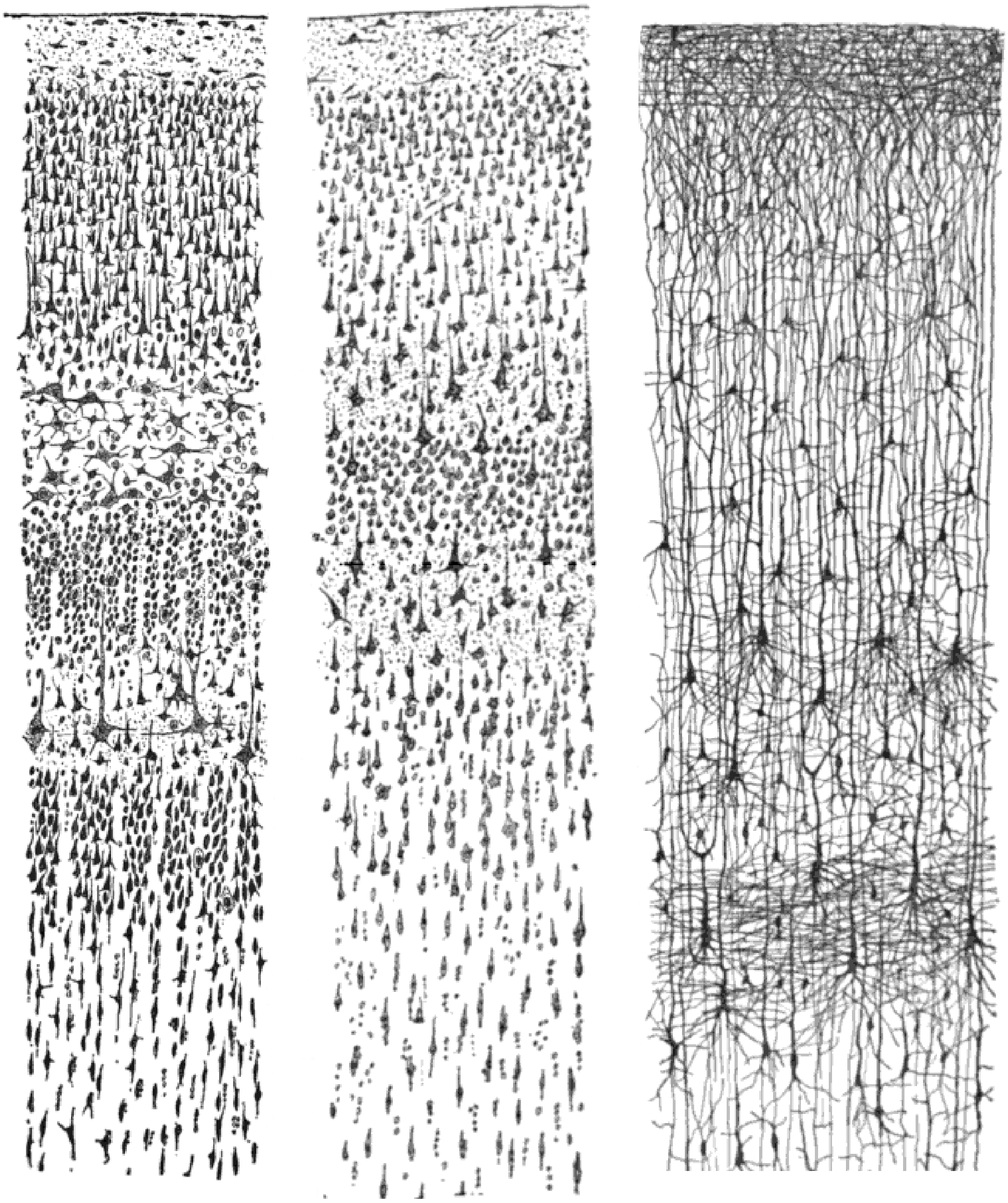

Figure 1.1: Drawing from cortical cells by Ramón y Cajal. Three different drawings side by side from a cross section of the neocortex. At the top layer I, at the bottom layer VI. From Newman et al. 2017

in neurons (Lorente de Nó and Davis 1947). In 1906 Cajal received the Nobel Prize in Physiology or Medicine together with Camillo Golgi *in recognition of their work on the structure of the nervous system.*

The first intracellular measurements of neuronal signals or action potentials (APs) became possible after the introduction of the Giant Squid Axon, which was large enough for insertion of regular electrodes (Young 1938). This set-up led to the most ground-breaking research in the field of electrophysiology by Alan Hodgkin and Andrew Huxley. They performed the first intracellular measurements of APs (Hodgkin and Huxley 1939). Later, they developed the first voltage clamp approach which led to a biophysical model of the AP, formalised by a set of mathematical equations. Their milestone work was published in five consecutive papers in 1952 (Hodgkin and Huxley 1952a,b,c,d; Hodgkin et al. 1952). This work became known as the Hodgkin-Huxley model of the AP and eventually earned them the Nobel Prize in Physiology or Medicine in 1963. In their mathematical analysis, Hodgkin and Huxley described the conductances of sodium (Na^+) and potassium (K^+) ions in the active propagation of the AP in the axon.

The first evidence that not only axons but also dendrites contain active conductance came shortly after that, from measurements in pyramidal cells in the rabbit (Cragg and Hamlyn 1955). Also around this time, the existence of calcium (Ca^{2+}) conductance in excitable membranes was introduced, due to the unexpected observation that electrical responses persisted in sodium-free media (Fatt and Ginsborg 1958).

Although Bernard Katz already submitted the idea of ion channels (del Castillo and Katz 1954), it took the invention of the patch clamp technique to allow the recording of currents through single channels (Neher and Sakmann 1976a,b; Neher et al. 1978). To form a *patch*, Neher and Sakmann (1976b) used suction to attach a micro-pipette filled with electrolyte solution to a neuronal membrane. By forming a high-resistance seal, a patch of the membrane is isolated which allows the measurement of the flow of currents across this section of the membrane.

Now over 100 different ion channels have been described and identified. Moreover, neurons may express dozens of different ion channels in their membranes, who's densities vary depending on the cellular compartment (Hille 2001). Ion channel expression and distribution make up an essential part of a cells machinery for neuronal signalling, and mutations in these channels can lead to severe diseases and disorders (Catterall et al. 2008). Therefore, the biophysical properties of ion channels are a fascinating field of research, and the subject of this thesis.

In the following sections, I will summarise the state of the art on voltage gated ion channel research and knowledge. I will explain the basic principles behind the resting membrane potential and ion conductance. Then I will focus on AP generation and backpropagation, specifically in layer 5 pyramidal neurons. Lastly, I will introduce the relevant ion channels and state the research questions addressed in this thesis.

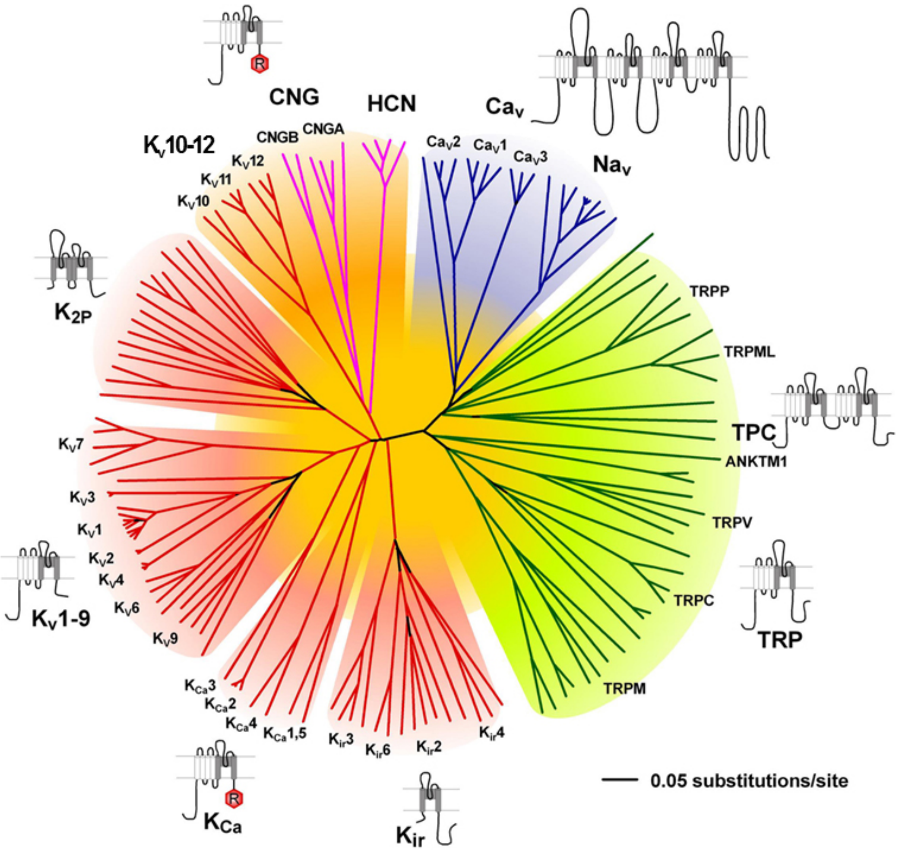

Figure 1.2: Representation of the amino acid sequence relations of the minimal pore regions of the voltage-gated ion channel superfamily. This global view of the 143 members of the structurally related ion channel genes highlights seven groups of ion channel families and their membrane topologies. Four-domain channels (Ca_v and Na_v) are shown as blue branches, potassium selective channels (K) are shown as red branches; cyclic nucleotide–gated channels are shown as magenta branches; and transient receptor potential (TRP) and related channels are shown as green branches. Background colors separate the ion channel proteins into related groups: light blue, Ca_v and Na_v; light green, TRP channels; light red, potassium channels, except K_v10–12, which have a cyclic nucleotide–binding domain and are more closely related to CNG and HCN channels; light orange, K_v10–12 channels and cyclic nucleotide–modulated CNG and HCN channels. The branches in the tree relate to the genetic similarities between the channel families. From Yu and Catterall (2004)

1.1 Voltage gated ion channels: a brief overview

Ion channels are pores spanning the cellular membrane and are formed by one or more proteins. Generally speaking, ion channel complexes consist of a central α subunit, and multiple auxiliary subunits, such as β and γ subunits, that modulate the functioning of the channel. Together, the pore-forming α subunits form the ion channel super family, which is composed of eight smaller families: voltage-gated sodium (Na_v or VGNC), calcium (Ca_v or VGCC), and potassium channels (K_v or VGKC); calcium-activated potassium channels (K_{Ca} or CAKC); cyclic nucleotide-modulated ion channels; transient receptor potential (TRP) channels; inwardly rectifying potassium channels (K_{ir}); and two-pore potassium channels (K_{2P}) (Yu and Catterall 2004) (see also figure 1.2). The ion channel members share a common pore-forming structure with varying ion selectivity filters, gating structures, ligand binding domains and voltage sensors. Here I will mostly focus on the voltage gated members.

1.1.1 Voltage gated sodium channels

After the recording of sodium currents by Hodgkin and Huxley (1952b), detailed analyses of sodium channel function led to the first mechanistic models of ion conductance (Armstrong 1981). These inspired the development of new techniques to study ion channel currents and purify these proteins, which eventually resulted in the discovery of the sodium channel protein (Beneski and Catterall 1980). By cloning the channel (Noda et al. 1986) and resolving parts of the three dimensional structure (Pérez-García et al. 1996; Rohl et al. 1999; Sato et al. 2001), various auxiliary subunits were identified, that complete the channel into a multimeric structure (Hartshorne et al. 1982). Now, ten different VGNC α subunits (Na_v1.1-9 and Na_vx) have been identified (figure 1.3), of which isoforms Na_v1.1, Na_v1.2, Na_v1.3, and Na_v1.6 are mainly expressed in the central nervous system.

Although the full structure of the sodium channel remains to be fully understood, we have already learned much about the function of the channel from its structure (Catterall 2000). For example, the principal α subunits are assembled from four homologous domains, each containing six membrane spanning helices (S1-S6). S1-S4 are the voltage sensing domains of the channels and are arranged around S5 and S6, which form a cylindrical shape with an opening, the pore, in the middle (Catterall et al. 2005a). VGNC α subunits associate with one or two β subunits, but they can also form functional channels on their own (Catterall 2017). However, Isom et al. (1995) showed that the β subunits are required for normal kinetics and voltage dependence of gating.

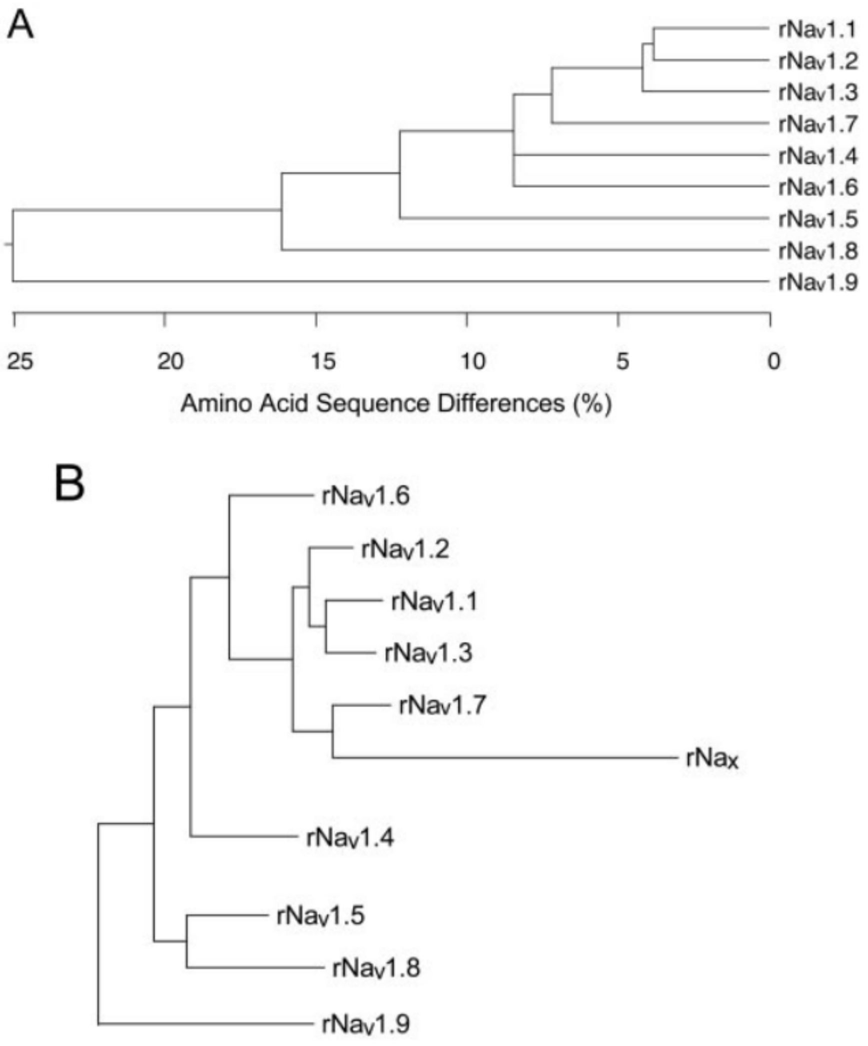

Figure 1.3: Amino acid sequence similarity and phylogenetic relationships of voltage-gated sodium channel α subunits. A, Amino acid similarity of rat VGNCs, showing a difference of ~8 % between Na$_v$1.2 and Na$_v$1.6. B, Phylogenetic tree from rat VGNC, drawn based on an analysis determining the genetic homology between the different subunits. From Catterall et al. (2005a).

Voltage-dependent activation of VGNCs is mediated by the movement of charge carried by the S4 helix through the membrane. These *gating charges* are stabilised by the formation of ion pairs with neighbouring residues. Essentially, voltage sensing is the exchange of those ion partners causing S4 to change position, forcing the S5 and S6 helixes to shift which forces the pore to an open state (Yarov-Yarovoy et al. 2012). Once opened, the selectivity of VGNCs for Na^+ is due to the side chains of four amino acids residues between S5 and S6 (Heinemann et al. 1992), which conduct Na^+ about 10-fold faster than K^+ or Ca^{2+} (Hille 1971). After rapid activation follows a second fast-gating process, namely the voltage-dependent fast inactivation, which is

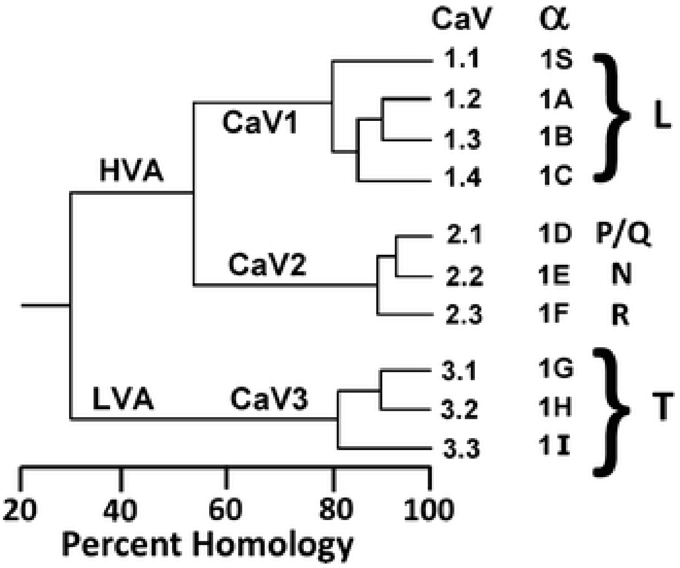

Figure 1.4: Sequence similarity of voltage-gated calcium channel $\alpha1$ subunits. Comparison of the membrane spanning regions and pore-forming sequences. Channels are mentioned by their protein name (Ca_v), gene ($\alpha1$ or CACNA1) and current type. HVA = high voltage activated, LVA = low voltage activated. Image from Pallone et al. 2018.

mediated by a cytoplasmic helix structure that blocks the pore within 1-2 ms after opening (Stühmer et al. 1989). This rapid inactivation controls sodium conductance, and allows VGNCs to open in rapid succession to mediate trains of electrical signals.

After inactivation VGNCs cannot reopen until they have recovered, which is time dependent and influenced by associated β subunits (Savio-Galimberti et al. 2012). This mechanism protects the cell and prevents firing during prolonged depolarization (Goldin 2003).

1.1.2 Voltage gated calcium channels

Similarly to VGNCs, the biochemical characterisation of VGCCs shows that these are large protein complexes composed of four or five subunits, which are encoded by multiple genes. The pore is formed by the $\alpha1$ subunit, which has four homologues domains which include the voltage sensor, whereas the other subunits and seconds messengers regulate the channel function. VGCCs are over 1000-fold more selective for Ca^{2+} over Na^{+} or K^{+} (Hess and Tsien 1984), which is determined by a glutamic acid repeat exactly in the same place as the selectivity filter in VGNCs (Heinemann et al. 1992).

Most VGCCs have auxiliary subunits such as the intracellular β subunit, γ subunit and membrane bound $\alpha2\delta$ complex. Although these subunits modulate the channel properties and functioning, the diversity of VGCCs arises from the different subtypes of the $\alpha 1$ subunit (figure 1.4) (Catterall et al. 2005b). VGCCs can be divided in high-voltage-activated (HVA) channels, which give rise to Ca_v1 (L-type current) and Ca_v2 channels (N-type, P/Q-type and R-type currents) and low-voltage-activated (LVA) channels which are the Ca_v3 channels (T-type current) (figure 1.4).

1.1.2.1 Ca_v1 calcium channels

L-type channels are present in all excitable cells, and many types of non-excitable cells as well (Tsien et al. 1991). In neurons, 90% of L-currents are mediated by the $\mathrm{Ca}_v1.2$ subunit, which are primarily present on post-synaptic sites, cell bodies and proximal dendrites (Hell et al. 1993; Sinnegger-Brauns et al. 2009). Their current was named L-type for long-lasting, as open channels do not inactivate significantly for hundreds of milliseconds (Scott et al. 1991).

1.1.2.2 Ca_v2 calcium channels

$\mathrm{Ca}_v2.1$ and $\mathrm{Ca}_v2.2$ channels are associated with the initiation of synaptic transmission at synapses (Olivera et al. 1994; Wessler et al. 1990). They share an intracellular loop with domains that can interact with synapse-associated proteins (Lévêque et al. 1994; Sheng et al. 1994). Neurotoxins produced by cone snails and spiders that target these channels specifically block fast synaptic transmission, thereby paralysing the organism (Dutar et al. 1989; Olivera et al. 1994).

$\mathrm{Ca}_v2.2$ gives rise to the P- and Q-currents through alternative splicing (Bourinet et al. 1999). The P-type channel is named for the Purkinje cell in which the current was first recorded (Regan et al. 1991).

N-type currents, mediated by $\mathrm{Ca}_v2.2$ VGCCs, were described together with L- and T-type channels by Nowycky et al. (1985) in dorsal root ganglion neurons. N-type channels, which received their name due to their difference from L- and T-type channels and primarily neuronal expression ('N' for neither or neuronal), were distinguishable because they required strong negative potentials for complete removal of inactivation (unlike L) and strong depolarizations for activation (unlike T) (Perez-Reyes 2003).

The last of the Ca_v2 channels is the $\mathrm{Ca}_v2.3$ or R-type channel, for residual or resistant, was the last VGCC to be identified as this channel is resistant to L-, N- and P/Q-type channel blockers (Randall and Tsien 1995). Not much is known about this channel, but expression of R-type channels in the cortex is mostly confined to the soma, with little channels in the dendrites (Yokoyama et al. 1995).

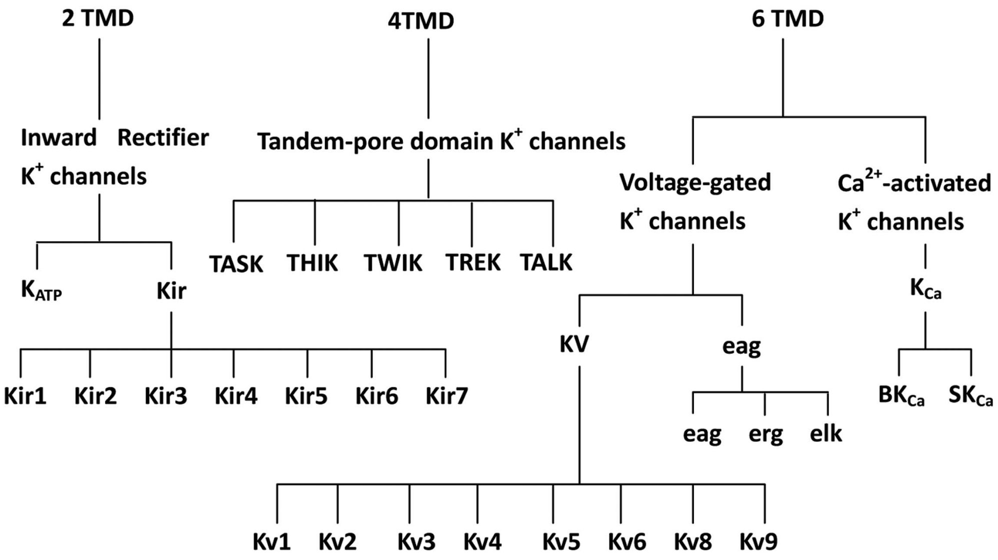

Figure 1.5: Classification of potassium ion channels. TMD, transmembrane domain; K_{ATP}, ATP-sensitive K^+ channel; Kir, inward-rectifier channel; K_v, voltage-gated K^+ channel; EAG, ether-á-go-go channel; K_{Ca}, Ca^{2+}-activated channel; BK_{Ca}, large conductance K_{Ca} channel; SK_{Ca}, small conductance K_{Ca} channel. From Zhong et al. (2013).

1.1.2.3 Ca_v3 calcium channels

T-type currents are mediated by $Ca_v3.1$-3. These channels have the smallest conductance of the VGCCs, but activate at much lower potentials than the HVA VGCCs, between -65 and -50 mV (Perez-Reyes 2003). T-type channels are known for their role in thalamic oscillations, due to their low-activation threshold that triggers rhythmic burst firing (Cueni et al. 2008). They are present in the neocortex as well, with highest expression in soma and dendrites (Child and Benarroch 2014; Talley et al. 1999).

1.1.3 Potassium channels

The potassium channel family is the largest known ion channel family, including several sub families: the voltage gated members, CAKCs, K_{ir}'s and K_{2P}'s (figure 1.5).

1.1.3.1 Voltage gated potassium channels

The VGKCs are responsible for the repolarisation of the AP, and their activation is triggered by a rise in membrane potential. Over 40 genes encode this large channel family, giving rise to extraordinary diversity (figure 1.6). The first VGKC was cloned from *Drosophila* before any biochemical purification of these channels

(Papazian et al. 1987). As for the other families, the pore is formed by the α subunit which has six membrane spanning domains, of which the positively charged S4 gives the channels their voltage sensitivity. In contrast to VGNCs, four channel subunits are required to form a functional channel, which may be homotetramers or heterotetramers formed from different subunits within the same family. In addition, accessory proteins modify individual channel characteristics, as do modifier subunits. This is a subgroup of channels that are not functional on their own, but modify or silence other VGKCs by forming heterotetramers. The K_v5, K_v6, K_v8 and K_v9 families belong to this group. Lastly, during protein production alternative splicing mechanisms and post-translational modifications may alter channel function (Gutman et al. 2005).

Because of this large diversity, it is easier to group these channels by their current characteristics. These will be discussed in more detail in later sections.

1.1.3.2 Calcium activated potassium channels

CAKCs are a small group of channels, which include a large (BK), intermediate (IK) and small (SK) conductance isoform. These channels are activated by Ca^{2+}, either through influx or from intracellular stores and allow K^+ through their pore. BK channels have two Ca^{2+} binding sites towards the C-terminus of the α-subunit, but are also voltage gated (Hille 2001). Binding of calcium or magnesium causes a shift in the activation curve of this channel towards more negative potentials, showing opening probability increases massively with the calcium concentration. At the same time, the pore of BK channels can open without involvement of the voltage sensor, but pore opening is favoured when the voltage sensor is activated. So, both Ca^{2+} and membrane depolarisation promote pore opening, and both Ca^{2+} binding and activation of the voltage sensor are favoured when the pore is opened (Cui 2010; Cui et al. 2009). SK and IK CAKCs are solely activated by calcium through interaction with calmodulin, a member of the endogenous Ca^{2+} buffer, at the C-terminus of the channel subunit (Schumacher et al. 2001).

Much of the research on the kinetics of voltage gated ion channels has been done in cell lines after cloning the channel. In physiological conditions however, and a central topic in this thesis, it is the synergy of these channels that determines electrical signalling and shapes APs. Before diving into channel interactions as well as their specific contributions I will first address the fundamentals of electrophysiology in neuronal membranes in the next sections.

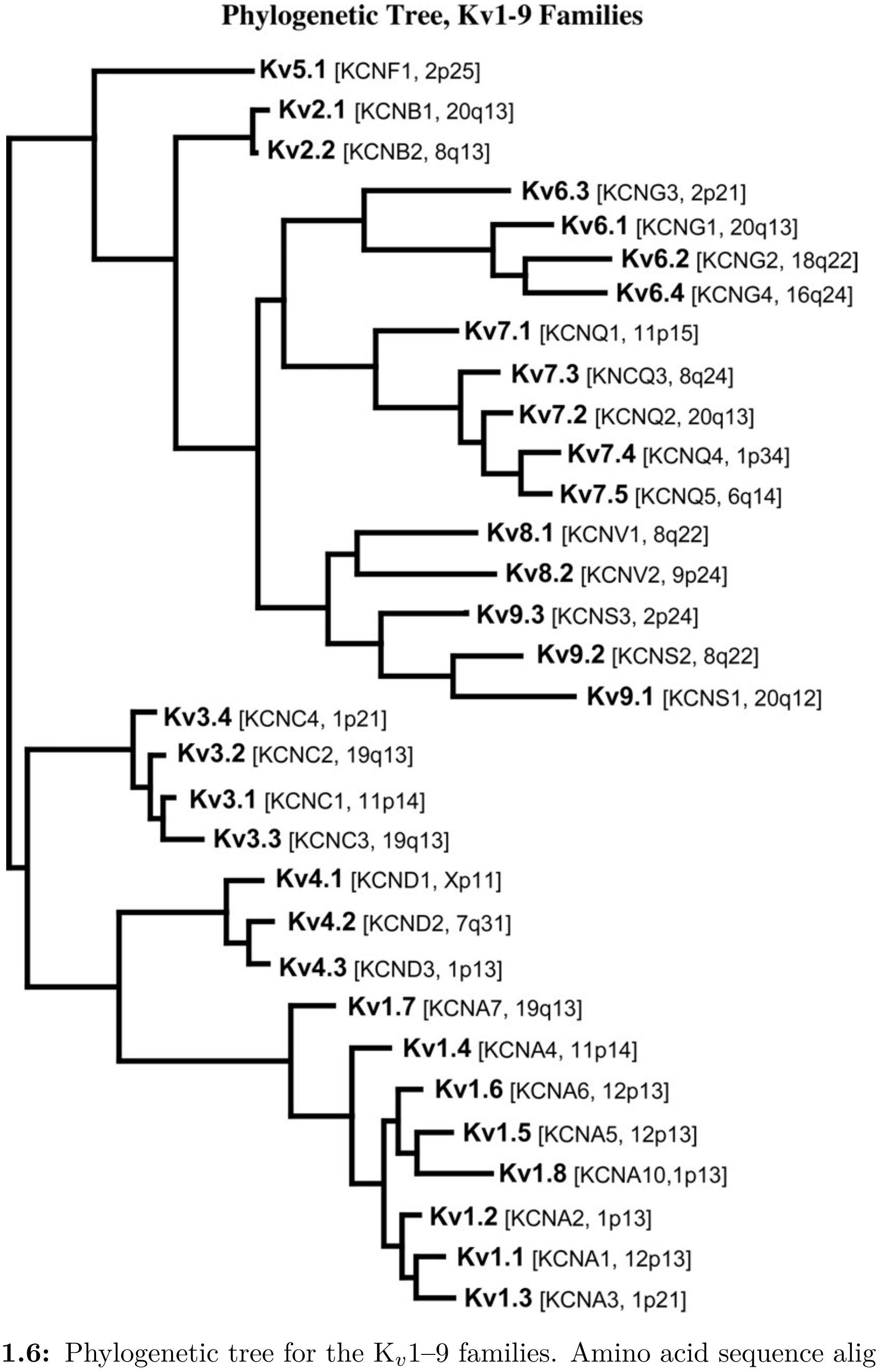

Figure 1.6: Phylogenetic tree for the K_v1–9 families. Amino acid sequence alignments of the human channel K_v proteins, indicating their genetic homology. From Gutman et al. (2005).

1.2 The excitable brain

1.2.1 The membrane potential and passive electrical properties of neurons

Neurons, and in fact all cells, have a *resting membrane potential* (V_m) due to the existence of an electrical potential across the membrane (Nicholls 2012). This membrane potential arises from different ion concentrations in the intra- and extracellular space, which is separated by the plasma membrane. This lipid bilayer is roughly 5 nm thick and is impermeable to water molecules and ions. Embedded in the membrane large protein complexes act like doorways between the cells' outside and the cytoplasm. These ion channels allow flow of selected ion species, in the same way metal wires allow electron flow. Thus, you can consider ion channels as conductance and use the same formalism of electrical circuits.

In a resting state, the intracellular of a neuron has relatively high concentrations of potassium and low concentrations of sodium (Na^+), calcium (Ca^{2+}) and chloride (Cl^-) (see also table 1.1 for a standard example of intra- and extracellular ion concentrations). Now for the purpose of demonstration, let us assume the cytosol roughly has an even number of cations (potassium (K^+)) and anions, as does the exoplasm although in lower concentrations. Then, we add passive ion channels, or leak channels, which are always open and allow the continuous passing of ions. We can consider a case in which K^+'s are allowed to pass the membrane; they will move with their concentration gradient. As the K^+'s diffuse outward, positive charges accumulate in the extracellular space and excess negative charges are left on the inside of the membrane. As a result, an electrical potential develops across the membrane, with a negative inside with respect to the outside. This electrical gradient slows the efflux of positively charged K^+'s, and when the potential becomes sufficiently large, further net efflux of K^+ stops. This potential is called the potassium equilibrium potential (E_K). At E_K, the effects of the concentration gradient and the potential gradient (together the electrochemical gradient) on ion flux through the membrane balance one another exactly and is described by the Nernst equation:

$$E_{ion} = \frac{RT}{Z_{ion}F} \ln \frac{[X]_{out}}{[X]_{in}}$$

Where $[X]_{in}$ and $[X]_{out}$ are the intracellular and extracellular concentrations of the ion in question, respectively. E_{ion} is the Nernst potential for that ion (R is the universal gas constant, T is the temperature, Z_{ion} is the number of electrons transferred, and F is the Faraday constant). However, to predict the resting membrane potential of a neuron one must consider Na$^+$ and Cl$^-$ in addition to K$^+$. Goldman (1943) and Hodgkin and Katz (1949) achieved this by assuming independent flow of these three ion species through the membrane and a total current equalling zero in a rest state. The resulting GHK equation for the reversal potential is as follows:

$$E_m = \frac{RT}{Z_x F} \ln \frac{P_K[K^+]_{out} + P_{Na}[Na^+]_{out} + P_{Cl}[Cl^-]_{in}}{P_K[K^+]_{in} + P_{Na}[Na^+]_{in} + P_{Cl}[Cl^-]_{out}}$$

Where P_K, P_{Na} and P_{Cl} are the membrane permeabilities to K$^+$, Na$^+$ and Cl$^-$, respectively. As expected, the GHK equation is equal to the Nernst equation when the permeability of ions is zero except for one species. The assumption here is that the permeability is not voltage dependent, but applies to open channels (Offner 1991). However, in a rest situation the membrane is about 20 fold more permeable to potassium compared to sodium (Frankenhaeuser 1960, 1963; Hodgkin and Keynes 1955). With physiological membrane permeabilities of the relevant ions therefore, the equilibrium membrane potential is around -70 mV (see also table 1.1) (Hille 1970).

Ion Species	**Intracellular** mM	**Extracellular** mM	**ratio in:out** in:out	**E$_{ion}$ at 37°C** mV
K^+	100	5	20:1	-80
Na^+	15	150	1:10	62
Ca^{2+}	0.0002	2	1:10000	123
Cl^-	13	150	1:12	-65

Table 1.1: Standard example of intracellular and extracellular concentrations of ions in neurons at a resting membrane potential around -70 mV.

1.2.2 Active properties of neurons: the action potential

At that time, Hodgkin and Huxley (1952b) did not realise voltage gated ion channels were responsible for the depolarisation and repolarisation of the membrane potential during an AP. However, they observed that APs are characterised by a sharp increase in membrane potential after passing a certain threshold (depolarisation), after which the potential peaks and then decreases towards the resting potential (-70 mV) (repolarisation). This may be followed by an after-hyperpolarisation (AHP) during which the membrane potential falls below the resting membrane potential before slowly recovering. They also found that the rise and fall of the membrane potential was accompanied by a large influx of Na$^+$, followed by an efflux of K$^+$. These conductances were the correct magnitude and time course to

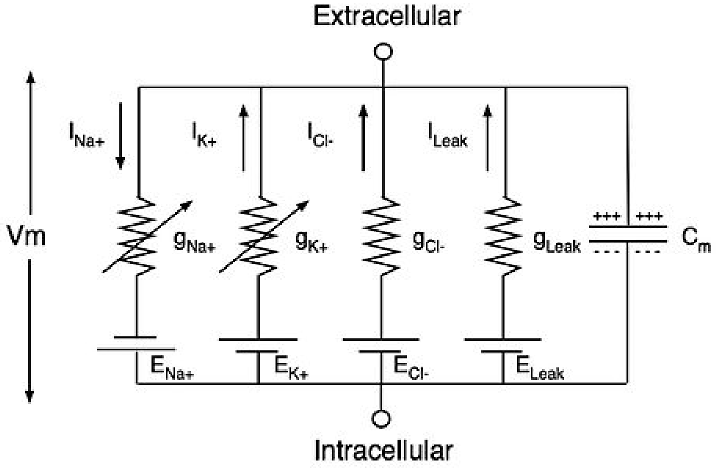

Figure 1.7: Electrical circuit representing a membrane. Where $g_{ion} = 1/R_{ion}$. g_{Na+}, g_{K+} and g_{Cl-} vary with time and membrane potential, the other components are constant. Adapted from Hodgkin and Huxley (1952a).

account exactly for the magnitude and time course of the AP itself (Hodgkin and Huxley 1952c). This is because besides passive ion channels, neurons express a set of active ion channels which have open, closed and inactivated states which dependent on the membrane potential, ligand interaction and ionic concentrations (Bowman 1990). During depolarisation sodium conductance increases (producing a sodium current or I_{Na}) due to the activation of VGNCs and the membrane potential rushes towards E_{Na}. As depolarisation increases, VGKCs activate, introducing an inward K^+ current (I_K). As the membrane potential becomes more positive, more and more potassium channels open, allowing additional current to flow through the membrane, until the reversal potential is reached. This is the potential during which sodium influx and potassium efflux are net zero again, directly after which the I_K becomes the larger current and VGNCs inactivate. This drives the repolarisation phase during which the membrane potential plummets towards E_K due to efflux of K^+. The following hyperpolarisation of the membrane is explained by the fact that VGKCs remain activated whereas all VGNCs are inactivated. The influx of K^+ drives the membrane potential towards E_K, which is lower than the resting membrane potential (Hodgkin and Huxley 1952a). From the above we already see that the time courses of the I_{Na} and I_K are very different. The I_K is much delayed relative to the onset of the I_{Na}, but once developed, it remains high throughout the duration of the AP. The I_{Na}, on the other hand, rises much more rapidly but then inactivates rapidly. VGNCs specifically have two inactivation gates, one time dependent following the *ball-and-chain* model, and one voltage dependent.

The magnitude of the ionic currents depend on the conductance (g_{ion}) and on the driving force ($V_m \breve{}\, E_{ion}$), so that

$$I_{ion} = g_{ion}(V_m - E_{ion})$$

The total ionic current then becomes the summation of the individual ionic currents and the membrane capacity current. We can deduce the total membrane current in a cell with sodium and potassium channels is described by the following equation:

$$I = I_{C_m} + I_m$$

With

$$I_{C_m} = C_M \frac{dV_m}{dt}$$

and

$$I_m = g_{Na}(V_m - E_{Na}) + g_K(V_m - E_K) + g_l(V_m - E_l)$$

Where C_M is the membrane capacity and g_l and E_l are the leak conductance per unit area and leak reversal potential, respectively. This electrical behaviour of the membrane may also be represented by a network as shown in figure 1.7.

From these basic components and using a series of voltage clamp experiments where they varied extracellular K^+ and Na^+ concentrations, Hodgkin and Huxley developed a model in which the properties of an excitable cell are described by a set of four differential equations:

$$I = C_M \frac{dV_m}{dt} + \bar{g}_{Na} m^3 h (V_m - E_{Na}) + \bar{g}_K n^4 (V_m - E_K) + \bar{g}_{leak}(V_m - E_{leak})$$

With

$$\frac{dn}{dt} = \alpha_n(V_m)(1-n) - \beta_n(V_m)n,$$

$$\frac{dm}{dt} = \alpha_m(V_m)(1-m) - \beta_m(V_m)m,$$

and

$$\frac{dh}{dt} = \alpha_h(V_m)(1-h) - \beta_h(V_m)h$$

Where α and β are rate constants which depend on voltage, $\bar{g}$ is the maximal value of the conductance. n, m and h are probabilities between 1 and 0 that are associated with K^+ channel activation, Na^+ channel activation and Na^+ channel inactivation, respectively. Although this is a simplified model (without Ca^{2+} and Cl^- currents), these equations are used to this day to characterise voltage gated ion channels and develop computational models of ion channels.

Ion channel expression varies between neuronal cell types, and between compartments of the same cell. For example, inward currents through VGCCs can enhance and prolong depolarization. At the same time, calcium entry into the cell can generate outward potassium currents through CAKCs and thereby shorten the AP. Thus, the characteristics of any given AP depend on which types of ion channels are present in the membrane and on how currents through these channels interact (Nicholls 2012).

Now that electrical properties of neuronal membranes have been explained, I will turn towards the neurons discussed in this thesis, namely layer 5 pyramidal neurons (L5PN).

1.3 Action potentials in layer 5 pyramidal neurons

Pyramidal cells are one of the most abundant neurons in the cerebral cortex of mammals (Elston 2003). These large cells are the primary source of cortical output and therefore have to be decisive integrators in cortical circuits (Hoffman 2013). Pyramidal neurons have distinct features, with a pyramid-shaped cell body, a long region-spanning axon and a bifurcating tree of dendrites. The dendritic tree has two distinct domains, the basal and apical dendrites. Basal dendrites are usually short, whereas one large apical dendrite extends from the soma giving rise to bifurcating oblique dendrites at variable distances from the soma and ending in the tuft (Spruston 2008). L5PNs receive the bulk of their excitatory synaptic input directly on the basal, apical and oblique dendrites, whereas inhibitory input is mostly received by the soma, axon initial segment and terminal tufts (Ramaswamy and Markram 2015). Local incoming signals from individual branches are summed, making dendrites coincidence detectors. Depending on the strength of these signals, forward propagating potentials may reach the soma, surpass the generation threshold and trigger an AP. Importantly, dendrites are not passive conductors, and excitatory input can trigger VGCC activation, generating local Ca^{2+} spikes (Markram and Sakmann 1994).

The site of AP generation in L5PNs, and in fact most neurons, is the axon initial segment (AIS). The AIS is first stretch of the axon and spans from the soma to the first myelinated section. Myelin is an insulating layer allowing fast passive

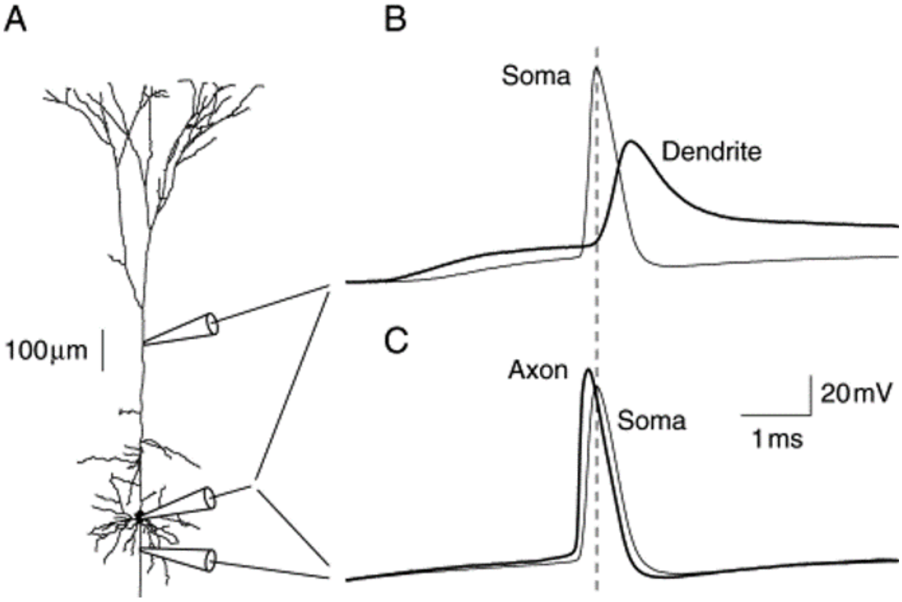

Figure 1.8: Recordings from a pyramidal cell. A, a layer 5 pyramidal cell with recording pipettes in the soma, axon and dendrite. B, recording from the soma and dendrite. From the soma a recorded AP travels down the dendrite (AP back propagation). This is apparent from the delay in the AP peak at the dendrite recording, compared to the soma. C, same recording from the soma, now paired with an axonal recording. The AP originates in the axon and travels back into the soma, as the axonal signal precedes the somatic recording. Image from Stuart et al. 1997b

propagation of generated APs towards the end of the axon. It was demonstrated the AIS is the site for AP generation through simultaneous whole-cell recordings from the AIS, soma and apical dendrite, showing synaptic stimulation always generates an AP at the AIS before the soma and independent of dendritic potentials (figure 1.8). In addition, they observed that once generated, APs propagate back into the dendrites (Stuart et al. 1997a,b). These back propagating APs (bAP) attenuate along the dendrite (figure 1.8B) (Waters et al. 2005), which is partly due to dendritic VGNC expression, which is about 30-fold lower compared to the AIS (Kole et al. 2008). bAPs rely on those VGNCs to drive the bAP towards the tuft in layer 1 where the apical dendrite bifurcates and where a burst of bAPs can trigger calcium electrogenesis, a large calcium spike (Stuart et al. 1997a; Williams and Stuart 2000). Attenuation of signals propagating from dendrite to soma is less compared to the decline of bAPs (Nevian et al. 2007).

In the next sections, I will focus on two parts of APs when triggered at the soma, specifically AP generation in the AIS and its subsequent back propagation in the proximal apical dendrite. I will explain how voltage gated ion channels are involved in these processes, and describe the current state of the art. As the research reported in this thesis has been exclusively performed with mice, the following numbers and measurements relate to the mouse as animal model unless stated otherwise.

1.3.1 Action potential generation in the axon initial segment

As mentioned, the AIS is where the AP is generated and shaped (Leterrier 2016, 2018). The whole AIS is ∼40 um long, has a semi-conical shape and separates the soma from the axon. The AIS can be defined and distinguished from the distal axon by its molecular composition and the lack of myelination. AIS proteins are organised in a layered fashion from microtubules to the plasma membrane. An important component of this scaffolding is ankyrin G, which is used as an AIS-marker due to its high concentration. Ankyrin G is involved in the anchoring of ion channels in the AIS. Its interaction with specifically VGNCs results in a 30-fold increase in density of these channels compared to dendrites.

1.3.1.1 Voltage gated sodium channels in the axon initial segment

In their AP generation experiments, Stuart et al. (1997a) showed the site of initiation is at least 30 µm from the soma. This is supported by the observation that VGNCs in the AIS are activated by more hyperpolarised potentials compared to somatic VGNCs (Colbert and Pan 2002). Indeed, activation of VGNCs is the first step in AP initiation. The sodium current in the AIS is characterised by a fast inactivating component and a persistent or non-inactivating current (Astman 2006; Filipis and Canepari 2021). To test the origin of the persistent Na^+ current Astman and colleagues applied TTX at different positions next to L5PNs in rat brain slices. They found that the persistent current remained unaffected by TTX application on the dendrite or soma, but gradually decreased with distance from the axon until around 50 µm from the soma there was no persistent current left after adding TTX. This suggests VGNC responsible for the persistent current are highest expressed in the AIS in a non-linear fashion.

$Na_v1.2$ and $Na_v1.6$ are the two VGNCs expressed in the AIS (Tian et al. 2014). Their distribution as well as biophysical properties have a unique contribution to the AP shape. During early development $Na_v1.2$ is the only isoform expressed in the axon (Gazina et al. 2015). After the first postnatal week in mice however, part of $Na_v1.2$ in the AIS is replaced by $Na_v1.6$. Using immunostainings, Hu et al. (2009) showed differential localisation of $Na_v1.2$ and $Na_v1.6$ in the AIS in adult rats. In the proximal AIS $Na_v1.2$ is the dominant VGNC whereas $Na_v1.6$ channels are dense between 30 and 50 µm from the soma, suggesting their direct involvement in AP initiation in the distal AIS. In addition, they confirmed the observation of Colbert and Pan (2002) that the activation threshold of VGNCs in the distal AIS is lower compared to the proximal part and soma.

To study the electrophysiological properties of the two Na^+ channels, Rush et al. (2005) expressed TTX-resistant versions of the channels in dorsal root ganglion neurons which enabled them to record both channels in isolation from the other. They observed neurons expressing $Na_v1.6$ displayed significantly more hyperpolarised activation values compared to neurons expressing $Na_v1.2$, which fit with the prediction made by Hu et al. (2009) that $Na_v1.6$ initiates the AP. Furthermore, their research showed that $Na_v1.6$ has a persistent current, as was previously shown in HEK293 cells (Burbidge et al. 2002), larger than the non-inactivating current of $Na_v1.2$ (Rush et al. 2005). Indeed, $Na_v1.6$ deficient mice show a reduction in the persistent sodium current (Katz et al. 2018). Interestingly, Katz et al. (2018) found that after $Na_v1.6$ deletion the full length of the AIS was occupied by $Na_v1.2$. Even more strikingly, they observed that APs were still generated in the AIS and the hyperpolarising shift in VGNC activation compared to channels in the soma was maintained. They concluded that the molecular environment of the AIS imposes certain properties to the VGNC present in the AIS, for instance by recruiting auxiliary subunits that influence gating. Thus, it is likely there is another benefit to the precise localisation of $Na_v1.6$ and $Na_v1.2$ channels in the AIS.

$Na_v1.2$ depletion studies showed impaired AP generation in developing, but not in mature excitatory neurons (Spratt et al. 2019). In addition, $Na_v1.2$ loss resulted in reduced AP backpropagation into dendrites, confirming the localisation-based theory of Hu et al. (2009) that $Na_v1.2$ promotes backpropagation of the generated AP into the soma.

Finally, it was recently shown that besides Na^+, $Na_v1.2$ channels are also permeable to Ca^{2+} (Hanemaaijer et al. 2020). While performing calcium imaging in rat brain slices they observed that Ca^{2+} currents were not only sensitive to VGCC blockers but also TTX. Subsequent expression of $Na_v1.2$ channels in HEK cells showed a TTX-sensitive internal calcium rise upon stimulation. This adds another possible function of $Na_v1.2$ as CAKC activator.

1.3.1.2 Potassium and calcium channels in the axon initial segment

Before it was suggested $Na_v1.2$ channels are also permeable to Ca^{2+}, Yu et al. (2010) showed Ca^{2+} currents in the AIS are mediated by P/Q-type and N-type VGCCs. In their study they showed ω-agatoxin IVA and ω-conotoxin GVIA blocked intracellular rises in Ca^{2+} in the AIS. In addition, they observed that blocking these VGCCs slowed AP repolarisation and increased neuronal excitability, suggesting reduced activation of CAKCs. Indeed, BK CAKCs have been identified in axonal segments in hippocampal neurons (Knaus et al. 1996). However, the possible functional coupling between VGCCs and CAKCs in the AIS specifically has never been reported.

Furthermore, little is known about the organisation of VGCCs in the AIS. Recently, Lipkin et al. (2021) showed that T-type VGCCs currents occur in spatially restricted hotspots, whereas Ca^{2+} influx through HVA VGCCs is more diffuse along the AIS. In addition, they show a coupling of T-type channels to calcium release from intracellular ryanodine receptors-dependent stores, an association which had been suggested before (Yang et al. 2016).

Lastly, VGKCs play a dominant role in repolarising the AP, modulating the firing threshold and shaping the AP waveform (Kang et al. 2000; Kole et al. 2007). We can distinguish three major groups in VGKCs, the delayed rectifier channels, the channels giving rise to the A-type or transient current (I_A) and the M-type current (I_M). The delayed rectifier potassium channels allow a sustained potassium efflux with a delay after membrane depolarisation (I_K). This outward current is mostly mediated by K_v1, and some K_v2 channels. They repolarise the membrane after the AP, are activated around the AP peak and show little or slow inactivation. The A-type current is distinguished from the delayed rectifier current by rapid rates of inactivation, and is mediated by K_v3 and some K_v4 channels. This current contributes to controlling repetitive firing frequencies and AP back propagation by rapid activation when depolarisation follows a hyperpolarisation (Guan et al. 2011; Gutman et al. 2005). Finally, K_v7 channels generate the M-current, which is a slowly activating and deactivating potassium conductance that plays a critical role in determining the subthreshold excitability of neurons (Brown and Passmore 2009).

Although there is high variability concerning VGKC expression in L5PNs (Guan et al. 2018), some general observations about VGKC densities in the AIS can be made (Trimmer 2015). To start, M-type VGKCs are compartmentalised in more distal regions (Battefeld et al. 2014). The same was observed of delayed rectifier K_v1 channels. K_v1 channels are highly expressed, with a 10-fold increase in channel density over the first 50 µm of the AIS (Kole et al. 2007). In their article, Kole et al. (2007) show K_v1s have fast activation kinetics that shorten the duration of axonal APs, as well as increase the amplitude of the after-hyperpolarization. Another member of the delayed rectifier VGKCs, $K_v2.1$ is present in low densities over the whole AIS (King et al. 2014). On the other hand, A-type K^+ channels are rarely recorded in the AIS, contrary to soma or dendrites where these channels are abundant (Colbert and Pan 2002).

To conclude this section, the AIS is a complex segment where the AP is generated through the interplay of multiple voltage gated ion channel families. Although much time and effort has been put into understanding the exact mechanism of AP generation, many uncertainties remain, such as the interaction of CAKCs with VGCCs which has been observed in other neuronal compartments (Vierra and Trimmer 2022), as well as the importance of Ca^{2+} entry through $Na_v1.2$ channels. Before going into these questions however, I will introduce and summarise the back propagation of a newly generated AP into the soma and beyond.

1.3.2 Action potential back propagation into the apical dendrite

As hinted at above, an AP triggered at the AIS not only travels down the axon, but also back propagates into the dendrite known as AP back propagation (Stuart and Sakmann 1994). The bAP is associated with a fast increase of dendritic Ca^{2+} concentration. This is associated with several neuronal events, such as synaptic integration and plasticity (Bereshpolova et al. 2007; Frick et al. 2004), the generation of calcium spikes (Larkum et al. 1999a), dendritic neurotransmitter release (Kaiser et al. 2004; Kreitzer and Regehr 2002; Zilberter et al. 1999) and the shaping of incoming synaptic signals (Bloodgood and Sabatini 2007; Waters et al. 2005). This calcium influx is mediated almost exclusively by VGCCs (Bloodgood and Sabatini 2007).

The most direct approach to study bAPs is through dendritic recordinds, using either sharp electrode impalement (Llinás and Sugimori 1980) or the patch clamp technique (Hamill et al. 1981) (see also figure 1.8A). This only allows recording from a single dendritic location however, which is why fluorescent imaging gained in popularity to study bAPs (Antic 2003; Antic et al. 1999; Kaiser et al. 2004). Using fluorescent voltage sensitive dyes and calcium indicators, one can record signals from many locations along the dendrite. Using these approaches the function of bAPs were studied extensively over the years.

1.3.2.1 The role of back propagating action potentials

One effect of bAPs is apparent from their influence on excitability. bAPs can lower the threshold for anterograde propagating postsynaptic potentials (PSP), thereby stimulating propagation towards the soma and subsequently AP generation in the AIS. Specifically, the interaction of a bAP with excitatory input from the distal dendrite can generate a *back-propagation activated* Ca^{2+} *spike* which can drive a short burst of APs at the soma (Larkum et al. 1999b, 2001; Williams et al. 1999).

In addition, there is evidence of long-term changes in efficacy of synapses through long-term potentiation (LTP) or long-term depression (LTD). Whether synaptic efficacy increases or decreases depends on the coincidence of the presynapic AP and bAP. This *spike time depend plasticity* (STDP) is thought to be dependent on bAP-mediated dendritic Ca^{2+} influx through NMDA receptors. Koester and Sakmann (1998) compared Ca^{2+} transients in spines of L5PNs evoked by the coincidence of excitatory PSPs and bAPs. They found that the amplitude of Ca^{2+} transients depended critically on the order and delay of PSPs and bAPs. Indeed, buffering postsynapic Ca^{2+} using BAPTA prevents STDP (Nevian and Sakmann 2006), as does blocking NMDA receptors (Inglebert and Debanne 2021).

In addition, L5PNs are sensitive to a critical frequency of bAPs between 60-200 Hz. A short train of 3-5 bAPs can trigger large regenerative potentials in the tuft of the apical dendrite. These potentials, named calcium electrogenesis, are mediated by a large VGCC-dependent Ca^{2+} influx (Larkum et al. 1999a). In distal basal dendrites a train of bAPs also triggers a Ca^{2+} spike, whereas single bAPs attenuate. Interestingly, differences in the ability of single APs and AP bursts to invade distal basal dendrites were regulated by fast-inactivating A-type VGKCs (Kampa and Stuart 2006).

In summary, bAPs seem to act as a retrograde messenger informing the input of a neuron at the synapse, about the output in the form of the axonal AP of that same neuron. This plays an important role in STDP, as the timing of the bAP to the synaptic input or PSP determines whether the synapse experiences LTP or LDP. However, to drive STDP bAPs need to reach the distal dendrite. Single bAPs, which undergo significant attenuation, often fail to activate NMDA receptors, whereas a dendritic calcium spike caused by a train of bAPs is effective at removing the voltage dependent magnesium block of NMDA receptors. The extent of bAPs and dendritic electrogenesis are therefore expected to play an important role in regulating the degree of synaptic NMDA receptor activation and so plasticity (Kampa and Stuart 2006; Ramaswamy and Markram 2015; Waters et al. 2005).

1.3.2.2 Voltage gated calcium channels during action potential back propagation

One study investigating the contribution of the different HVA VGCCs to the total calcium current in cortical pyramidal cells found that L-, P-, N-, Q- and R-type currents contribute 22% (±10), 19% (±12), 26% (±14), 24% (±12) and 13% (±7) to the total calcium current, respectively (Stewart and Foehring 2000). In the study, dissociated neurons in culture were patched, and the above currents were blocked in sequence. The left over current was named the R-type current and was blocked by cadmium. In agreement with the above findings, the contribution of L-type channels to the calcium current is about 30% (±9), and that of N-type currents 26% (±3) according to another study (Sun et al. 2003). In summary, L-type VGCC contribute most to the Ca^{2+} current during the bAP, but all HVA channels are expressed (Almog and Korngreen 2009; Giffin et al. 1991; Lorenzon and Foehring 1995; Stewart and Foehring 2000). Also, experiments recording Ca^{2+} currents along the dendrite found that the contribution of the various VGCC subtypes did not change along the dendrite (Almog and Korngreen 2009). This is confirmed by immunohistochemistry studies (Hell et al. 1993; Sinnegger-Brauns et al. 2009; Westenbroek et al. 1995).

The issue with the percentages reported above is that these values were calculated by simple subtraction using pharmacological data. This does not give the real contribution of that channel to the total I_{Ca}, because blocking one channel subtype causes a change in the membrane potential. Since the channels are voltage gated, this change in V_m changes the contribution of the other channels to the total I_{Ca}. Therefore, it is unhelpful to subtract the current with blocker from the total current. To extract individual VGCC subtype contributions a synergistic approach would give more information, as the involved channels have to be analysed together.

Another observation from the study done by Stewart and Foehring (2000) is that they ignored the T-type VGCCs, meaning their R-current might comprise both $Ca_v2.3$ and Ca_v3 channels. The apparent lack of T-type currents was also postulated in another study where they performed nucleated patches in L5PNs (Almog and Korngreen 2009). Using 5mM barium in the extracellular solution of the patches to extract clean channel currents, they showed a maximum total current around 15 mV. Subsequent inactivation of inward currents showed two components, of which the first component was blocked by SNX-482, a specific R-type channel blocker (Newcomb et al. 1998), and the second component corresponded to expected HVA channel inactivation characteristics. They concluded therefore that T-type VGCCs were not present in the patches.

From the above we can deduce that there are various explanations for our lacking understanding of T-type VGCCs in L5PNs. First of all, currents through T-type VGCCs are masked by the large I_{Ca} through HVA VGCCs. In addition, pharmacological analysis of T-type channels has been slowed due to the lack of selective and potent blockers. Lastly, R-type currents are difficult to distinguish from T-type current due to their comparatively hyperpolarized voltage range of activation and recovery from inactivation (Cueni et al. 2009). Despite these difficulties, T-type VGCCs have been identified in L5PNs. Using immunohistochemistry experiments, Talley et al. (1999) showed T-type VGCCs are expressed in the neocortical layer 5, with highest expression in soma and dendrites. Additionally, patch clamp experiments in the visual cortex showed T-type currents can be identified in a subset (53%) of colliculus-projecting L5 neurons (Giffin et al. 1991).

1.3.2.3 BK channels during action potential back propagation

When calcium enters the apical dendrite through VGCCs during a bAP the endogenous buffer will rapidly bind the free calcium ions (Helmchen et al. 1996). Therefore, other calcium targets must be readily available upon Ca^{2+} entry. For this reason, coupling of VGCCs to other Ca^{2+} targets has been studied extensively (Vierra and Trimmer 2022). One of those targets is are BK CAKCs, which are involved in repolarizing the membrane potential upon calcium entry. Blocking BK channels in pyramidal cells results in a widening of the somatic AP, and a decrease in fAHP (Sun et al. 2003). Depending on the resting membrane potential, blocking BK channels can also increase the peak of the AP (Pineda et al. 1992).

L-type and N-type calcium channels have been suggested as calcium sources for the activation of BK channels (Sun et al. 2003). In their experiments, Sun and colleagues show a transient outward current in dissociated L5 pyramidal is blocked by iberiotoxin but not apamin, suggesting this current is mediated by BK channels. Subsequently, they show both L- and N-type channel blockers reduce the magnitude of this fast-transient BK-sensitive current. These findings were supported by co-immunoprecipitation of L-type and BK channels in rat brain (Grunnet and Kaufmann 2004), and N-type and BK channels (Loane et al. 2007), showing a stronger association between BK and N-type than L-type channels in the last study. The same report stated that co-expression of N-type and BK channels resulted in functional coupling of the channels, but that was rarely observed with L-type and BK channels. Moreover, this coupling was resistant to intracellular BAPTA, suggesting a close physical coupling. This was confirmed by Berkefeld et al. (2006), who showed that calcium influx activates BK channels within a sub-millisecond range. Lastly, a large quantitative proteomics study looking at the nano-environment of Ca_v2 channels identified over 200 associated proteins, most of which are ion channels and transporters (Müller et al. 2010). One of those was the BK CAKC, which associated specifically with N-type VGCCs. These results indicate a functional, and according to Müller and colleagues even physical, coupling between HVA calcium channels and BK channels. However, to our knowledge, these BK associations have never been assessed in acute brain slices where the neuronal circuitry is largely intact.

1.3.2.4 SK channels during action potential back propagation

Contrary to BK CAKCs, small conductance CAKCs (SK) have been studied in acute brain slices (Bock et al. 2019; Jones and Stuart 2013). As mentioned before, SK channels are exclusively activated by Ca^{2+} through interaction with calmodulin, a member of the endogenous mobile buffer, at the C-terminus of the channel (Schumacher et al. 2001). Blocking SK channels with apamin, a toxin found in bee venom, results in a reduction of the AHP, but there is little effect on the AP peak itself (Grunnet et al. 2001; Pineda et al. 1992). More specifically, these channels are thought to mediate the medium AHP (mAHP), as apamin blocks this current but not the fast AHP (fAHP) (Lancaster et al. 1991; Schwindt et al. 1988). Moreover, TEA leaves the mAHP component unaffected, suggesting SK is solely responsible for this current. This is supported by studies showing the mAHP is absent in SK2 knock-out mice (Bond et al. 2004; Brown et al. 2020).

Activation of SK CAKCs in spines have been shown to decrease NMDA receptor activation and regulate the amplitude of excitatory PSP (Ngo-Anh et al. 2005). During bAPs, SK channels limit Ca^{2+} influx into spines (Jones and Stuart 2013). This suggests SK channels might play a role in STDP. Indeed, Jones et al. (2017) showed SK channel activation gates STDP induction during bAP and dendritic excitatory input pairing through suppression of NMDA receptors in spines. Paired stimulation frequencies that under control conditions do not induce STDP produced robust LTP or LDP (depending on the timing between applying apamin and stimulation) when SK channels were blocked, suggesting SK CAKCs play a key role in STDP.

Recently, an interesting location-dependent effect of SK channels in L5PNs has been suggested (Bock et al. 2019). In the study, local application of apamin to the soma decreased the somatic AHP and increased AP firing, as had been reported before. Application on the dendrite near the tuft however resulted in a decrease of dendritic spikes and somatic firing during dendritic current injection. Apamin had no effect on AHP during dendritic application. Together this indicates SK channels promote rather than suppress dendritic calcium spikes and bAPs. The same effect was observed when applying R-type channel blocker SNX-482 to the dendrite, which occluded the effect of SK channels on dendritic excitability (Bock et al. 2019). This suggests R-type channels supply the calcium for SK CAKC activation in dendrites. This coupling is supported by research showing apamin results in an increase in calcium influx into basal dendrites during AP back propagation, which again is occluded when R-type channels are blocked (Jones and Stuart 2013). The same study reported that in the soma however, calcium for the apamin-sensitive AHP component is provided by a combination of the other VGCCs, suggesting there is little coupling there.

1.3.2.5 Voltage gated potassium channels in the apical dendrite

Korngreen and Sakmann (2000) investigated VGKCs in the apical dendrite of L5PNs. They identified a fast inactivating outward potassium current (resembling an A-type current) and a slow inactivationg outward potassium current (conforming to a delayed rectifier), with similar activation kinetics. They found that the delayed rectifier was present in the proximal but not distal apical dendrite.

There is less consensus about A-type VGNC distribution, with different reports stating a decreasing density from the soma (Ramaswamy and Markram 2015), and others maintaining a homogeneous channel density (Migliore and Shepherd 2002). Functionally however, A-type VGKCs participate in bAP repolarisation (Bekkers 2000). Harnett et al. (2015) report the dendritic tuft is compartmentalised by VGKCs and they suggest these channels regulate the interaction between different apical and somatic segments to control neuronal output.

1.4 Open research questions addressed in this thesis

This thesis is motivated by the gaps in the current knowledge on AP initiation at the AIS and back propagation into the apical dendrite of L5PNs. In this section I highlight the open research questions addressed in the next chapters.

1.4.1 Challenges when studying voltage gated sodium channels in the axon initial segment

It is well established that the AIS expresses both Na$_v$1.2 and Na$_v$1.6 channels, that they are inhomogeneously distributed and that both contribute to AP generation (Hanemaaijer et al. 2020; Hu et al. 2009; Katz et al. 2018; Kole and Stuart 2012). Nevertheless, it has been challenging to dissociate between the two VGNC subtypes in their native environment. Ideally, we aimed to block one VGNC subtype to be able to extract the specific contributions of both channels. The preferred way to do this is through pharmacology. The most widely known and used toxin to block VGNCs is tetrodotoxin (TTX) (Al-Sabi et al. 2006). Although other toxins, like saxitoxin and huwentoxin, as well as anaesthetics like lidocaine exist, these blockers act on both VGNC isoforms and are not sufficient to target one isoform selectively (Catterall et al. 2005a). This greatly limits investigations into VGNC contribution to AP generation. Additionally, the inhomogeneous distribution of VGNCs, as well as the site-dependence of the AP waveform, requires recording ion concentrations and V_m transients at high spatial and temporal resolution for a proper understanding of the role of each channel subtype. Finally, the change of membrane potential transients induced by VGNC inhibition affects the activation of the other voltage-gated ion channels involved in the AP shaping. This important synergy of diverse ion channels, underlying the AP generation, makes the combined analysis of all these channels necessary.

Chapter 3 focusses on tackling these issues, using a peptide mutated from a wild-type animal toxin which partially but selectively blocks $Na_v1.2$ with respect to $Na_v1.6$. Specifically, we optically measured Na^+ currents (Filipis and Canepari 2021), V_m transients (Popovic et al. 2015) and Ca^{2+} currents (Ait Ouares et al. 2016; Jaafari and Canepari 2016; Jaafari et al. 2014) associated with APs elicited by somatic current injections and we analysed how the partial block of $Na_v1.2$ affected these signals. We then focussed on the changes of these signals produced by fully blocking VGCCs and/or CAKCs in order to correlate $Na_v1.2$ signalling with the activation of these channels. These experiments were performed by Dr Luiza Filipis, then a post-doctoral researcher in our lab, and myself. In order to reconstruct the sequence of activation of the channels underlying the shaping of the generating AP, Dr Filipis built a NEURON model reproducing the experimental profiles of ionic and V_m transients. This enabled us to extract and verify the interactions of the various channels in the AIS during AP generation we observed experimentally.

1.4.2 Understanding voltage gated ion channel interaction and functional coupling in the apical dendrite

Similarly to understanding AP generation in the AIS, it is the synergy of the diverse ion channels that shapes the bAP. Besides $Na_v1.6$, the apical dendrite expresses all the channels found in the AIS. One challenge is that the apical dendrite is a multi-compartment structure, where both propagation and regeneration of the bAP have to be taken into account. In the lab, we can record calcium transients using fluorescent calcium indicators in the apical dendrite. In addition, we can track the membrane potential using voltage sensitive dyes. Unfortunately, compared to the high intracellular K^+ concentration, K^+ currents are too small to record using available potassium indicators (Wu et al. 2022). Furthermore, recording Na^+ transients like we can do in the AIS is more difficult in the apical dendrite, as we would need to average a large number of trials due to the small VGNC-mediated current compared to the AIS, but the sodium indicator, ING2, induces cell toxicity when over-excited.

As mentioned earlier in this chapter (see section 1.3.2.2), VGCCs play an important role in AP propagation in the dendrite, and although the presence of HVA VGCCs have been demonstrated (Stewart and Foehring 2000; Sun et al. 2003), the presence of T-type VGCCs has been questioned. In addition, the activation of CAKCs through Ca^{2+} transients mediated by VGCCs is hypothesised to play an important role in dendritic APs (Bock et al. 2019; Sun et al. 2003; Vierra and Trimmer 2022). These interactions have mostly been studied in HEK cells (Loane et al. 2007) or dissociated neurons (Sun et al. 2003). The formation of ion channel complexes however, depends on complex interactions of intracellular and extracellular signalling, which is disrupted during slice dissociation and completely absent in HEK cell over-expression. (Vierra and Trimmer 2022). Therefore, studying the native interactions between voltage gated ion channels must be performed in the native environment.

To understand the synergy of voltage gated channels in mediating a bAP, we must acknowledge that blocking or stimulating one channel subtype has an effect on the other channels, due to the induced change in V_m. Due to this non-linearity it is not sufficient to subtract recorded currents after applying a channel blocker from the control current. The effects of a change in the kinetics of one channel, on the other channels must be taken into account. In summary, we must analyse the relevant channels together. The underlying experimental strategy is described in chapter 2, which includes a combination of electrophysiology, fluorescent imaging, pharmacological manipulations and computational modelling. Using these techniques, chapter 3 describes the ion channels involved in the AP generation in the AIS. In chapter 4 we show how using our synergistic approach enables recognition of specific ion channel interactions, focussing exclusively on the apical dendrite ∼100 µm from the soma. Using pharmacology we can again block specific subtypes and assess the effect on the bAP shape and Ca^{2+} transients. We analyse the contribution of both VGCCs and CAKCs in multiple time windows after the bAP peak and around the Ca^{2+} current. However, because of the large diversity of voltage gated ion channels in the apical dendrite, and there is no reliable way to directly measure K^+ transients in slices, it is challenging to extract each channel specific kinetics. We used NEURON modelling to verify our hypotheses based on the experimental results and connect the AIS and apical dendrite using a mouse L5PN morphology. Finally, in chapter 5 I discuss our research and provide future research perspectives.

2

Methodology

Contents

2.1 Cortical slice preparations 30
2.2 Electrophysiology 32
    2.2.1 Choosing a brain slice 32
    2.2.2 Identifying healthy pyramidal neurons 32
    2.2.3 Establishing a patch 33
    2.2.4 Electrophysiology recordings 34
2.3 Imaging 34
    2.3.1 The imaging system 34
    2.3.2 Fluorescent Indicators 37
2.4 Pharmacology 38
2.5 Experimental protocols 39
    2.5.1 Protocols used for the AIS 39
    2.5.2 Protocols used for the apical dendrite 40
2.6 Optical data analysis 40
    2.6.1 Calcium imaging 40
    2.6.2 Voltage imaging 42
    2.6.3 Sodium imaging 44
2.7 Statistical data analysis 45
    2.7.1 The Lilliefors test 45
2.8 Computational modelling 46
    2.8.1 In the axon initial segment 46
    2.8.2 In the apical dendrite 47
2.9 Methods extensions 48
    2.9.1 Cal520FF - a new calcium indicator 48
    2.9.2 Toxins to distinguish between $\mathrm{Na}_v1.2$ and $\mathrm{Na}_v1.6$ 51
    2.9.3 Photosensitive $\mathrm{G}^1\mathrm{G}^4\mathrm{K}^{36}$Huwentoxin-IV 54

This chapter details the materials and methods used in this thesis. First, I will describe the preparation of cortical slices for electrophysiology. Then I will detail the imaging system, fluorescent indicators and pharmacological tools. Afterwards, I detail the analysis and statistical tests, followed by the computational modelling to reproduce the experimental results. The final section is dedicated to two projects that extended our pharmacological and fluorescent indicator libraries.

2.1 Cortical slice preparations

For patch clamp experiments, I prepared slices from wild-type mice (strain C57/Bl6) that were 21 to 35 days old. Animal were purchased from Janvier (Saint-Berthevin Cedex, France), housed and fed in the Biology department of Université Grenoble-Alpes in Saint Martin d'Hères, France. All experiments were reviewed and approved by the ethics committee affiliated to the university (D3842110001). In addition, all procedures were carried out in accordance with the European Directive 2010/63/EU on the care, welfare and treatment of animals, in accordance with the three R's (refinement, reduction and replacement of animals wherever possible).

To harvest the brain, mice were anaesthetized by isoflurane inhalation and decapitated, using surgical instruments (figure 2.2A-B). The brain was immediately removed from the skull and immersed in ice-cold slicing solution saturated with a gas mixture of 95% O_2 and 5% CO_2. The slicing solution contained (in mM): 125 NaCl, 26 $NaHCO_3$, 2.5 $MgSO_4$, 3 KCl, 1 NaH_2PO_4, 0.5 $CaCl_2$ and 20 glucose. From the brain sagittal cortical slices were prepared as previously described (Blömer et al. 2021a). Briefly, after 3 minutes the brain was removed from the slicing solution to ensure complete cooling of the brain but before killing healthy neurons. The brain was placed on filter paper to remove excess fluid. Cerebellum and olfactory bulb were removed first, after which the brain was cut in half along the midline. Both hemispheres were glued on a stage, build in-house with a 15° angle from the horizontal plane (figure 2.2C-E). This angle is essential to obtain unblemished neurons that are parallel to the slice so that their extremities lie in the same focal plane as the soma (Andreone et al. 2015). As L5PNs have their dendrite extended all the way into the first layer and the cortex is curved around the midbrain, 2 to 3 sagittal slices per hemisphere contain unscathed PNs.

The ensemble of stage and glued hemispheres was submerged once more in the ice-cold slicing solution, and mounted onto a Vibratome (Leica VT1200, Wetzlar, Germany). Sagittal slices of 350 µm thickness were cut. After cutting, each slice

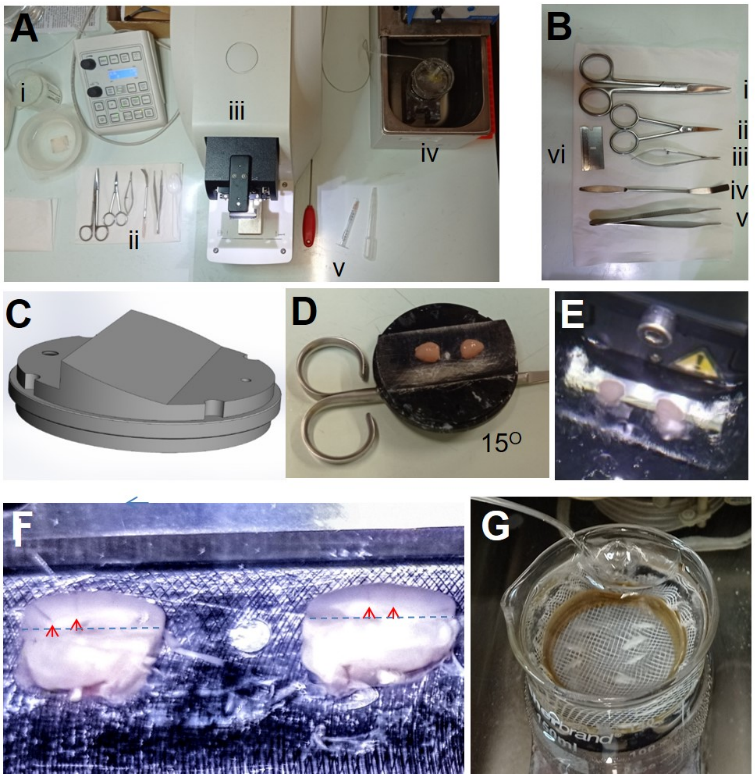

Figure 2.1: Dissection and slicing preparation. A, Preparation of tools and instruments for slicing: i) oxygenated slicing solution; ii) instruments for brain dissection; iii) vibratome; iv) slice holder with oxygenated ACSF in a 37°C water bath covered with a lid; v) vibratome screwdriver (left), syringe with a bent needle for cutting slices (middle), and plastic balloon pipet with its end cut off for transferring slices (right). B, Instruments for brain dissection: i) operating scissors used for decapitation; ii) fine scissors used for removing the skin from the skull; iii) spring scissors used for cutting through the skull; iv) Chattaway spatula used to move the brain; v) forceps used to remove the skull; vi) blade used to cut the cortices. C, Design of the slice holder with 15° inclination. D, Cortices glued on the holder. The scissors are used to prevent slices from sliding by counteracting the holder slope. E, Vibratome blade that has cut halfway through both cortices. Using the syringe with a bent needle, slices are cut at this point and moved to the slice holder. F, Cortices inside the vibratome right before cutting a slice. Visible blood vessels running throughout layers 1 to 6 are marked with red arrows, indicating that these slices have axons and dendrites that run parallel to the slice surface. The blue dashed lines indicate the position where the slices will be cut with the bent syringe needle. G, All 350 µm slices are placed in the slice holder inside the 37°C water bath for 30 min.

was immediately transferred into a chamber containing oxygenated extracellular solution at 37°C. Extracellular solution contained (in mM): 125 NaCl, 26 $NaHCO_3$, 1 $MgSO_4$, 3 KCl, 1 NaH_2PO_4, 2 $CaCl_2$ and 20 glucose. During the slicing process slices with visible veins running through all cortical layers were noted, as these slices are more likely to contain processes parallel to the focal plane (figure 2.2F). Slices were incubated at 37°C for 30 minutes, after which slices were allowed to return to room temperature for 1 hour before starting experiments (figure 2.2G).

2.2 Electrophysiology

2.2.1 Choosing a brain slice

After incubation, slices were transferred to a recoding chamber under the microscope and stabilized at the bottom of the chamber with a harp slice grid. The chamber was constantly perfused with extracellular solution saturated with 95%O_2-5%CO_2 gas at a constant flow rate of ∼2 mL/minute and the temperature was held at 32-34°C. Slices were selected by focussing on the slice surface and identifying blood vessels. I focussed at the widest part of the cortex, the somatosensory cortex, and looked for blood vessels running in parallel to the slice surface from the dorsal end towards the hippocampus just below the cortex. To determine if cells were parallel to the focal plane I identified dead L5PNs and examined whether their dendrites ran parallel to the slice. Dead neurons show high contrast under DIC (figure 2.2A) due to shrinkage, making it easy to follow the dendrite or axon of a dead cell up through the cortical layers and determine whether the area of the slice is indeed parallel.

2.2.2 Identifying healthy pyramidal neurons

After slice selection, healthy L5PNs were selected by eye after locating the large cell bodies in the middle part of the cortex, about 500 to 900 µm from the dorsal end of the cortex, given that the whole cortex is ∼1500 µm at its widest part. A healthy pyramidal neuron can be recognized by its typical large triangular shape. These cells are symmetrical and show little contrast with their surroundings, and the nucleus is difficult to identify (figure 2.2A). Unhealthy cells are usually swollen, and their enlarged round nucleus is clearly visible, indicating that the cell is about to release its contents and die. I selected cells located 20 to 35 µm below the slice surface. With superficial cells, there is a higher chance that the dendrite runs out of the slice and is cut off, whereas cells 35 µm below the surface are more difficult to image, as the larger scattering prevents good measurements.

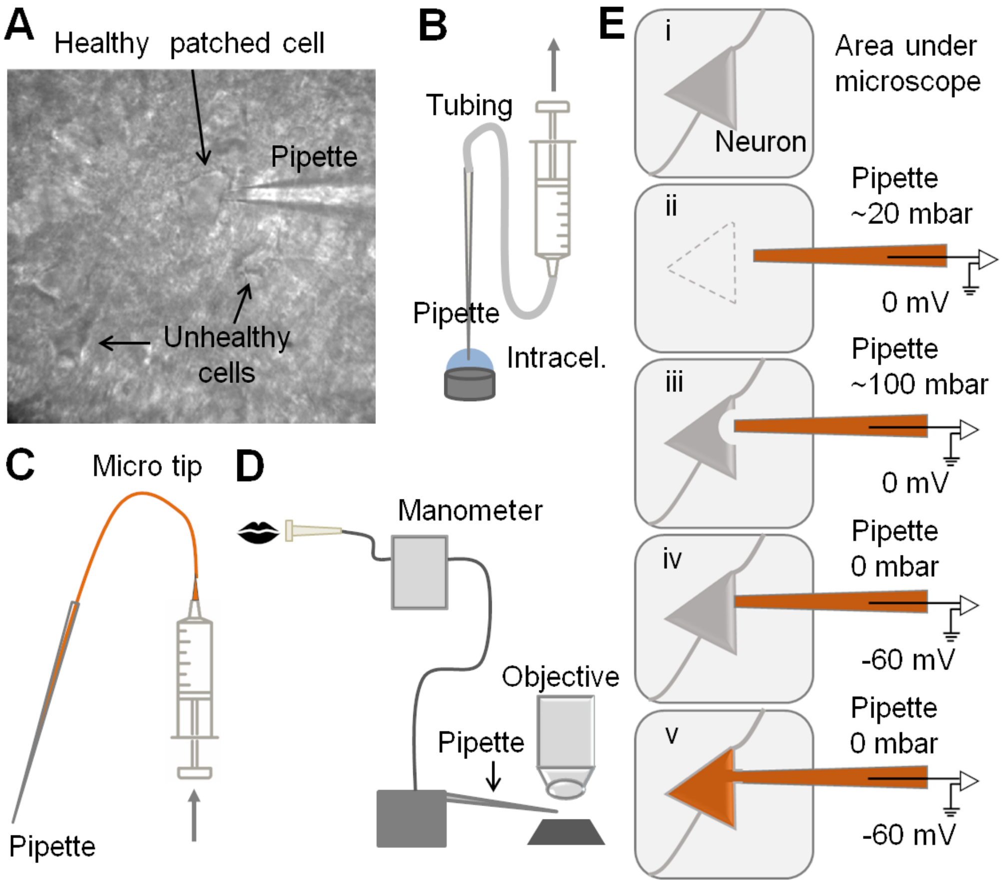

Figure 2.2: Patching a layer 5 pyramidal neuron. A picture from the area under the objective, healthy and dead cells are indicated by arrows. B Front filling of a pipette with intracellular solution. C back filling of a pipette with fluorescent indicator dissolved in intracellular solution. D schematic of the pipette mounted on the stage, with a manometer to control pressure. E patching of a neuron: first positioning the pipette just above the cell with a small positive pressure (ii), then increasing the pressure and approaching the cell (iii). Pressure is released and a giga seal forms with the cell (iv), after which a short suction breaks the membrane and whole-cell configuration is established (v). From Blömer et al. 2021a.

2.2.3 Establishing a patch

Patch pipettes were pulled from borosilicate pipettes with an external diameter of 1.5 mm and an internal diameter of 1.17 mm with a DMZ Puller and had a submerged tip resistance of 4-5 MΩ. Pipettes were front filled with intracellular solution (figure 2.2B), containing (in mM): 125 $KMeSO_4$, 5 KCl, 8 $MgSO_4$, 5 Na_2-ATP, 0.3 Tris-GTP, 12 Tris-Phosphocreatine, 20 HEPES, adjusted to a pH of 7.3 using KOH. Pipettes were then backfilled with specific indicators dissolved in intracellular solution (figure 2.2C). While approaching a selected neuron with a pipette (figure 2.2Ei), a weak positive pressure was applied (∼15 mbar) to maintain a clean tip and minimize exchange between the intra- and extracellular solution (figure 2.2D,Eii). The junction potential (further explained below) was compensated to 0 mV and continuous pulses of 0.5 ms duration and -5 mV amplitude were applied to monitor the pipette tip resistance. Just before the final approach to the cell, a strong positive pressure was applied (∼100 mbar) to blow away any tissue between the pipette tip and the neuron. For the final approach, the pipette is moved down into the tissue fast, until it is pushing the neuron (figure 2.2Eiii). Pressure is released immediately afterwards, to form a seal in voltage clamp mode at -60 mV (figure 2.2Eiv). IT is imperative to be fast during this step as maintaining a high pressure for increased period of time leads to a substantial leakage of the dye, preventing high-quality imaging recordings.

The position of the pipette is adjusted so the tip does not push the cell. Then, a short strong suction was applied to break the membrane under the pipette tip (figure 2.2Ev). At this point, the series resistance is estimated. Patches with a series resistance higher than ∼14 MΩ were discarded, along with the cells with significant dye spillage.

2.2.4 Electrophysiology recordings

After establishing a whole-cell configuration, the fluorescent indicator was allowed to diffuse through the neuron for ∼20 minutes in the case of Na^+ or Ca^{2+} indicators, or ∼30 minutes when patching with voltage sensitive dye. During this time the series resistance were monitored, while the cell was kept at a resting membrane potential of -60 mV. Recordings were performed using a Multiclamp 700A amplifier (Molecular Devices, CA) and acquired at 20 kHz using the A/D board of the CCD camera. During recordings, cells were kept in current clamp, which was adjusted every 100 ms to keep the V_m at -70 mV. Action potentials were triggered by injecting a short current of 3-5 nA for 3-5 ms. These somatic recordings were corrected for a junction potential of -11 mV, calculated for the composition of the intracellular solution (Canepari et al. 2010). In addition, the bridge potential, introduced as a stimulation artefact, was determined and balanced for each recording.

2.3 Imaging

2.3.1 The imaging system

Two imaging systems were used for the experiments reported in this thesis. Most reported data in this manuscript has been collected by me using system one, but wherever Dr Filipis performed experiments system two was used.

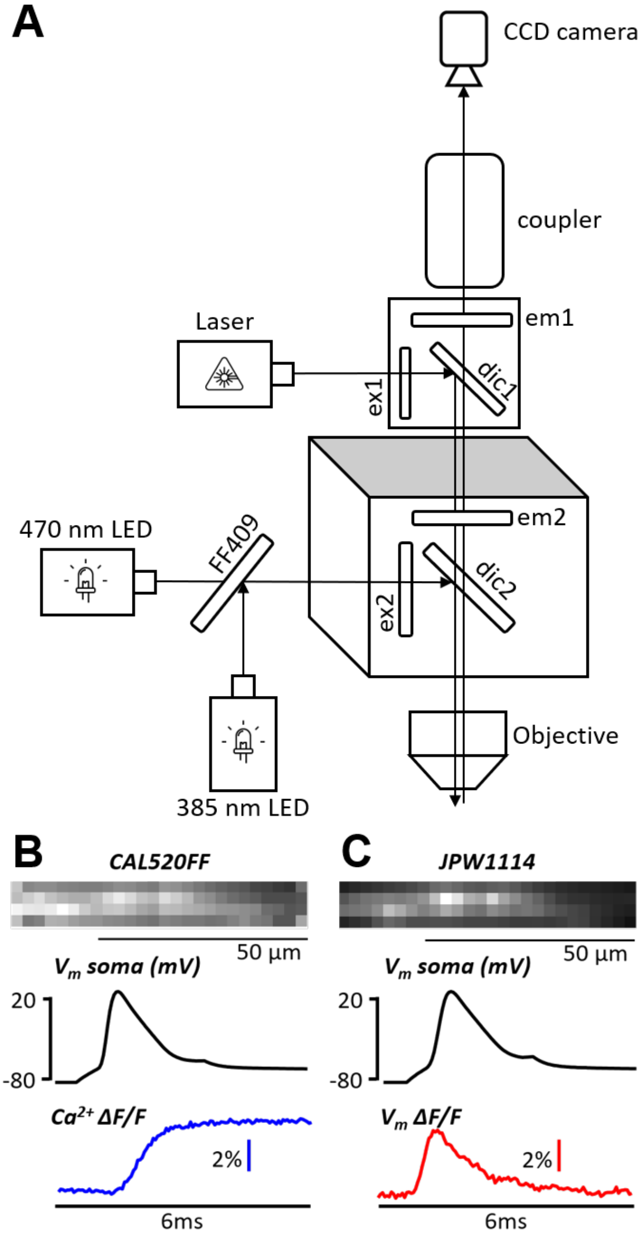

Figure 2.3: Imaging system one and example recordings. A Imaging setup schematic. B Example of a recording of calcium indicator Cal520FF. C Same cell as B, but recording the voltage sensitive dye JPW1114.

2.3.1.1 System one

Imaging was performed on an Olympus BX51 microscope (Tokyo, Japan) equipped with a 60×/1.0 NA Nikon (Tokyo, Japan) objective. Fluorophores were excited using either a laser or LEDs (365, 385 or 470 nm) provided through the epifluorescence port of the microscope. The 385 and 470 nm LEDs were controlled by an OptoLED (Cairn Research, Faversham, UK), and were used to excite various calcium indicators.

For uncaging photosensitive compounds the 365-nm LED was controlled by an OptoFlash (CAIRN Research Ltd., Faversham, UK). A DLI-7 laser (89 North, Williston, VT) was used to excite the voltage sensitive dye (VSD).

Excitation light from either LED or laser source was first filtered with an excitation filter before being directed to the brain slice by one or two dichroic mirrors. Emission light was passed through the dichroic mirrors and one (or two) emission filters, before being detected by the camera. Images were acquired with a NeuroCCD-SMQ camera (RedShirtImaging, Decatur, CA) at 5 or 20 kHz with a pixel resolution of ~2 µm in regions of 24 x 24 or 26 x 4 pixels, respectively (figure 2.3). Filters and dichroic mirrors were chosen to match the experiment and chosen light source (table 2.1). Fluorescent images were de-magnified by a ~0.5X projection lens.

Exposure time for experiments was either 8 or 300 ms. Time between consecutive trials was 9 seconds, or more in the case of the VSD to limit photo-damage and to allow recovery of the dye after excitation. Due to phototoxicity of the VSD, 4-5 trails were averaged for every condition. In the case of calcium indicators 6-9 trails were averaged to improve the signal-to-noise ratio (S/N). Finally, slow changes in fluorescence due to the bleaching of the dye were corrected by subtracting an appropriate exponential function matching the fluorescence average over time from a trial without stimulus.

Indicator	**Ex source**	**Excitation** nm	**Ex filter** nm	**Em filter** nm
JPW1114	laser	529	531 ± 40	>610
OG5N	LED	470	469 ± 17	530 ± 21
Cal520FF	LED	470	469 ± 17	530 ± 21
Fluo-4FF	LED	470	469 ± 17	530 ± 21
Fura2FF	LED	385	387 ± 6	525 ± 25

Table 2.1: Excitation and emission of fluorescent indicators. Showing excitation source and wavelength, and filters used in this thesis. JPW1114 is the voltage sensitive dye. OG5N, Cal520FF, Fura2FF and Fluo-4FF are calcium indicators. OG5N = Oregon-Green-BAPTA-5N, Ex = excitation, Em = emission.

2.3.1.2 System two

The Na^+ and Ca^{2+} imaging experiments and some of the V_m imaging described in chapter 3 were performed by Dr Luiza Filipis. These experiments were performed using an imaging system described in a previous report (Filipis and Canepari 2021), based on an upright Scientifica SliceScope microscope equipped with a motorised

XY translation stage, PatchStar manipulators (Scientifica, Uckfield, UK) and a 60X Olympus water immersion objective (NA = 1). Na^+ and V_m indicators were excited using the 520 nm line of a LaserBank (Cairn Research, Faversham, UK), band-pass filtered at 517 ± 10 nm and directed to the preparation using a 538 nm long-pass dichroic mirror. The Ca^{2+} indicator was excited using the 465 nm line of the LaserBank, band-pass filtered at 469 ± 17 nm and directed to the preparation using a 495 nm long-pass dichroic mirror. Na^+ and V_m fluorescence emission signals were band-pass filtered at 559 ± 17 nm or long-pass filtered at >610 nm respectively. Ca^{2+} fluorescence emission was band-pass filtered at 525 ± 25 nm. The size of the illumination spot, obtained using a custom-made telescope, was ~30 µm. Image sequences were demagnified by 0.5X and acquired with a DaVinci 2K CMOS camera (SciMeasure, Decatur, GA) at 10 kHz with a pixel resolution of 500 nm in regions of 30X128 pixels.

2.3.2 Fluorescent Indicators

2.3.2.1 Voltage sensitive dye

During all voltage imaging experiments, D-2-ANEPEQ (JPW1114, 0.2 mg/mL, Thermo Fisher Scientific) was used as VSD. This dye undergoes a large charge shift upon excitation and displays a linear electrochromic response to the membrane potential in the range of −100 to 100 mV. The dye is lipophilic but still sufficiently water soluble to be used for micro-injection. For experiments, 0.2-0.5 mg/mL was used to limit toxicity. Upon introduction into the neuron, the dye immediately binds to the plasma membrane and from there, diffuses slowly through the membrane (example recording shown in figure 2.3C).

Upon patching a neuron, the VSD was allowed to equilibrate for 25-30 minutes. The patch pipette was then slowly retracted to form an outside-out patch, allowing the plasma membrane to reseal without killing the cell. The same neuron was patched a second time with a pipette with clear intracellular solution. This is necessary to prevent pharmacological effects due to dye overload (Canepari et al. 2007).

2.3.2.2 Calcium indicators

Stock solutions for each dye (20 mM) were prepared, aliquoted and kept at $-20°C$. For experiments an aliquot was diluted to 2 mM with intracellular solution. The principal low affinity calcium indicator is Oregon-Green-BAPTA-5N (OG5N; Thermo Fisher Scientific, Waltham, MA) with a K_D of 35 µM, which is used to record fast calcium signals. One advantage is the high background fluorescence of this dye, as it makes it easier to see the neuronal processes while loading the cell. An alternative low affinity dye is Fura2FF ($K_D = 10$ µM; AAT Bioquest Scientific, Sunnyvale, CA), which was used in experiments combining voltage and calcium imaging, as OG5N emission overlaps with the VSD emission. Its performance in terms of S/N, however, is inferior with respect to the great performance of OG5N.

Recently, a new low-affinity indicator became available, Cal520FF (AAT Bioquest Scientific, Sunnyvale, CA) with a K_D of 10 µM. We decided to test this new indicator and compare it to OG2N and Fluo4FF (Blömer et al. 2021b). Briefly, we determined the signal to noise ratio for all three indicators in our experimental setup, and found Cal520FF to be the superior indicator for our experiments. The analysis can be found at the end of this chapter (see also the example recording in figure 2.3B).

Industrial name	**Target**	**Chemical name**
ML218	Ca_v3.2-3 (T-type)	3,5-dichloro-N-[[(1α,5α,6-exo,6α)-3-(3,3-dimethylbutyl)-3-zabicyclo[3.1.0]hex6-yl]methyl]-benzamide-hydrochloride
NNC550396	Ca_v3.1 (T-type)	(1S,2S)-2-[2-[[3-(1HBenzimidazol-2-yl)propyl]-methylamino]ethyl]-6-fluoro-1,2,3,4-tetrahydro-1-(1-methylethyl)-2-naphthalenyl-cyclopropanecarboxylate-dihydrochloride
Isradipine	Ca_v1.2-4 (L-type)	4-(2,1,3-Benzoxadiazol-4-yl)-1,4-dihydro-2,6-dimethyl-3,5-pyridinecarboxylic-acid-methyl-1-methylethyl-ester
PD173212	Ca_v2.2 (N-type)	N-[[4-(1,1-Dimethylethyl)phenyl]methyl-N-methyl-L-leucyl-N-(1,1-dimethylethyl)-O-phenylmethyl)-L-tyrosinamide
TRAM-34	IK CAKCs	1-[(2-Chlorophenyl)diphenylmethyl]-1H-pyrazole

Table 2.2: List of chemicals used to block ion channels. All chemicals were purchased from either Tocris (Bristol, UK) or Sigma-Aldrich (St. Louis, MO).

2.4 Pharmacology

All chemicals were purchased from either Tocris (Bristol, UK) or Sigma-Aldrich (St. Louis, MO). The full names of chemicals used in this thesis are shown in table 2.2.

Toxins were purchased from SmartTox (Saint Martin d'Hères, France), dissolved in water and used at the final concentration of 1 µM (see table 2.3). In all experiments, the blocker(s) was (were) locally delivered by gentle pressure application ~20 µm from the optical recording area using a pipette of 2-4 µm of diameter. The application lasted 1-2 minutes before recording in order to assure the stable blockade of the channel(s).

Toxin	**Target**
ω-Agatoxin IVA (agatx)	$Ca_v2.1$ (P/Q-type)
ω-Conotoxin GVIA (cntx)	$Ca_v2.2$ (N-type)
SNX-482	$Ca_v2.3$ (R-type)
Tetrodotoxin (TTX)	VGNCs
$G^1G^4K^{36}$-Huwentoxin-IV ($G^1G^4K^{36}$hwtx)	VGNCs
G^1G^4-Huwentoxin-IV (G^1G^4hwtx)	$Na_v1.2$
4,9-Anhydrotetrodotoxin (attx)	$Na_v1.6$
Iberiotoxin (ibtx)	BK CAKCs
Apamin	SK CAKCs

Table 2.3: List of toxins used to block ion channels. All toxins were purchased from SmartTox (Saint Martin d'Hères, France).

2.5 Experimental protocols

For all experiments, healthy L5PNs were selected in the somatosensory cortex and patched. Channel blockers were locally delivered through gentle pressure ejection by a pipette positioned next to the region of interest, as illustrated in figure 2.4A. Fluorescent imaging recordings of the region of interest were taken before (indicated as *control*) and after (indicated as *drug* or *block*) blocker application.

2.5.1 Protocols used for the AIS

In chapter 3, all reported fluorescent traces are averages of 4-5 trials with identical somatic responses, recorded at 20 kHz when using imaging system one or 10 kHz when using system two, respectively. Given the morphological variability of the AIS, we standardised our analyses to 5 µm long regions within the proximal (*prox*) part of the AIS, 5-15 µm from soma, indicated with *1* in all figures, and to regions of the same length within distal (*dist*) parts of the AIS, 30-40 µm from soma, indicated with *2* in all figures (figure 2.4B).

2.5.2 Protocols used for the apical dendrite

In the apical dendrite (detailed in chapter 4), one region ∼100 µm from the soma was analysed (figure 2.4C). We investigated the VGCCs mediating the Ca^{2+} influx associated with the bAP in the apical dendrite at ∼100 µm from the soma using the same approach utilised in CA1 hippocampal pyramidal neuron (Jaafari and Canepari 2016; Jaafari et al. 2014). In these experiments, L5 pyramidal neurons were loaded with 2 mM of a low-affinity Ca^{2+} indicator, either OG5N (Canepari and Ogden 2006) or the more sensitive Cal-520FF (Blömer et al. 2021b), and Ca^{2+} transients ($\Delta F/F_0$ signals) were measured at 20 kHz by averaging fluorescence from dendritic segments of 20-40 µm length. S/N was improved by averaging 6-9 trails in these experiments. We also analysed the waveform of the bAP ∼100 µm from the soma using the voltage indicator JPW1114, of which 4-5 trails were averaged.

2.6 Optical data analysis

All data were analysed with in-house code written using MATLAB (MathWorks Inc., Natick, MA). Ca^{2+}, Na^{+} and V_m data were initially expressed as fractional changes of fluorescence ($\Delta F/F_0$), calculated after subtraction of the autofluorescence background. Specifically, a bleach recording or fluorescence recording without stimulus, was fitted with a one-term power function:

$$y(x) = a * x^b$$

This autofluorescence fit was subtracted from the signal F. The change in fluorescence (ΔF) was then divided by the average fluorescence before the stimulus (F_0).

2.6.1 Calcium imaging

The Ca^{2+}-$\Delta F/F_0$ signal associated with each bAP, normalised to its asymptotic value, was initially fitted with a 4-sigmoid function (figure 2.5):

$$y(x) = \prod_{j=1}^{4} \frac{1}{1 + e^{-\varphi_j (t-\theta_j)}}$$

Where t is time and φ_j and θ_j are the parameters to be determined by the fit (Jaafari et al. 2015). The Ca^{2+}-$\Delta F/F_0$ signal was used to estimate the Ca^{2+} current (I_{Ca}). As the relaxation time of the Ca^{2+} indicators used in this thesis is faster than the calcium influx, Ca^{2+} binds the indicator linearly in time. This means the change in fluorescence tracks the kinetics of the Ca^{2+} source. Therefore, the Ca^{2+}-$\Delta F/F_0$ is proportional to the integral of the Ca^{2+} influx I_{Ca}. So, to estimate the I_{Ca}, the time derivative of the fitted Ca^{2+}-$\Delta F/F_0$ signal was then expressed as percentage change over milliseconds (%/ms).

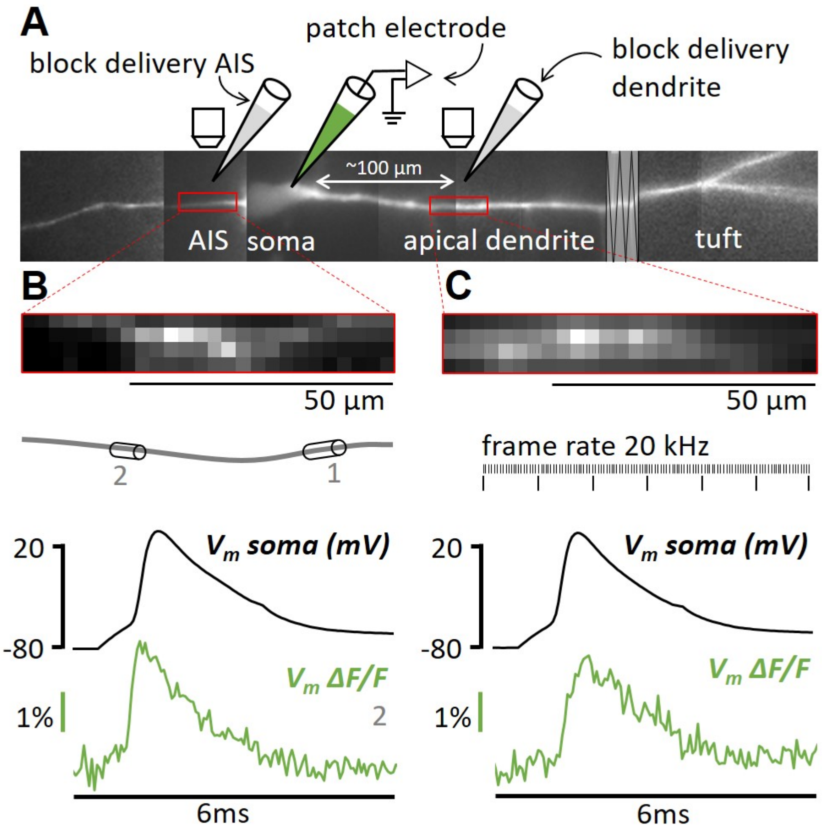

Figure 2.4: Experimental protocols. A, example of a neuron filled with a fluorescent indicator indicating the patch electrode at the soma filled with fluorescent dye. The somatic patch clamp electrode (also used to elicit APs and to record somatic V_m) is used to load a L5 pyramidal neuron with a fluorescent indicator, while a pipette positioned near the AIS or apical dendrite is used to locally deliver a solution containing a channel blocker, by gentle pressure application, for 1 minute. The red boxes indicate imaging positions. B, Example of a fluorescent image from the AIS with voltage sensitive dye JPW1114. Below, a schematic of the AIS in the image. To unambiguously distinguish signals from proximal and distal areas of the AIS, with respect to the soma, we systematically analysed every signal in a region 5 µm long at a position “1”, within 5 and 15 µm from the soma. Similar analyses was performed at position “2”, 30-40 µm from the soma. Below this, an AP is elicited and recorded at the soma (at 20 kHz) and the fluorescence signals (V_m in this example) at position 2 is reported. C, Example of a fluorescent image from the AIS with voltage sensitive dye JPW1114. Below, an AP elicited and recorded at the soma, with the back propagated V_m-$\Delta F/F_0$ signal recorded ∼100 µm from the soma at 20kHz.

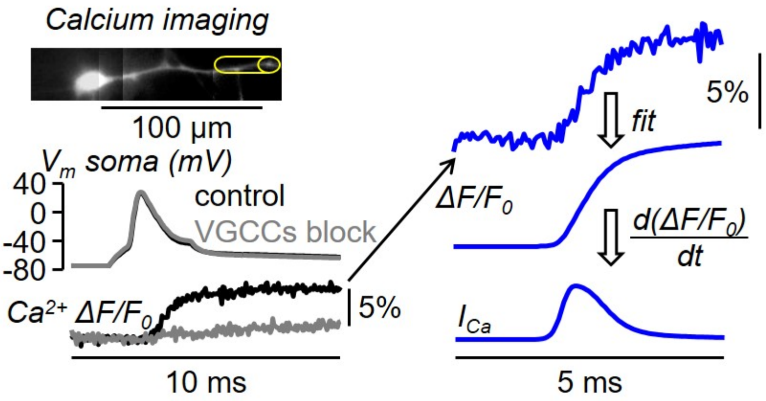

Figure 2.5: Calcium imaging in L5PNs. Ca^{2+} data was initially expressed as fractional change of fluorescence ($\Delta F/F_0$ signals), calculated after subtraction of the autofluorescence background. Left: example of a neuron filled with OG5N. Below: the recording of the somatic AP in control conditions and when blocking VGCCs. Below the APs: the Ca^{2+}-$\Delta F/F_0$ in both conditions, showing that blocking VGCCs eliminates the Ca^{2+} response. Right: The Ca^{2+}-$\Delta F/F_0$ signal associated with each bAP, normalised to its asymptotic value, was initially fitted with a 4-sigmoid function. The time derivative of the fitted Ca^{2+}-$\Delta F/F_0$ signal was then calculated to obtain the calcium current I_{Ca}.

2.6.2 Voltage imaging

In chapter 3, I discuss the effect of blocking voltage gated ion channels on the shape of the generating AP. For V_m imaging experiments, to unambiguously quantify a change in AP beyond the noise of the optical recording, we calculated the integral of the $\Delta F/F_0$ signal over a time window of 2.4 ms comprising the AP (figure 2.6). This enables us to obtain the cumulative change in V_m, which is the last value of the $\int V_m$.

In chapter 4, where I assess the effect of specific channel blockers on the shape of the bAP, a more elaborate analysis was required. There, we wanted to assess the temporal effect of channel blockers on the widening of the bAP. Hence, we determined three temporal windows after the peak of the bAP, based on the delay between the V_m and I_{Ca} peaks, and determined whether blocking one voltage gated channel subtype changed the measured V_m-$\Delta F/F_0$ using the Lilliefors statistical test (Lilliefors 1967). See section 2.7.1 for a detailed statistical description.

2.6.2.1 Calibrating the VSD

The building of realistic NEURON models of the apical dendrite requires the V_m-$\Delta F/F_0$ associated with the bAP had to be converted into mV. This is performed by calibrating the VSD and is possible because the resting V_m is uniform near the soma in the apical dendrite (Stuart et al. 1997a). Calibrations are necessary as the VSD fluorescence is not only generated by the dye bound to the plasma membrane but also

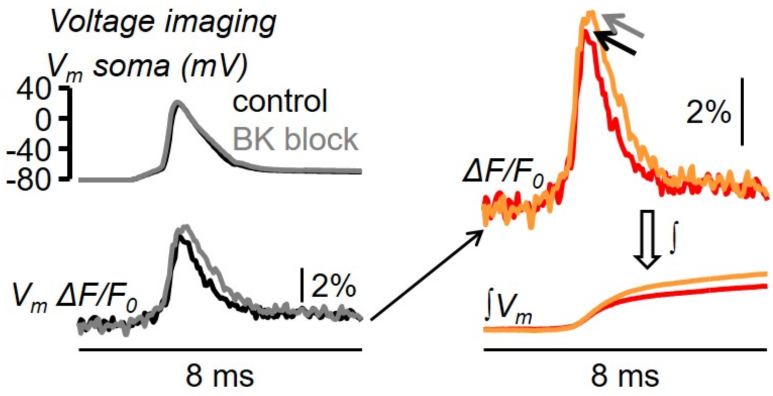

Figure 2.6: Voltage imaging in the AIS. V_m data was initially expressed as fractional change of fluorescence ($\Delta F/F_0$ signals), calculated after subtraction of the autofluorescence background. Left: example of voltage imaging while applying a BK CAKC blocker in the AIS. On the top the somatic AP, and at the bottom the fractional change in voltage (V_m-$\Delta F/F_0$). Right: For quantification of the V_m-$\Delta F/F_0$ signal in the AIS the cumulative change of fluorescence was calculated, by taking the integral of the $\Delta F/F_0$ signal.

internal membranes, which is effectively inactive dye. The first one contributes to both the resting fluorescence and the fluorescent change due to membrane potential changes, whereas the inactive dye only contributes to the resting fluorescence. As we measure the membrane potential as a relative change to the resting fluorescence, this signal depends on the ratio between active and inactive dye, which cannot be measured. Therefore, VSD recordings differ from cell to cell, and from one site within a cell to another site. Although calibration for all cells included in this thesis was not possible, we performed V_m calibrations on a subset of cells to assess AP attenuation along the dendrite and have a reference for the computational model.

The V_m-$\Delta F/F_0$ associated with the bAP was converted into mV considering an average attenuation of the somatic AP size, which was 4% on average. This value was obtained in a set of experiments in which the V_m-$\Delta F/F_0$ associated with the bAP was calibrated in mV using a previously reported method (Vogt et al. 2011). As shown in the example of figure 2.7A, the V_m-$\Delta F/F_0$ signal associated with an AP was measured in the apical dendrite at 100 µm from the soma. Then, in the presence of 1 µM tetrodotoxin to block APs and 100 µM cyclothiazide to inhibit AMPA receptors desensitization, L-glutamate was locally photo-released from 2.5 mM 4-Methoxy-7-nitroindolinyl-caged-L-glutamate (MNI-glutamate, TOCRIS) using an OPTOLED pulse of 1 ms at 365 nM wavelength. As this procedure brings the dendritic V_m to the reversal potential of ionotropic glutamate receptors (i.e. to 0 mV), the associated V_m-$\Delta F/F_0$ signal was used to calibrate the signal associated with the bAP. This assessment was repeated in N = 8 cells obtaining

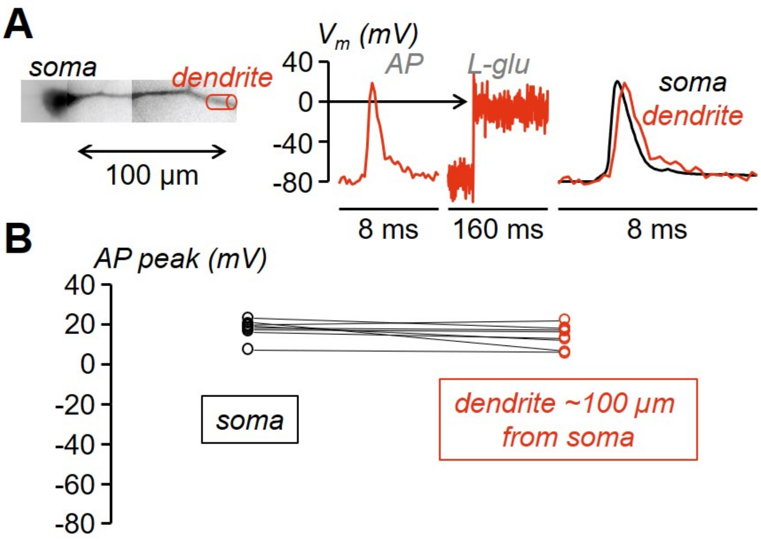

Figure 2.7: Calibration of the dendritic AP. A, Top-left, reconstruction of L5 pyramidal neuron with dendritic compartment at ~100 µm distance from the soma outlined by a cylinder (red). Top-right, V_m optical signal associated with an AP in the region on the left, calibrated using a depolarization to 0 mV obtained by uncaging L-glutamate, showing a slight attenuation of the dendritic bAP with respect to the somatic AP (black trace). Bottom, AP peak in the soma (20.37 ± 4.39 mV, mean ± SD) and in the dendrite at ~100 µm distance from the soma (16.63 ± 5.50 mV, mean ± SD) measured in N = 8 cells.

a consistent result (figure 2.7B). This has been observed before by Larkum et al. (2001), who showed bAPs have little attenuation, whereas forward propagating excitatory potentials in the apical dendrite attenuate fast. They postulated this is due to the nature of the APs, which are VGNC-mediated when back propagating, but rely more on VGCCs during forward propagation from the tuft.

2.6.3 Sodium imaging

For Na^+ imaging experiments, the Na^+ current was calculated as described in detail in a previous report (Filipis and Canepari 2021). Specifically, $\Delta F/F_0$ signals were initially converted into $\Delta[Na^+]$ signals. Using an internal solution without Na_2-ATP, ING-2 fluorescence at different NaCl concentrations (0, 2.5, 5, 7.5, 10, 12.5, 15 and 25 mM) was measured with the same apparatus used in the physiological recordings. We linearly fitted the fluorescence against the Na^+ concentration and we established that $\Delta F/F_0 = 1\%$ corresponds to $[Na^+] = 0.175$ mM at initial $[Na^+] = 10$ mM. The $\Delta[Na^+]$ was compensated for longitudinal diffusion and converted into a Na^+ (or a positive charge) superficial density using an estimate of the diameter of the axon. The signal was fitted with a model function based on the summation of a simple sigmoid (for the subthreshold component), the product of three sigmoids (for the suprathreshold component) and the current surface density (or simply the current) was finally obtained by calculating the time derivative of this fit. The detailed biophysical validation of this method is reported in Filipis and Canepari (2021).

2.7 Statistical data analysis

To assess the consistency of the experimental results obtained in groups of cells, three statistical tests were performed and in all tests we considered $p < 0.01$ as the threshold for significance.

The effect of a channel blocker on the Na^+, Ca^{2+} and I_{Ca} signals were studied in the same group of experiments, using a parametric paired t-test performed on the signals maxima under two different conditions. In each cell, the maxima were measured in control conditions and in the presence of one or several channel blockers. Equivalently, to assess the same effect in two different groups of experiments, the Wilcoxon rank non-parametric test was performed on the fractional changes of signals maxima under two different conditions in the two groups of cells.

2.7.1 The Lilliefors test

Finally, to establish the effect of a channel blocker on the shape of the dendritic bAP, we assessed the widening of the bAP over the photon noise of the recording using the following statistical analysis. Assuming that the photon noise is normally distributed, the hypothesis to test was whether or not the distribution of the difference between the samples at given intervals after the bAP peak in the presence of a channel blocker and in control conditions deviated the distribution from normality. The rationale of the analysis is illustrated in the simulations reported in figure 2.8. In the example reported on the top of the panel, two sets of normally distributed values with 5 mV standard deviation were added to a somatic AP recorded at 20 kHz. This was done once to simulate the control conditions and once to simulate the presence of the channel blocker. The normal distributions were centered at 0 mV except for the 500 µs following the bAP peak in the red trace for which the distribution was centered at +15 mV in order to mimic the widening. The distribution of the difference between the noise samples in the presence of the channel blocker and in control condition will be also normal with standard deviation equal to $\sqrt{2}$ times the standard deviation of the original signals. The distribution of the difference between the noise + signal samples, however, will deviate from normality since the two original distributions are centered at two different values. Thus, we repeated the simulations in N = 8 cells to illustrate the histograms of the difference in the noise, in the signal and in the noise + signal (figure 2.8). To visualize the normal behaviour of the noise difference and the deviation from normality of the noise + signal difference, we superimpose the two normal distributions on the histograms with mean and standard deviation calculated from the points. The test to obtain a quantitative assessment of the normal behavior is, in principle the Kolmogorov-Smirnov test. In practice, since in the experiments the noise varies from one cell to another, we opted for the stronger Lilliefors test, which is a generalization of the Kolmogorov-Smirnov test for unknown normal distributions (Lilliefors 1967). The p values of this test for the above simulations are reported in figure 2.8. In the experiments, to establish the kinetics of the widening, the test was repeated over three distinct time intervals during the falling phase of the AP, namely the first 500 µs following the AP peak, the next 500 µs and the next 1.5 ms.

2.8 Computational modelling

All modelling reported in this dissertation was performed in the NEURON language, and the complete models are available in the online NEURON ModelDB.

2.8.1 In the axon initial segment

An existing model from Hallermann et al. (2012) was used as the base for the modelling reported in this thesis. Briefly, the AIS of the existing model was replaced by the physiology of the mouse, which has a semi-conical shape with initial diameter of 4.22 µm and final diameter of 1.73 µm and it is divided into 20 compartments of 2 µm length. Next, VGNCs from Mainen et al. (1995) were introduced and adapted to fit the data. Calcium permeability to $Na_v1.2$ was introduced, corresponding to 0.4% with respect to Na^+ as has been suggested (Hanemaaijer et al. 2020). Next, a LVACC representing T-type VGCCs and HVACC, representing L-type, P/Q-type, N-type and R-type VGCCs, were introduced (Almog and Korngreen 2014). Distributions and densities were set to re-produce experimental data. When modelling Ca^{2+} transients, a mobile Ca^{2+} buffer with standard kinetics was introduced, to mimic the calcium indicator in the patch pipette. In addition, an immobile endogenous buffer was included in all simulations. For Ca^{2+} diffusion and extrusion, we used the model proposed by Kim et al. (2015). Lastly, an inward rectifier K^+ channel was introduced (Migliore et al. 2008), as well as two CAKCs; BK (Ait Ouares et al. 2019) and SK (Mahapatra et al. 2018). SK channels were dependent on Ca^{2+} entry exclusively entering through LVA VFCCs, whereas BK channels were activated by Ca^{2+} through $Na_v1.2$ and HVA VGCCs.

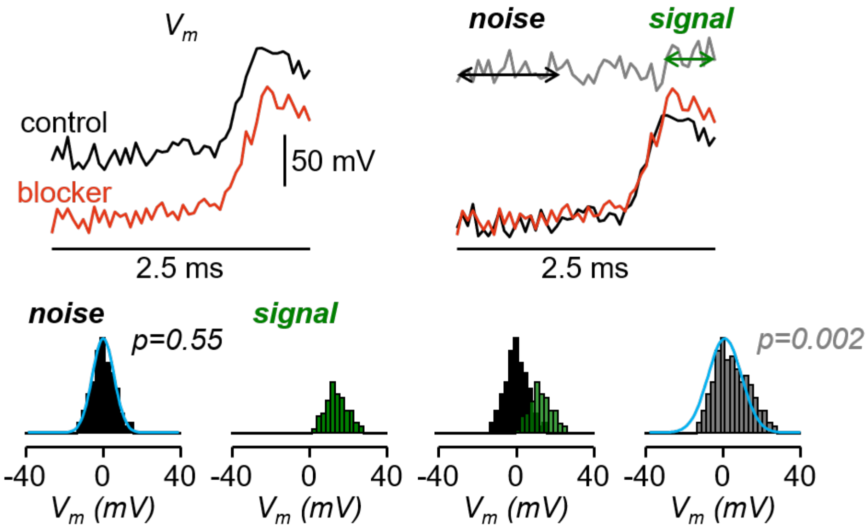

Figure 2.8: Statistical assessment of the AP widening following pharmacological manipulation. Top, to simulate an experimental widening two sets of normally distributed values with 5 mV standard deviation are added to a somatic AP recorded at 20 kHz, once in control conditions (black traces) and once in the presence of the channel blocker (red traces); the normal distributions are centered at 0 mV except for the 10 points (500 µs) following the AP peak in the red trace for which the distribution is centered at +15 mV; the gray trace on the right shows the difference between the red and black trace; the analysis is performed over the 20 points (1 ms) preceding the current injection (noise) and the 10 points following the AP peak (signal). Bottom, following the procedure illustrated above applied to N = 8 cells to obtain 160 points for the noise and 80 points for the signal, histograms of noise (black columns), of the signal (green columns) and of the noise+signal (240 points, gray columns); to qualitatively visualize the consistency with normality, normal distributions with mean and standard deviation calculated from noise and from the noise+signal are superimposed to the respective histograms (cyan traces); the p values of the two Lilliefors tests are indicated.

2.8.2 In the apical dendrite

For the simulations described in chapter 4, the above model was modified further. The morphology of the dendritic tree was changed to mouse morphology 36595 from the NeuroMorpho database, also reported in Buchanan et al. (2012). As in the AIS, an endogenous immobile Ca^{2+} buffer was introduced, as well as a mobile calcium indicator to mimic experimental conditions when necessary and Ca^{2+} extrusion system. The relevant K_{on} and K_{off} values were modified to reflect the indicator kinetics (Eberhard and Erne 1991; Schmidt et al. 2003). Next, we copied the channels for $Na_v1.2$, the delayer inward K^+ rectifier, CAKC BK and SK in the AIS to the apical and basal dendrites. VGCCs already present were replaced by specific models for a T-type and L-type current from Migliore et al. (2008), an R-type current from Mandge and Manchanda (2018) and identical N-type and P/Q-type currents from Wimmer et al. (2010). Channel distributions are in accordance with previous reports (Migliore and Shepherd 2002; Ramaswamy and Markram 2015). More specifically, VGNC $Na_v1.2$ has a uniform distribution which is decreased compared to the soma (Migliore and Shepherd 2002; Stuart and Sakmann 1994). A-type VGKCs linearly decreased in density from the soma along the dendrite. M-type currents and the delayed inward rectifier K^+ current have a uniform distribution (Kang et al. 2000; Korngreen and Sakmann 2000). BK channels were distributed homogeneously along the apical dendrite, in accordance with previous studies (Benhassine and Berger 2005). Similarly, SK channels are thought to be expressed homologues along the dendrite (Ramaswamy and Markram 2015). The depolarisaing I_h current activated by hyperpolarisation was inserted with increasing density of ∼50 fold from the soma to the distal apical dendrite (Harnett et al. 2015; Kole et al. 2006; Lörincz et al. 2002; Williams and Stuart 2000). Lastly, all VGCCs have a homogenous apical distribution (Ramaswamy and Markram 2015), but their individual contribution to the total current varied, depending on the experimental results.

The Ca^{2+} dependence of SK CAKCs in the model is controlled by L-type channels, as has been suggested in hippocampal neurons (Marrion and Tavalin 1998), and T-type VGCCs. Furthermore, BK channels are activated by Ca^{2+} entry through both N-type and L-type channels in accordance with the literature (Grunnet and Kaufmann 2004; Loane et al. 2007; Sun et al. 2003), with a preference for N-type VGCCs.

2.9 Methods extensions

During my thesis I worked on several projects to expand the methodology used in our lab. Specifically, I worked on the validation of two huwentoxin-IV analogues, one of which is a photosensitive version (Montnach et al. 2022). In addition, I tested a new calcium indicator, Cal520FF, and verified its high sensitivity compared to OG5N and Fluo4FF in our imaging setup (Blömer et al. 2021b).

2.9.1 Cal520FF - a new calcium indicator

2.9.1.1 Comparing low affinity calcium indicators

We compared the performance of the new Cal520FF to OG5N and Fluo-4FF. Fluo-4FF (K_D = 10 µM; Thermo Fisher Scientific, Waltham, MA) was selected because this indicator, unlike OG5N, has very dim fluorescence at zero Ca^{2+}, but

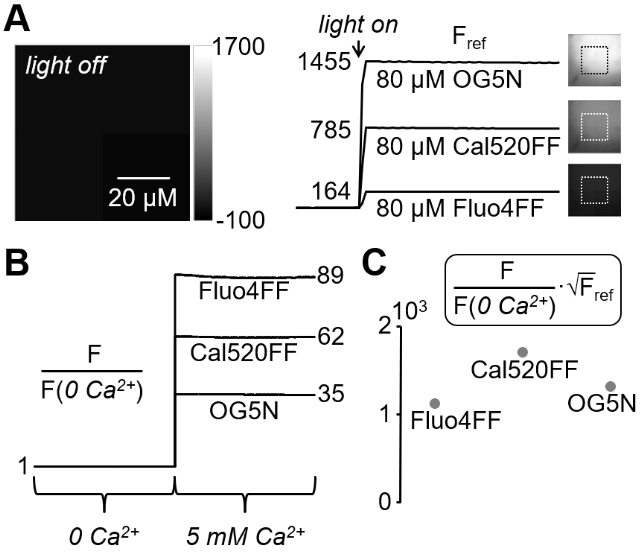

Figure 2.9: Evaluation of the three low-affinity indicators Fluo4FF, OG5N and Cal520FF. A, Left: field of view of the CCD camera; frame acquired without illumination. Right, three sequences of images acquired from a solution containing zero Ca^{2+} and 80 µM of either Fluo4FF (bottom), OG5N (top) or Cal520FF (middle); traces report the light intensity on the square region before and after turning on the 470 nm LED for the three indicators; the images are illustrated on the same greyscale to appreciate the different zero Ca^{2+} fluorescence levels; the values of the CCD digits in the three cases are reported. b In the three solutions of panel A, Ca^{2+} was increased from 0 to 5 mM and the ratio between the maximal and minimal Ca^{2+} (dynamic range) was calculated: 89 for Fluo4FF; 35 for OG5N; 62 for Cal520FF. C The product of the dynamic range (panel b) and of the square root of the CDD digits corresponding to zero Ca^{2+} (panel A): 1140 for Fluo4FF; 1335 for OG5N; 1737 for Cal520FF

a larger dynamic range with respect to OG5N. Thus, we could quantitatively position the performance of Cal520FF with respect to the different characteristics of the two indicators of comparison. Fluorescence was excited at 470 nm using the OptoLED and recorded at 530 ± 21 nm using imaging setup one. The S/N increases linearly with the sensitivity of the indicator, but it also increases with the square root of the basal fluorescence, which is close to the zero Ca^{2+} fluorescence. Thus, we initially evaluated the three low-affinity Ca^{2+} indicators Fluo4FF, OG5N and Cal520FF, with respect to these parameters. We prepared three solutions (1 mL each) containing 100 mM HEPES, buffered to pH 7.35 with KOH, 5 mM EGTA (to set 0 mM Ca^{2+}) and 80 µM of either Fluo4FF, OG5N or Cal520FF. We then evaluated each solution at zero Ca^{2+} separately in the microscope chamber by measuring the fluorescence excited with a light spot of ~ 100 µm diameter using the CCD camera (figure 2.9A). As expected, at zero Ca^{2+}, Fluo4FF had dim fluorescence quantified by 164 digits of the CCD camera, OG5N had brighter fluorescence quantified by 1455 digits and Cal520FF had intermediate fluorescence quantified by 785 digits. Next, we evaluated the dynamic range of each indicator by adding to each solution 10 µL of 1 M $CaCl_2$, to increase Ca^{2+} to ~5 mM and saturating the indicators (figure 2.9B). The maximal fluorescence, normalised to the zero Ca^{2+} fluorescence, was 89, 35, and 62 for Fluo4FF, OG5N and Cal520FF respectively. Finally, to evaluate the S/N performance that can be predicted in a physiological Ca^{2+} measurement, we calculated the product of the square root of the zero Ca^{2+} fluorescence (figure 2.9A) times the full dynamic range (figure 2.9B). As shown in figure 2.9C, OG5N performs better in terms of S/N than the dim Fluo4FF, but Cal520FF can potentially perform better than both indicators.

2.9.1.2 Comparing Cal520FF in brain slices

With this premise, we evaluated the performance of the three indicators in measuring the fast Ca^{2+} transient associated with an AP in L5 pyramidal neurons from acute brain slices (figure 2.10A) and the ability to reconstruct the underlying Ca^{2+} current by calculating the time-derivative of the Ca^{2+}-$\Delta F/F_0$ signal. Individual neurons were loaded with a Ca^{2+} indicator using whole cell patch clamp recordings (figure 2.10A) as described in the Materials and Methods. The Ca^{2+}-$\Delta F/F_0$ signal associated with an AP was used for this test. This signal is mediated by diverse VGCCs (L-type, P/Q-type, N-type, R-type and T-type) and it is locally blocked by a cocktail of VGCC inhibitors (20 µM Isradipine, 1 µM ω-Agatoxin IVA, 1 µM ω-Conotoxin GVIA, 1 µM SNX482, 5 µM ML218, 30 µM NNC550396) as shown in the example of figure 2.10A. For each indicator, 10 neurons were loaded with 2 mM of either Fluo4FF, Cal520FF or OG5N. We recorded the fluorescence time-course associated with an AP along a proximal segment of the apical dendrite and calculated the Ca^{2+}-$\Delta F/F_0$ signal from regions located at 80–100 µM from the soma at 20 kHz (figure 2.10B). Notably, in each cell tested, the loading conditions were standardized, fluorescence was excited at the same intensity and the auto-fluorescence was subtracted to accurately measure F_0. In each cell, we also averaged 9 recordings, and we corrected each trace for bleaching. In the three examples of figure 2.10B, F0 was the dimmest for Fluo4FF and the brightest for OG5N whereas the maximum $\Delta F/F_0$ after the AP was the largest for Fluo4FF and the smallest for OG5N. As expected from the preliminary analysis reported in figure 2.9, for both F0 and the maximum $\Delta F/F_0$, Cal520FF gave intermediate values with respect to the other two indicators. But when visually examining the normalized signals, Cal520FF exhibited the largest S/N among the three indicators. To quantify and assess the consistency of this result, for the three groups of 10 cells, we measured F0, the maximum $\Delta F/F_0$ and the S/N quantified by the ratio between the maximum $\Delta F/F_0$ and the $\Delta F/F_0$ standard deviation calculated from the samples before the AP (figure 2.10C). By applying either a parametric ANOVA test, or a non-parametric Kruskal-Wallis test, the three groups resulted significantly different for the three parameters analysed ($p < 0.001$) and Cal520FF signals had the largest S/N among the three indicators.

The importance of ultrafast Ca^{2+} imaging relies on the ability of tracking the kinetics of fast VGCCs by precisely reconstructing the shape of the Ca^{2+} current, which can be obtained in pyramidal neuron dendrites by calculating the time-derivative of the $\Delta F/F_0$ signal. Thus, we estimated the Ca^{2+} current kinetics by filtering fluorescence with a 20-points Savitsky-Golay smoothing filter and by calculating the time derivative (dF/dt) of the filtered fluorescence, as shown for the three examples in figure 2.10D. As in the case of the $\Delta F/F_0$ signal, the S/N of the dF/dt signal was visually larger in the example with Cal520FF. The S/N for the three groups of cells was then calculated for dF/dt (figure 2.10D). Again, for this signal, Cal520FF gave the largest S/N as revealed by the same two tests used above ($p < 0.001$). In summary, the significantly high performance of Cal520FF in ultrafast Ca^{2+} imaging makes this relatively new indicator the most ideal, at present, for this type of applications.

2.9.2 Toxins to distinguish between $Na_v1.2$ and $Na_v1.6$

In this thesis various toxins are utilised to block VGNCs. As both $Na_v1.2$ and $Na_v1.6$ are expressed in the AIS, we wanted to specifically target VGNCs to determine their contribution to AP generation. For this purpose we selected two toxins which are discussed below.

2.9.2.1 Selectivity of G^1G^4Huwentoxin-IV for $Na_v1.2$

The first necessary condition to investigate the role of $Na_v1.2$ in the AP generation at the AIS of L5PNs is the availability of a selective blocker of this channel that is specifically inert with respect to $Na_v1.6$. Phrixotoxin-3 (Bosmans et al. 2006) has been reported to be selective for $Na_v1.2$, but when we tested this peptide in L5 pyramidal neurons we found variable and rapidly reversible effects at the lowest concentrations where this selectivity is expected (data not shown). Thus, to produce a less reversible and still selective effect on $Na_v1.2$ channels, we used a peptide modified from huwentoxin-IV (hwtx), a toxin purified from tarantula venom which interacts with VGNCs to inhibit activation and fast inactivation of $Na_v1.7$ (Xiao et al. 2011), where the two glutamate residues at positions 1 and 4 were replaced with two glycine residues.

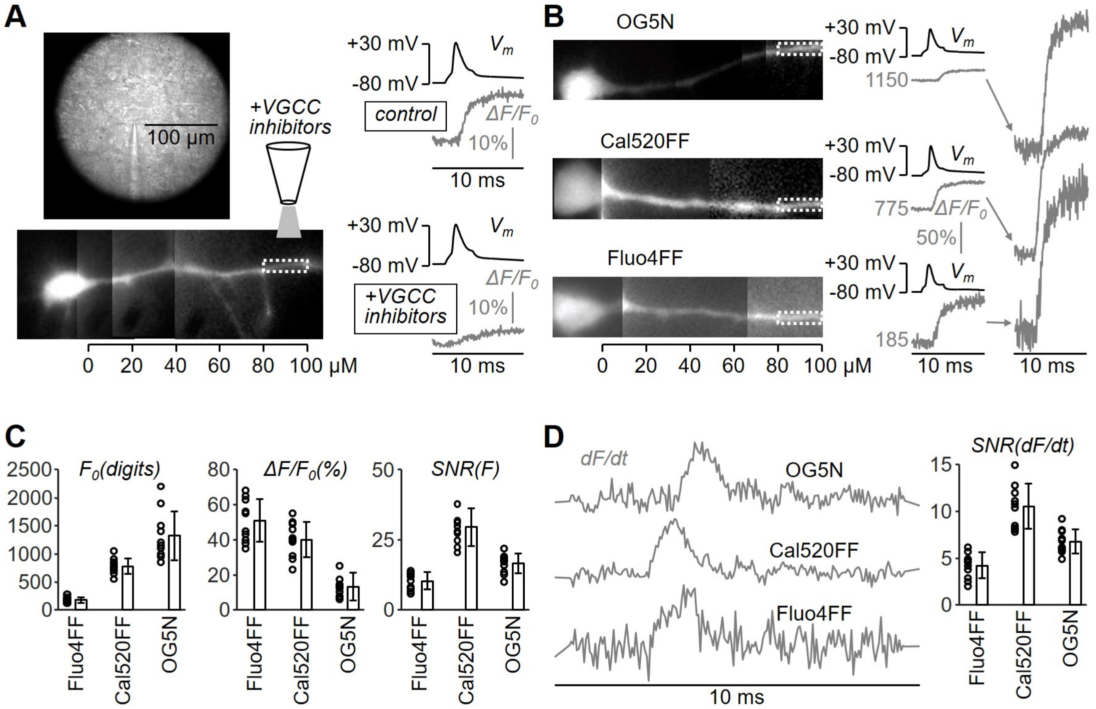

Figure 2.10: Performance of Fluo4FF, OG5N and Cal520FF for ultrafast Ca^{2+} imaging and optical recording of Ca^{2+} currents. A, Image of a brain (cortical) slice with patched L5 pyramidal neuron. On the bottom, a fluorescence image of a neuron loaded with 2 mM OG5N with a region of interest (white-dotted rectangle) indicated; a pipette locally delivering a cocktail of VGCC inhibitors (see main text) is drawn to indicate its position. On the right: somatic V_m with evoked AP and associated Ca^{2+}-$\Delta F/F_0$ signal in control condition and after locally delivering the VGCC inhibitors showing the block of the Ca^{2+} transient and no effect on the somatic AP. B, Left: fluorescence images of L5 pyramidal neurons loaded with 2 mM of either Fluo4FF (bottom), Cal520FF (middle) or OG5N (top); the white-dotted rectangles outline the regions (80–100 µm from the soma) from where fluorescence was averaged. Centre: $\Delta F/F_0$ signals (grey) associated with an AP (black); the camera digits corresponding to F0 are indicated. Right: the normalised $\Delta F/F_0$ signals showing the different S/N. C, Left: F0 values (digits) in 10 cells for each indicator and mean ± SD for Fluo4FF (174 ± 48), Cal520FF (780 ± 139) and OG5N (1325 ± 425). Centre: maximum $\Delta F/F_0$ (%) values in the 10 cells and mean ± SD for Fluo4FF (51 ± 12), Cal520FF (40 ± 10) and OG5N (13 ± 8). Right: $\Delta F/F_0$ S/N values in the 10 cells and mean ± SD for Fluo4FF (10.3 ± 3.0), Cal520FF (29.5 ± 6.6) and OG5N (16.5 ± 3.5). D, Left: normalised time-derivative of F after smoothing (dF/dt) in the three cells of panel A. Right: dF/dt S/N values in the 10 cells and mean ± SD for Fluo4FF (4.2 ± 1.4), Cal520FF (10.5 ± 2.4) and OG5N (6.8 ± 1.3). All data are from averages of 9 trials (Figure from (Blömer et al. 2021b)

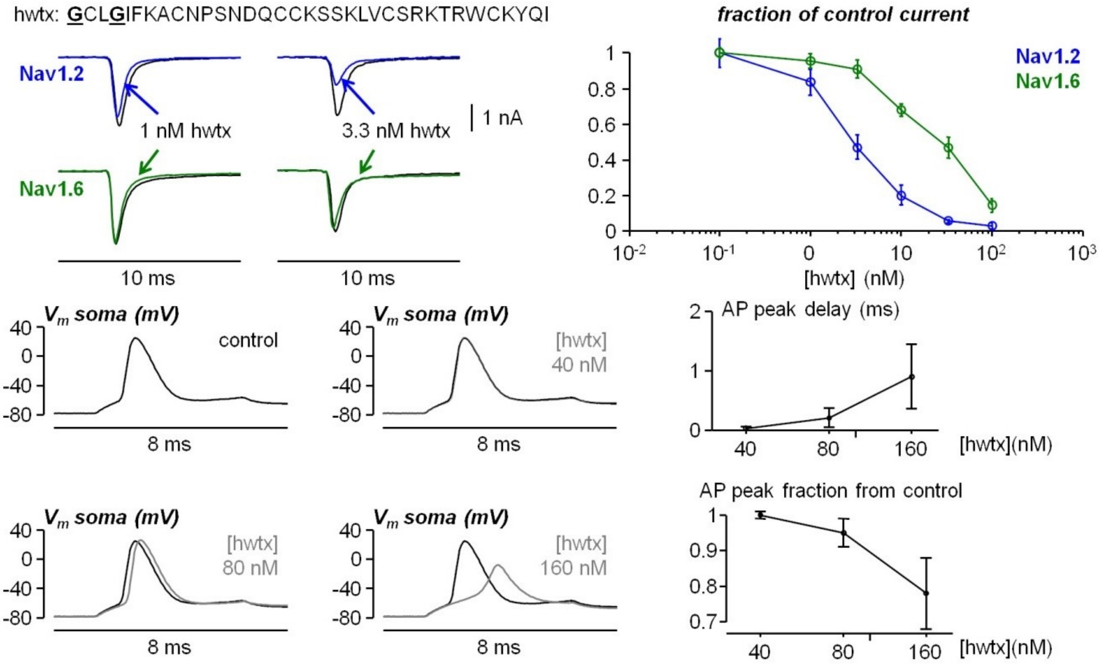

Figure 2.11: Selectivity of G^1G^4-Huwentoxin-IV (G^1G^4hwtx). Top-left, currents in HEK293 cells expressing either $Na_v1.2$ (blue) or $Na_v1.6$ (green) in control solution and after addition of G^1G^4hwtx (hwtx) at 1 nM (left traces) or at 3.3 nM (right traces); the 35-aminoacids sequence of G^1G^4hwtx is reported; the two residues mutated from the wild type peptide are indicated with bold-underlined characters. Top-Right, fraction of $Na_v1.2$ (green) or $Na_v1.6$ (blue) current peak from control condition (no G^1G^4hwtx) against G^1G^4hwtx concentration (mean ± SD); each concentration-point has been calculated over 10-15 cells. Bottom-Left, in a L5 pyramidal neuron in brain slices, AP elicited in control condition (no G^1G^4hwtx) or in the presence of 40 nM, 80 nM or 160 nm G^1G^4hwtx. Bottom-Right, delay of the AP peak and AP peak fraction from control condition against G^1G^4hwtx concentration (mean ± SD, N = 7 cells).

This peptide, G^1G^4Huwentoxin-IV (G^1G^4hwtx), was developed by the team of Michel de Waard (Nantes, France) who initially wanted to develop a photosensitive version of this 35 amino acid toxin, with convergent blocking potencies for $Na_v1.1$, $Na_v1.2$, $Na_v1.6$, and $Na_v1.7$ channels. Therefore, they synthesised 20 analogues of n-hwtx based on earlier structure-function analyses using single amino-acid mutations and 3D structures (Agwa et al. 2020; Peng et al. 2002). One of those analogues was the G^1G^4hwtx mutant. They found that G^1G^4hwtx exhibits higher selectivity for $Na_v1.2$ with respect to $Na_v1.6$ at nanomolar concentrations as measured in HEK293 cells using automated patch-clamp recordings (figure 2.11). Specifically, at 1 nM and 3.3 nM, G^1G^4hwtx blocks 16 ± 7% and 53 ± 7% of $Na_v1.2$ currents respectively, and only 5 ± 4% and 9 ± 5% $Na_v1.6$ currents respectively. The challenge remained to exploit this selectivity by locally blocking $Na_v1.2$ in the AIS of L5 pyramidal neurons in the context of brain slices in which effective concentrations may differ. Thus, L5 pyramidal neurons were patched in the cell body and another pipette near the AIS was used to locally deliver selective channel blockers, for 1 minute, by gentle pressure application. This way, when we delivered G^1G^4hwtx at 40 nM, the peptide did not affect the AP (figure 2.11). The smallest concentration at which we consistently observed an affect was 80 nM and this effect was a delay in the AP onset and peak with occasionally a small decrease in amplitude (figure 2.11). Finally, at 160 nM, G^1G^4hwtx consistently produced a longer delay and decreased the amplitude of the AP. Importantly for this project, at all concentrations, the consistent effects of G^1G^4hwtx were stable for several minutes after delivery, in sharp contrast to phrixotoxin application. We could therefore use G^1G^4hwtx at 80 nM concentration on the hypothesis that at this minimal concentration, the peptide should produce a partial but selective block on $Na_v1.2$ because this channel type is more sensitive than $Na_v1.6$ to G^1G^4hwtx.

2.9.2.2 Selectivity of 4,9-anhydrotetrodotoxin for $Na_v1.6$

To validate whether the findings obtained by local delivery of G^1G^4hwtx were exclusively due to $Na_v1.2$, we used the $Na_v1.6$ inhibitor 4,9-anhydrotetrodotoxin (attx) in the control experiments. Once more our collaborators in Nantes assessed, in experiments performed in HEK293 cells using automated patch clamp recordings (figure 2.12), that this molecule exhibits a small selectivity for $Na_v1.6$ with respect to $Na_v1.2$. Specifically, at 10 nM and 33 nM, attx blocks 20 ± 13% and 30 ± 13% $Na_v1.6$, respectively, whereas it blocks 9 ± 11% and 16 ± 12% $Na_v1.2$ respectively. In AP tests performed in brain slices in our lab, attx at 400 nM did not affect the AP, whereas the smallest concentration at which we consistently observed a delay in the AP offset was 800 nM (figure 2.12). At 1600 nM, attx consistently produced a stronger AP inhibition. Similarly to G^1G^4hwtx, the effects of attx at all concentrations were stable for several minutes after delivery. Thus, experiments to target $Na_v1.6$ channels were performed by using attx at the concentration of 800 nM that provides the minimal perturbation of the somatic AP.

2.9.3 Photosensitive $G^1G^4K^{36}$Huwentoxin-IV

For the photosensitive hwtx mutant, $G^1G^4K^{36}$Huwentoxin-IV ($G^1G^4K^{36}$hwtx) was selected from the 20 analogues (Montnach et al. 2022). This analogue is one amino-acid longer than native hwtx. Again using HEK293 cells they determined that this hwtx analogue was the most potent for a pan-Na_v action.

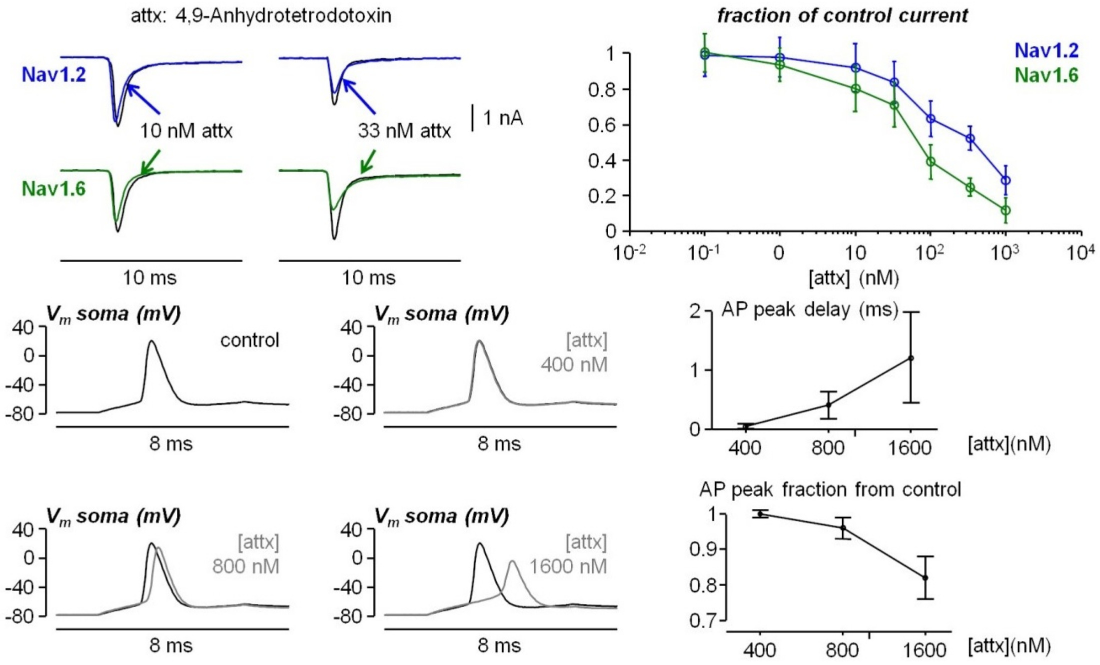

Figure 2.12: Selectivity of 4,9-Anhydrotetrodotoxin (attx). Top-left, currents in HEK293 cells in control solution and after addition of attx at 10 nM (left traces) or at 33 nM (right traces). Top-Right, fraction of $Na_v1.2$ or $Na_v1.6$ current peak from control condition (no attx) against attx concentration (mean ± SD); each concentration-point has been calculated over 10-15 cells. Bottom-Left, in a L5 pyramidal neuron in brain slices, AP elicited in control condition (no attx) or in the presence of 400 nM, 800 nM or 1600 nm attx. Bottom-Right, delay of the AP peak and AP peak fraction from control condition against attx concentration (mean ± SD, N = 7 cells).

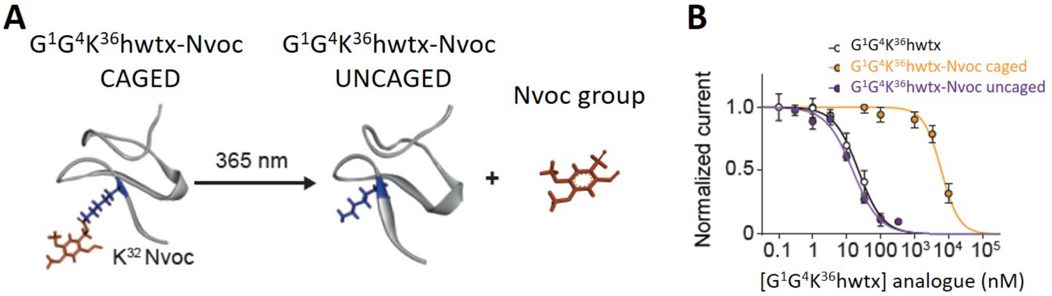

Figure 2.13: Selectivity of $G^1G^4K^{36}$Huwentoxin-IV-Nvoc. A, Photolysis of $G^1G^4K^{36}$hwtx-Nvoc by illumination at 365 nm. B, Light-induced inhibition of $Na_v1.6$ current by uncaged $G^1G^4K^{36}$hwtx-Nvoc analog (100 nM).

2.9.3.1 Development of $G^1G^4K^{36}$huwentoxin-IV-Nvoc

The most straightforward chemical strategy to achieve photosensitivity is to add a photosensitive cage on the side chain of a residue that is key for activity (Bourgault et al. 2007). The activity of hwtx, as well as many other toxins, relies on a limited set of amino acids. Often, a lysine (Lys) residue, or a residue that can be substituted by Lys, appears critical for biological activity (Dauplais et al. 1997). Montnach et al. (2022) found that the K^{32} residue is an ideal amino acid residue for chemical modifications aimed at reducing hwtx potency. By mutating K^{32} to N^{32} the potency of hwtx for $Na_v1.7$ decreased >100 fold. They proceeded with covalent attachment of an orthogonal o-nitroveratryloxycarbonyl (Nvoc) protecting group to K^{32} of $G^1G^4K^{36}$hwtx ($G^1G^4K^{36}$hwtx-Nvoc).

The presence of the aromatic Nvoc group on K^{32} for $G^1G^4K^{36}$hwtx-Nvoc disturbs the chemical environments of a series of residues on the side of the molecule where K^{32} is located without affecting the global fold of the peptide. The Nvoc group can be cleaved by photolysis under physiological conditions, exposing the critical K^{32} amino acid and activating the toxin. Specifically, photolysis of caged $G^1G^4K^{36}$hwtx-Nvoc occurred up to a wavelength of 405 nm (figure 2.13A) but was negligible at wavelengths in the 435-740 nm range which offers the possibility to use fluorophores excited above 405 nm for additional recordings. After testing $G^1G^4K^{36}$hwtx-Nvoc in HEK293 cells they found that, compared to uncaged $G^1G^4K^{36}$hwtx-Nvoc, caged $G^1G^4K^{36}$hwtx-Nvoc is ~300 times less effective in blocking VGNCs, and the uncaged toxin is indistinguishable from noncaged $G^1G^4K^{36}$hwtx in its blocking abilities (figure 2.13B). In our research, photo-activable toxins are interesting as they offer the possibility of uncaging said toxin locally with high spatial and temporal precision. Dr Luiza Filipis, then a post-doctoral scientist in our team, and I both contributed to these experiments.

2.9.3.2 $G^1G^4K^{36}$huwentoxin-IV-Nvoc in brain slices

To asses $G^1G^4K^{36}$hwtx-Nvoc in brain slices we first determined that APs recorded in L5PNs were inhibited by local application of 500 nM non-caged $G^1G^4K^{36}$hwtx from the surface of the brain slice near the cell body (figure 2.14A). Similar experiments conducted with the caged $G^1G^4K^{36}$hwtx-Nvoc analog show that the AP shape is unaltered. As expected, photolysis of $G^1G^4K^{36}$hwtx-Nvoc leads to a significant decrease of the maximal membrane potential (V_m) 1 min after illumination (figure 2.14B,C). This block was only partially reversible by washout for ~30 minutes (examples shown in figure 2.15). Spatial selectivity was next precisely examined by

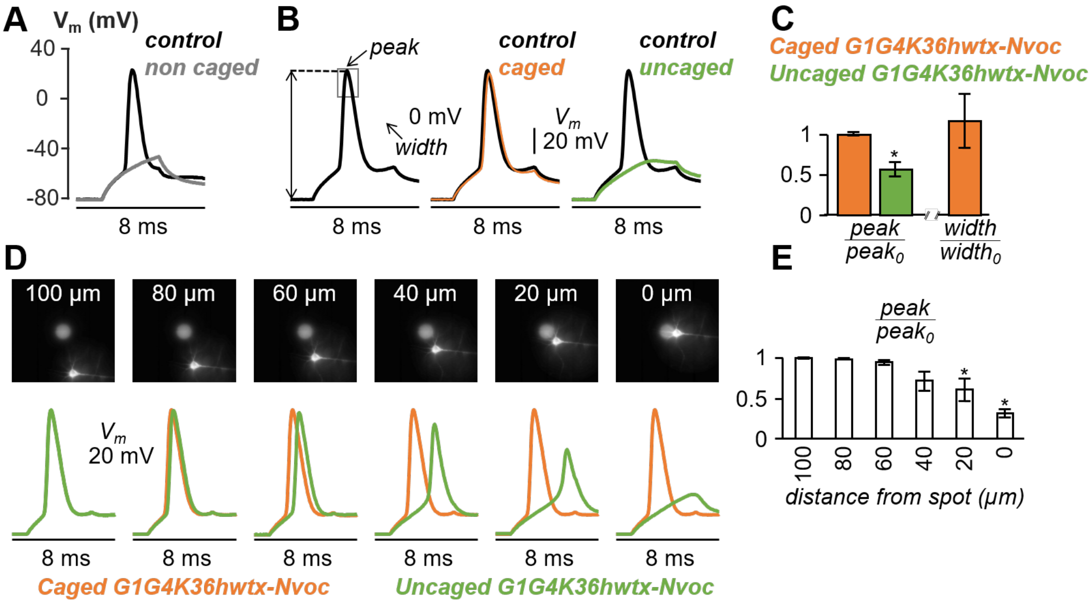

Figure 2.14: $G^1G^4K^{36}$hwtx-Nvoc assessments in L5 pyramidal neurons from mouse brain slices. A, Gray trace: AP in control solution. Black trace: the AP is inhibited by application of 500 nM non-caged $G^1G^4K^{36}$hwtx analog (consistently observed in n = 6 cells tested). B, left: AP in control solution, centre: in the presence of 2.5 µM of caged $G^1G^4K^{36}$hwtx-Nvoc, right: recording 1 minute after uncaging the toxin showing full AP block; the peak of the depolarization and the width of the AP used in the statistical analysis are illustrated; black traces are the control recording reported for comparison. C, left: mean ± SEM (n = 8 cells) of the depolarization peak, normalized to the control values, after addition of caged $G^1G^4K^{36}$hwtx-Nvoc (1.00 ± 0.01) and 1 minute after photolysis (0.43 ± 0.03). "*" indicates a significant decrease of the peak ($p < 0.01$, paired t-test). Right: mean ± SEM (n = 5 cells) of the AP width, normalized to the control values, after addition of $G^1G^4K^{36}$hwtx-Nvoc (1.18 ± 0.11). D, Top: images of L5 pyramidal neuron filled with a fluorescent indicator relative to the position of a UV (405 nm) illumination spot with distance from the center indicated in each frame. Bottom: AP in the presence of caged $G^1G^4K^{36}$hwtx-Nvoc (orange traces) and 1 minute after uncaging (purple traces) with the cell positioned at distances from the spot center of 100, 80, 60, 40, 20 and 0 µm. E, Left: image of the UV spot (∼40 µm diameter); the purple curve indicates the light intensity profile; cells are depicted to indicate the different positions with respect to the spot. Right: mean ± SEM (n = 5 cells) of the depolarization peak, normalized to the control values, 1 minute after uncaging with the cell positioned at distances from the spot centre of 100 µm (1.00±0.01), 80 µm (0.99±0.01), 60 µm (0.95±0.03), 40 µm (0.77±0.12), 20 µm (0.61±0.14) and 0 µm (0.32±0.05). "*" indicates a significant decrease ($p < 0.01$, paired t-test). "*" indicates a significant decrease ($p < 0.01$, paired t-test).

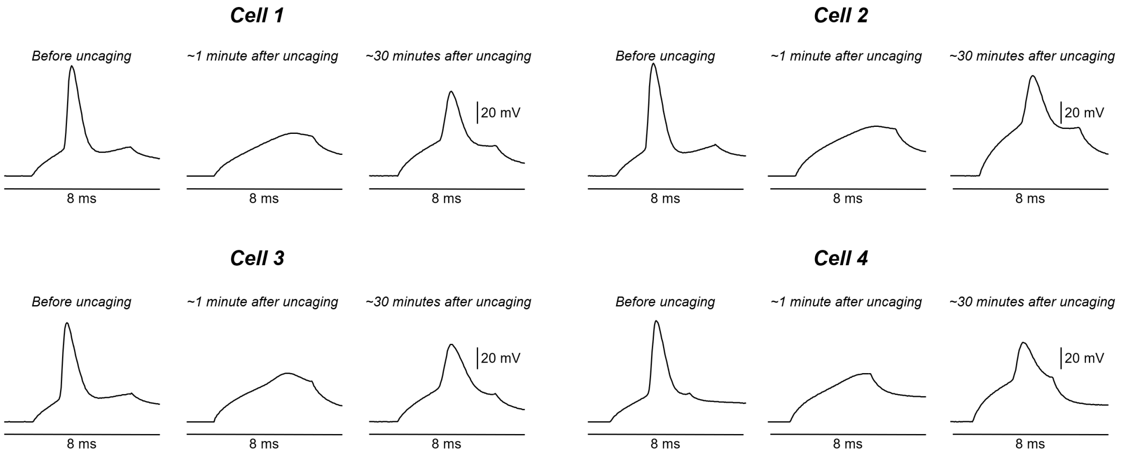

Figure 2.15: Recovery from $G^1G^4K^{36}$hwtx-Nvoc. Examples of four cells of a control measurement before uncaging the toxin, approximately one minute after uncaging showing a full block of the AP in all examples, and lastly partial recovery after 30 minutes.

using a 405 nm laser spot of ∼40 µm diameter positioned at varying distance from the soma. The somatic AP was not affected when the cell was at distances >80 µm from the spot center, whereas it was partially inhibited at distances between 60 and 20 µm from the spot center (figure 2.14D,E). With the larger 365 nm UV LED spot, the somatic AP was not affected by illuminating a spot centered at ∼100 µm away from the soma. These results provide information about the spatial resolution that can be attained by uncaging of $G^1G^4K^{36}$hwtx-Nvoc inside the area of photolysis.

Luiza Filipis then recorded Na^+ influx directly via voltage-gated Na^+ channels, associated with an AP, to unambiguously assess the effect of the uncaged toxin on the channels expressed in the AIS (figure 2.16A) using a recent ultrafast Na^+ imaging approach (Filipis and Canepari 2021). Illumination of caged $G^1G^4K^{36}$hwtx-Nvoc in the soma (500 ms, 2 mW) fully prevented Na^+ influx in the AIS, even at the same depolarized V_m of the AP (figure 2.16B,C). This result demonstrates that photo-release of $G^1G^4K^{36}$hwtx analog blocks voltage-gated Na^+ channels and AP propagation even at positive V_m. Altogether, these results provided proof-of-principle that controlled photolysis of caged $G^1G^4K^{36}$hwtx-Nvoc can be used to spatially modulate neuronal AP initiation and sodium influx in brain tissues.

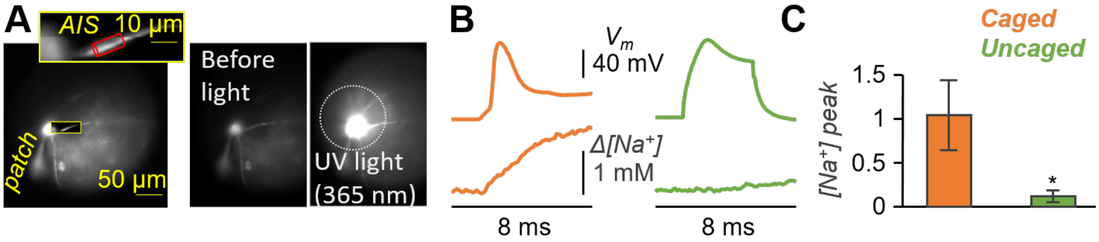

Figure 2.16: Sodium imaging with G^{1}G^{4}K^{36}hwtx-Nvoc. A, left, L5 pyramidal neuron filled with 500 µM of the Na$^+$ indicator ING-2; the patch pipette filling the cell is visible; outlined in yellow the AIS area of $\Delta[\text{Na}^+]$ measurement; right, images taken before and during the uncaging pulse of UV light illustrating the area of photolysis. B, left, somatic AP (top) and associated $\Delta[\text{Na}^+]$ signal over the red cylinder depicted in panel A (bottom) in the presence of caged G^{1}G^{4}K^{36}hwtx-Nvoc; right, after uncaging the toxin, V$_m$ transient depolarizing the cell to the AP peak (top) and and associated $\Delta[\text{Na}^+]$ signal (bottom). C, mean ± SEM ($n = 4$ cells) of the $\Delta[\text{Na}^+]$ signal maximum (peak) before and after uncaging the toxin. "*" indicates a significant decrease ($p < 0.01$, paired t-test).

3

Study of the ion channels involved in generating the action potential in the axon initial segment

Contents

3.1 The effect of blocking Na$_v$1.2 channels and VGCCs in the AIS 61

3.1.1 The selective block of Na$_v$1.2 reduces the Na$^+$ current associated with the AP waveform in the AIS 61

3.1.2 The selective block of Na$_v$1.2 widens the generating AP waveform in the AIS 63

3.1.3 The distal I$_{Ca}$ precedes the proximal I$_{Ca}$ in the AIS . . 65

3.1.4 VGCCs mediate part of the Ca^{2+} influx in the AIS . . . 67

3.1.5 Na$_v$1.2 mediates Ca^{2+} influx associated with the AP in the AIS 68

3.2 The effect of blocking CAKCs in the AIS 70

3.2.1 The block of CAKCs widens the AP in the AIS after blocking VGCCs 70

3.2.2 The block of BK CAKCs widens the AP in the AIS preventing the widening caused by blocking Na$_v$1.2 . . . 73

3.3 The effect of blocking Na$_v$1.6 channels in the AIS . . . 73

3.3.1 Na$_v$1.6 does not mediate Ca^{2+} influx associated with the AP in the AIS 74

3.4 The Na$_v$1.2-BK channels interaction is mimicked by simulations in a NEURON model 76

3.5 Summary and significance 79

This chapter addresses the contribution and roles of Na$_v$1.2 and Na$_v$1.6 during the generation of the AP in the AIS. Until recently, specific targeting of these two VGNCs was not possible as VGNC blockers did not discriminate between the two. Here we solved this issue and optically measured Na$^+$ currents (Filipis and Canepari 2021), V$_m$ transients (Popovic et al. 2015) and Ca^{2+} currents (Ait Ouares et al. 2016; Jaafari and Canepari 2016; Jaafari et al. 2014) associated with APs elicited by somatic current injections and we analysed how the partial block of Na$_v$1.2 affected these signals. We then focussed on the changes of these signals produced by fully blocking VGCCs and/or CAKCs in order to correlate Na$_v$1.2 signalling with the activation of these channels.

In the experiments reported below, Dr Luiza Filipis, a post-doctoral researcher in the lab, performed most of the Na$^+$ and Ca^{2+} imaging, whereas I contributed mostly to the V$_m$ transient experiments. All experiments are included here as they illustrate the synergy of the ion channels involved in shaping the generating AP in the AIS. In addition, Luiza developed the NEURON model, which I use as the basis for the model described in chapter 4, connecting the AIS and apical dendrite.

3.1 The effect of blocking Na$_v$1.2 channels and VGCCs in the AIS

The analysis of G^{1}G^{4}hwtx detailed in chapter 2 allowed investigating how the membrane voltage, sodium and calcium transients changed following a partial block of Na$_v$1.2. To investigate how the partial block of Na$_v$1.2 effects the signals associated with the generating AP in the AIS, we analysed the consequences of G^{1}G^{4}hwtx application on the Na$^+$ and Ca^{2+} currents and the V$_m$ in the AIS.

3.1.1 The selective block of Na$_v$1.2 reduces the Na$^+$ current associated with the AP waveform in the AIS

Figure 3.1A shows the AIS of a neuron filled with the Na$^+$ indicator Ion Natrium Green-2 (ING-2). We first measured the sodium concentration change (Δ[Na$^+$]) associated with an AP. Then, we calculated the Na$^+$ current (I$_{Na}$) as the time-derivative of the fit of the Δ[Na$^+$] signal using a model function (figure 3.1B). In the example of figure 3.1A, application of 80 nM G^{1}G^{4}hwtx produced a decrease of ~30% of the Δ[Na$^+$] signal in the proximal part of the AIS and a ~15% decrease in the distal part. On average, G^{1}G^{4}hwtx decreased the Δ[Na$^+$] with 30% and 23% in proximal

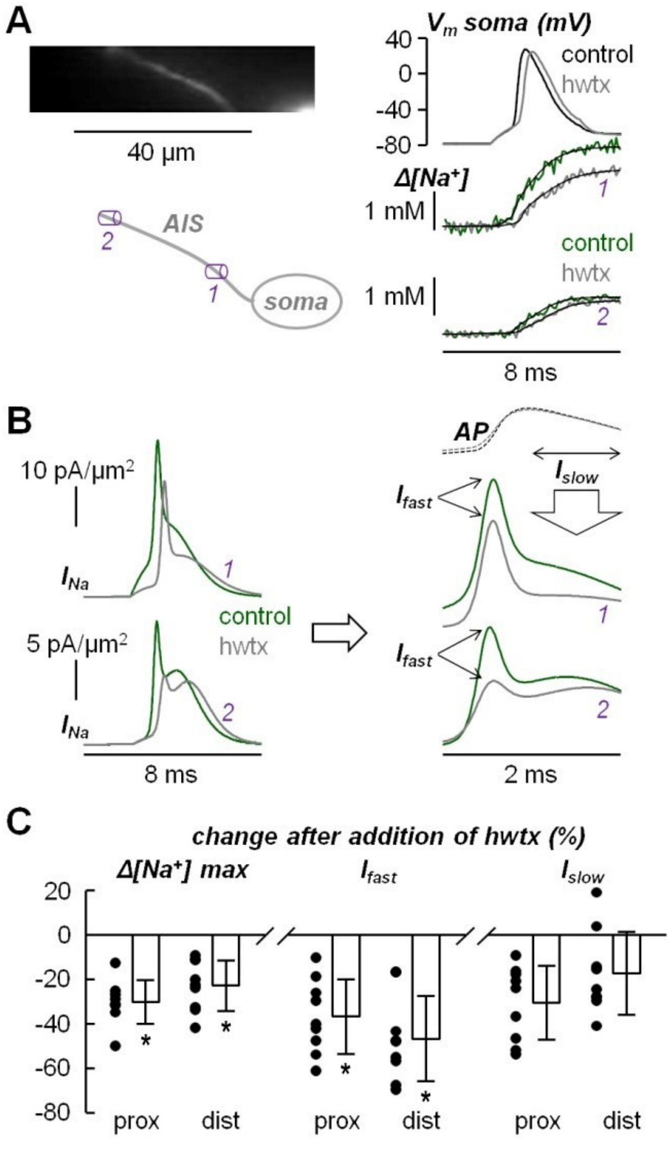

Figure 3.1: Effect of G^{1}G^{4}hwtx (block of Na$_v$1.2) on the Na$^+$ influx in the AIS. A, Left, fluorescence image (Na$^+$ indicator ING-2) of the AIS and its reconstruction with a proximal region (1) and a distal region (2) indicated. Right, Somatic AP in control solution and after local delivering 80 nM of G^{1}G^{4}hwtx (hwtx) (top) and associated corrected Na$^+$ transients fitted with a model function in 1 and 2. B, Left, from the experiment in A, Na$^+$ currents calculated from the time-derivative of the Na$^+$ transient fits. Right, zoom of the Na$^+$ currents 1 ms before and 1 ms after the AP peak indicating the fast component of the Na$^+$ current (I$_{fast}$) and the slow component of the Na$^+$ current (I$_{slow}$) defined as the mean Na$^+$ current during the 1-ms interval after the AP peak. C, Left, single cell values and percentage change (N=9 cells) of the Na$^+$ transient maximum after locally delivering of G^{1}G^{4}hwtx in proximal regions (mean ± SD = -30.3 ± 9.8), and in distal regions (mean ± SD = -22.9 ± 11.4). Centre, single cell values and percentage change of I$_{fast}$ after locally delivering G^{1}G^{4}hwtx in proximal regions (mean ± SD = -36.6 ± 16.7), and in distal regions (mean ± SD = -46.8 ± 19.2). Right, single cell values and percentage change of I$_{slow}$ after addition of G^{1}G^{4}hwtx in proximal regions (mean ± SD = -30.7 ± 16.6), and in distal regions (mean ± SD = -17.5 ± 18.6). "*" indicates a significant change ($p<0.01$, paired t-test).

and distal regions, respectively. This fits with previous observations $Na_v1.2$ density is highest in the proximal AIS but is also present in more distal parts (Hu et al. 2009).

As already reported (Filipis and Canepari 2021), the I_{Na} is characterised by a fast inactivating component (I_{fast}) and a slow non-inactivating component (I_{slow}). Thus, we systematically evaluated the change in the I_{fast} peak and in the I_{slow} (defined as the mean I_{Na} in the millisecond following the AP peak) after applying G^1G^4hwtx. On average, in 9 cells analysed, we found a significant ($p<0.01$, paired t-test) decrease in the $\Delta[Na^+]$ and in the I_{fast} signals, both in proximal and distal regions, whereas a consistent but more variable decrease in the I_{slow} signals was estimated. This is in accordance with previous electrophysiological studies, showing the I_{slow} is mostly mediated by $Na_v1.6$ (Burbidge et al. 2002; Rush et al. 2005).

In proximal regions, where $Na_v1.2$ is expected to be dominant (Hu et al. 2009), the decrease in $\Delta[Na^+]$ and I_{fast} signals were 30% and 36% respectively, indicating a block of 30-40% of Na^+ channels (figure 3.1C). According to the selectivity curve reported in figure 3.2, this percentage block is within the range where G^1G^4hwtx is inert to $Na_v1.6$. It also shows that I_{fast} is almost exclusively mediated by $Na_v1.2$.

3.1.2 The selective block of $Na_v1.2$ widens the generating AP waveform in the AIS

The important finding that local delivery of 80 nM G^1G^4hwtx blocks 30-40% of $Na_v1.2$ without affecting $Na_v1.6$ allowed us to perform further experiments with high confidence using G^1G^4hwtx at 80 nM. It permitted the analysis of the axonal AP waveform change after reducing $Na_v1.2$, using V_m imaging with the voltage-sensitive dye JPW1114. In the example of figure 3.2A, application of 80 nM G^1G^4hwtx delayed the onset of the AP, consistently to what we reported in figure 3.1 and in figure 3.2. In the distal AIS, however, it also changed the shape of the AP by widening its waveform (figure 3.2B). To reliably quantify the waveform change beyond the noise limitations, we calculated the time integral of the V_m signal in control conditions and after G^1G^4hwtx application over a time-window of 2.4 milliseconds containing the AP ($\int V_m$). Notably, in 9 cells analysed, the $\int V_m$ at its last value significantly increased by 21.3 ± 10.5% ($p<0.01$, paired t-test) in the distal regions of the AIS (figure 3.2C).

This result indicates that $Na_v1.2$ is contributing to the shaping of the generating AP by sharpening its waveform. The widening of the AP waveform, however, cannot be produced by a reduction of an (inward) Na^+ current. The phenomenon reported in figure 3.2 can only be explained if the partial block of $Na_v1.2$ is also associated with a reduction of the outward current which must be larger than the Na^+ current

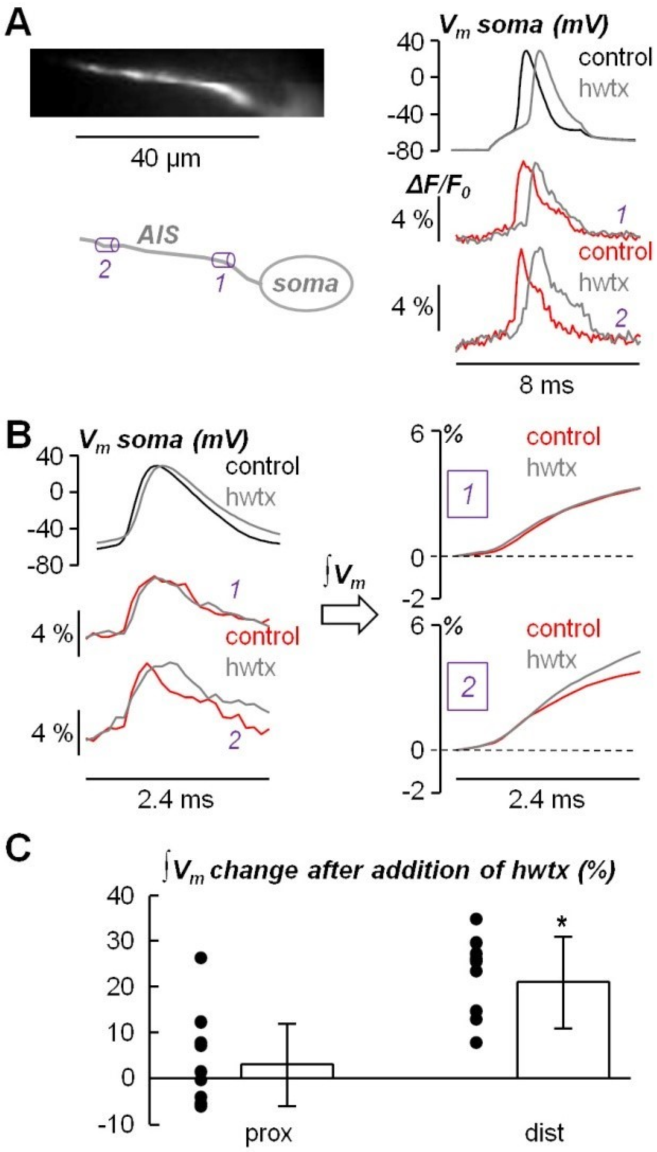

Figure 3.2: Effect of G^1G^4hwtx (block of $Na_v1.2$) on the AP waveform in the AIS. A, Left, fluorescence image (voltage sensitive dye JPW1114) of the AIS and its reconstruction with a proximal region (1) and a distal region (2) indicated. Right, Somatic AP in control solution and after locally delivering 80 nM of G^1G^4hwtx (hwtx) (top) and associated V_m transients in 1 and 2. B, Left, somatic and axonal APs at a different time scale (2.4 ms duration) visually indicating a widening of the AP waveform, in the distal position only, after locally delivering G^1G^4hwtx. Right, quantification of the AP waveform shape by calculation of V_m integral ($\int V_m$) over the 2.4 ms time window comprising the AP signal. C, Single cell values and percentage change (N=9 cells) of the $\int V_m$ signal maximum after locally delivering G^1G^4hwtx in proximal regions (mean ± SD = 3.2 ± 8.8), and in distal regions (mean ± SD = 21.3 ± 10.5). "*" indicates a significant change ($p<0.01$, paired t-test).

change in the early phase of the AP repolarisation. The outward current underlying the AP repolarisation is mediated by K^+ channels. Since the AP amplitude is not significantly affected by the partial block of $Na_v1.2$, any variation of current mediated by VGKCs is minimal. The most likely hypothesis is therefore that CAKCs are also contributing to the shaping of the generating AP and that these channels are activated by Ca^{2+} influx via $Na_v1.2$. Since $Na_v1.2$ is also permeable to Ca^{2+} and it was reported that $Na_v1.2$ mediates Ca^{2+} influx in the AIS during APs (Hanemaaijer et al. 2020), we next investigated this phenomenon in detail using G^1G^4hwtx.

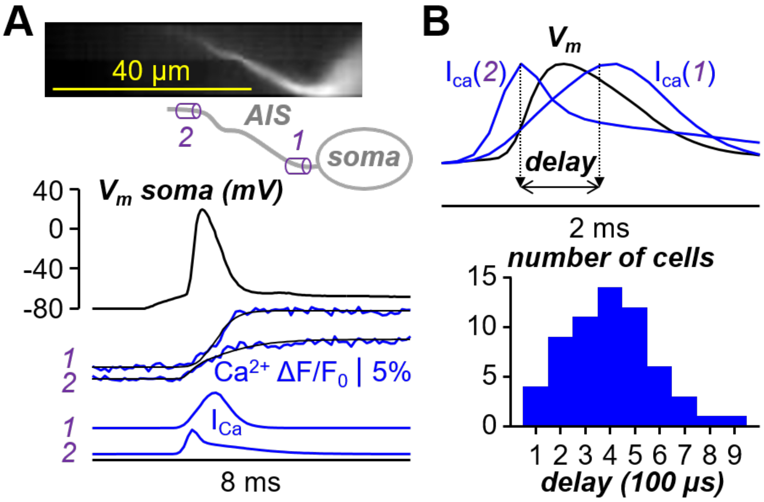

Figure 3.3: Calcium transients in the AIS. A, Top, fluorescence image (OG5N) of the AIS and its reconstruction with a proximal (1) and distal region (2). Bottom, somatic AP and associated Ca^{2+} transients fitted with a 4-sigmoid (product of four sigmoids) function in 1 and 2; the Ca^{2+} currents calculated as the time-derivative of the fits are reported below. B, Top, from the experiment in A, Ca^{2+} currents superimposed to the somatic AP. Bottom, over N = 61 cells tested, distribution of the delay between the distal and the proximal Ca^{2+} current peaks.

3.1.3 The distal I_{Ca} precedes the proximal I_{Ca} in the AIS

To investigate Ca^{2+} influx and currents associated with an AP in the AIS, we recorded Ca^{2+} fluorescence from the indicator Oregon Green BAPTA-5N (OG5N) and estimated the Ca^{2+} current waveform by calculating the time derivative of the fluorescence transient. Specifically, we fitted the fluorescence transient with a 4-sigmoid fit and calculated its time-derivative as done in a previous study (Jaafari and Canepari 2016) and described in chapter 2.

First, we analysed the kinetics of the Ca^{2+} current at different locations of the AIS as shown in the example of figure 3.3A. As already reported by Hanemaaijer et al. (2020), the kinetics of the Ca^{2+} signal associated with the AP varied with the distance from the soma with the onset of the Ca^{2+} transient in the distal axon preceding that in the proximal axon. In terms of Ca^{2+} currents calculated as time-derivatives of the Ca^{2+} transients, a substantial delay between the peak of the Ca^{2+} current in the distal axon and the peak of the Ca^{2+} in the proximal part of the AIS was measured (figure 3.3B). This behaviour was consistently observed in N = 61 cells tested in this way (figure 3.3B), with a significant delay between the peaks of 402 ± 177 µs ($p<0.01$, paired t-test).

The evident anticipation of the distal Ca^{2+} current peak, also with respect to the somatic AP peak, is surprising, as previous studies show that Ca^{2+} influx occurs

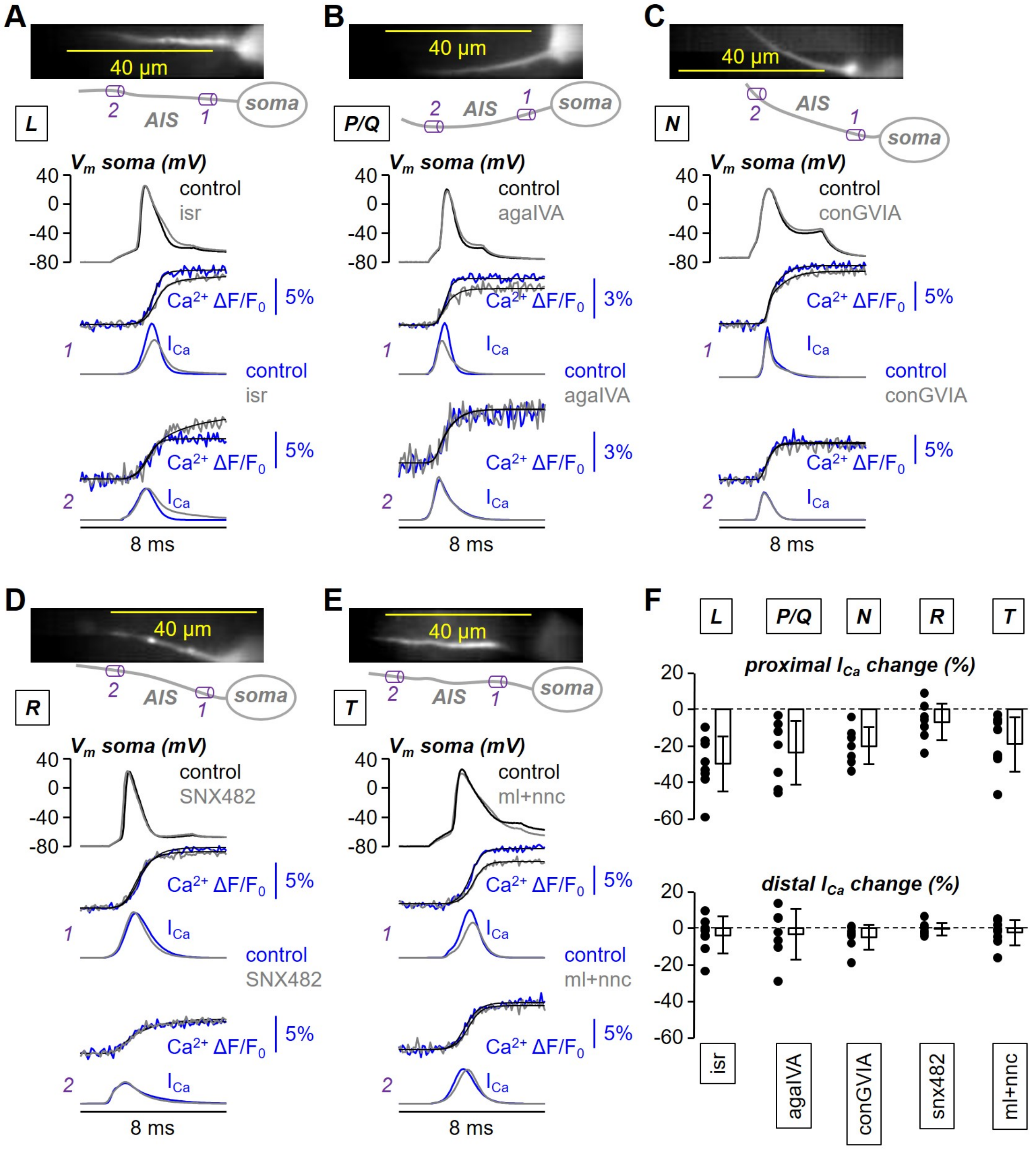

Figure 3.4: Analysis of the Ca^{2+} current (I_{Ca}) components mediated by individual VGCC types in the AIS. A, Top, fluorescence image (Ca^{2+} indicator OG5N) of the AIS and its reconstruction with a proximal (1) and distal (2) region. Middle, Somatic AP in control solution and after locally delivering 20 µM of the L-type VGCC inhibitor isradipine (isr). Bottom, Ca^{2+} transients associated with the APs above fitted with the product of four sigmoid functions (black traces) and I_{Ca} signals derived from the fits. B-E, Same protocol as panel A, but delivering 1 µM of P/Q-type VGCC inhibitor ω-agatoxin-IVA (agaIVA, B), 1 µM of the N-type VGCC inhibitor ω-conotoxin-GVIA (conGVIA, C), 1 µM of the R-type VGCC inhibitor SNX482 (D) and 5 µM and 30 µM, respectively, of the T-type VGCC inhibitors ML218 and NNC550396 (ml+nnc, E). F, All reported values are mean ± SD. Top, single values and percentage change of the I_{Ca} peak in proximal regions after addition of isr (N = 7 cells, -29.9 ± 17.0), after addition of agaIVA (N = 8 cells, -23.9 ± 17.4), after addition of conGVIA (N = 7 cells, -20.2±10.1), after addition of SNX482 (N = 8 cells, -7.1 ± 10.0) or after addition of ml+nnc (N = 8 cells, -19.0 ± 14.9). Bottom, in the same cells, single values and percentage change of the I_{Ca} peak in distal regions after addition of isr (-3.8 ± 10.0), agaIVA (-3.3 ± 13.9), conGVIA (-4.8 ± 6.8), SNX482 (-0.2 ± 3.4) or ml+nnc (-2.3 ± 7.0).

during the falling phase of the axonal AP (Lipkin et al. 2021). This is different than what we have observed in dendrites of hippocampal pyramidal neurons (Jaafari and Canepari 2016) as well as L5PNs (chapter 4). During dendritic AP back propagation, the peak of the I_{Ca} is on average 0.5 ms delayed compared to the V_m peak. In the AIS this is not the case, suggesting Ca^{2+} conductance through faster opening channels such as VGNCs. Hanemaaijer et al. (2020) showed that $Na_v1.2$ channels are permeable to Ca^{2+}, which would explain the fast I_{Ca} in the distal AIS. In the distal AIS there is a clear difference between a fast initial I_{Ca} peak and a subsequent lower Ca^{2+} influx which coincides with the proximal I_{Ca} (see example figure 3.3B). This supports an initial fast Ca^{2+} influx through $Na_v1.2$ channels and a subsequent slower I_{Ca} through VGCCs.

3.1.4 VGCCs mediate part of the Ca^{2+} influx in the AIS

Since diverse types of VGCCs are expressed in L5 pyramidal neurons, we assessed the effects of inhibiting individual types of VGCCs. In detail, we blocked L-type VGCCs with 20 µM isradipine, P/Q-type VGCCs with 1 µM ω-agatoxin-IVA, N-type VGCCs with 1 µM ω-conotoxin-GVIA, R-type VGCCs with 1 µM of SNX482, and T-type VGCCs with 5 µM ML218 and 30 µM NNC550396. The results of this accurate analysis, reported in figure 3.4, indicate that all types of VGCCs, at different extent, contribute to the axonal Ca^{2+} influx and current associated with the AP.

To summarise these results in more detail, the I_{Ca} is mostly mediated by VGCCs in the proximal AIS, whereas individual VGCCs blockers have less effect in the distal parts (figure 3.4F). Currents mediated by HVA VGCCs are mostly L, N and P/Q-type but not R-type currents (figure 3.4A-D). Additionally, T-type currents mediate part of the total I_{Ca} (figure 3.4E). These observations are in agreement with previously published work (Lipkin et al. 2021; Yu et al. 2010). Interestingly, I_{Ca} signals in the apical dendrite during AP back propagation (detailed in chapter 4) show clear differences from the currents recorded in the AIS. More notably, when blocking N-type currents in the apical dendrite this results in an increase in the Ca^{2+} transient and I_{Ca}, contrary to the effect reported here. Moreover, blocking N-type currents causes a widening of the bAP waveform similar to the widening effect of G^1G^4hwtx on the V_m in the AIS. We hypothesised therefore that as CAKCs in the AIS seem activated by Ca^{2+} entry through $Na_v1.2$, N-type VGCCs activate the same CAKC in the apical dendrite.

Together, this suggests that the Ca^{2+} influx associated with the AP is mainly mediated by VGNCs in the distal axon, whereas it is mainly mediated by VGCCs in the proximal axon.

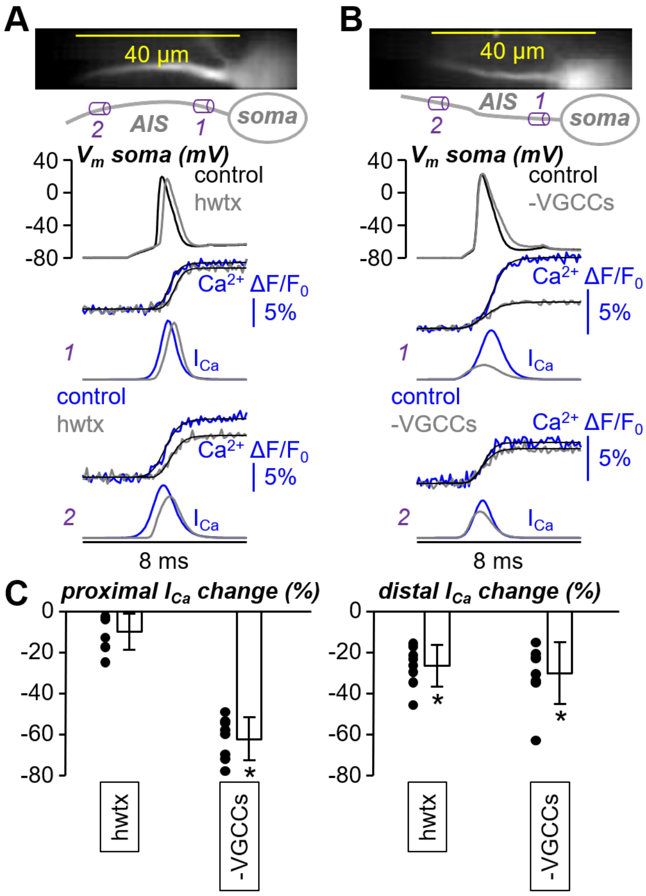

Figure 3.5: Effect of G^1G^4hwtx on the Ca^{2+} influx in the AIS. A, Top, fluorescence image (OG5N) of the AIS and its reconstruction with a proximal (1) and distal region (2). Bottom, somatic AP and associated Ca^{2+} transients and currents in control solution and after local delivery of 80 nM of G^1G^4hwtx (hwtx) in regions 1 and 2. B, In another cell, same protocol as in panel A, but with locally blocking all VGCCs (-VGCCs) with 20 µM isradipine (L-type), 1 µM ω-agatoxin-IVA (P/Q-type), 1 µM ω-conotoxin-GVIA (N-type), 1 µM SNX482 (R-type), 5 µM ML218 + 30 µM NNC550396 (T-type). C, Single values and percentage change (mean ± SD) of the proximal Ca^{2+} current peak (left) after addition of G^1G^4hwtx (N = 8 cells, -9.7 ± 8.9) or after addition of VGCCs blockers (N = 8 cells, -62.2 ± 10.5), and of the distal Ca^{2+} current peak (right) after addition of G^1G^4hwtx (-26.2 ± 10.1) or after addition of VGCCs blockers (-30.0 ± 15.1). "*" indicates a significant change ($p<0.01$, paired t-test).

3.1.5 $Na_v1.2$ mediates Ca^{2+} influx associated with the AP in the AIS

To address the role of Nav1.2 in this hypothesis, we assessed the effect of locally delivering 80 nM G^1G^4hwtx on the Ca^{2+} influx and current associated with the AP in the AIS. In the example of figure 3.5A, G^1G^4hwtx substantially decreased the distal Ca^{2+} influx and current associated with the AP, whereas it only slightly decreased the proximal Ca^{2+} influx. Since all VGCCs contribute to the Ca^{2+} signal, to assess the effect of blocking VGCCs we locally delivered a cocktail with all inhibitors of the tests reported in figure 3.4 at the same concentrations. In the example of figure 3.5B, the block of VGCCs substantially decreased the proximal Ca^{2+} influx and current associated with the AP, whereas the decrease of the distal Ca^{2+} current was only comparable to that produced by local delivery of 80 nM G^1G^4hwtx. We then compared the analysis of the change of the Ca^{2+} current peak in N = 8 cells where the effect of locally delivering G^1G^4hwtx was tested, and in N = 8 cells where the effect of locally delivering the VGCC blockers cocktail was tested (figure 3.5C). Whereas the partial block of $Na_v1.2$ produced a marginal decrease of ∼10% of the Ca^{2+} current in the proximal AIS, compared to the significant decrease of >60% produced by blocking VGCCs ($p<0.01$, paired t-test), in the distal AIS G^1G^4hwtx and VGCCs blockers produced a similar and significant decrease of the Ca^{2+} current ($p<0.01$, paired t-test). The effect of the cocktail of VGCC blockers on the I_{Ca} was as expected from the sum of the individual VGCC subtype blocks detailed in figure 3.4.

Although Ca^{2+} entry through $Na_v1.2$ channels was predicted, one might expect that the $Na_v1.2$ mediated I_{Ca} would be highest in proximal regions where $Na_v1.2$ is the dominant VGKC. This might be explained by the high apparent density of VGCCs in the proximal AIS. Alternatively, Ca^{2+} permeability of $Na_v1.2$ channels might depend on or influenced by auxiliary subunits. In general, the properties of VGNCs in the AIS seem to depend on the molecular environment, as also the hyperpolarising shift in VGNC activation seems to be location-dependent in the AIS and soma of L5PNs (Katz et al. 2018). Therefore, $Na_v1.2$ channels in distal regions might be more permeable to Ca^{2+} compared to the same channels in proximal regions. Moreover, in the dendrite using our methodology, Ca^{2+} entry through $Na_v1.2$ channels is undetectable (detailed in chapter 4), as the cocktail of VGCC blockers abolishes the I_{Ca} completely. Furthermore, in the dendrite, the I_{Ca} is significantly delayed compared to the peak of the bAP, whereas VGNC activation is much faster (chapter 4). It seems that in L5PNs, significant $Na_v1.2$-mediated Ca^{2+} entry is exclusively related to the AIS.

In distal regions, the reduction of ∼26% of the Ca^{2+} current (figure 3.5C) and the block of 30-40% $Na_v1.2$ produced by locally delivering 80 nM G^1G^4hwtx are consistent with a scenario where ∼70% of the Ca^{2+} influx associated with the AP, at distal sites of the AIS, is mediated by $Na_v1.2$. This also fits with the observation that VGCCs mediate ∼30% of the total distal I_{Ca} (figure 3.5C). The significant effect of a 30-40% $Na_v1.2$ block on the I_{Ca} shows that blocking $Na_v1.2$ can reduce the K^+ current mediated by CAKCs widening the AP waveform at distal sites (figure 3.2).

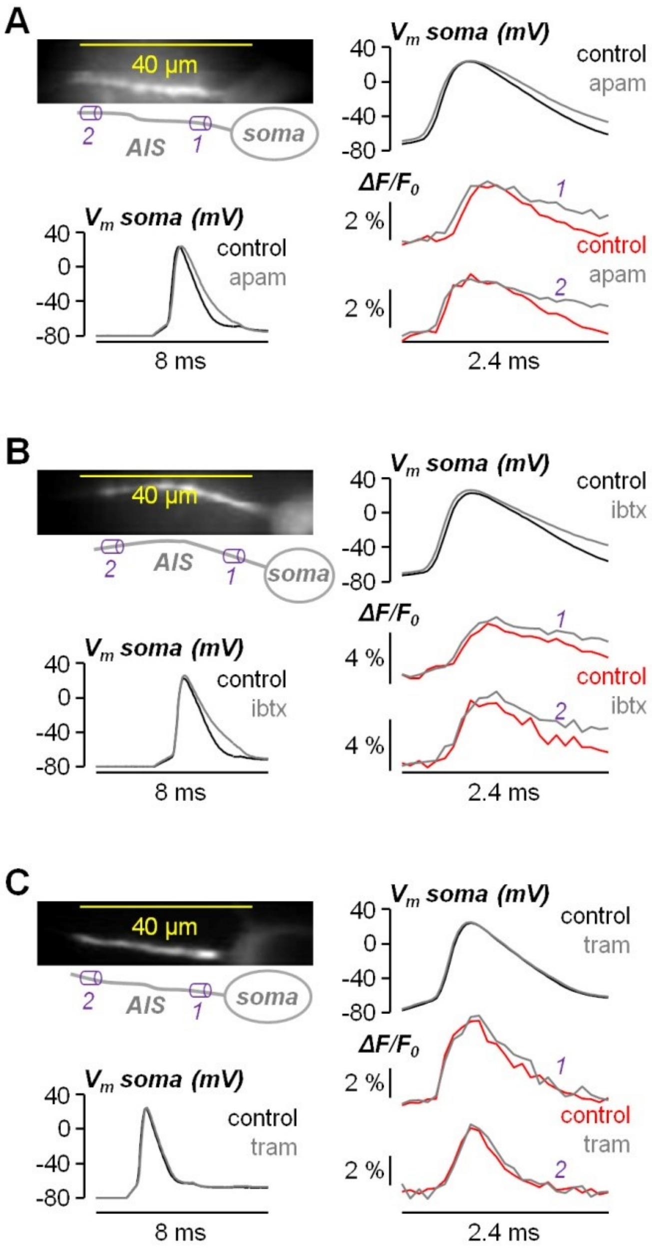

Figure 3.6: Effect of blocking SK CAKCs, BK CAKCs or IK CAKCs on the AP waveform in the AIS. A, Left, fluorescence image (JPW1114) of the AIS and its reconstruction with a proximal region (1) and a distal (2) region indicated; somatic AP before and after locally delivering 1 µM of the SK CAKC inhibitor apamin (apam) reported below. Right, somatic AP in control solution and after apamin delivery and associated V_m transients in 1 and 2. B, In another cell, same protocol of panel A but by locally delivering 1 µM of the BK CAKC inhibitor iberiotoxin (ibtx). C, In another cell, same protocol of panel A but by locally delivering 1 µM of the IK CAKC inhibitor tram-34 (tram).

3.2 The effect of blocking CAKCs in the AIS

3.2.1 The block of CAKCs widens the AP in the AIS after blocking VGCCs

We observed that when we blocked $Na_v1.2$ channels, the AP waveform widened, suggesting the involvement of K^+ channels. Then we showed the distal I_{Ca} anticipates the AP peak, mediated by $Na_v1.2$ channels. Taken together, we suggest the involved K^+ channels are CAKCs, activated by Ca^{2+} influx through $Na_v1.2$ channels. Therefore, we next assessed the regulation of the AP waveform by individual CAKCs. In the example of figure 3.6A, locally delivering 1 µM of the SK CAKC inhibitor apamin widened the AP waveform in the soma and in the proximal and distal sites of the AIS. Visually, this widening was larger towards the late phase of the repolarisation. Similarly, in the example of figure 3.6B, locally delivering 1 µM of the BK CAKC inhibitor ibtx also widened the somatic and axonal AP waveforms, but in this case the widening was observed earlier during the repolarisation. The widening behaviours produced by apamin or ibtx were consistently observed in all cells tested. In contrast, the effects produced by 1 µM of the IK CAKC inhibitor tram-34 were not significant. In the example of figure 3.6C, locally delivering tram-34 did not change the AP waveforms in the soma nor in the AIS.

In agreement with this initial analysis of CAKCs, we conducted a further analysis on SK and BK CAKCs only. To see whether a Ca^{2+} source activates a particular CAKC, one can block only this particular Ca^{2+} source and see whether this block prevents the effects produced by CAKCs. Thus, we first tested the combination of VGCCs as Ca^{2+} source by using the cocktail of blockers already used in the experiments of figure 3.5. In the example of figure 3.7A, we first blocked VGCCs, observing a widening of the AP waveform in the soma and in the proximal and distal sites of the AIS, and then added apamin to the VGCCs blockers cocktail. The block of SK CAKCs did not further change the somatic and axonal AP waveforms once VGCCs were blocked. In contrast, in the example of figure 3.7B, after observing a widening of the somatic and axonal AP waveforms produced by blocking VGCCs, addition of ibtx caused a further widening of the V_m signals.

The quantitative assessment of the effects of apamin and ibtx was done in four separate groups of 7 cells in which the two inhibitors were tested first in control conditions and then after blocking VGCCs. In control conditions, the delivery of SK CAKC, BK CAKC or VGCCs inhibitors, but not the delivery of the IK CAKC inhibitor, produced a significant ($p<0.01$, paired t-test) increase of the $\int V_m$ signal (figure 3.7C) both in the proximal and in the distal sites of the AIS. Visually, this effect was larger at distal sites of the AIS for the BK CAKC inhibitor whereas the widening effects produced by apamin were similar to those produced by blocking VGCCs ($N = 14$ cells). When VGCCs were previously blocked, further addition of apamin did not change the $\int V_m$ signal (figure 3.7D). The occlusion of the widening effect of apamin on the axonal AP shows SK channels were indirectly blocked by the cocktail of VGCC blockers. Therefore, Ca^{2+} for SK activation is supplied exclusively by VGCCs. In contrast, further addition of ibtx after blocking VGCCs increased the $\int V_m$ signal, in a significant manner ($p<0.01$, paired t-test), by ∼12% at the proximal AIS sites and by ∼21% at the distal AIS sites (figure 3.7D). We concluded that whereas SK CAKCs are activated exclusively by VGCCs, BK CAKCs are also activated by other Ca^{2+} sources.

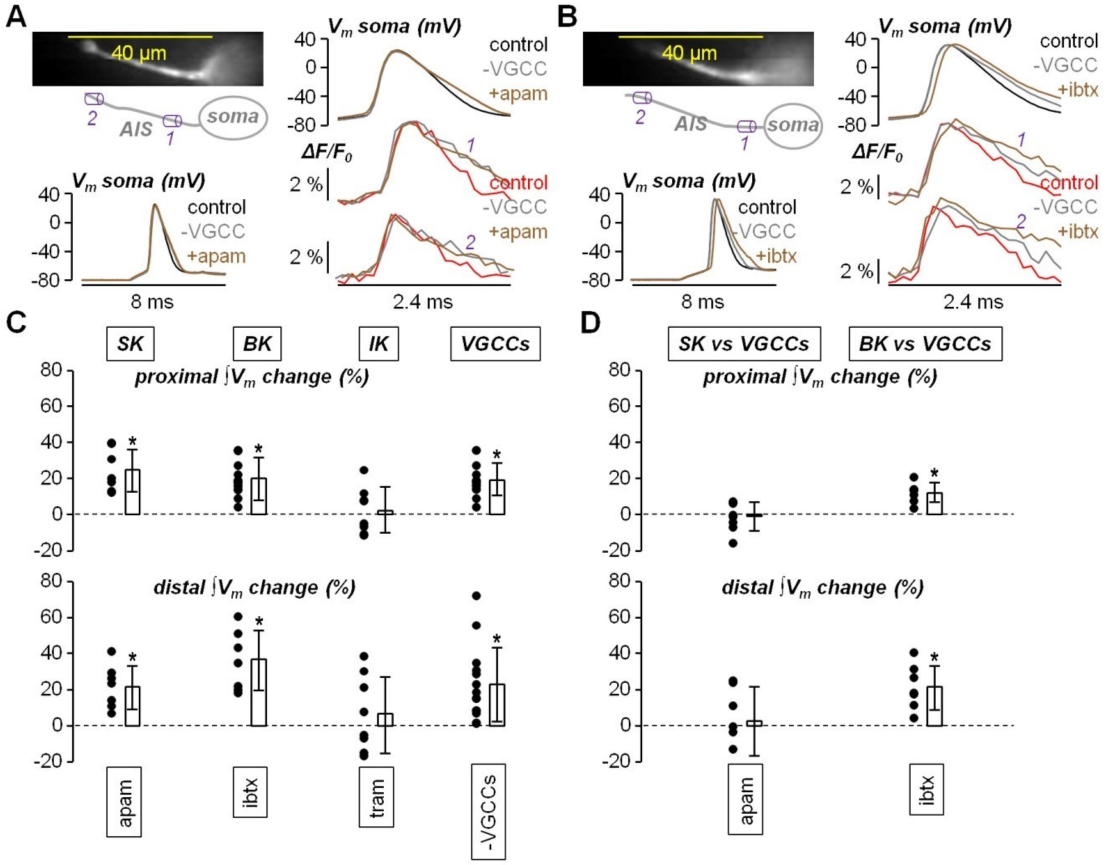

Figure 3.7: Effect of blocking SK CAKCs or BK CAKCs on the AP waveform in the AIS, after blocking VGCCs. A, Left, fluorescence image (JPW1114) of the AIS and its reconstruction with a proximal region (1) and a distal (2) region indicated; somatic AP before and after sequentially blocking first VGCCs only and then VGCCs and SK CAKCs with additional apamin. Right, somatic AP and associated V_m transients in 1 and 2 in control solution and after sequentially blocking first VGCCs only and then VGCCs and SK CAKCs with additional apamin. B, In another cell, same protocol of panel A but by sequentially blocking first VGCCs only and then VGCCs and BK CAKCs with additional iberiotoxin (ibtx). C, Top, single values and percentage change of the proximal $\int V_m$ signal maximum after delivering apamin (N = 7 cells, mean ± SD = 24.7 ± 11.7), ibtx (N = 7 cells, mean ± SD = 20.1 ± 11.9), tram-34 (N = 8 cells, mean ± SD = 2.2 ± 12.7) or the cocktail of VGCCs blockers (N = 14 cells, mean ± SD = 19.0 ± 8.9). Bottom, in the same cells, single values and percentage change of the distal $\int V_m$ signal maximum after delivering apamin (mean ± SD = 21.7 ± 12.0), ibtx (mean ± SD = 36.9 ± 16.6), tram-34 (mean ± SD = 6.7 ± 21.1) or the cocktail of VGCCs blockers (mean ± SD = 22.9 ± 20.5). D, Top, with respect to the block of VGCCs, single values and percentage change of the proximal $\int V_m$ signal maximum after delivering apamin (N = 7 cells, mean ± SD = -2.1 ± 7.9) or ibtx (N = 7 cells, mean ± SD = 12.1 ± 5.4). Bottom, in the same cells, single values and percentage change of the distal $\int V_m$ signal maximum after delivering apamin (mean ± SD = 2.4 ± 19.1) or ibtx (mean ± SD = 21.5 ± 12.2). "*" indicates a significant change ($p<0.01$, paired t-test).

3.2.2 The block of BK CAKCs widens the AP in the AIS preventing the widening caused by blocking $Na_v1.2$

To finally establish whether BK CAKCs are the target of Ca^{2+} entering through $Na_v1.2$, we measured the change in the AP waveform produced by locally delivering 80 nM G^1G^4hwtx, in the presence of 1 µM ibtx. In contrast to the cell of figure 3.2A-B where G^1G^4hwtx was applied in control solution, in the cell of figure 3.8A G^1G^4hwtx local delivery did not change the $\int V_m$ signals. In this final quantitative assessment performed in a group of 7 cells (figure 3.8B), addition of G^1G^4hwtx in the presence of ibtx did not change the $\int V_m$ signal, in contrast to the increase of the $\int V_m$ signal observed without ibtx. This result indicates that the block of BK CAKCs prevents the widening of the AP waveform, in the AIS, produced by the block of $Na_v1.2$. We concluded that the $Na_v1.2$ Ca^{2+} influx targets BK CAKCs, in this way shaping the AP waveform at its generating site.

Taken together with the observation that blocking $Na_v1.2$ channels causes a widening in the AP waveform only in the distal AIS (figure 3.2), this suggests BK density is higher in the distal compared to the proximal AIS. As $Na_v1.2$ is dominantly expressed in proximal regions we can expect a close coupling between the two channels. Nevertheless, it does not mean that BK channels are activated by $Na_v1.2$ mediated Ca^{2+} influx exclusively. HVA VGCCs, although probably in low densities, are another possible source of Ca^{2+}, and have been associated with BK channels in the past (Berkefeld et al. 2006; Gutzmann et al. 2019; Loane et al. 2007). Moreover, BK channels are also voltage gated. Therefore, when delivering G^1G^4hwtx, BK channel activation might be delayed due to the change in V_m associated with the ∼30% decrease of available $Na_v1.2$ channels. That gives a scenario where BK channels are not activated by Ca^{2+} through $Na_v1.2$ channels but by the sudden change in V_m due to collective $Na_v1.2$ channel activation mediating the I_{fast}. Whether this is a likely scenario remains to be investigated, as the peak of the axonal V_m as well as the rising phase do not seem to change significantly, besides being delayed, after applying G^1G^4hwtx. Nevertheless, the above experiments do not dismiss the possibility.

3.3 The effect of blocking $Na_v1.6$ channels in the AIS

The experiments reported in figures 3.1-10 demonstrate that $Na_v1.2$ in the AIS shapes the AP waveform during the rising phase, by providing a large fraction of the

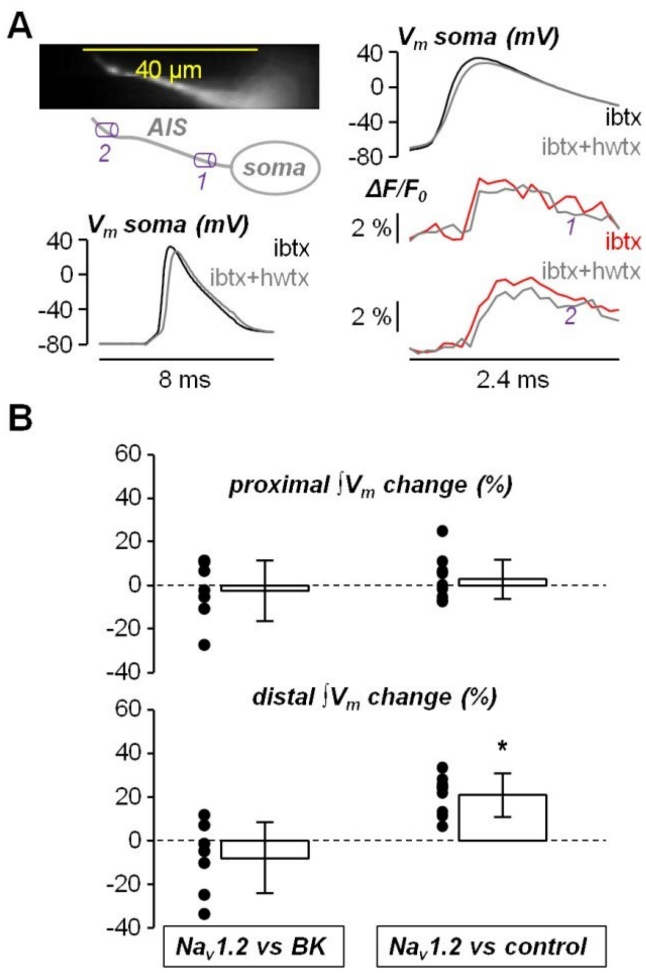

Figure 3.8: Effect of G^1G^4hwtx on the AP waveform in the AIS after blocking BK channels. A, Left, fluorescence image (JPW1114) of the AIS and its reconstruction with a proximal region (1) and a distal region (2) indicated; somatic AP before and after locally delivering 80 nM G^1G^4hwtx (hwtx) in the presence of iberiotoxin (ibtx, 1 µM) reported below. Right, somatic AP and associated V_m transients in 1 and 2 in the presence of ibtx before and after G^1G^4hwtx delivery. B, Single cell values and percentage change (N=7 cells) of the $\int V_m$ signal maximum after locally delivering G^1G^4hwtx in the presence of ibtx in proximal regions (mean ± SD = -2.3 ± 13.8), and in distal regions (mean ± SD = -7.9 ± 16.3). The statistics of the $\int V_m$ signal maximum after locally delivering G^1G^4hwtx in control solution (figure 3.2C) are also reported for comparison on the right. "*" indicates a significant change ($p<0.01$, paired t-test).

inward current, and in the falling phase by regulating the Ca^{2+} activated outward current. The other VGNC ($Na_v1.6$) also contributes to the AP shaping by providing the other Na^+ inward current, but whether it also regulates the Ca^{2+}-activated outward current remained to be established.

3.3.1 $Na_v1.6$ does not mediate Ca^{2+} influx associated with the AP in the AIS

In a final set of experiments, we addressed this question by performing the same tests we did with G^1G^4hwtx (figure 3.1, figure 3.2 and figure 3.5), but in this case using the $Na_v1.6$ inhibitor 4,9-anhydrotetrodotoxin (attx) (see figure 3.3). Surprisingly, in the cell reported in figure 3.9A, local delivery of 800 nM produced an increase of the distal Na^+ transient, associated with a large increase of the slow non-inactivating component of the Na^+ current (figure 3.9B). A large increase of the

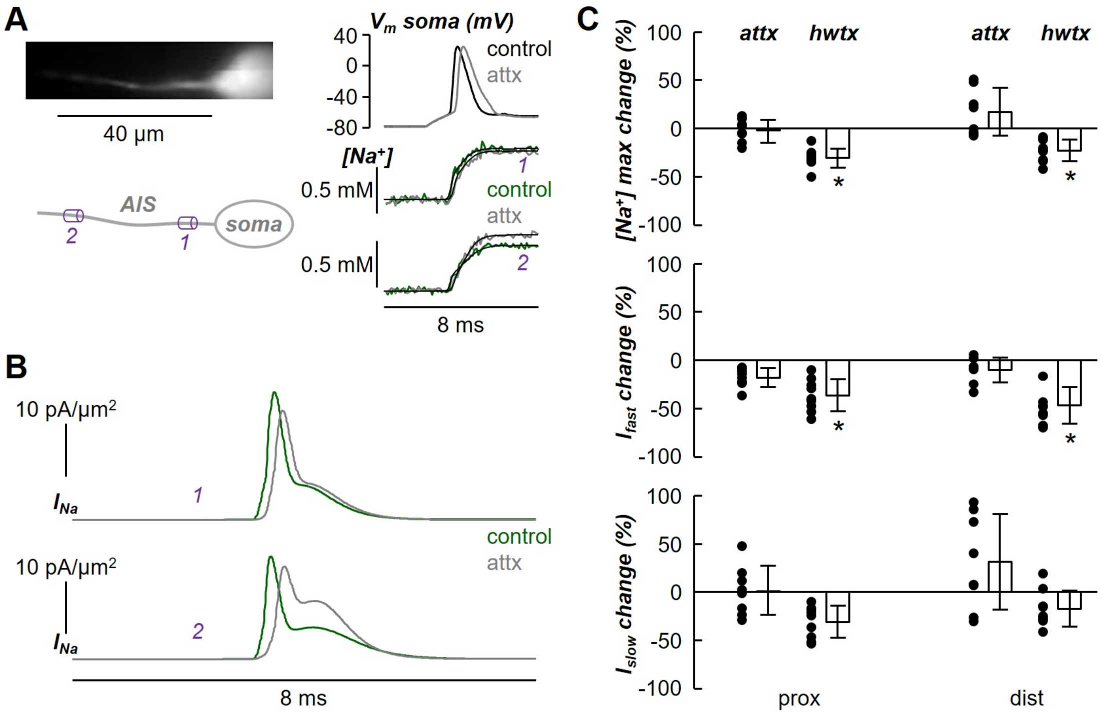

Figure 3.9: Analysis of the effect of 4,9-anhydrotetrodotoxin (attx) on the Na$^+$ influx in the AIS. A, Left, fluorescence image (Na$^+$ indicator ING-2) of the AIS and its reconstruction with a proximal region (1) and a distal (2) region indicated. Right, Somatic AP in control solution and after locally delivering 800 nM of attx (top) and associated corrected Na$^+$ transients fitted with a model function in 1 and 2. B, From the experiment in A, Na$^+$ currents calculated from the time-derivative of the Na$^+$ transient fits. C, Top, percentage change of the Na$^+$ transient maximum after addition of attx (N = 8 cells) in proximal regions (mean ± SD = -1.9 ± 11.6), and in distal regions (mean ± SD = 16.8 ± 24.8); the values and statistics of the equivalent experiments with G^{1}G^{4}hwtx (hwtx) (figure 3.1) are reported for comparison. Middle, percentage change of the fast component of the Na$^+$ current (I_{fast}) after addition of attx in proximal regions (mean ± SD = -17.9 ± 9.9), and in distal regions (mean ± SD = 10.2 ± 13.1); the values and statistics of the equivalent experiments with G^{1}G^{4}hwtx are reported for comparison. Bottom, percentage change of the slow component of the Na$^+$ current (I_{slow}) after addition of attx in proximal regions (mean ± SD = 1.4 ± 25.2), and in distal regions (mean ± SD = 31.5 ± 49.4); the values and statistics of the equivalent experiments with G^{1}G^{4}hwtx (figure 3.1C) are reported for comparison; "*" indicates a significant change (p<0.01, paired t-test).

Na^+ transient and of the I_{slow} at distal sites was observed in 4/8 tested with this protocol (figure 3.9C), suggesting that attx slows down the kinetics of inactivation of VGNCs. Consistently with a variable modulation of the I_{slow}, attx also produced inconsistent effects on the axonal AP waveform. While in the cell reported in figure 3.10A-B the local delivery of attx did not change the AP waveform in the AIS, in the cell reported in figure 3.10C-D attx widened the AP at the distal site of the AIS. In N = 7 cells tested with this protocol, the widening of the distal axonal AP was not statistically significant (figure 3.10E). The complex interaction of attx with VGNCs does not allow the use of this tool to analyse the role of $Na_v1.6$ in detail. Nevertheless, since attx prolongs the Na^+ influx (figure 3.9A), the Ca^{2+} influx should be also prolonged if the channel affected by attx is permeable to Ca^{2+}. In the cell of figure 3.11A, however, the local delivery of attx did not change the axonal Ca^{2+} current and no significant change of the proximal or distal axonal Ca^{2+} current was measured in N = 7 cells tested with this protocol (figure 3.11B). Since $Na_v1.2$ is permeable to Ca^{2+} (figure 3.5), this result indicates that attx affects the kinetics of inactivation of $Na_v1.6$ in murine brain slices and that this VGNC isoform is not contributing to the early Ca^{2+} influx. We concluded that only $Na_v1.2$ mediates Ca^{2+} influx during the generating AP in the AIS and that only this isoform is functionally coupled to BK CAKCs.

Although we can be confident $Na_v1.6$ channels do not mediate Ca^{2+} influx, we were not able to fully investigate the role of $Na_v1.6$ channels during AP generation. In figure 3.9 we show attx does not change the maximum Na^+ concentration nor I_{Na} in the AIS, but we know from previous studies that $Na_v1.6$ channels do mediate a significant portion of the I_{Na}, specifically the persistent current (Kole and Stuart 2012; Rush et al. 2005). To study their contribution in slices, the development of novel toxin analogues that show selectivity for $Na_v1.6$ over $Na_v1.2$ would be constructive. On the other hand, realistic computational models could help us extract the kinetics of $Na_v1.6$ and its role in shaping the AP.

3.4 The $Na_v1.2$-BK channels interaction is mimicked by simulations in a NEURON model

To mimic the experimental AP generation in the AIS, we built a NEURON model on the basis of our dataset. Starting from the model reported in Hallermann et al. (2012) already utilised in our previous article (Filipis and Canepari 2021), we adapted the AIS morphology to the mouse L5 pyramidal neuron and replaced the $Na_v1.2$ and $Na_v1.6$ channel models with those proposed in Mainen et al. (1995),

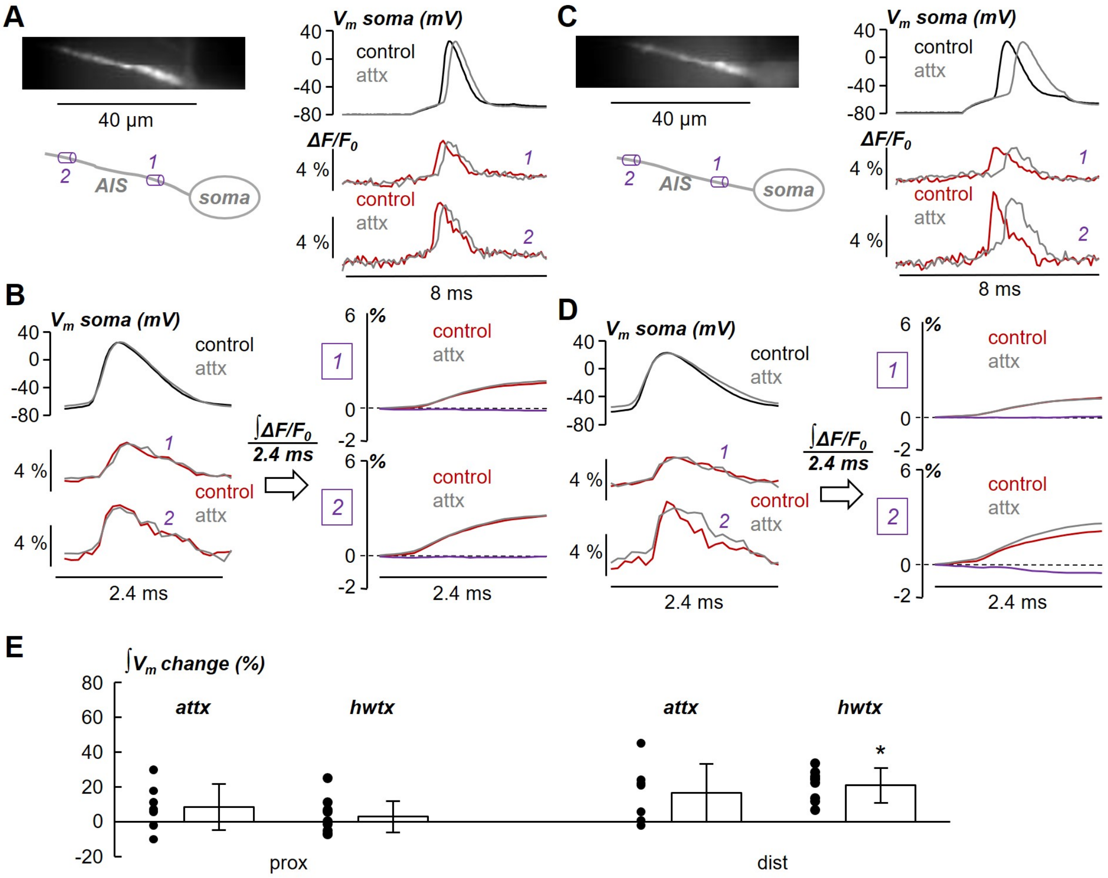

Figure 3.10: Analysis of the effect of attx on the AP waveform in the AIS. A, Left, fluorescence image (JPW1114) of the AIS and its reconstruction with a proximal region (1) and a distal (2) region indicated. Right, Somatic AP in control solution and after locally delivering 800 nM attx (top) and associated V_m transients in 1 and 2. B, Left, somatic and axonal APs at a different time scale (2.4 ms duration). Right, quantification of the AP waveform shape by calculation of V_m integral ($\int V_m$) over the 2.4 ms time window comprising the AP signal. In this cell, the local delivery of attx does not change the waveform of the axonal AP. C and D, same as A and B in another cell where the local delivery of attx widens the waveform of the axonal AP at the distal site. E, Percentage change of the $\int V_m$ signal maximum after delivery of attx (N=7 cells) in proximal regions (mean ± SD = 8.6 ± 13.1), and in distal regions (mean ± SD = 16.7±16.5); the values and statistics of the equivalent experiments with G^1G^4hwtx (hwtx) (figure 3.2C) are reported for comparison; "*" indicates a significant change ($p<0.01$, paired t-test).

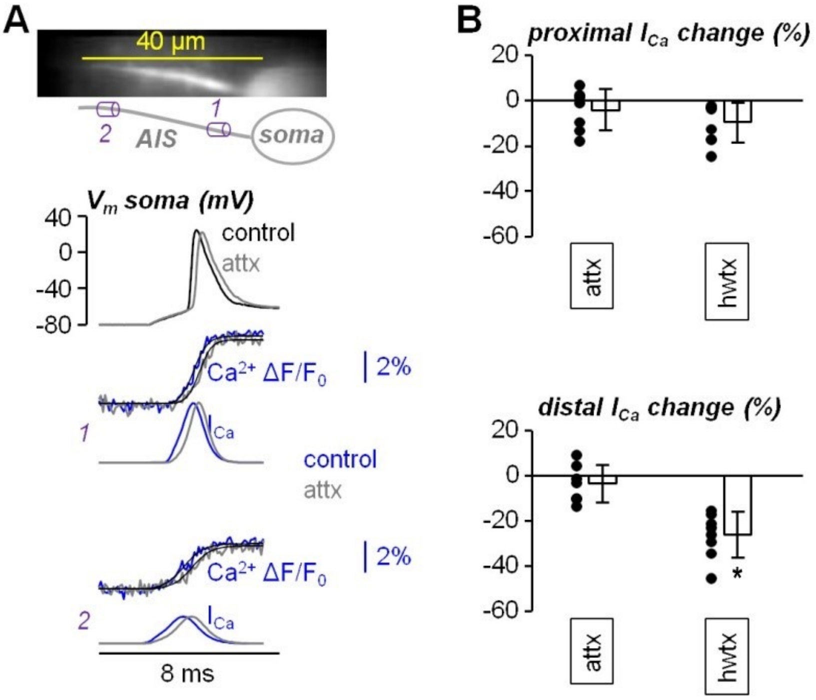

Figure 3.11: Analysis of the effect of attx on the Ca^{2+} influx in the AIS. A, Top, Ca^{2+} fluorescence image (OG5N) of the AIS and its reconstruction with a proximal region (1) and a distal (2) region indicated. Bottom, somatic AP and associated Ca^{2+} transients and currents in 1 and 2 in control solution and after locally delivering 800 nM attx. B, Top, single values and percentage change of the proximal Ca^{2+} current peak after addition of attx (N = 7 cells, mean ± SD = -4.5 ± 9.2). Right, in the same cells, single values and percentage change of the distal Ca^{2+} current peak after addition of attx (mean ± SD = -3.6 ± 8.3); the values and statistics of the equivalent experiments with G^1G^4hwtx (hwtx) (figure 3.3A) are reported for comparison; "*" indicates a significant change ($p<0.01$, paired t-test).

distributed consistently with the results reported by Hu et al. (2009) (see figure 3.12A). From this starting model, we modified the channel functions, as described in chapter 2, in order to match the experimental Na^+ and V_m signals in the AIS. We then introduced Ca^{2+} permeability to $Na_v1.2$ corresponding to 0.4% with respect to the permeability for Na^+ (as suggested by Hanemaaijer et al. (2020)) and we introduced a LVA and a HVA VGCC. We introduced an endogenous Ca^{2+} buffer and, when matching Ca^{2+} imaging experiments only, a Ca^{2+} buffer corresponding to 2 mM OG5N. Finally, we introduced SK and BK CAKCs and we explicitly introduced a coupling between SK channels and LVA VGCCs and between BK channels and $Na_v1.2$ as well as HVA VGCCs, as described in chapter 2.

The relative spatial distributions of VGNCs, VGCCs, BK and SK channels, reported in figure 3.12A, were set in order to reproduce the experimental results. Figure 3.12B shows the proximal and distal V_m waveforms, the Na^+ transients and the Ca^{2+} transients obtained by running computer simulations with the NEURON model. To validate the ability of the model to match the experimental evidence, we simulated the block of 80% VGCCs, of 80% SK channels (experiments with apamin) or of 80% BK channels (experiments with ibtx). As shown in figure 3.12C, computer simulations qualitatively replicate the experimental changes of the AP shape reported in figure 3.6, indicating that the model realistically reproduces the activation of CAKCs during the AP generation; the widening effect on the AP of both CAKCs blockers. Simulating the block of SK channels produces an effect on the AHP, which is decreased, as was observed in the experimental data (figure 3.6A). Blocking BK channels had an earlier effect (figure 3.6B) which is also observed in the model. Reflecting BK distribution in the model, the effect is most pronounced in the distal AIS. Besides CAKCs, mimicking a block of VGCCs produced a widening effect in the model, as was observed experimentally (figure 3.7).

Then, we mimicked the effect of G^1G^4hwtx to produce a partial block of $Na_v1.2$, that replicates the experimental shift of the AP with minimal change of the peak and the reduction of the global Na^+ transient of ∼30% (see figure 3.1). As shown in figure 3.12D, the simulation reproduces the experimental reduction of the Na^+ and Ca^{2+} transients and, more importantly, the widening of the distal AP (figure 3.2). This widening was most pronounced in the distal region as observed experimentally.

The model has provided a scenario to explain our experimental results. In the distal AIS relative $Na_v1.2$ expression is low, but $Na_v1.6$ density is high, which is reflected in their contribution to the I_{Na}. The widening effect of blocking $Na_v1.2$ channels distally despite the small effect on the I_{Na} is explained by the high density of BK channels, which are functionally coupled. This also shows how BK channels, activated by Ca^{2+} influx through $Na_v1.2$, drive fast repolarisation in the AIS. In the proximal AIS, $Na_v1.2$ density is higher but BK density is much lower, which explains why there is no widening effect on the AP waveform when applying hwtx. However, it does not explain the small effect on the I_{Ca}. From the model we can deduce this is likely due to VGCCs. Proximally, the relative high density of VGCCs results in a significant contribution to the total I_{Ca}, leaving $Na_v1.2$ channels to contribute a smaller fraction.

3.5 Summary and significance

In this chapter we demonstrate that the exclusive permeability of $Na_v1.2$ to Ca^{2+} allows activation of BK CAKCs in the AIS. In this way, the interplay between $Na_v1.2$, mediating the AP rise, and BK channels regulating the peak and the early

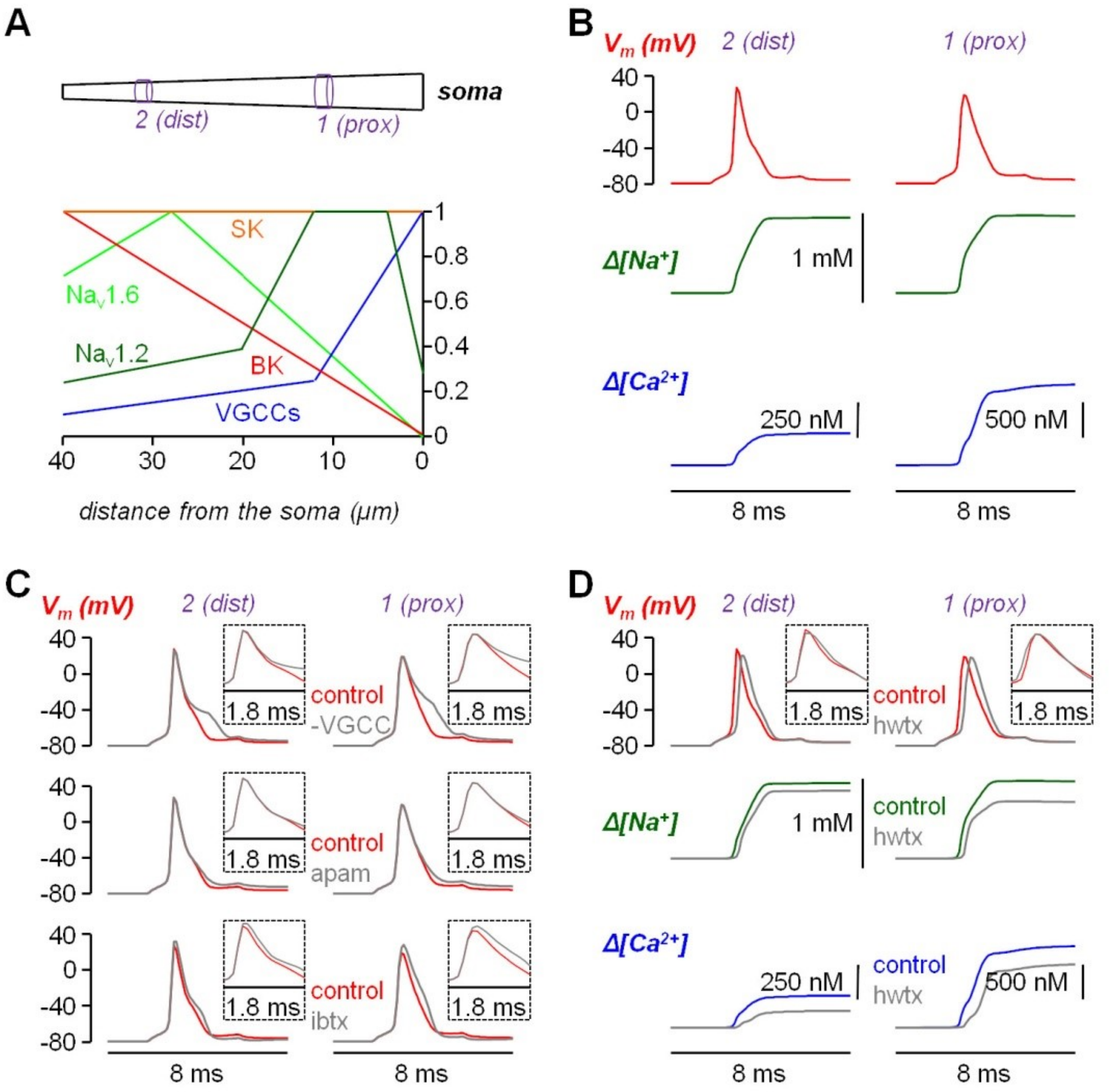

Figure 3.12: NEURON simulations of the AP generation in the AIS. A, Top, structure of the AIS (40 μm long) with proximal (1) compartment and distal (2) compartment at 10-12 μm and 30-32 μm from the soma, respectively. Bottom, normalised distributions of Na$_v$1.2 VGNCs (dark green), Na$_v$1.6 VGNCs (light green), VGCCs (blue), SK CAKCs (orange) and BK CAKCs (red) along the AIS. B, V$_m$ (AP waveform), free Na$^+$ and free Ca^{2+} from a computer simulation of the NEURON model in the proximal and distal regions. The presence of OG5N was taken into account for the free Ca^{2+} estimate. C, V$_m$ (AP waveform) from computer simulations of the NEURON model in the proximal and distal regions in control conditions and after mimicking the delivery of VGCCs blockers (80% VGCCs reduction, top trace), of apamin (80% SK CAKCs reduction, middle trace) or of iberiotoxin (ibtx, 80% BK CAKCs reduction, bottom trace). The changes of the AP waveform are reported in the insets. The simulations qualitatively reproduce the experimental results reported in figure 3.6. D, V$_m$ (AP waveform), free Na$^+$ and free Ca^{2+} from computer simulations of the NEURON model in the proximal and distal regions in control conditions and after mimicking the delivery of G^{1}G^{4}hwtx (hwtx). The presence of OG5N was taken into account for the free Ca^{2+} estimate. The changes of the AP waveform are reported in the insets. The simulations qualitatively reproduce the experimental results reported in figure 3.1, figure 3.2 and figure 3.5.

phase of the AP repolarisation, shapes the AP waveform at the site of generation. The NEURON model that we built predicts the interplay between $\mathrm{Na}_v1.2$ and BK CAKCs associated with the generation of the AP in the AIS and replicates, in a computer simulation, the experimental widening of the axonal AP produced by $\mathrm{G}^1\mathrm{G}^4$hwtx delivery. A preprint version of these results is available on bioRxiv DOI 10.1101/2022.04.12.488116.

This provides a model that can be used to further evaluate the role of $\mathrm{Na}_v1.2$ during AP generation. Specifically we would like to utilise this model to study neurological disorders caused by $\mathrm{Na}_v1.2$ channel mutations, like epilepsy and autism spectrum disorders (ASD). Using the model, we can predict the effects of the malfunctioning $\mathrm{Na}_v1.2$ on the V_m and the kinetics of the other channels, and match this to experimental data. In addition, we can find suitable candidates for interventions to rescue detrimental effects of mutant $\mathrm{Na}_v1.2$. For further discussions see chapter 5.

This chapter shows how the synergy of the voltage gated ion channels in the AIS shape the generating AP. After its generation, the AP travels down the axon, but also back propagates into the apical dendrite. And although the same channels are expressed in the dendrite, their synergy differs, which I will discuss in the next chapter.

4

Study of the ion channels involved in action potenial back propagation in the apical dendrite

Contents

4.1 The effect of blocking VGCCs and CAKCs on the Ca^{2+} currents during a bAP 83

4.1.1 The dendritic Ca^{2+} influx associated with the bAP is exclusively mediated by diverse VGCCs 83

4.1.2 Blocking N-type VGCCs increases Ca^{2+} influx in the apical dendrite during a bAP 86

4.1.3 BK CAKCs are activated by Ca^{2+} influx through N-type VGCCs during the bAP 87

4.2 The effect of blocking VGCCs and CAKCs on the shape of the bAP 89

4.2.1 The peak of the inward I_{Ca} is delayed compared to the peak of the bAP 90

4.2.2 The effect of N-type VGCC and BK CAKC coupling occurs in the first 500 µs after the AP peak 90

4.2.3 The effect of blocking L-type VGCCs on the bAP waveform mimics the effect of SK CAKC block 94

4.2.4 The block of T-type VGCCs decreases the bAP peak . . 96

4.3 Simulations with a NEURON model reproduce the experimental results 97

4.3.1 The NEURON model reproduces the AP waveforms and changes in Ca^{2+} transients 98

4.3.2 N-type VGCC and BK CAKC interaction is mimicked by simulations in the NEURON model 101

4.4 Summary and significance 104

Similarly to the study of the ion channels underlying the generation of the AP in the AIS, this chapter reports on our study of the VG ion channels activated by bAPs in the apical dendrite. Apical dendrites of L5 pyramidal neurons express all VGCCs and a bAP is associated with a fast increase in the dendritic Ca^{2+} concentration. Besides VGCCs, the apical dendrite also expresses $Na_v1.2$ channels, as well as CAKCs and VGKCs. Specifically, this chapter focuses on the interplay of VGCCs and CAKCs during a bAP triggered by a current injection at the soma.

We investigated the contribution of the different types of VGCCs to the total calcium transient and we strive to establish the role of CAKCs during the rise in intracellular Ca^{2+}. Initially, we recorded the effect of various VGCC blockers on the calcium current along the apical dendrite ∼100 µm from the soma. We found that blocking N-type VGCCs caused an unexpected increase in intracellular calcium. Next, we looked closer at the possible functional coupling of VGCCs and CAKCs. To this end, we performed a set of voltage imaging experiments, using the voltage indicator JPW1114. We present evidence suggesting N-type VGCCs and BK CAKCs are functionally coupled in the proximal apical dendrite of pyramidal neurons. By collaborating with the team of Dr. Michele Migliore in Palermo, Italy, we developed a computational model of a complete layer 5 pyramidal cell using the NEURON software which we used to confirm our experimental results.

4.1 The effect of blocking VGCCs and CAKCs on the Ca^{2+} currents during a bAP

4.1.1 The dendritic Ca^{2+} influx associated with the bAP is exclusively mediated by diverse VGCCs

To investigate the contribution of the diverse VGCCs, we locally delivered one or several channel blockers using a pipette positioned near the recording region, as previously done (Ait Ouares et al. 2019) and as described in chapter 2. Specifically we blocked L-type VGCCs with 20 µM isradipine, P/Q-type VGCCs with 1 µM ω-agatoxin-IVA, N-type VGCCs with 1 µM ω-conotoxin-GVIA, R-type VGCCs with 1 µM of SNX482, and T-type VGCCs with 5 µM ML218 and 30 µM NNC550396. Figure 4.1A shows a Ca^{2+} transient associated with a bAP that was fully inhibited by the cocktail of all VGCC blockers, a result consistently observed in 6 cells tested. This is contrary to what we observed in the AIS (detailed in chapter 3), where $Na_v1.2$

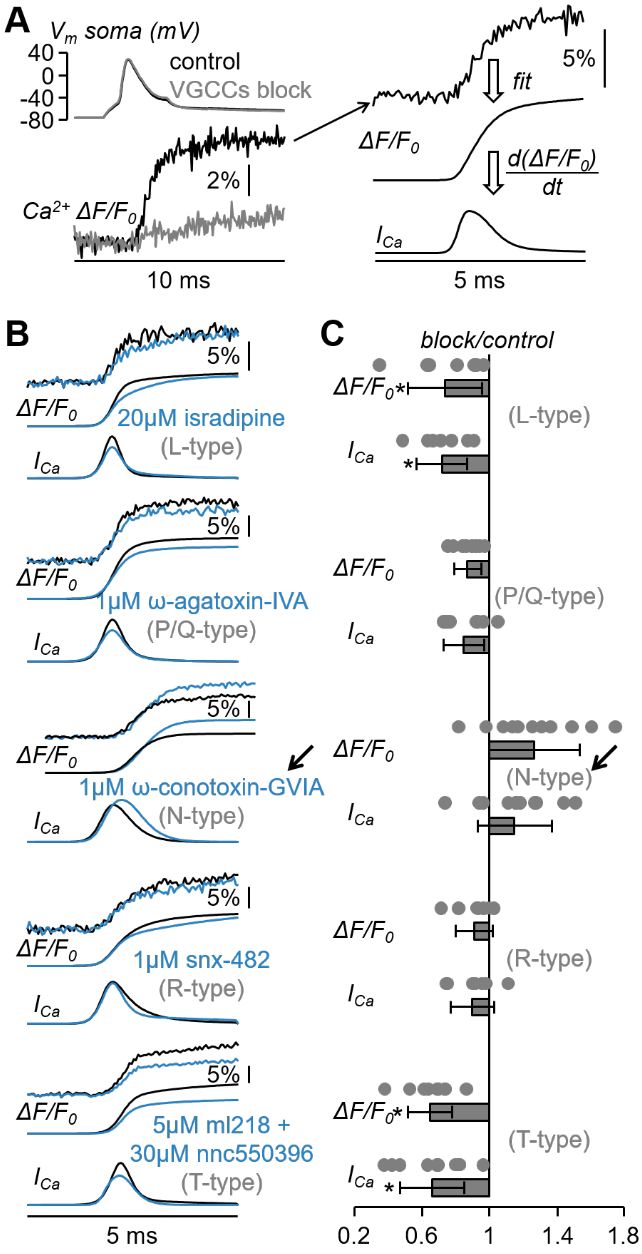

Figure 4.1: Analysis of the diverse VGCCs mediating the Ca^{2+} transient associated with the bAP. A, On the left V_m somatic recording (top) and Ca^{2+} transient (bottom) in control solution and after blocking all VGCCs. On the right, procedure of analysis of the raw Ca^{2+} transient (top trace) with a 4-sigmoid fit (middle trace) and the calculation of the time-derivative (I_{Ca}, bottom trace). B, Five representative examples of Ca^{2+} transients with 4-sigmoid fit ($\Delta F/F_0$, top traces) and time derivatives (I_{Ca}, bottom traces) in control solution and after local delivery of either 20 μM of the L-type VGCC inhibitor isradipine, 1 μM of the P/Q-type VGCC inhibitor ω-agatoxin-IVA, 1 μM of the N-type VGCC inhibitor ω-conotoxin-GVIA, 1 μM of the R-type VGCC inhibitor SNX482 or 5 μM and 30 μM, respectively, of the T-type VGCC inhibitors ML218 and NNC550396. The arrow indicates the unexpected boosting of the Ca^{2+} transient produced by ω-conotoxin-GVIA. C, Single values and fractional change with respect to control of the maxima of the $\Delta F/F_0$ and I_{Ca} signals for the blockade of L-type VGCCs (N = 7, $\Delta F/F_0$: 0.74 ± 0.22, I_{Ca}: 0.72±0.15); for the blockade of P/Q-type VGCCs (N = 8, $\Delta F/F_0$: 0.87 ± 0.08, I_{Ca}: 0.85 ± 0.12); for the blockade of N-type VGCCs (N = 11, $\Delta F/F_0$: 1.27 ± 0.27, I_{Ca}: 1.15 ± 0.22); for the blockade of R-type VGCCs (N = 7, $\Delta F/F_0$: 0.91 ± 0.11, I_{Ca}: 0.90 ± 0.13); for the blockade of T-type VGCCs (N = 7, $\Delta F/F_0$: 0.65 ± 0.13, I_{Ca}: 0.66 ± 0.19). "*" indicates that $p < 0.01$ in paired t-test performed on the signal maxima in control solution and after delivery of the channel blocker; all values are mean ± SD.

channels mediate part of the Ca^{2+} transient and blocking VGCCs did not fully eliminate this current. However, Ca^{2+} influx mediated by VGCCs is overwhelming in the apical dendrite, whereas any contribution from $Na_v1.2$ is negligible.

Figure 4.1A also shows the analysis of the Ca^{2+} transient consisting in fitting the signal with a 4-sigmoid function and to calculate the time-derivative of the fit to extrapolate the kinetics of the I_{Ca}. We applied this analysis on the Ca^{2+} transient recorded first in control solution and then after locally blocking each individual VGCC. The five representative examples reported figure 4.1B show that the blockade of L-type, P/Q-type, R-type and T-type VGCCs decreased, at different extent, the size of both $\Delta F/F_0$ and I_{Ca} signals, but surprisingly the blockade of N-type VGCCs increased the size of both $\Delta F/F_0$ and I_{Ca} signals.

The test was repeated in 7-10 different cells for each channel blocker and the effect of the inhibitor was quantified by measuring the maximum of the $\Delta F/F_0$ and I_{Ca} signals (figure 4.1C). Except for the blockade of N-type VGCCs, the individual blockade of each VGCC type produced on average a decrease of both $\Delta F/F_0$ and I_{Ca} signals, an effect that was more important for L-type and T-type VGCCs. Specifically, blocking L-type VGCCs decreased the Ca^{2+} current by 28 ± 15% ($p = 0.0037$, t-test). P/Q-type and R-type VGCCs blocks caused a 15 ± 12% ($p = 0.0286$, t-test) and 10 ± 13% ($p = 0.0842$, t-test) decrease of the I_{Ca}, respectively. These values are in accordance with a previous study in rat dissociated neocortical PNs, showing L-type, P/Q-type and R-type VGCCs decrease the isolated Ca^{2+} current by ∼22%, ∼19% and ∼13%, respectively (Stewart and Foehring 2000). As mentioned in the introduction, these results do not give the true contribution of each channel to the total I_{Ca}, because blocking one channel subtype causes a change in the membrane potential, which in turn influences the activation patterns of the other channels. Therefore we can only report the effect of the block on the total I_{Ca}. This might explain why Stewart and Foehring (2000) reported a lack of T-type VGCCs whereas here we show a major involvement of T-type channels, decreasing the I_{Ca} significantly by 34 ± 19% when selectively blocked ($p = 0.0013$, t-test).

Stewart and Foehring (2000) also show that blocking N-type VGCCs decreases the Ca^{2+} current with ∼26%. However, here the blockade of N-type channels increased both $\Delta F/F_0$ and I_{Ca} signals in 8/11 cells tested, with an average increase of 27 ± 27% and 15 ± 22%, respectively.

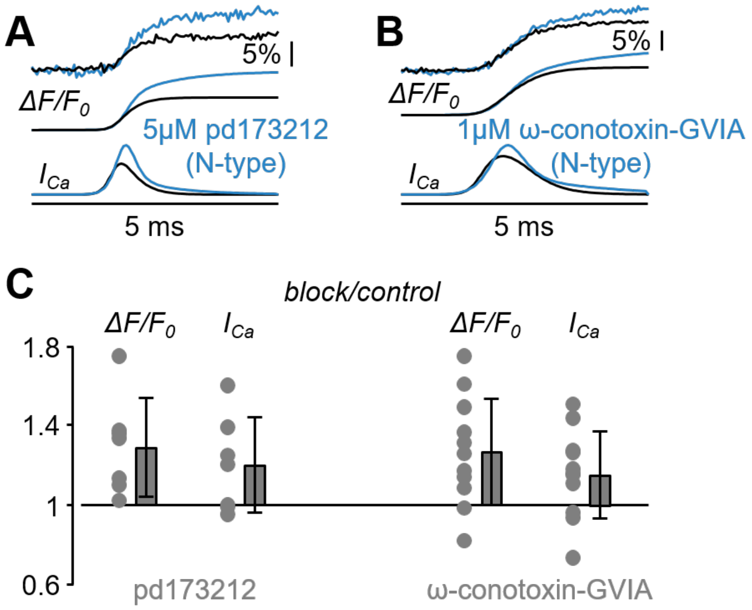

Figure 4.2: Analysis of the blockade of N-type VGCCs using pd173212. A, Representative example of Ca^{2+} transient with 4-sigmoid fit ($\Delta F/F_0$, top traces) and time derivative (I_{Ca}, bottom traces) in control solution and after local delivery of either 5 µM of the N-type VGCC inhibitor pd173212. B, Another representative example of Ca^{2+} transient with 4-sigmoid fit ($\Delta F/F_0$, top traces) and time derivative (I_{Ca}, bottom traces) in control solution and after local delivery of either 1 µM of the N-type VGCC inhibitor ω-conotoxin-GVIA. C, On the left, single values and fractional change with respect to control of the maxima of the $\Delta F/F_0$ and I_{Ca} signals for the blockade of N-type VGCCs with pd173212 ($N = 7$, $\Delta F/F_0$: 1.29 ± 0.25, I_{Ca}: 1.20 ± 0.24 (mean ± SD)). The single values and fractional change with respect to control of the maxima for the blockade of N-type VGCCs with ω-conotoxin-GVIA are reported on the right for comparison.

4.1.2 Blocking N-type VGCCs increases Ca^{2+} influx in the apical dendrite during a bAP

The unexpected result of locally delivering 1 µM ω-conotoxin-GVIA could be explained by the coupling of the N-type VGCC with a mechanism that boosts the Ca^{2+} influx associated with the bAP, or with the toxin binding to a different target. To discriminate between these two hypothesis, we repeated the analysis of the Ca^{2+} transient of figure 4.1 by blocking the N-type VGCC with another selective inhibitor, namely pd173212 (Hu et al. 1999). As shown in the two representative examples of figure 4.2A and B, local delivery of either 5 µM pd173212 or 1 µM ω-conotoxin-GVIA increased the size of both $\Delta F/F_0$ and I_{Ca} signals in a qualitatively similar manner. Altogether, the $\Delta F/F_0$ signal increased in all 7 cells tested after delivery of pd173212, and the I_{Ca} signal increased in 4/7 cells tested after delivery of pd173212. This shows the results obtained using ω-conotoxin-GVIA can be trusted, and the

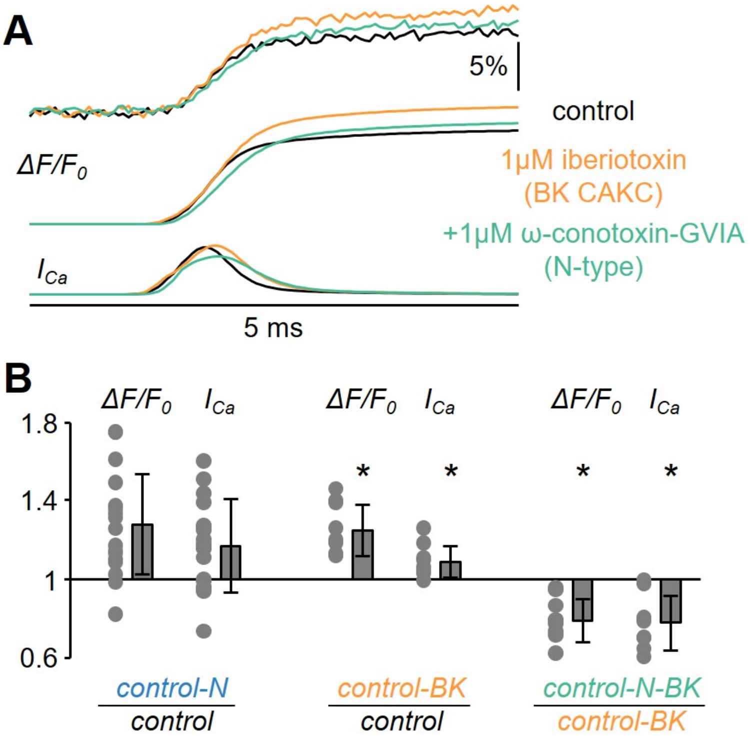

Figure 4.3: Analysis of the blockade of N-type VGCCs after blocking BK CAKCs. A, Representative example of Ca^{2+} transient with 4-sigmoid fit ($\Delta F/F_0$, top traces) and time derivative (I_{Ca}, bottom traces) in control solution, after local delivery of 1 µM of the BK CAKCs inhibitor iberiotoxin and after further delivery of either 1 µM of the N-type VGCC inhibitor ω-conotoxin-GVIA. C, On the left, single values and fractional change with respect to control solution of the maxima of the $\Delta F/F_0$ and I_{Ca} signals for the blockade of N-type VGCCs (either with ω-conotoxin-GVIA, N = 18, $\Delta F/F_0$: 1.27 ± 0.26, I_{Ca}: 1.17 ± 0.22). On the center, single values and fractional change with respect to control solution of the maxima of the $\Delta F/F_0$ and I_{Ca} signals for the blockade of BK CAKCs (N = 9, $\Delta F/F_0$: 1.25 ± 0.13, I_{Ca}: 1.09 ± 0.08). On the right, single values and fractional change with respect to the blockade of BK CAKCs only of the maxima of the $\Delta F/F_0$ and I_{Ca} signals for the combined blockade of N-type VGCCs and BK CAKCs (with ω-conotoxin-GVIA, N = 9, $\Delta F/F_0$: 0.79 ± 0.11, I_{Ca}: 0.78 ± 0.14). "*" indicates that $p < 0.01$ in paired t-test performed on the signal maxima.

increase in Ca^{2+} transients is not due to the toxin being unspecific. We concluded that the blockade N-type VGCCs boosts the Ca^{2+} influx associated with the bAP.

4.1.3 BK CAKCs are activated by Ca^{2+} influx through N-type VGCCs during the bAP

The boosting of the Ca^{2+} influx observed in figure 4.1 can be due to an enhancement of the depolarisation produced by the loss of Ca^{2+} influx via N-type VGCCs. It was shown in freshly dissociated mouse neocortical pyramidal neurons that BK

CAKCs are partly activated by N-type VGCCs (Sun et al. 2003). Specifically, Sun et al. (2003) identified an iberiotoxin sensitive current that was decreased by blocking either N-type or L-type VGCCs. Thus, we repeated the analysis of the Ca^{2+} transient of figure 4.1 and figure 4.2 by blocking in sequence first BK CAKCs with local delivery of 1 µM iberiotoxin and then BK CAKCs and N-type VGCCs together with local delivery of 1 µM iberiotoxin and 1 µM ω-conotoxin-GVIA. In the representative example of figure 4.3A, the blockade of BK CAKCs increased both $\Delta F/F_0$ and I_{Ca} signals, but the further blockade of N-type VGCCs decreased both $\Delta F/F_0$ and I_{Ca} signals. This result was consistently obtained in $N = 9$ cells tested. As shown in figure 4.3B, the blockade of BK CAKCs boosted the Ca^{2+} transient similarly to the blockade of N-type VGCCs. In contrast, the blockade of N-type VGCCs in the presence of iberiotoxin reduced the Ca^{2+} transient. To statistically assess the consistency of this result we performed a Wilcoxon rank non-parametric test on the groups of cells where a blocker was applied under different conditions, using $p<0.01$ as discriminator to establish whether two groups were different. As show in table 4.1, the effects on both $\Delta F/F_0$ and I_{Ca} signals were similar when comparing the groups of cells where ω-conotoxin-GVIA, pd173212 or iberiotoxin were applied in control solutions, or when the effects of iberiotoxin were compared with the ensemble of cells where N-type VGCCs were blocked in control solution. In contrast, the effects on both $\Delta F/F_0$ and I_{Ca} signals were different when comparing the cells where ω-conotoxin-GVIA was applied in the presence of iberiotoxin with the groups of cells where ω-conotoxin-GVIA or pd173212 where applied in control solution, or when the comparison was done with the ensemble of cells where N-type VGCCs were blocked in control solution.

This points to a scenario where N-type channels provide the Ca^{2+} for BK CAKCs activation. Blocking N-type VGCCs indirectly decreases the opening-probability of BK channels, which would delay afterhyperpolarisation and widen the shape of the bAP. Logically, this would increase Ca^{2+} entry through other VGCCs, resulting in the increased Ca^{2+} current. Since the blockade of BK CAKCs prevents the boosting of the Ca^{2+} influx when blocking N-type VGCCs, we concluded that this effect was due to the functional coupling of the two channels.

The coupling between N-type VGCCs and BK CAKCs has been shown before by Sun et al. (2003). In their experiments they showed that blocking either N-type or L-type currents reduced the ibtx-sensitive outward current in dissociated L5PNs. Although an association between BK channels and L-type VGCCs is not excluded here, we do suggest a stronger coupling with N-type VGCCs due to the increase of the I_{Ca} after blocking N-type channels, indicating a substantial involvement of

BK channels. Interestingly, besides a Ca^{2+}-dependent activation mechanism, BK channels are also voltage gated and are thought to activate fast upon depolarisation to mediate a fast repolarisation current. We observed this fast activation during AP generation in the AIS. There, BK channels were functionally coupled to Nav1.2 channels, which is not the case in the apical dendrite. In comparison, VGCCs activate much slower, raising the question whether the activation of BK channels is also slower down. Thus, to investigate the timing of the functional coupling between BK and N-type channels, we examined the effect of blocking these channels on the waveform of the bAP.

		p $\Delta F/F_0$	**p I_{Ca}**
cntx/control	pd173212/control	0.8601	0.7914
cntx/control	ibtx/control	0.9998	0.2875
cntx/control	cntx/ibtx	$\mathbf{4.74 \cdot 10^{-4}}$	**0.0024**
pd173212/control	ibtx/control	0.8371	0.7577
pd173212/control	cntx/ibtx	$\mathbf{1.75 \cdot 10^{-4}}$	**0.0012**
(cntx&pd173212)/control	ibtx/control	0.9385	0.3681
(cntx&pd173212)/control	cntx/ibtx	$\mathbf{6.71 \cdot 10^{-5}}$	$\mathbf{4.26 \cdot 10^{-4}}$

Table 4.1: Wilcoxon rank non-parametric tests performed on the effects on Ca^{2+} transient produced by blocking N-type VGCCs and BK CAKCs. The considered groups are: delivery of 1 µM ω-conotoxin-GVIA in control conditions (cntx/control, N = 11 cells); delivery of 5 µM pd173212 in control conditions (pd173212/control, N = 7 cells); delivery of either 1 µM ω-conotoxin-GVIA or 5 µM pd173212 in control conditions ((cntx&pd173212)/control, N = 18 cells); delivery of 1 µM iberiotoxin in control conditions (ibtx/control, N = 9 cells); delivery of 1 µM ω-conotoxin-GVIA in the presence of 1 µM iberiotoxin (cntx/ibtx, N = 9 cells). In each line, the two groups compared are reported in the left columns and the p values for the $\Delta F/F_0$ and I_{Ca} signals are reported on the right columns. Tests where p-value was < 0.01 are reported in bold characters. cntx = ω-conotoxin-GVIA, ibtx = iberiotoxin, $I_{Ca} = Ca^{2+}$ current, $\Delta F/F_0$ = change in intracellular Ca^{2+} transient, p = p-value determined by the Wilcoxon rank non-parametric test

4.2 The effect of blocking VGCCs and CAKCs on the shape of the bAP

To investigate the effect of the coupling between N-type VGCCs and BK CAKCs on the shape of the bAP and to analyse the timing of the interaction, we first determined the delay between the I_{Ca} and the peak of the bAP. Subsequently, we performed voltage imaging in the apical dendrite and locally applied blockers for VGCCs and CAKCs as described for the calcium imaging analysis above, and correlated the effects on the bAP shape to the timing of the I_{Ca}.

4.2.1 The peak of the inward I_{Ca} is delayed compared to the peak of the bAP

Before further analyzing the interaction between N-type VGCCs and BK CAKCs, we compared the kinetics of the dendritic Ca^{2+} current with that of the eliciting bAP at ∼100 µm from the soma. In chapter 3, we showed that in L5PNs the peak of the Ca^{2+} current occurs before the AP peak in the distal part of the axon initial segment whereas it is delayed the proximal part. In another study, using ultrafast combined V_m and Ca^{2+} imaging, we showed that the Ca^{2+} current was further delayed with respect to the AP peak in the proximal part of the apical dendrite of CA1 hippocampal pyramidal neurons (Jaafari and Canepari 2016). Thus, to study the relationship between the I_{Ca} and V_m waveform we performed combined calcium and voltage imaging recordings, using Cal520FF or Fura2FF as calcium indicator and JPW1114 to record the V_m (figure 4.4A). From the Ca^{2+}-$\Delta F/F_0$ the I_{Ca} was determined as explained in Figure 4.1A, after which the peak-to-peak delay of the I_{Ca} compared to the V_m of the bAP was calculated (figure 4.4B). Unsurprisingly, we observed that the peak of the I_{Ca} was delayed compared to the V_m maximum. This is due to the relative late activation of VGCCs compared to $Na_v1.2$ which is responsible for the upstroke of the bAP. A delay ranging from 500 µs to 800 µs was observed in N = 8 cells (figure 4.4C). From the kinetics of the Ca^{2+} transient we concluded that VGCCs start opening during the rising phase of the AP, but they remain open during the entire falling phase of the AP increasing the cytosolic Ca^{2+} concentration over this period. As a consequence, if the activation of a Ca^{2+}-binding protein is linear with the cytosolic Ca^{2+}, the maximal effect of this activation must be observed at least 500 µs after the AP peak.

4.2.2 The effect of N-type VGCC and BK CAKC coupling occurs in the first 500 µs after the AP peak

Then, using ultrafast V_m imaging (Popovic et al. 2015), as shown in the examples reported in figure 4.5, we investigated the kinetics of the dendritic bAP after blocking L-type VGCCs (figure 4.5A), P/Q-type VGCCs (figure 4.5B), N-type VGCCs (figure 4.5C), R-type VGCCs (figure 4.5D) and T-type VGCCs (figure 4.5E). In addition, we investigated the kinetics of the dendritic bAP after blocking the two major types of CAKCs, namely the SK channel using 1 µM apamin (figure 4.5F) and the BK channel (figure 4.5G). Consistently with the observation that the blockade of P/Q-type and R-type VGCCs caused, on average, the smallest decrease in the Ca^{2+} current (figure 4.1C), in the two representative cells of figure

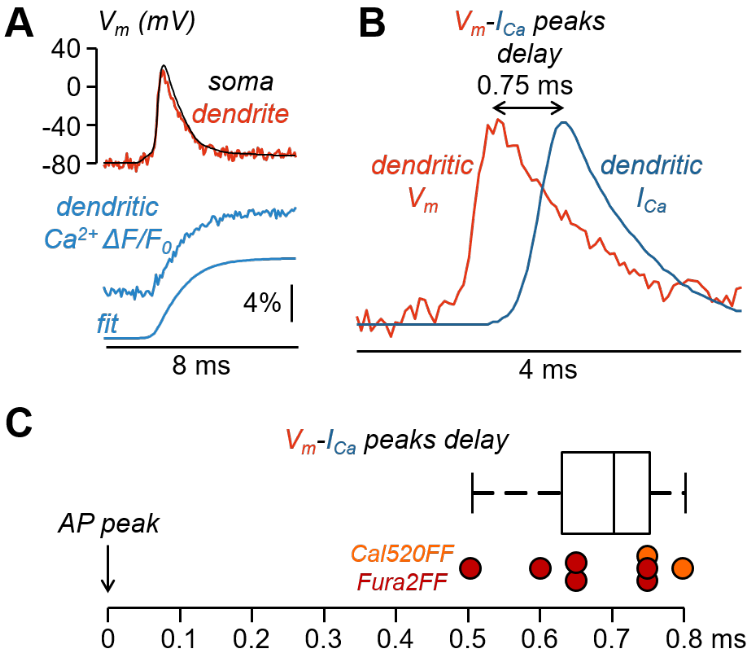

Figure 4.4: Delay between the calcium current and the back-propagating action potential peak. A, Top, membrane voltage measured through the patch pipette at the soma and using voltage-sensitive dye in the apical dendrite. Below change in calcium indicator fluorescence in the same cell at the same location along the dendrite, and fit of the $\Delta F/F_0$. B, Calcium current superimposed on the change in membrane potential in the apical dendrite. In this example the delay between the two peaks is 0.75 ms. C, Quantification of the delay of the calcium current peak after the voltage peak, which is 0.68 ± 0.09 ms (mean ± SD, $p = 2.49*10^{-7}$) for $N = 8$ cells. Individual cells are plotted as circles, red when using Fura2FF as calcium indicator and orange for the cells filled with Cal520FF.

4.5B and D the blockade of these two channels did not change the AP shape. Surprisingly, in the representative cell of figure 4.5E, the blockade of T-type VGCCs decreased the amplitude of the bAP, suggesting an effect on dendritic excitability. This effect can potentially be attributed to the drugs acting on a target other than T-type VGCCs. Besides, it suggests that the AP weakening may contribute to the relatively large inhibition of the Ca^{2+} current reported in figure 4.1C. In all other representative cells, the blockade of the channels caused a visually detectable widening of the AP shape. In the case of N-type VGCCs (figure 4.5C) and of BK CAKS (figure 4.5G), a widening seemed occurring during the first 500 µs following the AP peak, therefore during the phase of increasing of VGCC activation. In contrast, in the case of L-type VGCCs (figure 4.5A) and of SK CAKS (figure 4.5F), the widening seemed occurring mostly >500 µs after the AP peak, therefore during or after the expected peak of the Ca^{2+} current.

In these examples the observed widening can be detected by eye. In the vast majority of cells tested however, the peak-to-peak noise was >10 mV. Therefore we

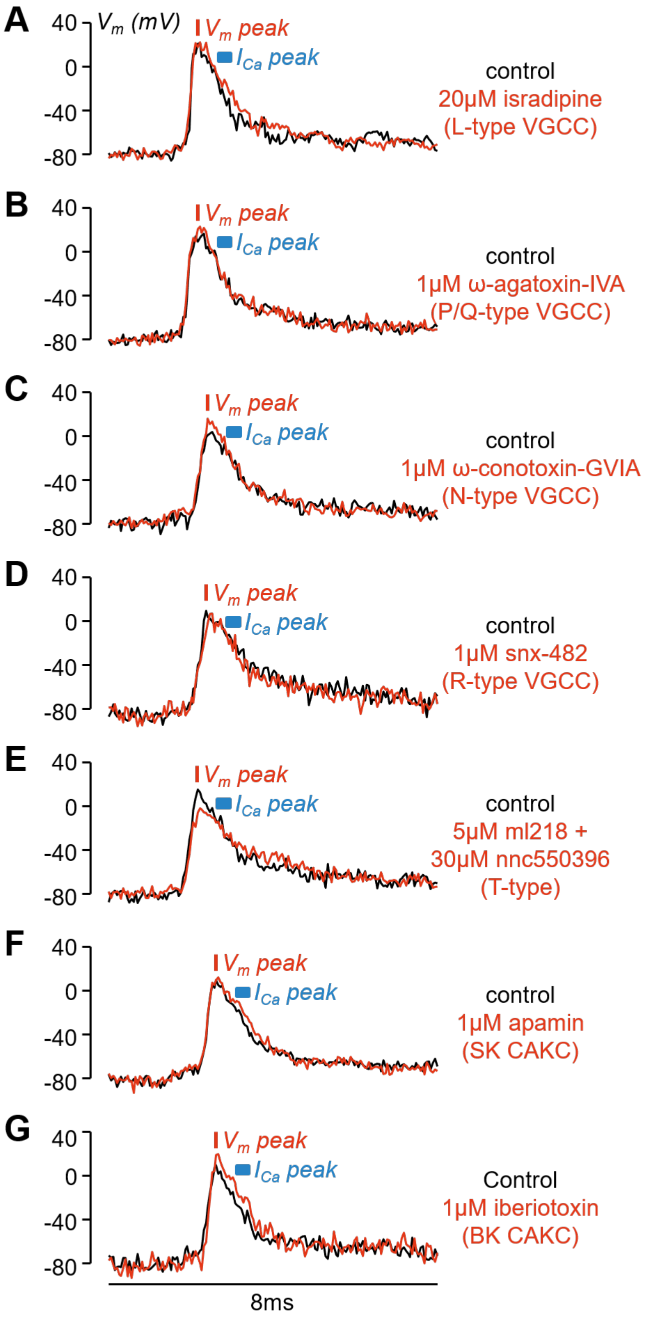

Figure 4.5: Examples of the effects of the diverse VGCC and CAKC blockades on the bAP shape. A, Optical V$_m$ transient from an apical dendrite region ($\sim$100 µm from the soma) in a representative L5 pyramidal neuron in control conditions (black trace) and after blocking L-type VGCCs with 20 µM isradipine (red trace). B, Representative experiment as in A, but by blocking P/Q-type VGCCs with 1 µM ω-agatoxin-IVA. C, Representative experiment as in A, but by blocking N-type VGCCs with 1 µM ω-conotoxin-GVIA. D, Representative experiment as in A, but by blocking R-type VGCCs with 1 µM snx-482. E, Representative experiment as in A, but by blocking T-type VGCCs with 5 µM ml218 and 30 µM nnc5503961. F, Representative experiment as in A, but by blocking SK CAKCs with 1 µM apamin. G, Representative experiment as in A, but by blocking BK CAKCs with 1 µM iberiotoxin. In each cell the red bar shows the timing of the AP peak and the blue segment the expected range for the peak of the Ca^{2+} current (500-800 µs after the AP peak).

performed a statistical analysis on the ensemble of cells for each channel blocker. Our aim was to assess the effect of blocking VGCCs or CAKCs on the shape of the bAP and to correlate these effects on the timing of the I_{Ca} as reported on in figure 4.4. Therefore, we compared the effect of blocking one channel subtype in three different time windows after the V_m peak. Specifically, 500 µs (10 data points) after the peak of the bAP and therefore before the expected peak of the Ca^{2+} current (bin *1* in figure 4.6A), 500 - 1000 µs (10 data points) after the bAP peak, so around the expected peak of the I_{Ca} (bin *2* in figure 4.6A), 1000 - 2500 µs (30 data points) after the bAP peak and around the expected Ca^{2+} current tail (bin *3* in figure 4.6A) and 1000 µs (20 data points) noise before the AP trigger as a reference (*noise* in figure 4.6A). Statistical significance was calculated using the Lilliefors test which determines if the difference between control and blocker-applied recordings follows a normal distribution when the parameters of this normal distribution are unknown (see chapter 2 for a detailed description).

Figures 4.6 and 4.7 show this voltage imaging analysis, with the histograms displaying the difference between control and blocker recordings in each bin (1 bottom left, 2 bottom middle, 3 bottom right). A normal distribution is superimposed over the histograms to provide contrast to the skewness of the plots. P-values calculated using the Lilliefors test are indicated in table 4.2. To summarise, there was no significant change in the V_m shape when blocking R-type or P/Q-type VGCCs (figure 4.6D,E). Blocking T-type channels resulted in a decrease in depolarisation (figure 4.6F), whereas a significant widening of the bAP waveform was recorded when blocking either N-type, L-type, SK or BK channels (figures 4.6B,C and 4.7).

Strikingly, the effect of blocking N-type channels occurred before the expected I_{Ca} peak (bin 1 figure 4.6B). A similar effect was observed when blocking BK channels (figure 4.7B). In both cases the bAP was also significantly widened in bin 2 around the expected I_{Ca} peak. The fact that the AP widening occurs before the expected Ca^{2+} current peak, when only a fraction of inflowing Ca^{2+} via N-type VGCCs is detected, indicates that BK channels are activated within 500 µs after the bAP peak. It also confirms N-type VGCCs are responsible for this activation, providing Ca^{2+} to BK channels before the current reaches its peak. Since the Ca^{2+}-dye equilibration is faster than we measure the Ca^{2+} influx, we cannot be sure whether the Ca^{2+} interaction with BK CAKCs is faster than the binding to the Ca^{2+} indicator. Nevertheless, the current anticipating effect suggests a physical interaction between N-type VGCCs and the BK CAKCs. These observations are in accordance with our finding that N-type VGCCs and BK CAKCs are functionally coupled in the apical dendrite.

This early timing of the effect of blocking fits with previous reports on the BK-mediated outward current, which has been described as a fast transient repolarising current (Benhassine and Berger 2005, 2009; Cui 2010), and a similar early effect of BK channels in the AIS (see chapter 3). In the AIS however, BK activation is partly mediated by Ca^{2+} influx through $Na_v1.2$ channels, which is not the case here. Although Hanemaaijer et al. (2020) hint that Ca^{2+} influx through $Na_v1.2$ channels in the dendrite is easily missed due to its small contribution compared to VGCC mediated Ca^{2+} influx, we have not observed any residual Ca^{2+} transient after blocking all VGCCs (figure 4.1A). Taken together with the early effect of blocking N-type channels which matches the BK block, we conclude N-type VGCCs are coupled to BK CAKCs by supplying Ca^{2+} for their fast activation.

	N cells	**p noise**	**p bin 1**	**p bin 2**	**p bin 3**
L-type VGCC	8	0.16	0.13	$\mathbf{5*10^{-4}}$	$\mathbf{2.5*10^{-5}}$
P/Q-type VGCC	8	0.17	0.015	0.21	0.022
N-type VGCC	10	0.82	$\mathbf{8.3*10^{-4}}$	**0.0082**	0.29
R-type VGCC	8	0.49	0.57	0.48	0.56
T-type VGCC	8	0.69	$\mathbf{1*10^{-4}}$	**0.0017**	0.012
SK CAKC	8	0.17	0.44	**0.0042**	$\mathbf{1.3*10^{-4}}$
BK CAKC	9	0.19	$\mathbf{7.1*10^{-4}}$	**0.0011**	0.18

Table 4.2: Lilliefors test to assess whether a set of values is consistent with a normal distribution performed on sample differences in V_m imaging experiments after blocking a channel and in control conditions. The five columns report, for each channel tested, the total number of cells (N) and the values of p (p) for the noise (number of samples 20*N), for the signal in bin 1 (first 500 µs after the AP peak, number of samples 10*N), for the signal in bin 2 (following 500 µs after the AP peak, number of samples 10*N), for the signal in bin 3 (following 1.5 ms after the AP peak, number of samples 30*N). Tests where p was < 0.01 are reported in bold characters and indicate a significant change of the AP shape caused by the blockade of the channel.

4.2.3 The effect of blocking L-type VGCCs on the bAP waveform mimics the effect of SK CAKC block

Adding apamin to block SK channels caused a widening of the bAP around the expected Ca^{2+} current peak and tail (bins 2 and 3 in figure 4.7A). These effects of apamin are consistent with the slow afterhyperpolarising role of SK channels, as previously reported (Bond et al. 1999; Sah 1996). The time-course of the AP change due to the block with apamin is consistent with an activation of K^+ channels by cytosolic Ca^{2+}, but the hypothesis that these channels are also selectively activated

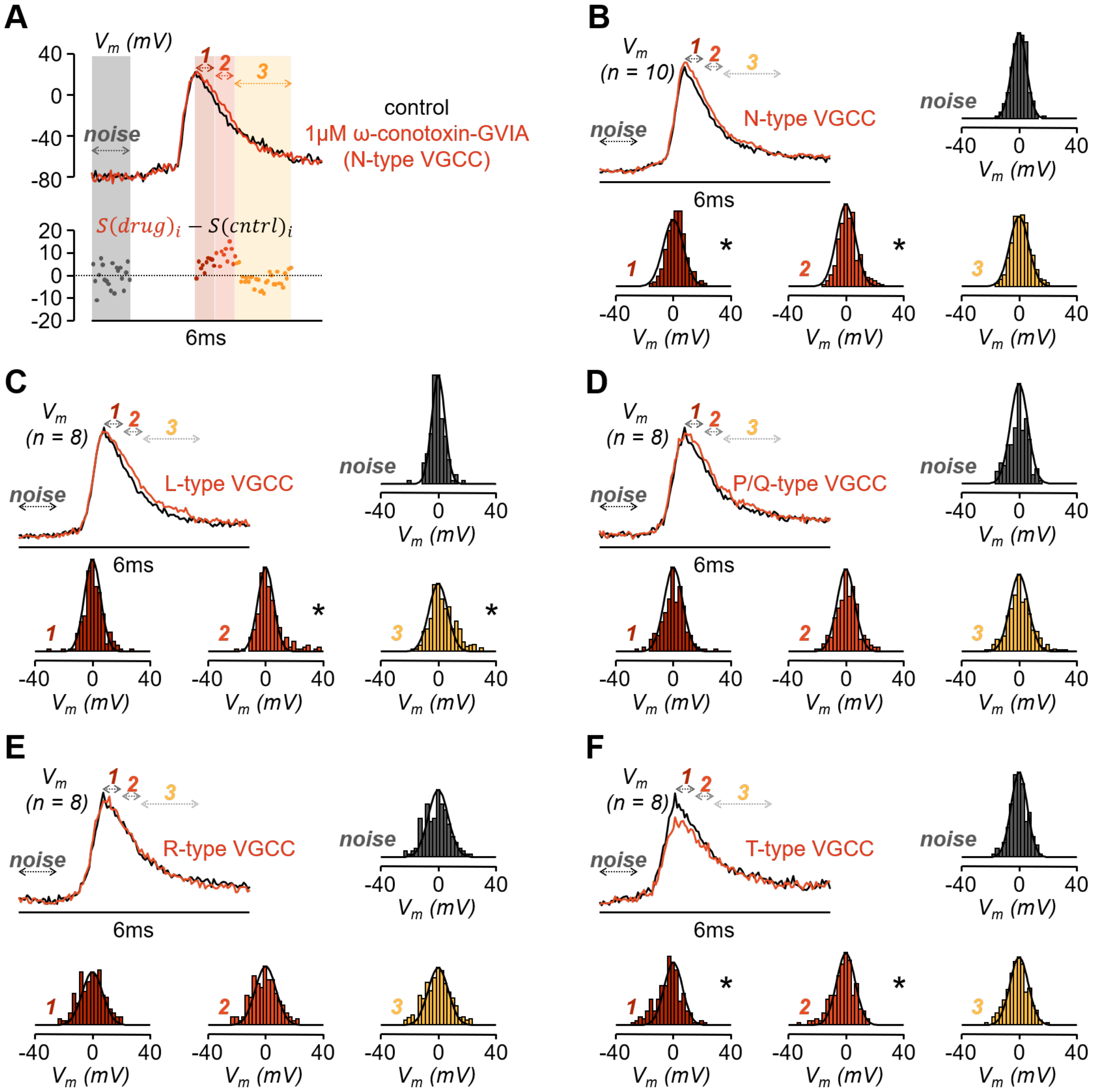

Figure 4.6: Analysis of the effect of the diverse VGCCs on the bAP shape. A, Top, optical V_m transient from an apical dendrite region (∼100 µm from the soma) in a representative L5 pyramidal neuron in control conditions (black trace) and after blocking N-type VGCCs (red trace); arrows at different gray tones indicate the time windows corresponding to the noise (1 ms before current injection), signal “1” (first 500 µs after the AP peak), “2” (following 500 µs) and “3” (following 1.5 ms). Bottom, sample difference of the signals after the channel blockade and in control conditions in the four time windows. B, Averaged signals aligned to the AP peak from N = 10 cells in control conditions (black trace) and after blocking N-type VGCCs (red trace) and histograms of the sample differences in the illustrated four time windows; normal distributions with mean and standard deviations calculated from the points are reported (red plots) for comparison with the histograms. C, Same as in B, but in 8 cells where L-type VGCCs were blocked. D, Same as in B, but in 8 cells where P/Q-type VGCCs were blocked. E, Same as in B, but in 8 cells where R-type VGCCs were blocked. F, Same as in B, but in 8 cells where T-type VGCCs were blocked. In panels B-F “*” indicates that the distribution deviates from normality ($p < 0.01$, Lilliefors test).

by a specific Ca^{2+} source cannot be excluded since the delayed widening can be due to a slower kinetics of the K^+ channels.

In L5 pyramidal neurons, SK activation has been linked to R-type VGCCs (Jones and Stuart 2013). The same study shows a significant decrease in the calcium current when blocking R-type currents, which is not observed in this work. In hippocampal pyramidal neurons however, L-type VGCCs are thought to supply Ca^{2+} for SK channel activation, which was shown through inside-out patches while blocking the other VGCCs (Marrion and Tavalin 1998). Interestingly, when blocking L-type VGCCs we observed a significant widening of the bAP, specifically during the expected I_{Ca} peak (figure 4.6B), similar to blocking SK CAKCs. This is speculation about an interaction between SK and L-type channels. As L-type VGCCs have also been linked to BK channels (Sun et al. 2003), there might be a combined effect of L-type mediated Ca^{2+} influx on BK and SK activation. This however, is not clear in this analysis.

Then, blocking either P/Q-type or R-type channels had no significant effect on the bAP shape (figure 4.6D). Interestingly, however, in 4/8 cells tested for the blockade of P/Q-type VGCCs, an early widening of the AP was also observed, leading to a low value of p (table 4.2). In the case of P/Q-type channels this might reflect another CAKC interaction, which seems insignificant probably due to the small contribution of the P/Q-type current to the total Ca^{2+} current. In addition, the high variability within this group of cells make a strong interaction unlikely.

4.2.4 The block of T-type VGCCs decreases the bAP peak

In contrast to the other VGCCs, blocking T-type channels resulted in a decrease in the V_m of the bAP (figure 4.6F) in 6/8 cells tested. This effect was most notable and significant directly after the bAP peak and around the expected peak of the I_{Ca}, with p-values of $7.1*10^{-4}$ and 0.0011, respectively (table 4.2). Controversially, the effect of the blockers is similar to what we would expect when blocking $Na_v1.2$ channels. As $Na_v1.2$ activates rapidly it is responsible for the upstroke of the bAP and the initial depolarisation. As the observed effect when blocking T-type VGCCs influences the maximum depolarisation, this might indicate T-type VGCCs influence excitability, creating a link with $Na_v1.2$ channels. To our knowledge however, an interaction between $Na v1.2$ and T-type VGCCs in PNs has not been reported.

To verify the targets of the used drugs and to confirm the role of T-type VGCCs in shaping the peak of the bAP additional experiments have to be planned. First of all, using different blockers confirming we are targeting T-type channels

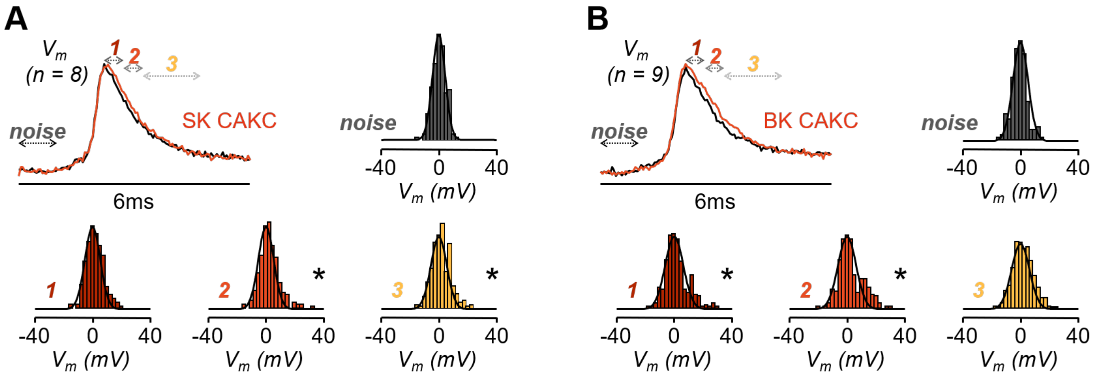

Figure 4.7: Analysis of the effect of the diverse CAKCs on the bAP shape. Same analysis as in figure 4.6, where the signal is divided into bins of 500 µs after the voltage peak (1), 500 µs around the expected calcium current peak (2), 1500 µs after the expected calcium current peak (3) and 1000 µs noise. A, Averaged signals aligned to the AP peak from N = 8 cells in control conditions (black trace) and after blocking SK CAKCs (red trace) and histograms of the sample differences in the illustrated four time windows; normal distributions with mean and standard deviations calculated from the points are reported (red plots) for comparison with the histograms. B, Same as in A, but in 9 cells where BK CAKs were blocked. “*” indicates that the distribution deviates from normality ($p < 0.01$, Lilliefors test).

exclusively. Then, the interaction with Nav1.2 can be addressed, which is further discussed in chapter 5.

To be able to correlate the findings described so far we need to review voltage and calcium gated channels together. Particularly due to the complexity of the interactions we again used computational modelling to interpret the experimental results.

4.3 Simulations with a NEURON model reproduce the experimental results

To mimic the experimental results detailed above, we constructed a NEURON model based on our dataset together with our collaborators Dr. Michele Migliore and Elisabetta Giacalone. We extended the model described in chapter 3 detailing the AP generation in the AIS. The full details of the NEURON model are explained in chapter 2. Briefly, we first changed the dendritic morphology to that of a mouse L5PN 5 (figure 4.8), and exchanged or inserted the relevant voltage gated ion channels (see table 4.3 for channel distributions). Identical models for Na$_v$1.2, SK and BK CAKCs as inserted in the AIS were expressed uniformly along the dendrites. Na$_v$1.2 expression was $\sim$50 fold lower compared to the AIS, as suggested by Kole et al. (2008). To be able to link specific VGCCs to CAKCs, separate currents

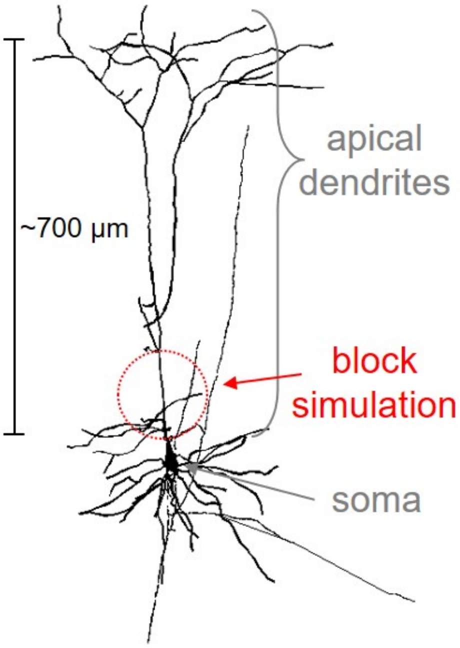

Figure 4.8: Morphology of the layer 5 pyramidal neuron model in NEURON. Soma and apical dendrite are indicated in grey. When simulating a specific channel block we decreased the density of the specific channel with 90%. The area of the simulated spread of the blocker is indicated in red.

for T-type, L-type, R-type, P/Q-type and N-type channels were inserted from previously published models (Mandge and Manchanda 2018; Wimmer et al. 2010), and were homologous distributed. An inward current (I_h) generated by HCN cation channels was inserted with a density increasing exponentially to 50 fold in the distal apical dendrite compared to the soma, as suggested by other studies (Harnett et al. 2015; Kole et al. 2006; Lörincz et al. 2002). Lastly, VGKCs models were introduced grouped by current. Specifically, channels generating a I_A, I_M and delayed rectifier current (I_{KDR}) were inserted. The delayed rectifier K^+ current and I_A were inserted with decreasing density with respect to the soma in a linear fashion as previously suggested (Kang et al. 2000; Ramaswamy and Markram 2015).

4.3.1 The NEURON model reproduces the AP waveforms and changes in Ca^{2+} transients

To determine the current densities of the model, we used a calibrated voltage imaging recording (shown in chapter 2) to compare and adjusted the channel densities to reflect the experimental traces. Specifically, we first modified the VGNC conductances in the AIS and soma to match the simulated somatic AP to the electrophysiology recording, while respecting $Na_v1.2$ to $Na_v1.6$ ratios and distribution. Secondly, we reproduced the bAP ~100 µm from the soma, by changing channel conductances and parameters of $Na_v1.2$, VGCCs, VGKCs and CAKCs to match the calibrated V_m-$\Delta F/F_0$ recording. Figure 4.9 shows the experimental traces as well as the simulations of the somatic AP and dendritic bAP and Ca^{2+}

Channel	**Current**	**Apical distribution**
Ca_v1.2-4	L-type	Uniform
Ca_v2.1	P/Q-type	Uniform
Ca_v2.2	N-type	Uniform
Ca_v2.3	R-type	Uniform
Ca_v3.1-3	T-type	Uniform
SK CAKC	I_K	Uniform
BK CAKC	I_K	Uniform
K_v3 and K_v4	I_A	Linear decreasing
K_v7	I_M	Uniform
Delayed rectifier VGKC	I_{KDR}	Linear decreasing
Na_v1.2	I_{Na}	Uniform
HCN	I_h	Exponential increasing

Table 4.3: Channel distribution in the apical dendrite in the computational model. Ca_v = voltage gated calcium channel, CAKC = calcium-activated potassium channel, K_v and VGKC = voltage gated potassium channel, Na_v = voltage gated sodium channel, SK = small conductance, BK = large conductance, HCN = hyperpolarization-activated cyclic nucleotide–gated.

currents. The simulations fit well the experimental data. Despite the noise in the voltage imaging recording, the dendritic AP follows the V_m closely (figure 4.9B). Figure 4.9C and D show the change in Ca^{2+} concentration during the bAP and the calculated Ca^{2+} current superimposed on the bAP waveform, respectively. The peak to peak difference between the bAP waveform and the I_{Ca} is 0.5 ms in this simulation, respecting our experimental observations shown in figure 4.4.

Before coupling VGCC-mediated rises in intracellular Ca^{2+} to specific CAKCs, we simulated the effect of blocking each VGCC subtype by decreasing the density of the channel by 90% (figure 4.8). For this purpose a calcium indicator with OG5N properties was added to the model to account for the buffering effect of the calcium indicator. Figure 4.10A shows the results of this simulation, which are in accordance with our experimental observations detailed in figure 4.1. Similar to our experiments, L-type and T-type VGCCs contribute most to the change in Ca^{2+} concentration during a bAP, whereas the contributions of P/Q-type and R-type channels are small. Without specific CAKC coupling, simulating the block of N-type VGCCs decreases the change in Ca^{2+} concentration, as well as the peak of the calculated I_{Ca}. This is different than reported in our experiments, which further confirms our conclusion that Ca^{2+} entry through N-type VGCCs does not directly contribute to the intracellular Ca^{2+} concentration but rapidly binds to other targets. To verify our previous conclusion that N-type channels are functionally coupled to BK CAKCs we introduced specific Ca^{2+} dependencies for the activation of both CAKCs.

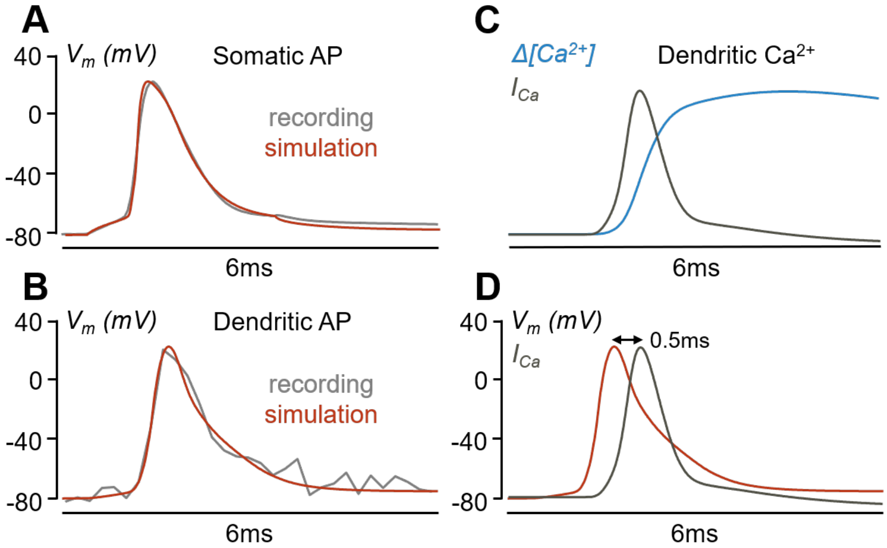

Figure 4.9: Simulation of a bAP and Ca^{2+} current ~100 µm from the soma. A, Somatic AP from a electrophysiology recording (grey trace) and the simulation (red trace). B, From the same neuron as in A, the dendritic AP by calculating the V_m from the JPW1114 $\Delta F/F_0$ (grey trace), as described in chapter 2. Superimposed the simulated dendritic AP (red trace). C, Change in Ca^{2+} concentration ~100 µm from the soma and the I_{Ca} calculated by taking the time derivative of the simulated Ca^{2+} concentration. D, I_{Ca} superimposed on the bAP waveform.

SK channel activation was controlled by all VGCCs except N-type channels. This was done as various VGCC subtypes have been linked to SK activation in the past in various cell types (Jones and Stuart 2013; Marrion and Tavalin 1998; Wolfart and Roeper 2002). In addition, we did not find clear evidence for a specific VGCC to be functionally coupled to SK channels. Moreover, Jones and Stuart (2013) suggested that SK CAKCs might have more than one Ca^{2+} source.

BK channels were coupled to Ca^{2+} entry through both N-type and L-type channels, as was suggested before (Loane et al. 2007; Sun et al. 2003), with a N-type:L-type dependence ratio of 8:1. With this specific VGCC-CAKC coupling simulating a block of N-type VGCCs has a different effect, showing an increase in the Ca^{2+} concentration compared to the control simulation (figure 4.10B), as we have observed experimentally (figure 4.6B). Besides an increase in the Ca^{2+} concentration we also found a slight increase in the peak of the I_{Ca}. However, simulating the block caused a small temporal shift in both the change in Ca^{2+} and the I_{Ca}, caused by the fast activation of N-type channels in the simulation. This shift was not apparent from our experimental data, indicating our model can be further optimised. There was no significant change in Ca^{2+} concentrations between the two coupling scenarios when blocking the other VGCC subtypes.

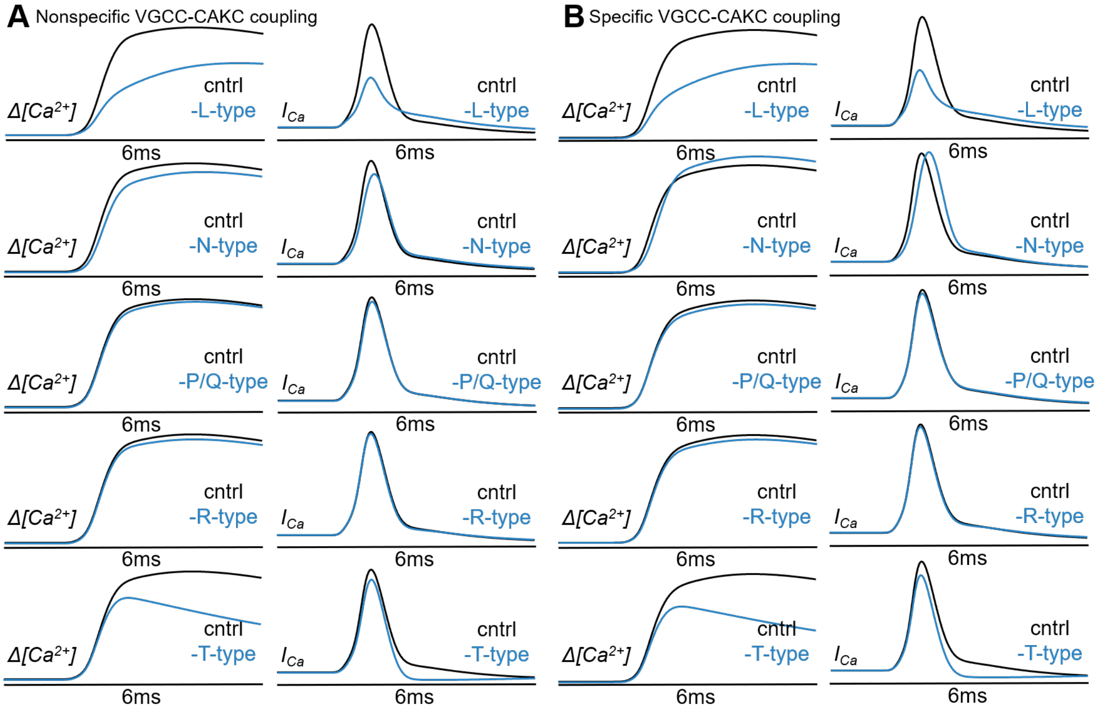

Figure 4.10: Simulations on the effect of blocking VGCCs on the Ca^{2+} currents. Showing the change in Ca^{2+} concentration during a simulated bAP, plotted as the Ca^{2+} bound to the indicator (left column) and the Ca^{2+} current (I_{Ca}) calculated by taking the time derivative of the Ca^{2+} concentration (right column). We stimulated the blocking of VGCCs (L-type VGCCs, N-type VGCCs, P/Q-type VGCCs, R-type VGCCs or T-type VGCCs) by locally decreasing their densities with 90%. A, In this simulation Ca^{2+}-dependent CAKC activation is coupled to Ca^{2+} entry through all VGCCs. B, Same channel densities, but specific coupling of N-type and L-type VGCCs to BK CAKCs and all VGCCs except N-type channels to SK CAKCs.

4.3.2 N-type VGCC and BK CAKC interaction is mimicked by simulations in the NEURON model

To further verify the introduced Ca^{2+} dependencies we simulated the block of VGCCs and CAKCs, again by decreasing the density with 90%, and observed the effect of their blocks on the bAP waveforms (figure 4.11).

Firstly, simulating the block of R-type or P/Q-type VGCCs had little effect on the bAP waveform (figure 4.11C,D), as reported in figure 4.6D and E.

Next, simulating the block of L-type channels resulted in a late widening of the bAP, with the largest effect after the I_{Ca} peak (figure 4.11A). This is comparable to bin 3 in figure 4.6. In our experimental data, blocking L-type VGCCs caused a widening around and after the I_{Ca} peak (figure 4.6C). This is partly mimicked by the model, with a very small effect in the 500 µs around the peak of the I_{Ca}. This earlier widening after simulating the block of L-type VGCCs was specifically dependent on

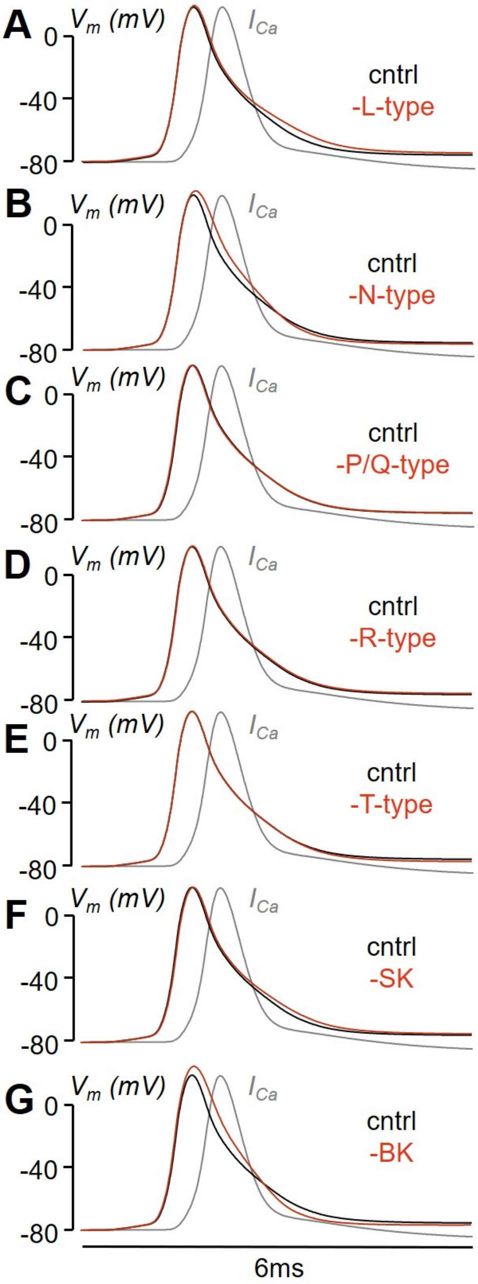

Figure 4.11: Simulations on the effect of blocking VGCCs and CAKCs on the bAP waveform. In black the bAP waveform in control conditions, as in figure 4.9B, and in red the simulations of blocking VGCCs or CAKCs by locally decreasing their densities with 90%. As a reference, the dark red, red and yellow columns indicate the bins used in the analysis of figures 4.6 and 4.7 to investigate the temporal effect of applying the used blockers. The red traces are the bAPs after simulating the block of L-type VGCCs (A), N-type VGCCs (B), P/Q-type VGCCs (C), R-type VGCCs (D), T-type VGCCs (E), SK CAKCs (F) or BK CAKCs (G).

the coupling to BK channels. The later widening was dependent on the coupling to SK channels. This was reflected in the similarity between blocking L-type VGCCs and SK CAKCs in the model. Simulating a SK channel block also caused a widening in the bAP waveform (figure 4.6F), as was shown in our experiments (figure 4.7A). Similar to blocking L-type VGCCs however, the bAP widening was recorded after the Ca^{2+} current peak in the simulation. Taken together, this shows it is likely L-type VGCCs supply Ca^{2+} for both BK and SK CAKC activation. In addition, the kinetics of the L-type channel might be optimised to reflect a slightly earlier effect on the bAP waveform when blocked.

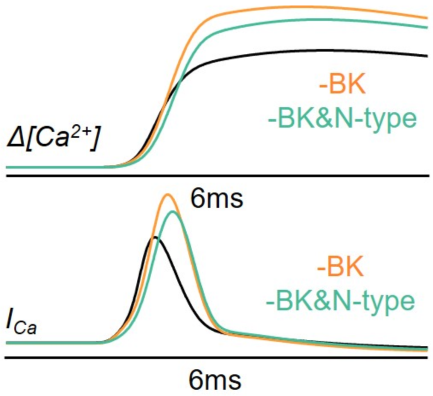

Figure 4.12: The functional coupling of BK CAKCs and N-type VGCCs simulated with the NEURON model. Simulating the block of N-type VGCCs (green traces) or BK CAKCs (orange traces), showing the effect on the change in Ca^{2+} concentration when blocking N-type VGCCs alone (top) or after also blocking BK CAKCs (bottom).

Besides L-type channels, SK CAKCs were also coupled to T-type VGCCs in the model. Simulating a T-type VGCC block caused a small increase in the AHP (figure 4.11E), but had no effect on the peak of the bAP as was observed in experiments (figure 4.6F). We suggest, as mentioned above, that T-type activation is linked to Na_v1.2 channels. However, this remains to be incorporated in the NEURON model and could therefore not be assessed here.

Lastly, we observed a widening in the first 1000 µs after the peak of the bAP when decreasing dendritic N-type densities (figure 4.11B). A similar effect was observed when simulating the block of BK CAKCs (figure 4.11G), confirming the results shown in figures 4.6B and 4.7B. Additionally, when blocking BK channels we observed an increase in the AHP, due to the increase in Ca^{2+} influx following the bAP widening. This effect was not observed experimentally, but was due to an increased late I_K, as the already hypothesised increase in depolarisation increased VGCC activation which in turn increased SK channel contribution.

Then, to show the effect of N-type VGCC coupling to BK CAKCs on the Ca^{2+} concentration, figure 4.12 shows the simulation of blocking BK and N-type channels in sequence. Blocking only N-type channels results in an increase in the Ca^{2+} concentration compared to control, as shown above. However, when N-type channel densities are decreased after simulating a BK CACK block a decrease in Ca^{2+} concentration follows. These simulations conform to the experimental results shown in figure 4.3A. They also explain how blocking N-type VGCCs results in a decrease of I_K through BK channels, which results in a decrease or delay of repolarisation, which is similar to blocking BK channels directly as shown in the simulation in figure 4.11B and G and experimentally in figures 4.6B and 4.7B.

4.4 Summary and significance

This chapter focussed on the role and interplay of voltage gated ion channels in the apical dendrite during a bAP. We show that all neuronal VGCCs are present in the dendrite and together are responsible for the I_{Ca} during AP back propagation. Contrary to the AIS, where $Na_v1.2$ also mediates Ca^{2+} influx (chapter 3). Furthermore, we show that N-type VGCCs are functionally coupled to BK CAKCs, who are responsible for fast repolarisation. Using voltage imaging experiments we confirm the effect of their interplay is measurable after the peak of the bAP but before the expected I_{Ca} peak, as blocking N-type VGCCs results in an early widening of the bAP peak. These results are confirmed with a NEURON model, connecting the AIS and apical dendrite. Taken together, we propose a dual, spatially restricted role of BK channels, shaping the generating AP in the AIS through its interaction with $Na_v1.2$ channels and driving fast repolarisation through functional coupling with N-type VGCCs during AP back propagation in the apical dendrite.

In our computational model we couple BK CAKCs not only to N-type, but also L-type VGCCs. Moreover, the best approximation of our experimental results was by coupling L-type channels to both CAKCs. These interactions, together with the large part of the total I_{Ca} carried by L-type VGCCs, give this channel a crucial role during back propagation.

Lastly, we made the observation that blocking T-type VGCCs causes a significant decrease in the bAP peak. This was unexpected, as the effect anticipated the I_{Ca}, and T-type currents are described as *transient* and are marked by relatively slow activation. Therefore, we suggest T-type VGCCs interact with $Na_v1.2$, as blocking this VGNC has a similar effect. This possible interaction would need investigating, which is further discussed in chapter 5.

Unfortunately, nature seems unaware of our intellectual need for convenience and unity, and very often takes delight in complication and diversity.

— Santiago Ramón y Cajal

5

Discussion

Contents

5.1 Challenges of working with brain slices 106
5.2 A synergistic approach to understanding VG ion channel functioning 108
5.3 Voltage gated Na^+ channels in the AIS 109
    5.3.1 Channelopathies caused by $Na_v1.2$ mutations 111
5.4 On the properties of BK CAKCs 113
    5.4.1 BK CAKC and $Na_v1.2$ interaction 115
    5.4.2 BK CAKC and N-type VGCC interaction 116
5.5 VGCCs in the apical dendrite during AP back propagation 117
    5.5.1 Ca^{2+} electrogenesis and plasticity at the tuft of the apical dendrite 119
5.6 Anterograde action potential propagation and neuronal firing 122
5.7 Importance of sub-microsecond activation of Ca^{2+} binding proteins 123
5.8 Future perspectives 124

This thesis reports on our research concerning the role of voltage gated ion channels in AP generation and back propagation in L5PNs of the mouse somatosensory cortex. I will shortly summarise our results before commencing their discussion.

In the first part of this work, we focused on AP generation in the AIS, where we aimed at investigating the contribution of $Na_v1.2$. In the past, the study of the activation and signaling of specific VGNC isoforms has been limited by a series of experimental obstacles. Most importantly, unambiguous discrimination between

Na$_v$1.2 and Na$_v$1.6 had not been achieved using the available pharmacological tools. To overcome this difficulty, we used the novel peptide G^{1}G^{4}hwtx which partially but selectively blocks Na$_v$1.2 with respect to Na$_v$1.6. This permitted the detailed investigation of Na$^+$ currents, V$_m$ waveforms and Ca^{2+} currents associated with the AP. Most notably, we demonstrated that the permeability of Na$_v$1.2 to Ca^{2+} allows activation of BK CAKCs. We show that the interplay between Na$_v$1.2, mediating depolarisation, and BK CAKCs, regulating the peak and the early phase of the AP repolarisation, shapes the AP waveform. To confirm our findings, Dr Luiza Filipis adapted a NEURON model of the AIS to fit our results. Using this model, we could simulate the functional interaction between Na$_v$1.2 and BK channels and mimic the experimental results obtained by blocking Na$_v$1.2 with G^{1}G^{4}hwtx.

The second part of this thesis addresses the role of voltage gated ion channels during AP back propagation into the apical dendrite. By recording Ca^{2+} transients in the apical dendrite ∼100 µm from the soma we show that all neuronal VGCCs are expressed in the dendrite. Furthermore, together these channels sustain the total Ca^{2+} current during a bAP. Contrary to the AIS, Ca^{2+} influx through Na$_v$1.2 in the apical dendrite is undetectable, which is likely due to the low expression of Na$_v$1.2. Most fascinating, we show that blocking N-type VGCCs further increases, rather than inhibits, the measured I$_{Ca}$ through an interaction with BK CAKCs. By analysing the V$_m$ waveform during AP back propagation we observe the effect of their functional coupling occurs in the first 500 µs after the bAP peak before the I$_{Ca}$ peak, indicating their coupling is faster than the kinetics of VGCCs. These results are confirmed with a preliminary NEURON model, connecting the AIS and apical dendrite.

The physiological consequences of these results are discussed below. Also, I include some further speculations based on our findings and will propose additional experiments to test these hypotheses. I conclude with future research perspectives and directions.

5.1 Challenges of working with brain slices

In our laboratory we work with brain slices as they are the best compromise between working in the living animal and being able to observe as well as manipulate subcellular processes at a molecular level. In the data described in the previous chapters, the effect of used toxins and drugs often varied from cell to cell. This may results from varied levels of ion channel expression patterns or variations in the currents carried by these channels. L5PNs are a large group of neurons including various morphologies, such as thick- or regular-tufted, and sparse or large basal dendrites (Gouwens et al. 2019; Ramaswamy and Markram 2015). Also, L5 can be divided into two layers, L5A and L5B. PNs in these two sub-layers have slightly different morphologies (Spruston 2008). Furthermore, L5PNs project to different brain areas and can therefore also be divided based on their projections. The three main groups are corticospinal, corticostriatal and corticothalamic projecting PNs (Ramaswamy and Markram 2015). All this L5PN variability is likely reflected in a variable contribution of voltage gated channels to ionic currents. For instance, Stewart and Foehring (2000) showed that the contribution of VGCC subtypes to the total Ca^{2+} current varied greatly between L5PNs categorised by their projection. This illustrates the large variety within L5PNs, and helps explain part of our data variability. Particularly in brain slices, it is difficult to distinguish between different subtypes of L5PNs. Consequently, we expect a variability of varying channel expression patterns in our dataset.

In addition, we may question the efficacy of local blocker application through pressure ejection. Specifically, the diffusion and the penetration efficiency of the blocker introduce another layer of variability. As we patch cells ~30 µm from the slice surface, the blockers we apply need to penetrate a small layer of tissue before arriving at the membrane of the neuron we are recording from. While the drug pipette is positioned carefully, we cannot determine exactly how much blocker is injected into the tissue, and how far the drug has diffused. Many researchers choose to work with HEK293 cells expressing the proteins of interest. Although this would solve the issue of pressure ejection of blockers, HEK293 cells lack the neuronal morphology essential in this thesis, as well as the unique expression pattern driven by the neuronal environment. When working with brain slices one could add a fluorescent molecule to the drug solutions, which will provide visual feedback about the diffusion of the drug into the slice. However, one should take into account that most fluorescent molecules such as fluorescin are much smaller than the toxins reported in this thesis. In addition, a fluorescent molecule should be selected that does not interfere with the excitation and detection of the indicator used.

Lastly, the importance of conducting these experiments in their physiological circuitry is also shown in this thesis. When using acute brain slices, a significant part of the essential circuitry of the cortical layers is left intact. As the connectivity of the brain is an important factor in anchoring ion channels in the membrane, we can assume this circuitry also influences coupling between channels. To give one example, the synaptic proteome, including VG ion channels, is recruited and stabilised by the interaction of pre- and post-synaptic proteins (Maximov and

Bezprozvanny 2002; Shibasaki et al. 2004), illustrating the importance of neuronal circuits. Therefore, the use of brain slices enabled us to highlight how interactions between specific channels shape the measured electrical potentials.

5.2 A synergistic approach to understanding VG ion channel functioning

A major analytical contribution of this thesis is analysing voltage gated ion channel kinetics using a synergistic approach. This includes three major ingredients; ultrafast imaging of the V_m as well as Ca^{2+} and Na^+ transients, pharmacological manipulation, and NEURON modelling. One limitation of the patch clamp technique is that one cannot measure currents locally through the patch electrode, which is why imaging is essential in our approach. It allows us to record the V_m and ionic currents at many different positions sequentially, at a high spatio-temporal resolution, without the need for additional patches. To study the role of specific channels we employ animal toxins and synthetic drugs that are highly selective. This enabled us to analyse the effect of blocking one or a few channel subtypes in a physiological situation while taking into account other channels or ion currents. This is important, as the activation and inactivation patterns of VG ion channels is driven by the differences in voltage across the plasma membrane. The same V_m which in turn is determined by the ion currents through these channels. Therefore the contribution of a specific channel is not equal to the subtraction of a recording while blocking from a control measurement. To circumvent this non-linearity in channel interactions an to be able to extract individual channel contributions we employ computational modelling. We use NEURON to reconstruct the sequence of channels activation underlying the shaping of the AP waveforms.

This approach allowed for the identification of the functional coupling of BK CAKCs to $Na_v1.2$ channels and N-type VGCCs in the AIS and apical dendrite, respectively. It also explains why many studies investigating VG ion channels did not uncover these interactions, as often isolated currents are studied without taking into account the other channels. This shows why Stewart and Foehring (2000) did not observe the increase in intracellular Ca^{2+} when blocking N-type channels. In their study they blocked all Na^+ and K^+ currents in order to isolate the I_{Ca}, after which they sequentially blocked HVA VGCCs. This approach gives very little information about the contribution of the various VGCCs to the Ca^{2+} current during neuronal events such as APs. In addition, it masks any channel interaction as all currents except Ca^{2+} transients were blocked.

We have shown how the interplay of BK CAKCs and $Na_v1.2$ channels shapes the waveform of the AP in the AIS. The shape of this waveform determines how a neuron responds to prolonged input through a train of APs, which determines the signal encoding ability of the cell (Kole and Stuart 2012). After its generation, the AP propagates along the axonal branches, regenerates at Ranvier nodes, and the waveform at synaptic terminals regulates neurotransmitter release providing an analog modulation of synaptic transmission (Rama et al. 2018). Simultaneously, while back propagating to the soma and then along the dendrites, the bAP progressively changes its shape and regulates synaptic integration (Gulledge et al. 2005). The shape of the AP is related to all consequent physiological processes, and is involved in neurotransmitter release and therefore synaptic transmission but also dendritic processes such as Ca^{2+} electrogenesis (Larkum et al. 1999a).

To investigate these processes, it is imperative to evaluate the AP shape and propagation as one phenomenon, built up by many ionic currents. For this approach highly selective blockers are essential, as they allow targeting one channel subtype with high precision. As mentioned above, the development and use of G^1G^4hwtx (Montnach et al. 2022) was fundamental for the investigation of $Na_v1.2$ in the AIS. However, continued efforts are necessary to develop selective toxins for the channels that are still difficult to target, for example T-type VGCCs and $Na_v1.6$. The development of new toxin analogues will enlarge the database of drugs and enable us to selectively target VG ion channels for which selective toxins are unavailable at this moment.

5.3 Voltage gated Na^+ channels in the AIS

In the AIS, AP generation is dependent on high sodium channel densities (Kole et al. 2008; Tian et al. 2014). This high VGNC density lowers the threshold for AP initiation up to 15 mV compared to the soma (Colbert and Pan 2002). In pyramidal neurons specifically, the different temporal and spatial patterns of expression of $Na_v1.2$ and $Na_v1.6$, but also the diverse biophysical properties underlying activation and inactivation, suggest that these two channels contribute differently to the generation/propagation of APs (Hu et al. 2009), as well as in the ability to mediate high or low frequency firing (Rush et al. 2005). Whereas the threshold for the AP initiation is largely determined by $Na_v1.6$ (Royeck et al. 2008), our results point for a major contribution of $Na_v1.2$ in the Na^+ current during the rising phase of the AP, in particular at the AP upstroke, even in the distal sites of the AIS where $Na_v1.6$ expression is dominant. Importantly, an early Ca^{2+} current occurring with kinetics similar to that of the Na^+ current allows Ca^{2+} binding to its targets before the AP reaches its peak. Evolutionary speaking, the Ca^{2+} permeability of $Na_v1.2$ is unsurprising as the α subunits of VGNCs and VGCCs have similar structures and are closely related (Yu and Catterall 2004). The short motifs that ensure ion selectivity are located at the same place in the respective channel genes. Moreover, when Heinemann et al. (1992) replaced the amino acid lysine at position 1422 or alanine at position 1714 by glutamic acid of a rat $Na_v1.2$ channel, they altered the ion selectivity properties of the channel to resemble those of VGCCs, with Ca^{2+} replacing Na^+ as the main charge carrier at high extracellular Ca^{2+} concentrations.

Contrary to $Na_v1.2$, the specific contribution and kinetics of $Na_v1.6$ are still in need of investigation. Attx proved an unreliable tool to investigate this channel in the present study, as applying the toxin had variable effects on the recorded Na^+ transients. We can be confident however that $Na_v1.6$ is not permeable to Ca^{2+}, as the I_{Ca} was unchanged after applying attx. Future development of peptides or toxins able to selectively block activation of $Na_v1.6$ will enable studying their contribution to AP generation in the distal AIS, and their interaction with other channels.

Although we were not able to study the involvement of $Na_v1.6$ in detail using pharmacology, our computational model confirmed previous reports on its localisation in the AIS (Hu et al. 2009). Moreover, the NEURON model of the AIS confirmed the preferential localisation of $Na_v1.2$ in the proximal part of the AIS, where blocking this channel produced a large decrease in the fast component of the I_{Na}. From the completed model of the AIS, we can extrapolate some of the differences in current densities between the proximal and distal AIS (figure 5.1), which are reflected in our experimental results. In the proximal AIS, $Na_v1.2$ contribution to the I_{Na} is higher compared to $Na_v1.6$. However, as VGCCs are also expressed, the contribution of $Na_v1.2$ to the I_{Ca} is relatively small. In addition, BK CAKCs are sparse compared to the distal region, leading to a smaller contribution to the repolarisation of the AP. In the distal AIS, VGCCs are less prevalent, resulting in a larger contribution of $Na_v1.2$ to the I_{Ca}, despite its lower density compared to the proximal AIS. Moreover, the model suggests BK channels are more dense here, making the coupling with $Na_v1.2$ more evident. This is reflected in our experiments where blocking $Na_v1.2$ resulted in a widening of the AP waveform, which was occluded by also blocking BK channels, specifically in distal sites.

This NEURON model can help us at least two-fold. Firstly, it provides insight into the role of $Na_v1.6$, without the pharmacological tools to specifically target the channel, with respect to the other present VG channels. Once blockers become available we will verify the contribution of $Na_v1.6$ in the model. Second, we can

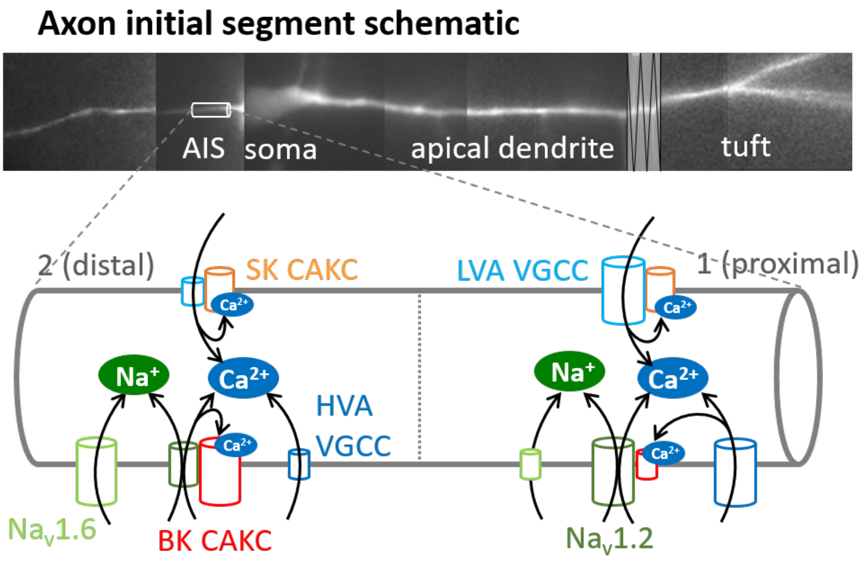

Figure 5.1: Schematic of voltage gated ion channel distributions in the AIS of L5PNs. Top, composed image of L5PN loaded with a calcium indicator. A white rectangle shows the location of the AIS. Bottom, schematic of relevant ion channels present in the NEURON model of the AIS. Arrows indicate the direction of currents, and functionally coupled channels are shown together. The size of the channels relates to the contribution of their respective ionic current to that total current: in the proximal AIS, $Na_v1.2$ contribution to the I_{Na} is higher compared to $Na_v1.6$. However, as VGCCs are also expressed, the contribution of $Na_v1.2$ to the I_{Ca} is relatively small. In addition, BK CAKCs are sparse compared to the distal region, leading to a smaller contribution to the repolarisation of the AP. In the distal AIS, VGCCs are less prevalent, resulting in a larger contribution of $Na_v1.2$ to the I_{Ca}, despite its lower density compared to the proximal AIS. Moreover, the model suggests BK channels are more dense here, making the coupling with $Na_v1.2$ more evident.

use the model to investigate the behaviour of $Na_v1.2$ channels in channelopathies. Following our investigation into the role of $Na_v1.2$ channels during AP generation in the AIS we have become interested in channelopathies caused by $Na_v1.2$ dysfunction. Together with the development of G^1G^4hwtx enabling targeted manipulation of $Na_v1.2$ and our synergistic analysis of the voltage gated channels present in the AIS and dendrite we can now investigate the effect of $Na_v1.2$ mutations on AP generation.

5.3.1 Channelopathies caused by $Na_v1.2$ mutations

In the introduction I already mentioned one importance of studying voltage gated ion channels is their implication in neurological diseases and disorders, examples of which are epilepsy, neuropsychiatric syndromes and neuropathic pain (Catterall et al. 2008; Lorenzon and Beam 2005). The list of channelopathies is long and over the years many mutations in channel genes have been identified, causing a complex array of channel dysfunctions.

Variants in the *SCN2a* gene, which encodes the $\mathrm{Na}_v1.2$ α-subunit, cause a range of neuropathologies, from autism spectrum disorder (ASD) and intellectual disability (ID) to early-onset epilepsy and epileptic encephalopathy (Hedrich et al. 2019) (figure 5.2). Gain of function (GOF) mutations increase the open probability of $\mathrm{Na}_v1.2$, for instance by decreasing the activation threshold, increasing the opening time of the channel or slowing inactivation. This leads to hyper excitability of glutamatergic neurons which may trigger seizures. Severe effects of larger GOF results in neonatal-early infantile developmental and epileptic encephalopathies (NEIDEE). Loss of function (LOF) mutations are associated with late infantile-childhood neurodevelopmental disorders, with different features such as various degrees of ASD and severe ID with or without epilepsy and schizophrenia without epilepsy (Mantegazza et al. 2021). Patients with GOF mutations are treated with non-selective VGNC inhibitors, but often with serious side effects. Sadly, for LOF mutations channel inhibitors only worsen patients' symptoms, and no other therapies are available. A better understanding of the effect of LOF of $\mathrm{Na}_v1.2$ is needed, as well as therapies to restore $\mathrm{Na}_v1.2$ functioning, possibly by stimulating transcription of the *SCN2a* wild-type copy.

Much knowledge on *SCN2a* mutations originates from animal models where mutations have been introduced into their genome (*knocked-in* or KI) or the *Scn2a* gene has been removed or *knocked-out* (KO), mimicking a complete LOF of the channel. Although homozygous *Scn2a* KO ($Scn2a^{-/-}$) mice do not survive the embryonic stage (Ogiwara et al. 2018), heterozygous $Scn2a^{+/-}$ mice show a relatively mild and age-dependent phenotype including short absence-like seizures, autistic/schizophrenic traits and memory dysfunctions (Léna and Mantegazza 2019). From this model we might conclude that the wild-type copy of *Scn2a* is partially able to restore $\mathrm{Na}_v1.2$ functioning. Interestingly, patients with LOF mutations may present with severe ASD and ICDEE, suggesting a larger $\mathrm{Na}_v1.2$ LOF compared to the heterozygous KO mouse. This might point to a dominant effect of the *Scn2a* mutation, affecting the functioning of the wild-type $\mathrm{Na}_v1.2$ variant. On the other hand, in another $Scn2a^{+/-}$ mouse model (Miyamoto et al. 2019) the phenotype is also characterised by epileptic seizures, consistent with hyperexcitability in L5PNs and the opposite to what we would expect in a LOF situation (Spratt et al. 2021). Therefore, transgenic lines carrying specific mutations will be essential to study the pathology of *Scn2a* LOF. Some KI mouse lines have been generated carrying specific GOF mutations, such as the transgenic KI mouse $Scn2a^{Q54}$ with

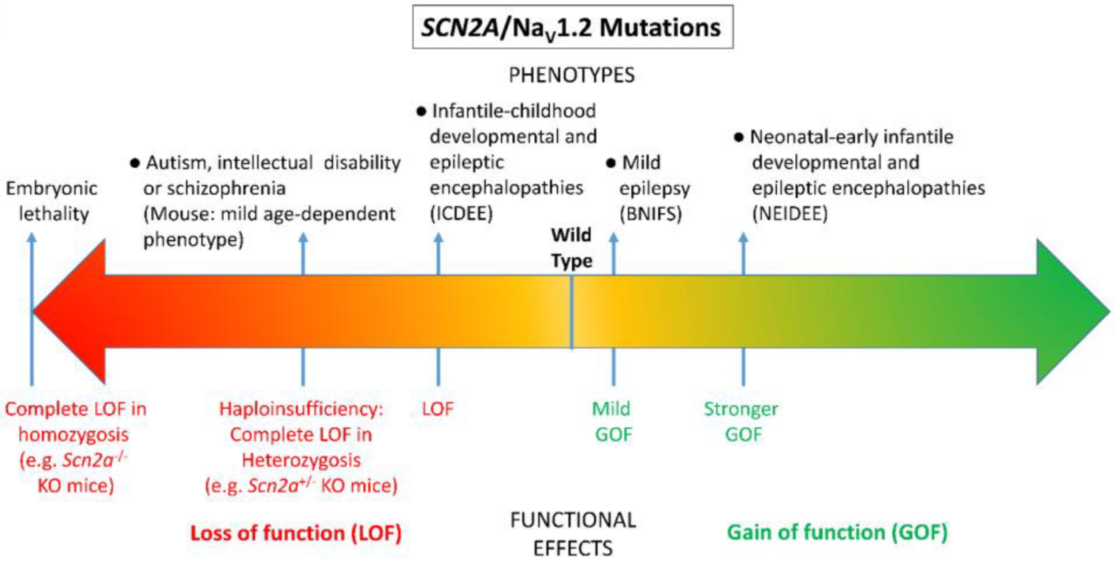

Figure 5.2: Spectrum of mutations and phenotypes for *SCN2a*/Na$_v$1.2. A, Mild gain of function induced by *SCN2a* mutations cause benign neonatal-infantile familial seizures (BNIFS). Larger gain of function mutations cause neonatal-early infantile developmental and epileptic encephalopathies (NEIDEE). Loss of function mutations cause infantile-childhood developmental and epileptic encephalopathies (ICDEE). Haploinsufficiency or complete loss of function in heterozygosis leads to behavioural/cognitive phenotypes without epilepsy such as autism spectrum disorder (ASD), intellectual disability or schizophrenia. Haploinsufficiency in $Scn2a^{+/-}$ mice causes a relatively mild and age-dependent phenotype including short absence-like seizures, autistic/schizophrenic traits and memory dysfunctions. Homozygote $Scn2a^{-/-}$ knock-out mice show embryonic mortality. Figure from Mantegazza et al. (2021).

a GAL879-881QQQ variant resulting in partial seizures (Kearney et al. 2001). Another mouse line carrying the K1422A mutation is characterised by an increase in Ca^{2+} permeability of Na$_v$1.2 and a mix of phenotypes including rare seizures (Echevarria-Cooper et al. 2022). However, as far as we are aware, mouse models carrying a LOF mutation have not yet been generated.

5.4 On the properties of BK CAKCs

In this thesis we uncovered two specific interactions of BK channels, without directly measuring CAKC mediated K^+ currents. In neurons, but not exclusively, BK CAKCs play an important role in regulating resting and action potentials by hyperpolarising the membrane upon activation (Lancaster and Adams 1986; Sah and Davies 2000; Sun et al. 2003). In humans, BK channels are widely expressed in the body including nervous, muscular, skeletal, endocrine, cardiovascular, digestive, urinary, and reproductive systems (Bailey et al. 2019). Dysfunction of BK channels associated with mutations of *KCNMA1*, the gene encoding BK channels, causes a heterogeneous combinations of disorders including seizures, movement disorders, developmental delay and intellectual disability (Bailey et al. 2019). Unfortunately, the consequences of BK channel dysfunction in humans are not well characterised. A global deletion of *Kcnma1* in a mouse model showed the animal is viable, but exhibits pathophysiology in many organs. In addition, $Kcnma1^{-/-}$ mice show motor impairments and present with learning difficulties (Typlt et al. 2013). Contrary to LOF mutations, GOF alterations in BK channel activity have been related to epilepsy in mice. Deletion of the regulatory $\beta 4$ subunit, which slows BK channel activation, produced temporal lobe seizures in mice (Brenner et al. 2005). Also, Shruti et al. (2008) found that induced seizures in mice triggered a GOF in BK CAKCs in PNs in the somatosensory cortex. They also showed BK antagonists normalized neuronal responses to control values, indicating BK channels as a possible target for anti-epileptic therapies.

BK channels are activated by a combination of depolarisation and an elevation of intracellular Ca^{2+} to micromolar levels (Yang et al. 2015), requiring a combination of electrical activity and cytosolic Ca^{2+} influx, as observed during an AP. The high Ca^{2+} concentrations necessary for BK activation are thought to be attained in local micro domains through tight coupling of BK channels to intracellular Ca^{2+} stores and VGCCs (Fakler and Adelman 2008).

In this thesis, we have identified two important sources of Ca^{2+} for BK CAKC activation, $Na_v1.2$ in the AIS and N-type VGCCs in the apical dendrite, adding $Na_v1.2$ channels to the list of possible Ca^{2+} suppliers in BK channel microdomains. This shows that multiple Ca^{2+} sources may exist in one cell, although it remains unclear what determines the coupling of BK channels to their Ca^{2+} source in different cellular compartments. It is known that BK CAKCs are regulated by extensive alternative splicing as well as multiple auxiliary subunits, giving CAKCs both cell and tissue-specific properties (Kyle and Braun 2014; Latorre et al. 2017). Even within the L5PN population, BK expression varies (Guan et al. 2015). Coupling to N-type VGCCs or $Na_v1.2$ channels might therefore be determined by alternative splicing of the channel or through auxiliary subunits. In recent years, various β and γ auxiliary subunits of BK channels have been identified which can modulate activation and inactivation dependencies (Gonzalez-Perez and Lingle 2019). For instance, in the presence of the $\beta 1$ auxiliary subunit, BK channels activate at more negative potentials in the presence of Ca^{2+} (McManus et al. 1995). However, further research will have to gain insight into the exact composition of BK-containing micro domains and the determinants of their Ca^{2+} supply.

5.4.1 BK CAKC and $Na_v1.2$ interaction

In the AIS, $Na_v1.2$ channels mediate Ca^{2+} influx. Importantly, this early Ca^{2+} current occurring with kinetics similar to that of the Na^+ current allows Ca^{2+} binding to its targets before the AP reaches its peak. At the peak of the AP, BK channels contribute to the total K^+ current that counterbalances the non-inactivated Na^+ current, together with the diverse voltage-gated K^+ channels expressed in the AIS (Trimmer 2015). Thus, a decrease of the $Na_v1.2$ current is counterbalanced by a decrease of the BK current, resulting in widening of the early phase of AP repolarisation with a modest change of the AP peak. The interplay between $Na_v1.2$ and BK channels is therefore a major determinant of the AP peak and a key regulator of the AP shape. This is illustrated by the study of Echevarria-Cooper et al. (2022), using the previously mentioned *Scn2a*^{K1422A} mouse line carrying a mutation in the $Na_v1.2$ channel. This mutation causes a simultaneous increase in Ca^{2+} and decrease in Na^+ permeability of $Na_v1.2$. When recording Na^+ currents in cortical PN cultures from these mice, Echevarria-Cooper et al. (2022) observed a decrease in the total current, AP peak and AP frequency compared to wild-type. In addition, when performing Ca^{2+} imaging, they showed an earlier onset of the Ca^{2+} transient only in the proximal AIS, where $Na_v1.2$ expression is high. Specifically, this increase preceded the AP peak, consistent with increased Ca^{2+} influx through $Na_v1.2$ channels. Taken together with the BK channel coupling, an alternative explanation for a decrease in Na^+ current in *Scn2a*^{K1422A} neurons might be due to a stronger activation of BK CAKCs, driving voltage dependent inactivation of $Na_v1.2$ channels. This mouse model could help us better understand what determines the Ca^{2+} permeability of $Na_v1.2$.

Another unknown facet of BK-$Na_v1.2$ interaction is their coupling at a molecular level. The AIS is a complex structure with a unique scaffolding proteome (Leterrier 2016). $Na_v1.2$ channels are known to interact with ankyrin G, which increases the density of the channel in the AIS (Leterrier 2018). Not much is known about BK recruitment in the AIS. However, BK CAKCs co-localise with an ankyrin-repeat containing protein in axonal segments (Lim and Park 2005), suggesting ankyrin might interact with the channel, thereby recruiting it in the AIS. However, this mechanism is still poorly understood and requires further investigation.

5.4.2 BK CAKC and N-type VGCC interaction

In the apical dendrite we show N-type VGCCs supply Ca^{2+} for the activation of BK CAKCs. Co-assembly of BK CAKCs with various VGCCs, specifically P/Q-type, N-type and L-type, had been shown before in heterologues expression systems (Berkefeld et al. 2006; Grunnet and Kaufmann 2004; Loane et al. 2007). Berkefeld et al. (2006) showed that adding Ca^{2+}-buffering BAPTA in said system interfered with the coupling but EGTA did not. Showing that Ca^{2+} binding to BK channels was faster than EGTA-Ca^{2+} binding but slower than buffering by BAPTA. Taking into account estimated channel conductances, channel size and Ca^{2+}-binding properties of BAPTA and EGTA, a likely scenario is therefore that coupling is predominantly mediated by the α subunits. While heterologous expression does not reflect the physiological situation, it shows α subunits of BK CAKCs and some VGCCs can interact. Consistent with this, Sun et al. (2003) showed that BK CAKCs are activated both by L-type and N-type VGCCs in whole-cell patch-clamp recordings from freshly dissociated neocortical PNs.

The close interaction between the Ca^{2+} source and BK CAKCs implies not only selective coupling, but also the ability of activation of the K^+ channel at sub-millisecond time scale (Berkefeld et al. 2006). The kinetics of activation and deactivation of VGCCs, however, is of the order of 1 ms (Kay and Wong 1987) introducing the hypothesis of faster activation kinetics for BK CAKCs. While investigating the effect of blocking BK channels on the AP waveform we find that AP widening occurs before we can detect the inflowing Ca^{2+} through N-type VGCCs, in the 500 µs directly after the bAP peak. The fact that the AP widening occurs when only a fraction of inflowing Ca^{2+} via N-type VGCCs is detected indicates that BK channels are activated before the I_{Ca} peaks. This current anticipating effect suggests a physical interaction between N-type VGCCs and the BK CAKCs at nanoscopic domain (Shah et al. 2022).

A possibility to verify this is to investigate the physical coupling through Fluorescence Resonance Energy Transfer (*FRET*). This technique uses the emission of one fluorophore (the donor) to excite a second fluorophore (the acceptor). For FRET to occur the donor and acceptor have to be at a maximum distance of 10 nm. By tagging N-type VGCCs and BK CAKCs with a donor-acceptor fluorophore pair we will be able to determine whether these channels are spatially less than 10 nm away from each other. Although never performed before, the channel-targeted fluorophores will be introduced through the patch pipette in our usual preparation. This would allow recording from the apical dendrite in identified L5 single neurons.

5.5 VGCCs in the apical dendrite during AP back propagation

In the introduction I stated that bAPs act as retrograde messengers informing the input of a neuron about its output. This role seems particularly strong in L5PNs, as bAPs ∼100 µm from the soma attenuate little, increasing the chance of the bAP reaching the tuft and distal dendrites in layer 1.

In chapter 4, I confirm that VGCCs drive the increase of cytosolic Ca^{2+}. This Ca^{2+} is coupled to the activation of diverse CAKCs, creating a system of VGCC-CAKC driven modulation. Specifically, we analysed the bAP and the associated Ca^{2+} transient at 50 µs time resolution in the apical dendrite of L5PNs, and we correlated the kinetics of the AP waveform with that of the Ca^{2+} current. Importantly, BK CAKCs contributes to the bAP repolarisation before the peak of the Ca^{2+} current. The NEURON model we built to reproduce these effects confirmed that the anticipation of this Ca^{2+}-triggered phenomenon, with respect to the Ca^{2+} that generates it, can be only explained if the Ca^{2+} source and its target physically interact. Therefore the full activation of the target, BK CAKCs, occurs before the Ca^{2+} equilibration in the cytosol, which is eventually governed by the slope of the Ca^{2+} current. The first important biophysical consequence of this finding is that only a fraction of the initial Ca^{2+} influx from a particular source can trigger a process, whereas the rest of the Ca^{2+} contributes to the increase of intracellular Ca^{2+} concentration. The second important consequence is that, in this way, a VGCC can down-regulate the global Ca^{2+} influx because it can change the V_m profile during the opening phase of the other VGCCs. This means that VGCCs can modulate each other through their coupling to CAKCs, as we observed through the blocking of N-type channels which increased the recruitment of other VGCCs. Besides, the activation of VGCCs alters the cytosolic Ca^{2+} concentration, which influences the Ca^{2+} driving force, and therefore when one VGCC is blocked this influences the contributions of the other channels.

Depending on their kinetics, VGCC subtypes have different effects on the V_m and I_{Ca}, which is well illustrated by L-type and T-type channels. Although blocking L-type and T-type VGCCs had the largest effect on the Ca^{2+} current, only when blocking L-type VGCCs we observed a decrease in the bAP after-hyperpolarisation. Indicating a functional coupling with CAKCs strong enough to counterbalance the large Ca^{2+} current mediated by L-type VGCCs. Controversially, blocking T-type channels decreased the bAP peak, suggesting a specific role for T-type channels in Ca^{2+}-mediated excitability. The decrease in the peak of the bAP was measured

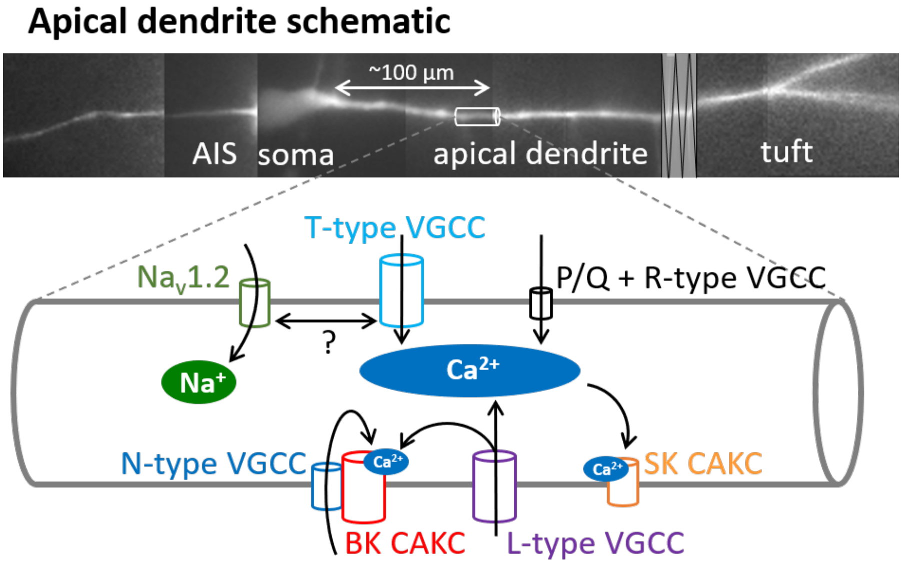

Figure 5.3: Schematic of voltage gated ion channel distributions in the apical dendrite of L5PNs. The size of the channels loosely reflects their relative contribution to their respective ionic current. BK channels are coupled to N-type channels, whereas SK CAKCs are activated by cytosolic Ca^{2+} supplied by the other VGCCs. In the NEURON model described in chapter 4, BK CAKCs receive Ca^{2+} from N-type and L-type VGCCs. The coupling between N-type channels however, is stronger compared to L-type channels. Another important difference is that L-type VGCCs also supply Ca^{2+} for SK activation, together with P/Q-type, R-type and T-type channels.

before the expected peak of the I_{Ca}. This is remarkable, as T-type channels are responsible for a large part of that current. T-type VGCCs seem to have a strong depolarising effect, which is dampened when blocked. Preliminary data shows this is similar to the effect of G^1G^4hwtx on the bAP in the apical dendrite (data not shown). Therefore, we proposed an interaction with $Na_v1.2$ channels. If T-type VGCCs interact with $Na_v1.2$ channels in the dendrite this would directly link T-type channels to excitability. To investigate this, the first step would be to confirm our block of T-type VGCCs using different drugs and compare the blocking effects.

Figure 5.3 shows a schematic with the ion channels studied in Chapter 4, based on our NEURON model of a short section of the apical dendrite ~100 µm from the soma. As in figure 5.1, the size of the channels reflects their relative contribution to their respective ionic current. BK channels are coupled to N-type channels, whereas SK CAKCs are activated by cytosolic Ca^{2+} supplied by the other VGCCs. In the NEURON model described in chapter 4, BK CAKCs receive Ca^{2+} from N-type and L-type VGCCs. The coupling between N-type channels however, is stronger compared to L-type channels. Another important difference is that L-type VGCCs also supply Ca^{2+} for SK activation, together with P/Q-type, R-type and T-type channels. Although it reproduces the BK-N-type channel interaction, the model is preliminary, and needs optimising. Firstly, simulating the block of both SK and L-type channel should have bigger effects. In addition, simulating the BK CAKC block has a small AHP effect that is not observed experimentally, due to a larger involvement of SK CAKCs following increased VGCC activation. Lastly, the model does not reproduce the effects of blocking T-type VGCCs. We have not focused on this, as we hypothesise an interaction with $Na_v1.2$ channels, which needs further experimental investigation before we can model it.

We recorded Ca^{2+} transients and their effect on excitability ∼100 µm from the soma, but we cannot confirm similar roles for VGCCs and CAKCs in distal parts of the dendrite. For example, while recording Ca^{2+} transients in L5PNs, Bock and Stuart (2016) did not observe the interaction between N-type and BK channels in the distal apical dendrite. Nevertheless, the tuft of L5PNs is a structure with unique properties, such as the ability to sustain Ca^{2+} electrogenesis (Larkum et al. 1999a). We are interested in investigating the role of N-type and T-type VGCCs during Ca^{2+} electrogenesis specifically, due to their unique contributions to the bAP. N-type channels because of their coupling to BK CAKCs and T-type channels as they seem directly related to the excitability of the dendrite.

5.5.1 Ca^{2+} electrogenesis and plasticity at the tuft of the apical dendrite

At the tuft, Ca^{2+} electrogenesis can occur when a train of bAPs with a critical frequency arrive at the tuft and cause a Ca^{2+} spike larger than the summation of Ca^{2+} entry triggered by single bAPs (Larkum et al. 1999a): whereas a single bAP attenuates, a train causes a regenerative potential, driven by VGCCs. This phenomenon is also observed in basal dendrites, where there is a marked difference between single APs and an AP burst. In distal basal dendrites a train of bAPs also triggers a Ca^{2+} spike, whereas single bAPs attenuate. Here, their ability to invade distal projections is regulated by fast-inactivating A-type VGKCs (Kampa and Stuart 2006).

We observed this phenomenon in our experiments (figure 5.4), although we did not record from a high enough number of cells to perform proper statistical analyses. We can, however, observe and speculate. In the examples shown in figure 5.4 we recorded OG5N fluorescence at the tuft of L5PNs (figure 5.4A) after a train of three action potentials triggered at the soma. Preliminary, we found that the Ca^{2+} spike during electrogenesis is indeed more than the summation of the Ca^{2+} spike from a single bAP, which is often very small in the tuft. A clear example of this is from cell

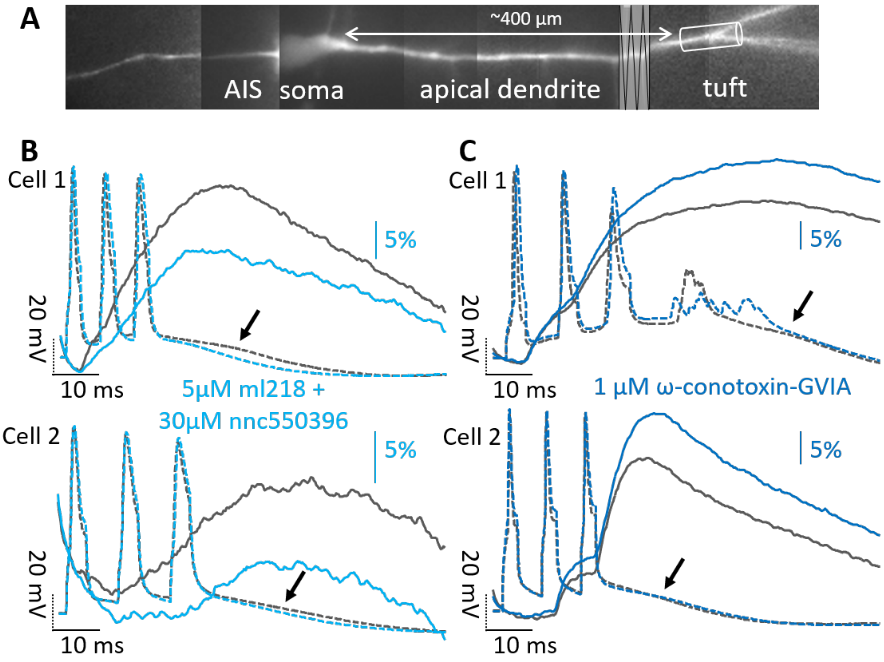

Figure 5.4: The effect of blocking N-type or T-type VGCCs on Ca^{2+} electrogenesis. A, Example L5PN loaded with OG5N, tuft indicated. B,C, L5PNs were loaded with OG5N and non-bleach-corrected Ca^{2+} transients (solid lines) were recorded at the dendritic tuft after triggering three APs at the soma (dotted lines) by current injection through the patch pipette before (grey traces) and after applying 5µM ml218 + 30µM nnc550396 (light blue traces) to block T-type VGCCs (B) or 1 µM ω-conotoxin-GVIA (dark blue traces) to block N-type VGCCs (C).

2 in figure 5.4C, where the first bAP does not trigger visible Ca^{2+} influx, but the second and third bAP drive a large Ca^{2+} spike, increasing indicator fluorescence with 20-30%. This electrogenesis is also measured at the soma through the patch pipette as after-depolarisations indicated by the arrows in figure 5.4.

When we block T-type channels the Ca^{2+} transient is decreased and resembles a simple summation of the Ca^{2+} entry triggered by three bAPs (figure 5.4B). The block of electrogenesis can also be seen in the increase of the AHP after the last AP from the electrophysiology trace (indicated by arrows in figure 5.4B). This was consistently observed in 4 cells tested, providing support for T-type VGCCs as drivers of excitability. Clearly, they play an important role in AP back propagation and Ca^{2+} electrogenesis.

In contrast, when blocking N-type VGCCs we observed an increase in the Ca^{2+} transient (two examples in figure 5.4C). This is however in accordance with our conclusion that N-type VGCCs are functionally coupled to BK CAKCs, and suggests this coupling is also relevant in the tuft. If this case, N-type VGCCs could indirectly dampen Ca^{2+} electogenesis by promoting BK CAKC activation, which is opposite to the effect of T-type channels. This increase in electrogenesis was observed in 3/4 cells tested this way, in contrast to measurements from Bock and Stuart (2016), who did not observe this distinct coupling.

These preliminary results suggest both T-type and N-type VGCCs play important roles during Ca^{2+} electrogenesis. Nevertheless, the synergy among VGCCs and K^{+} channels remains to be investigated during this phenomenon. Although the function of Ca^{2+} electrogenesis itself remains poorly understood, it has been shown that distal Ca^{2+} influx is necessary for LTD induction during STDP (Hamilton et al. 2013).

STDP is characterised by the precise timing between APs in presynaptic and postsynaptic neurons (Inglebert and Debanne 2021). This phenomenon is strongly dependent on intracellular Ca^{2+} influx for its induction, as buffering postsynaptic Ca^{2+} prevents both LTP and LTD (Nevian and Sakmann 2006).

LTP is dependent on NMDA receptor-mediated Ca^{2+} influx, which fits with the observation that incoming synaptic potentials are unable to drive Ca^{2+} spikes at distal sites without NMDA receptor activation (Larkum et al. 2009). However, NMDA receptor-independent mechanisms for LTD have been proposed. Examples include metabotropic glutamate receptors, VGCCs and cannabinoid receptors. This provides a role for Ca^{2+} electrogenesis at the tuft, which depends specifically on bAP-driven VGCC activation.

LTD occurs when postsynaptic firing, for example in the form of bAPs, repeatedly precedes presynaptic firing during an STDP event (Tazerart et al. 2020; Zilberter et al. 2005). This is thought to be driven by dendritic release of endocannabinoids in L5PNs (Sjöström et al. 2004). Sjöström et al. (2003) propose a mechanism in L5PNs where postsynaptic activity triggers Ca^{2+}-driven endocannabinoid release, which activates presynaptic cannabinoid receptors. If at the same time presynaptic glutamate release activates presynaptic NMDA receptors, LTD occurs by reducing subsequent presynaptic neurotransmitter release.

One study investigating the role of VGCCs during LTP in layer 2/3 PNs, found that blocking postsynaptic L-type VGCCs partially blocked LTP (Bender 2006). However, when blocking T-type VGCCs they blocked LTP completely, suggesting these channels are required for this type of plasticity. Although many Ca^{2+} targets during STDP remain elusive, the above hints at an important role of Ca^{2+} electrogenesis in plasticity, specifically during LTD. It also seems multiple VGCCs are involved in driving the essential Ca^{2+} influx during LTD, with possibly a central role for T-type VGCCs. Nevertheless, it remains to be investigated if this is the case in L5PNs as it is in L2/3 neurons.

5.6 Anterograde action potential propagation and neuronal firing

The process of AP generation starts with a sub-threshold depolarisation that spreads from the soma (or physiologically from the dendrites through the soma) to the AIS. The observation of an early subthreshold component of the Na^+ influx (Filipis and Canepari 2021) indicates that VGNCs also contribute to amplify the axonal depolarisation before the AP onset (Goldwyn et al. 2019). The early Ca^{2+} current, which closely follows the early Na^+ current, through $Na_v1.2$ channels is crucial since BK CAKCs require concomitant Ca^{2+} binding and depolarisation in order to open (Cui et al. 2009). After generation, the AP propagates along the axonal branches, regenerates at Ranvier nodes, and the waveform at synaptic terminals regulates neurotransmitter release providing an analog modulation of synaptic transmission (Rama et al. 2018). The AP is amplified at each node of Ranvier by clusters of VGNCs. At adult nodes of Ranvier VGNCs clusters are mainly composed of $Na_v1.6$ channels (Kaplan et al. 2001). This would suggest that the coupling of $Na_v1.2$ and BK channels is of importance in the AIS specifically during AP generation, but not during axonal anterograde propagation.

Eventually, the AP waveform in the AIS sets the way in which a neuron can respond to prolonged depolarisation by firing several APs at high frequencies, determining the ability of the neuron to encode signals (Kole and Stuart 2012). The shape of the AP at its site of origin is therefore the starting point of the consequent physiological processes occurring at the other sites of the cells. First, the AP waveform, modulated during propagation along the axons, regulates neurotransmitter release and therefore synaptic transmission at synaptic terminals, in this way providing an analogue component of the digital information process (Rama et al. 2015). Second, the AP waveforms regulate neuronal firing. Interestingly, in CA1 hippocampal pyramidal neurons, it has been shown that BK CAKCs facilitate high-frequency firing and cause early spike frequency adaptation (Gu et al. 2007). The regulation of the firing frequency is crucial for the coupling among the different sites of the cell that are believed to underlie conscious processing (Aru et al. 2020) and, in L5 pyramidal neurons, high-frequency bursts of APs back-propagate along the apical dendrite reaching the tuft and provoking Ca^{2+} electrogenesis (Larkum et al. 1999a), confirming that the dendrites of L5PNs are highly electrogenic and heavily influence spiking output (Larkum et al. 2009). In the apical dendrite BK CAKCs are selectively activated by N-type VGCCs. This activation is rapid and is not linear with the increase of intracellular Ca^{2+} concentration associated with the transient activation of VGCCs. Thus, the blockade of N-type VGCCs widens the AP peak prolonging Ca^{2+} entry through the other VGCCs and boosting the increase of intracellular Ca^{2+} concentration associated with the AP. In other words, BK CAKCs activation by N-type VGCCs anticipates the full activation of VGCCs, which provided a negative feedback to the Ca^{2+} current. Although we show the existence of this coupling during AP back propagation, it is plausible the same interaction is functional during anterograde propagation. In that case, activation of N-tpye VGCCs could limit depolarisation during PSPs by activating BK channels, thereby effectively shunting said PSP. To preliminary test the importance of the interaction between N-type and BK channels we can simulate synaptic input to the oblique dendrites, using the computational model described in chapter 4, and analyse the response of the neuron with and without coupling BK CAKCs and N-type VGCCs.

5.7 Importance of sub-microsecond activation of Ca^{2+} binding proteins

We showed that upon cell entry, Ca^{2+} targets Ca^{2+}-activated proteins, such as BK channels, at sub millisecond speed during bAPs. bAPs are important modulators of excitability by lowering or increasing the threshold for incoming synaptic potentials. As just highlighted, much of the plasticity driven by bAPs is dependent on Ca^{2+} influx.

The ability of Ca^{2+} to activate a target within microseconds is allowed by local Ca^{2+} nanodomains, including VGCCs, Ca^{2+} binding proteins and other auxiliary proteins (Heck et al. 2021). Their efficacy has been shown at synaptic terminals where VGCCs are coupled with neurotransmitter release proteins to trigger synaptic transmission (Gandini and Zamponi 2022). Localized BK channel activity can modulate both the amplitude and duration of depolarization-evoked Ca^{2+} entry as a result of the rapid repolarization and deactivation of voltage-gated P/Q-type and N-type VGCCs (Fakler and Adelman 2008). In turn, reduced Ca^{2+} influx will limit vesicle fusion at active zones, leading to decreased neurotransmitter release (Kyle and Braun 2014).

Less is known about Ca^{2+} nanodomains in postsynaptic spines of L5PNs. However, BK CAKCs have been identified in dendritic spines, although their activity is only detected in small head volume spines (Tazerart et al. 2022). Interestingly, Ca^{2+} influx in spines with small head volume is significantly larger compared to spines with a larger volume. BK channels in these spines are activated by synaptic Ca^{2+}, their role being to down-regulate the amplitude of the excitatory

PSP. Hence, if the activation of BK CAKCs by N-type VGCCs is maintained in those spines and occurs before synaptic activity, this might prevent the further BK channel activation by synaptic Ca^{2+}, leading to a modulation of the synaptic input. For the regulation of the cytosolic Ca^{2+} elevation in the dendritic bulk, which is reported in this study, this might play a role in the Ca^{2+} modulation of proteins that intervene during firing activity.

CAKCs are coupled targets of VGCCs and at least BK channels can activate at sub-millisecond time scale. This regulates the shape of the AP near its peak and, as a consequence, modulates the other voltage-dependent conductance including VGCCs, eventually translating into a regulation of the cytosolic Ca^{2+} transient. The functional meaning of the sub-millisecond activation of BK CAKCs leading to a regulation of the cytosolic Ca^{2+} transient remains elusive.

5.8 Future perspectives

The research described in this thesis leads to new questions which I have introduced above. First of all, we can use our current findings to investigate how channel kinetics are disrupted in channelopathies, specifically a LOF of *Scn2a* encoding $Na_v1.2$ channels in the AIS. To start characterising the effect of *Scn2a* LOF in L5PNs, we will perform the experiments described in chapter 3 using the $Scn2a^{+/-}$ mouse line. We will cross-correlate our findings and the effect on AP generation with the AIS model to verify the model itself and make predictions on $Na_v1.2$ expression patterns in the AIS of the KO mouse. To this end, we can use our knowledge on Ca^{2+} entry through $Na_v1.2$. As we know the percentage of the $Na_v1.2$-mediated Ca^{2+} transient, we can investigate any LOF $Na_v1.2$ compensation mechanisms. This research will be funded by the recently awarded ANR (agence nationale de la recherche) grant entitled *Nav12RESCUE*. The objectives of this project are to develop drugs and strategies for counteracting reduced $Na_v1.2$ function and dominant LOF mutations, which are unavailable at this moment. In addition, a new $Na_v1.2$ LOF mouse model will be generated, to study pathological mechanisms as described above and test effects of treatments.

Second, we will make an effort to show physical coupling of N-type VGCCs and BK CAKCs in the apical dendrite. To this end we will use the FRET technique discussed above. Other methods to verify the physical coupling between BK and N-type channels include expansion microscopy, where the sample is expanded to be able to identify co-localisations in tissues with dense expression of the protein of interest. Alternatively, proximity ligation assay technology uses a pair of labelled antibodies which, when localised within 40 nm catalyse an amplification reaction to generate a fluorescent signal. Due to this amplification, this enables visualising single interactions. In these examples the challenge remains to identify dendrites of L5PNs specifically, which in slices is not straightforward.

Lastly, we are intrigued by the apparent role of T-type VGCCs in excitability of the apical dendrite. We plan to confirm our V_m imaging observations, in the proximal apical dendrite as well as in the tuft, all supported by NEURON modelling. In addition, we could perform a series of occlusion experiments to verify whether blocking either $Na_v1.2$ or T-type channels occludes the effect of then blocking the other channel. Also, to test excitability, we could determine the attenuation of the bAP towards the tuft after applying T-type or $Na_v1.2$ channel blockers on the apical dendrite closer to the soma. Moreover, we would investigate the role of T-type and other VGCCs in Ca^{2+} electrogenesis. This would further our understanding about the role of VGCCs in excitability, Ca^{2+} electrogenesis and plasticity.

Bibliography

Agwa, A. J. et al. (2020). “Manipulation of a Spider Peptide Toxin Alters Its Affinity for Lipid Bilayers and Potency and Selectivity for Voltage-Gated Sodium Channel Subtype 1.7”. *Journal of Biological Chemistry* 295.15, pp. 5067–5080. DOI: `10.1074/jbc.RA119.012281`.

Ait Ouares, K., Filipis, L., Tzilivaki, A., Poirazi, P., and Canepari, M. (2019). “Two Distinct Sets of Ca $^{2+}$ and K $^{+}$ Channels Are Activated at Different Membrane Potentials by the Climbing Fiber Synaptic Potential in Purkinje Neuron Dendrites”. *The Journal of Neuroscience* 39.11, pp. 1969–1981. DOI: `10.1523/JNEUROSCI.2155-18.2018`.

Ait Ouares, K., Jaafari, N., and Canepari, M. (2016). “A Generalised Method to Estimate the Kinetics of Fast Ca2+ Currents from Ca2+ Imaging Experiments”. *Journal of Neuroscience Methods* 268, pp. 66–77. DOI: `10.1016/j.jneumeth.2016.05.005`.

Almog, M. and Korngreen, A. (2014). “A Quantitative Description of Dendritic Conductances and Its Application to Dendritic Excitation in Layer 5 Pyramidal Neurons”. *Journal of Neuroscience* 34.1, pp. 182–196. DOI: `10.1523/JNEUROSCI.2896-13.2014`.

Almog, M. and Korngreen, A. (2009). “Characterization of Voltage-Gated Ca2+ Conductances in Layer 5 Neocortical Pyramidal Neurons from Rats”. *PLoS ONE* 4.4, e4841. DOI: `10.1371/journal.pone.0004841`.

Andreone, B. J., Lacoste, B., and Gu, C. (2015). “Neuronal and Vascular Interactions”. *Annual Review of Neuroscience* 38.1, pp. 25–46. DOI: `10.1146/annurev-neuro-071714-033835`.

Antic, S. D. (2003). “Action Potentials in Basal and Oblique Dendrites of Rat Neocortical Pyramidal Neurons”. *The Journal of Physiology* 550.1, pp. 35–50. DOI: `10.1113/jphysiol.2002.033746`.

Antic, S. D., Major, G., and Zecevic, D. (1999). “Fast Optical Recordings of Membrane Potential Changes From Dendrites of Pyramidal Neurons”. *Journal of Neurophysiology* 82.3, pp. 1615–1621. DOI: `10.1152/jn.1999.82.3.1615`.

Armstrong, C. M. (1981). “Sodium Channels and Gating Currents.” *Physiological Reviews* 61.3, pp. 644–683. DOI: `10.1152/physrev.1981.61.3.644`.

Aru, J., Suzuki, M., and Larkum, M. E. (2020). “Cellular Mechanisms of Conscious Processing”. *Trends in Cognitive Sciences* 24.10, pp. 814–825. DOI: `10.1016/j.tics.2020.07.006`.

Astman, N. (2006). “Persistent Sodium Current in Layer 5 Neocortical Neurons Is Primarily Generated in the Proximal Axon”. *Journal of Neuroscience* 26.13, pp. 3465–3473. DOI: `10.1523/JNEUROSCI.4907-05.2006`.

Bailey, C. S., Moldenhauer, H. J., Park, S. M., Keros, S., and Meredith, A. L. (2019). “KCNMA1-linked Channelopathy”. *The Journal of General Physiology* 151.10, pp. 1173–1189. DOI: `10.1085/jgp.201912457`.

Battefeld, A., Tran, B. T., Gavrilis, J., Cooper, E. C., and Kole, M. H. P. (2014). "Heteromeric Kv7.2/7.3 Channels Differentially Regulate Action Potential Initiation and Conduction in Neocortical Myelinated Axons". *Journal of Neuroscience* 34.10, pp. 3719–3732. DOI: `10.1523/JNEUROSCI.4206-13.2014`.

Bekkers, J. M. (2000). "Distribution and Activation of Voltage-gated Potassium Channels in Cell-attached and Outside-out Patches from Large Layer 5 Cortical Pyramidal Neurons of the Rat". *The Journal of Physiology* 525.3, pp. 611–620. DOI: `10.1111/j.1469-7793.2000.t01-2-00611.x`.

Bender, V. A. (2006). "Two Coincidence Detectors for Spike Timing-Dependent Plasticity in Somatosensory Cortex". *Journal of Neuroscience* 26.16, pp. 4166–4177. DOI: `10.1523/JNEUROSCI.0176-06.2006`.

Beneski, D. A. and Catterall, W. A. (1980). "Covalent Labeling of Protein Components of the Sodium Channel with a Photoactivable Derivative of Scorpion Toxin." *Proceedings of the National Academy of Sciences* 77.1, pp. 639–643. DOI: `10.1073/pnas.77.1.639`.

Benhassine, N. and Berger, T. (2005). "Homogeneous Distribution of Large-Conductance Calcium-Dependent Potassium Channels on Soma and Apical Dendrite of Rat Neocortical Layer 5 Pyramidal Neurons: BK Channel in Layer 5 Pyramidal Neurons". *European Journal of Neuroscience* 21.4, pp. 914–926. DOI: `10.1111/j.1460-9568.2005.03934.x`.

— (2009). "Large-Conductance Calcium-Dependent Potassium Channels Prevent Dendritic Excitability in Neocortical Pyramidal Neurons". *Pflügers Archiv - European Journal of Physiology* 457.5, pp. 1133–1145. DOI: `10.1007/s00424-008-0569-3`.

Bereshpolova, Y., Amitai, Y., Gusev, A. G., Stoelzel, C. R., and Swadlow, H. A. (2007). "Dendritic Backpropagation and the State of the Awake Neocortex". *Journal of Neuroscience* 27.35, pp. 9392–9399. DOI: `10.1523/JNEUROSCI.2218-07.2007`.

Berkefeld, H. et al. (2006). "BKCa-Cav Channel Complexes Mediate Rapid and Localized Ca2+-Activated K+ Signaling". 314, p. 6.

Blömer, L. A., Canepari, M., and Filipis, L. (2021a). "Ultrafast Sodium Imaging of the Axon Initial Segment of Neurons in Mouse Brain Slices". *Current Protocols* 1.3. DOI: `10.1002/cpz1.64`.

Blömer, L. A., Filipis, L., and Canepari, M. (2021b). "Cal-520FF Is the Present Optimal Ca2+ Indicator for Ultrafast Ca2+ Imaging and Optical Measurement of Ca2+ Currents". *Journal of Fluorescence* 31.3, pp. 619–623. DOI: `10.1007/s10895-021-02701-8`.

Bloodgood, B. L. and Sabatini, B. L. (2007). "Nonlinear Regulation of Unitary Synaptic Signals by CaV2.3 Voltage-Sensitive Calcium Channels Located in Dendritic Spines". *Neuron* 53.2, pp. 249–260. DOI: `10.1016/j.neuron.2006.12.017`.

Bock, T., Honnuraiah, S., and Stuart, G. J. (2019). "Paradoxical Excitatory Impact of SK Channels on Dendritic Excitability". *The Journal of Neuroscience* 39.40, pp. 7826–7839. DOI: `10.1523/JNEUROSCI.0105-19.2019`.

Bock, T. and Stuart, G. J. (2016). "The Impact of BK Channels on Cellular Excitability Depends on Their Subcellular Location". *Frontiers in Cellular Neuroscience* 10, p. 206. DOI: `10.3389/fncel.2016.00206`.

Bond, C. T., Herson, P. S., Strassmaier, T., Hammond, R., Stackman, R., Maylie, J., and Adelman, J. P. (2004). "Small Conductance Ca2+-Activated K+ Channel Knock-out Mice Reveal the Identity of Calcium-Dependent Afterhyperpolarization Currents".

The Journal of Neuroscience: The Official Journal of the Society for Neuroscience 24.23, pp. 5301–5306. DOI: `10.1523/JNEUROSCI.0182-04.2004`.

Bond, C. T., Maylie, J., and Adelman, J. P. (1999). "Small-Conductance Calcium-Activated Potassium Channels". *Annals of the New York Academy of Sciences* 868 (1 MOLECULAR AND), pp. 370–378. DOI: `10.1111/j.1749-6632.1999.tb11298.x`.

Bosmans, F., Rash, L., Zhu, S., Diochot, S., Lazdunski, M., Escoubas, P., and Tytgat, J. (2006). "Four Novel Tarantula Toxins as Selective Modulators of Voltage-Gated Sodium Channel Subtypes". *Molecular Pharmacology* 69.2, pp. 419–429. DOI: `10.1124/mol.105.015941`.

Bourgault, S., Létourneau, M., and Fournier, A. (2007). "Development of Photolabile Caged Analogs of Endothelin-1". *Peptides* 28.5, pp. 1074–1082. DOI: `10.1016/j.peptides.2007.02.013`.

Bourinet, E., Soong, T. W., Sutton, K., Slaymaker, S., Mathews, E., Monteil, A., Zamponi, G. W., Nargeot, J., and Snutch, T. P. (1999). "Splicing of a1A Subunit Gene Generates Phenotypic Variants of P- and Q-type Calcium Channels". *nature neuroscience* 2.5, p. 9.

Bowman, W. C. (1990). "Excitable Membranes". *Pharmacology of Neuromuscular Function.* Elsevier, pp. 8–35. DOI: `10.1016/B978-0-7236-0913-1.50006-2`.

Brenner, R., Chen, Q. H., Vilaythong, A., Toney, G. M., Noebels, J. L., and Aldrich, R. W. (2005). "BK Channel Beta-4 Subunit Reduces Dentate Gyrus Excitability and Protects against Temporal Lobe Seizures". *Nature Neuroscience* 8.12, pp. 1752–1759. DOI: `10.1038/nn1573`.

Brown, B. M., Shim, H., Christophersen, P., and Wulff, H. (2020). "Pharmacology of Small- and Intermediate-Conductance Calcium-Activated Potassium Channels". *Annual Review of Pharmacology and Toxicology* 60.1, pp. 219–240. DOI: `10.1146/annurev-pharmtox-010919-023420`.

Brown, D. A. and Passmore, G. M. (2009). "Neural KCNQ (Kv7) Channels: Neural KCNQ (Kv7) Channels". *British Journal of Pharmacology* 156.8, pp. 1185–1195. DOI: `10.1111/j.1476-5381.2009.00111.x`.

Buchanan, K. A., Blackman, A. V., Moreau, A. W., Elgar, D., Costa, R. P., Lalanne, T., Tudor Jones, A. A., Oyrer, J., and Sjöström, P. J. (2012). "Target-Specific Expression of Presynaptic NMDA Receptors in Neocortical Microcircuits". *Neuron* 75.3, pp. 451–466. DOI: `10.1016/j.neuron.2012.06.017`.

Burbidge, S. A., Dale, T. J., Powell, A. J., Whitaker, W. R., Xie, X. M., Romanos, M. A., and Clare, J. J. (2002). "Molecular Cloning, Distribution and Functional Analysis of the NAV1.6. Voltage-gated Sodium Channel from Human Brain". *Molecular Brain Research* 103.1-2, pp. 80–90. DOI: `10.1016/S0169-328X(02)00188-2`.

Canepari, M., Djurisic, M., and Zecevic, D. (2007). "Dendritic Signals from Rat Hippocampal CA1 Pyramidal Neurons during Coincident Pre- and Post-Synaptic Activity: A Combined Voltage- and Calcium-Imaging Study". *The Journal of Physiology* 580 (Pt. 2), pp. 463–484. DOI: `10.1113/jphysiol.2006.125005`.

Canepari, M. and Ogden, D. (2006). "Kinetic, Pharmacological and Activity-Dependent Separation of Two Ca $^{2+}$ Signalling Pathways Mediated by Type 1 Metabotropic Glutamate Receptors in Rat Purkinje Neurones: Divergent mGluR1 Signalling in Purkinje Neurones". *The Journal of Physiology* 573.1, pp. 65–82. DOI: `10.1113/jphysiol.2005.103770`.

Canepari, M., Vogt, K., Willadt, S., and Zecevic, D. (2010). “Subcellular Resolution Recordings of Inhibitory Postsynaptic Potentials via Voltage-Sensitive Dye Imaging”. *Frontiers in Cellular Neuroscience* 4. DOI: `10.3389/conf.fnins.2010.15.00024`.

Catterall, W. A. (2000). “From Ionic Currents to Molecular Mechanisms: The Structure and Function of Voltage-Gated Sodium Channels”. *Neuron* 26.1, pp. 13–25. DOI: `10.1016/s0896-6273(00)81133-2`.

— (2017). “Forty Years of Sodium Channels: Structure, Function, Pharmacology, and Epilepsy”. *Neurochemical Research* 42.9, pp. 2495–2504. DOI: `10.1007/s11064-017-2314-9`.

Catterall, W. A., Dib-Hajj, S., Meisler, M. H., and Pietrobon, D. (2008). “Inherited Neuronal Ion Channelopathies: New Windows on Complex Neurological Diseases”. *Journal of Neuroscience* 28.46, pp. 11768–11777. DOI: `10.1523/JNEUROSCI.3901-08.2008`.

Catterall, W. A., Goldin, A. L., and Waxman, S. G. (2005a). “International Union of Pharmacology. XLVII. Nomenclature and Structure-Function Relationships of Voltage-Gated Sodium Channels”. *Pharmacological Reviews* 57.4, pp. 397–409. DOI: `10.1124/pr.57.4.4`.

Catterall, W. A., Perez-Reyes, E., Snutch, T. P., and Striessnig, J. (2005b). “International Union of Pharmacology. XLVIII. Nomenclature and Structure-Function Relationships of Voltage-Gated Calcium Channels”. *Pharmacological Reviews* 57.4, pp. 411–425. DOI: `10.1124/pr.57.4.5`.

Child, N. D. and Benarroch, E. E. (2014). “Differential Distribution of Voltage-Gated Ion Channels in Cortical Neurons: Implications for Epilepsy”. *Neurology* 82.11, pp. 989–999. DOI: `10.1212/WNL.0000000000000228`.

Colbert, C. M. and Pan, E. (2002). “Ion Channel Properties Underlying Axonal Action Potential Initiation in Pyramidal Neurons”. *Nature Neuroscience* 5.6, pp. 533–538. DOI: `10.1038/nn0602-857`.

Cragg, B. G. and Hamlyn, L. H. (1955). “Action Potentials of the Pyramidal Neurones in the Hippocampus of the Rabbit”. *The Journal of Physiology* 129.3, pp. 608–627. DOI: `10.1113/jphysiol.1955.sp005382`.

Cueni, L., Canepari, M., Adelman, J. P., and Lüthi, A. (2009). “Ca2+ Signaling by T-type Ca2+ Channels in Neurons”. *Pflügers Archiv - European Journal of Physiology* 457.5, pp. 1161–1172. DOI: `10.1007/s00424-008-0582-6`.

Cueni, L., Canepari, M., Luján, R., Emmenegger, Y., Watanabe, M., Bond, C. T., Franken, P., Adelman, J. P., and Lüthi, A. (2008). “T-Type Ca2+ Channels, SK2 Channels and SERCAs Gate Sleep-Related Oscillations in Thalamic Dendrites”. *Nature Neuroscience* 11.6, pp. 683–692. DOI: `10.1038/nn.2124`.

Cui, J. (2010). “BK-type Calcium-Activated Potassium Channels: Coupling of Metal Ions and Voltage Sensing: BK Channel Activation by Voltage and Metal Ions”. *The Journal of Physiology* 588.23, pp. 4651–4658. DOI: `10.1113/jphysiol.2010.194514`.

Cui, J., Yang, H., and Lee, U. S. (2009). “Molecular Mechanisms of BK Channel Activation”. *Cellular and Molecular Life Sciences* 66.5, pp. 852–875. DOI: `10.1007/s00018-008-8609-x`.

Dauplais, M. et al. (1997). “On the Convergent Evolution of Animal Toxins”. *Journal of Biological Chemistry* 272.7, pp. 4302–4309. DOI: `10.1074/jbc.272.7.4302`.

Del Castillo, J. and Katz, B. (1954). “Quantal Components of the End-Plate Potential”. *The Journal of Physiology* 124.3, pp. 560–573. DOI: `10.1113/jphysiol.1954.sp005129`.

Dutar, P., Rascol, O., and Lamour, Y. (1989). "Omega-Conotoxin GVIA Blocks Synaptic Transmission in the CA1 Field of the Hippocampus". *European Journal of Pharmacology* 174.2-3, pp. 261–266. DOI: `10.1016/0014-2999(89)90318-x`.

Eberhard, M. and Erne, P. (1991). "Calcium Binding to Fluorescent Calcium Indicators: Calcium Green, Calcium Orange and Calcium Crimson". *Biochemical and Biophysical Research Communications* 180.1, pp. 209–215. DOI: `10.1016/S0006-291X(05)81278-1`.

Echevarria-Cooper, D. M. et al. (2022). "Cellular and Behavioral Effects of Altered NaV1.2 Sodium Channel Ion Permeability in Scn2aK1422E Mice". *Human Molecular Genetics* 31.17, pp. 2964–2988. DOI: `10.1093/hmg/ddac087`.

Elston, G. N. (2003). "Cortex, Cognition and the Cell: New Insights into the Pyramidal Neuron and Prefrontal Function". *Cerebral Cortex* 13.11, pp. 1124–1138. DOI: `10.1093/cercor/bhg093`.

Fakler, B. and Adelman, J. P. (2008). "Control of KCa Channels by Calcium Nano/Microdomains". *Neuron* 59.6, pp. 873–881. DOI: `10.1016/j.neuron.2008.09.001`.

Fatt, P. and Ginsborg, B. L. (1958). "The Ionic Requirements for the Production of Action Potentials in Crustacean Muscle Fibres". *The Journal of Physiology* 142.3, pp. 516–543. DOI: `10.1113/jphysiol.1958.sp006034`.

Filipis, L. and Canepari, M. (2021). "Optical Measurement of Physiological Sodium Currents in the Axon Initial Segment". *The Journal of Physiology* 599.1, pp. 49–66. DOI: `10.1113/JP280554`.

Finger, S. (2000). *Minds behind the Brain: A History of the Pioneers and Their Discoveries.* Oxford ; New York: Oxford University Press. 364 pp.

Fleidervish, I. A., Lasser-Ross, N., Gutnick, M. J., and Ross, W. N. (2010). "Na+ Imaging Reveals Little Difference in Action Potential–Evoked Na+ Influx between Axon and Soma". *Nature Neuroscience* 13.7, pp. 852–860. DOI: `10.1038/nn.2574`.

Frankenhaeuser, B. (1960). "Sodium Permeability in Toad Nerve and in Squid Nerve". *The Journal of Physiology* 152, pp. 159–166. DOI: `10.1113/jphysiol.1960.sp006477`.

— (1963). "A QUANTITATIVE DESCRIPTION OF POTASSIUM CURRENTS IN MYELINATED NERVE FIBRES OF XENOPUS LAEVIS". *The Journal of Physiology* 169, pp. 424–430. DOI: `10.1113/jphysiol.1963.sp007268`.

Frick, A., Magee, J., and Johnston, D. (2004). "LTP Is Accompanied by an Enhanced Local Excitability of Pyramidal Neuron Dendrites". *Nature Neuroscience* 7.2, pp. 126–135. DOI: `10.1038/nn1178`.

Gandini, M. A. and Zamponi, G. W. (2022). "Voltage-Gated Calcium Channel Nanodomains: Molecular Composition and Function". *The FEBS journal* 289.3, pp. 614–633. DOI: `10.1111/febs.15759`.

Gazina, E. V. et al. (2015). "'Neonatal' Nav1.2 Reduces Neuronal Excitability and Affects Seizure Susceptibility and Behaviour". *Human Molecular Genetics* 24.5, pp. 1457–1468. DOI: `10.1093/hmg/ddu562`.

Ghosh, A. and Greenberg, M. E. (1995). "Calcium Signaling in Neurons: Molecular Mechanisms and Cellular Consequences". *Science (New York, N.Y.)* 268.5208, pp. 239–247. DOI: `10.1126/science.7716515`.

Giffin, K., Solomon, J. S., Burkhalter, A., and Nerbonne, J. M. (1991). "Differential Expression of Voltage-Gated Calcium Channels in Identified Visual Cortical Neurons". *Neuron* 6.3, pp. 321–332. DOI: `10.1016/0896-6273(91)90242-R`.

Goldin, A. L. (2003). “Mechanisms of Sodium Channel Inactivation”. *Current Opinion in Neurobiology* 13.3, pp. 284–290. DOI: `10.1016/S0959-4388(03)00065-5`.

Goldman, D. E. (1943). “POTENTIAL, IMPEDANCE, AND RECTIFICATION IN MEMBRANES”. *The Journal of General Physiology* 27.1, pp. 37–60. DOI: `10.1085/jgp.27.1.37`.

Goldwyn, J. H., Remme, M. W. H., and Rinzel, J. (2019). “Soma-Axon Coupling Configurations That Enhance Neuronal Coincidence Detection”. *PLOS Computational Biology* 15.3. Ed. by B. G. Ermentrout, e1006476. DOI: `10.1371/journal.pcbi.1006476`.

Gonzalez-Perez, V. and Lingle, C. J. (2019). “Regulation of BK Channels by Beta and Gamma Subunits”. *Annual Review of Physiology* 81, pp. 113–137. DOI: `10.1146/annurev-physiol-022516-034038`.

Gouwens, N. W. et al. (2019). “Classification of Electrophysiological and Morphological Neuron Types in the Mouse Visual Cortex”. *Nature Neuroscience* 22.7, pp. 1182–1195. DOI: `10.1038/s41593-019-0417-0`.

Grunnet, M., Jensen, B. S., Olesen, S. P., and Klaerke, D. A. (2001). “Apamin Interacts with All Subtypes of Cloned Small-Conductance Ca 2+ -Activated K + Channels”. *Pflügers Archiv European Journal of Physiology* 441.4, pp. 544–550. DOI: `10.1007/s004240000447`.

Grunnet, M. and Kaufmann, W. A. (2004). “Coassembly of Big Conductance Ca2+-Activated K+ Channels and L-type Voltage-gated Ca2+ Channels in Rat Brain”. *Journal of Biological Chemistry* 279.35, pp. 36445–36453. DOI: `10.1074/jbc.M402254200`.

Gu, N., Vervaeke, K., and Storm, J. F. (2007). “BK Potassium Channels Facilitate High-Frequency Firing and Cause Early Spike Frequency Adaptation in Rat CA1 Hippocampal Pyramidal Cells”. *The Journal of Physiology* 580 (Pt.3), pp. 859–882. DOI: `10.1113/jphysiol.2006.126367`.

Guan, D., Armstrong, W. E., and Foehring, R. C. (2015). “Electrophysiological Properties of Genetically Identified Subtypes of Layer 5 Neocortical Pyramidal Neurons: Ca2+ Dependence and Differential Modulation by Norepinephrine”. *Journal of Neurophysiology* 113.7, pp. 2014–2032. DOI: `10.1152/jn.00524.2014`.

Guan, D., Horton, L. R., Armstrong, W. E., and Foehring, R. C. (2011). “Postnatal Development of A-type and Kv1- and Kv2-mediated Potassium Channel Currents in Neocortical Pyramidal Neurons”. *Journal of Neurophysiology* 105.6, pp. 2976–2988. DOI: `10.1152/jn.00758.2010`.

Guan, D., Pathak, D., and Foehring, R. C. (2018). “Functional Roles of Kv1-mediated Currents in Genetically Identified Subtypes of Pyramidal Neurons in Layer 5 of Mouse Somatosensory Cortex”. *Journal of Neurophysiology* 120.2, pp. 394–408. DOI: `10.1152/jn.00691.2017`.

Gulledge, A. T., Kampa, B. M., and Stuart, G. J. (2005). “Synaptic Integration in Dendritic Trees”. *Journal of Neurobiology* 64.1, pp. 75–90. DOI: `10.1002/neu.20144`.

Gutman, G. A. et al. (2005). “International Union of Pharmacology. LIII. Nomenclature and Molecular Relationships of Voltage-Gated Potassium Channels”. *Pharmacological Reviews* 57.4, pp. 473–508. DOI: `10.1124/pr.57.4.10`.

Gutzmann, J. J., Lin, L., and Hoffman, D. A. (2019). “Functional Coupling of Cav2.3 and BK Potassium Channels Regulates Action Potential Repolarization and Short-Term Plasticity in the Mouse Hippocampus”. *Frontiers in Cellular Neuroscience* 13, p. 27. DOI: `10.3389/fncel.2019.00027`.

Hallermann, S., de Kock, C. P. J., Stuart, G. J., and Kole, M. H. P. (2012). "State and Location Dependence of Action Potential Metabolic Cost in Cortical Pyramidal Neurons". *Nature Neuroscience* 15.7, pp. 1007–1014. DOI: `10.1038/nn.3132`.

Hamill, O. P., Marty, A., Neher, E., Sakmann, B., and Sigworth, F. J. (1981). "Improved Patch-Clamp Techniques for High-Resolution Current Recording from Cells and Cell-Free Membrane Patches". *European Journal of Physiology* 391.2, pp. 85–100. DOI: `10.1007/BF00656997`.

Hamilton, T. J., Xapelli, S., Michaelson, S. D., Larkum, M. E., and Colmers, W. F. (2013). "Modulation of Distal Calcium Electrogenesis by Neuropeptide Y1 Receptors Inhibits Neocortical Long-Term Depression". *The Journal of Neuroscience: The Official Journal of the Society for Neuroscience* 33.27, pp. 11184–11193. DOI: `10.1523/JNEUROSCI.5595-12.2013`.

Hanemaaijer, N. A., Popovic, M. A., Wilders, X., Grasman, S., Pavón Arocas, O., and Kole, M. H. P. (2020). "Ca2+ Entry through NaV Channels Generates Submillisecond Axonal Ca2+ Signaling". *eLife* 9, e54566. DOI: `10.7554/eLife.54566`.

Harnett, M. T., Magee, J. C., and Williams, S. R. (2015). "Distribution and Function of HCN Channels in the Apical Dendritic Tuft of Neocortical Pyramidal Neurons". *Journal of Neuroscience* 35.3, pp. 1024–1037. DOI: `10.1523/JNEUROSCI.2813-14.2015`.

Hartshorne, R. P., Messner, D. J., Coppersmith, J. C., and Catterall, W. A. (1982). "The Saxitoxin Receptor of the Sodium Channel from Rat Brain. Evidence for Two Nonidentical Beta Subunits." *Journal of Biological Chemistry* 257.23, pp. 13888–13891. DOI: `10.1016/S0021-9258(19)45312-X`.

Heck, J., Palmeira Do Amaral, A. C., Weißbach, S., El Khallouqi, A., Bikbaev, A., and Heine, M. (2021). "More than a Pore: How Voltage-Gated Calcium Channels Act on Different Levels of Neuronal Communication Regulation". *Channels* 15.1, pp. 322–338. DOI: `10.1080/19336950.2021.1900024`.

Hedrich, U. B. S., Lauxmann, S., and Lerche, H. (2019). "SCN2A Channelopathies: Mechanisms and Models". *Epilepsia* 60 Suppl 3, S68–S76. DOI: `10.1111/epi.14731`.

Heinemann, S. H., Terlau, H., Stühmer, W., Imoto, K., and Numa, S. (1992). "Calcium Channel Characteristics Conferred on the Sodium Channel by Single Mutations". *Nature* 356.6368, pp. 441–443. DOI: `10.1038/356441a0`.

Hell, J. W., Westenbroek, R. E., Warner, C., Ahlijanian, M. K., Prystay, W., Gilbert, M. M., Snutch, T. P., and Catterall, W. A. (1993). "Identification and Differential Subcellular Localization of the Neuronal Class C and Class D L-type Calcium Channel Alpha 1 Subunits". *The Journal of Cell Biology* 123.4, pp. 949–962. DOI: `10.1083/jcb.123.4.949`.

Helmchen, F., Imoto, K., and Sakmann, B. (1996). "Ca2+ Buffering and Action Potential-Evoked Ca2+ Signaling in Dendrites of Pyramidal Neurons". *Biophysical Journal* 70.2, pp. 1069–1081. DOI: `10.1016/S0006-3495(96)79653-4`.

Hess, P. and Tsien, R. W. (1984). "Mechanism of Ion Permeation through Calcium Channels". *Nature* 309.5967, pp. 453–456. DOI: `10.1038/309453a0`.

Hille, B. (1970). "Ionic Channels in Nerve Membranes". *Progress in Biophysics and Molecular Biology* 21, pp. 1–32. DOI: `10.1016/0079-6107(70)90022-2`.

— (1971). "The Permeability of the Sodium Channel to Organic Cations in Myelinated Nerve". *Journal of General Physiology* 58.6, pp. 599–619. DOI: `10.1085/jgp.58.6.599`.

— (2001). *Ion Channels of Excitable Membranes.* 3rd ed. Oxford University Press.

Hodgkin, A. L. and Huxley, A. F. (1939). “Action Potentials Recorded from Inside a Nerve Fibre”. *Nature* 144.3651, pp. 710–711. DOI: `10.1038/144710a0`.

— (1952a). “A Quantitative Description of Membrane Current and Its Application to Conduction and Excitation in Nerve”. *The Journal of Physiology* 117.4, pp. 500–544. DOI: `10.1113/jphysiol.1952.sp004764`.

— (1952b). “Currents Carried by Sodium and Potassium Ions through the Membrane of the Giant Axon of Loligo”. *The Journal of Physiology* 116.4, pp. 449–472. DOI: `10.1113/jphysiol.1952.sp004717`.

— (1952c). “The Components of Membrane Conductance in the Giant Axon of Loligo”. *The Journal of Physiology* 116.4, pp. 473–496. DOI: `10.1113/jphysiol.1952.sp004718`.

— (1952d). “The Dual Effect of Membrane Potential on Sodium Conductance in the Giant Axon of Loligo”. *The Journal of Physiology* 116.4, pp. 497–506. DOI: `10.1113/jphysiol.1952.sp004719`.

Hodgkin, A. L., Huxley, A. F., and Katz, B. (1952). “Measurement of Current-voltage Relations in the Membrane of the Giant Axon of *Loligo*”. *The Journal of Physiology* 116.4, pp. 424–448. DOI: `10.1113/jphysiol.1952.sp004716`.

Hodgkin, A. L. and Katz, B. (1949). “The Effect of Sodium Ions on the Electrical Activity of Giant Axon of the Squid”. *The Journal of Physiology* 108.1, pp. 37–77. DOI: `10.1113/jphysiol.1949.sp004310`.

Hodgkin, A. L. and Keynes, R. D. (1955). “The Potassium Permeability of a Giant Nerve Fibre”. *The Journal of Physiology* 128.1, pp. 61–88. DOI: `10.1113/jphysiol.1955.sp005291`.

Hoffman, D. A. (2013). “K+ Channel Regulation of Multicompartmental Signal Integration”. *Neuron* 79.3, pp. 403–405. DOI: `10.1016/j.neuron.2013.07.017`.

Hu, L. Y. et al. (1999). “Structure-Activity Relationship of N-methyl-N-aralkyl-peptidylamines as Novel N-type Calcium Channel Blockers”. *Bioorganic & Medicinal Chemistry Letters* 9.15, pp. 2151–2156. DOI: `10.1016/S0960-894X(99)00359-5`.

Hu, W., Tian, C., Li, T., Yang, M., Hou, H., and Shu, Y. (2009). “Distinct Contributions of Nav1.6 and Nav1.2 in Action Potential Initiation and Backpropagation”. *Nature Neuroscience* 12.8, pp. 996–1002. DOI: `10.1038/nn.2359`.

Inglebert, Y. and Debanne, D. (2021). “Calcium and Spike Timing-Dependent Plasticity”. *Frontiers in Cellular Neuroscience* 15, p. 727336. DOI: `10.3389/fncel.2021.727336`.

Isom, L. L., Ragsdale, D. S., De Jongh, K. S., Westenbroek, R. E., Reber, B. F., Scheuer, T., and Catterall, W. A. (1995). “Structure and Function of the Beta 2 Subunit of Brain Sodium Channels, a Transmembrane Glycoprotein with a CAM Motif”. *Cell* 83.3, pp. 433–442. DOI: `10.1016/0092-8674(95)90121-3`.

Jaafari, N. and Canepari, M. (2016). “Functional Coupling of Diverse Voltage-Gated Ca $^{2+}$ Channels Underlies High Fidelity of Fast Dendritic Ca $^{2+}$ Signals during Burst Firing: Functional Coupling of Voltage-Gated Ca $^{2+}$ Channels”. *The Journal of Physiology* 594.4, pp. 967–983. DOI: `10.1113/JP271830`.

Jaafari, N., De Waard, M., and Canepari, M. (2014). “Imaging Fast Calcium Currents beyond the Limitations of Electrode Techniques”. *Biophysical Journal* 107.6, pp. 1280–1288. DOI: `10.1016/j.bpj.2014.07.059`.

Jaafari, N., Marret, E., and Canepari, M. (2015). “Using Simultaneous Voltage and Calcium Imaging to Study Fast Ca $^{2+}$ Channels”. *Neurophotonics* 2.2, p. 021010. DOI: `10.1117/1.NPh.2.2.021010`.

Jones, S. L. and Stuart, G. J. (2013). “Different Calcium Sources Control Somatic versus Dendritic SK Channel Activation during Action Potentials”. *Journal of Neuroscience* 33.50, pp. 19396–19405. DOI: `10.1523/JNEUROSCI.2073-13.2013`.

Jones, S. L., To, M.-S., and Stuart, G. J. (2017). “Dendritic Small Conductance Calcium-Activated Potassium Channels Activated by Action Potentials Suppress EPSPs and Gate Spike-Timing Dependent Synaptic Plasticity”. *eLife* 6, e30333. DOI: `10.7554/eLife.30333`.

Kaiser, K. M. M., Lübke, J., Zilberter, Y., and Sakmann, B. (2004). “Postsynaptic Calcium Influx at Single Synaptic Contacts between Pyramidal Neurons and Bitufted Interneurons in Layer 2/3 of Rat Neocortex Is Enhanced by Backpropagating Action Potentials”. *Journal of Neuroscience* 24.6, pp. 1319–1329. DOI: `10.1523/JNEUROSCI.2852-03.2004`.

Kampa, B. M. and Stuart, G. J. (2006). “Calcium Spikes in Basal Dendrites of Layer 5 Pyramidal Neurons during Action Potential Bursts”. *Journal of Neuroscience* 26.28, pp. 7424–7432. DOI: `10.1523/JNEUROSCI.3062-05.2006`.

Kang, J., Huguenard, J. R., and Prince, D. A. (2000). “Voltage-Gated Potassium Channels Activated During Action Potentials in Layer V Neocortical Pyramidal Neurons”. *Journal of Neurophysiology* 83.1, pp. 70–80. DOI: `10.1152/jn.2000.83.1.70`.

Kaplan, M. R., Cho, M.-H., Ullian, E. M., Isom, L. L., Levinson, S., and Barres, B. A. (2001). “Differential Control of Clustering of the Sodium Channels Nav1.2 and Nav1.6 at Developing CNS Nodes of Ranvier”. *Neuron* 30.1, pp. 105–119. DOI: `10.1016/S0896-6273(01)00266-5`.

Katz, E., Stoler, O., Scheller, A., Khrapunsky, Y., Goebbels, S., Kirchhoff, F., Gutnick, M. J., Wolf, F., and Fleidervish, I. A. (2018). “Role of Sodium Channel Subtype in Action Potential Generation by Neocortical Pyramidal Neurons”. *Proceedings of the National Academy of Sciences* 115.30. DOI: `10.1073/pnas.1720493115`.

Kay, A. R. and Wong, R. K. (1987). “Calcium Current Activation Kinetics in Isolated Pyramidal Neurones of the Ca1 Region of the Mature Guinea-Pig Hippocampus”. *The Journal of Physiology* 392, pp. 603–616. DOI: `10.1113/jphysiol.1987.sp016799`.

Kearney, J., Plummer, N., Smith, M., Kapur, J., Cummins, T., Waxman, S., Goldin, A., and Meisler, M. (2001). “A Gain-of-Function Mutation in the Sodium Channel Gene Scn2a Results in Seizures and Behavioral Abnormalities”. *Neuroscience* 102.2, pp. 307–317. DOI: `10.1016/S0306-4522(00)00479-6`.

Kim, Y., Hsu, C.-L., Cembrowski, M. S., Mensh, B. D., and Spruston, N. (2015). “Dendritic Sodium Spikes Are Required for Long-Term Potentiation at Distal Synapses on Hippocampal Pyramidal Neurons”. *eLife* 4, e06414. DOI: `10.7554/eLife.06414`.

King, A. N., Manning, C. F., and Trimmer, J. S. (2014). “A Unique Ion Channel Clustering Domain on the Axon Initial Segment of Mammalian Neurons: Ion Channel Clustering on the Axon Initial Segment”. *Journal of Comparative Neurology* 522.11, pp. 2594–2608. DOI: `10.1002/cne.23551`.

Knaus, H. G. et al. (1996). “Distribution of High-Conductance Ca(2+)-Activated K+ Channels in Rat Brain: Targeting to Axons and Nerve Terminals”. *The Journal of Neuroscience: The Official Journal of the Society for Neuroscience* 16.3, pp. 955–963.

Koester, H. J. and Sakmann, B. (1998). “Calcium Dynamics in Single Spines during Coincident Pre- and Postsynaptic Activity Depend on Relative Timing of

Back-Propagating Action Potentials and Subthreshold Excitatory Postsynaptic Potentials". *Proceedings of the National Academy of Sciences* 95.16, pp. 9596–9601. DOI: `10.1073/pnas.95.16.9596`.

Kole, M. H. P., Hallermann, S., and Stuart, G. J. (2006). "Single I_{h} Channels in Pyramidal Neuron Dendrites: Properties, Distribution, and Impact on Action Potential Output". *The Journal of Neuroscience* 26.6, pp. 1677–1687. DOI: `10.1523/JNEUROSCI.3664-05.2006`.

Kole, M. H. P., Ilschner, S. U., Kampa, B. M., Williams, S. R., Ruben, P. C., and Stuart, G. J. (2008). "Action Potential Generation Requires a High Sodium Channel Density in the Axon Initial Segment". *Nature Neuroscience* 11.2, pp. 178–186. DOI: `10.1038/nn2040`.

Kole, M. H. P., Letzkus, J. J., and Stuart, G. J. (2007). "Axon Initial Segment Kv1 Channels Control Axonal Action Potential Waveform and Synaptic Efficacy". *Neuron* 55.4, pp. 633–647. DOI: `10.1016/j.neuron.2007.07.031`.

Kole, M. H. P. and Stuart, G. J. (2012). "Signal Processing in the Axon Initial Segment". *Neuron* 73.2, pp. 235–247. DOI: `10.1016/j.neuron.2012.01.007`.

Korngreen, A. and Sakmann, B. (2000). "Voltage-gated K^+ Channels in Layer 5 Neocortical Pyramidal Neurones from Young Rats: Subtypes and Gradients". *The Journal of Physiology* 525.3, pp. 621–639. DOI: `10.1111/j.1469-7793.2000.00621.x`.

Kreitzer, A. C. and Regehr, W. G. (2002). "Retrograde Signaling by Endocannabinoids". *Current Opinion in Neurobiology* 12.3, pp. 324–330. DOI: `10.1016/S0959-4388(02)00328-8`.

Kyle, B. D. and Braun, A. P. (2014). "The Regulation of BK Channel Activity by Pre- and Post-Translational Modifications". *Frontiers in Physiology* 5. DOI: `10.3389/fphys.2014.00316`.

Lancaster, B., Nicoll, R., and Perkel, D. (1991). "Calcium Activates Two Types of Potassium Channels in Rat Hippocampal Neurons in Culture". *The Journal of Neuroscience* 11.1, pp. 23–30. DOI: `10.1523/JNEUROSCI.11-01-00023.1991`.

Lancaster, B. and Adams, P. R. (1986). "Calcium-Dependent Current Generating the Afterhyperpolarization of Hippocampal Neurons". *Journal of Neurophysiology* 55.6, pp. 1268–1282. DOI: `10.1152/jn.1986.55.6.1268`.

Larkum, M. E., Kaiser, K. M. M., and Sakmann, B. (1999a). "Calcium Electrogenesis in Distal Apical Dendrites of Layer 5 Pyramidal Cells at a Critical Frequency of Back-Propagating Action Potentials". *Proceedings of the National Academy of Sciences* 96.25, pp. 14600–14604. DOI: `10.1073/pnas.96.25.14600`.

Larkum, M. E., Nevian, T., Sandler, M., Polsky, A., and Schiller, J. (2009). "Synaptic Integration in Tuft Dendrites of Layer 5 Pyramidal Neurons: A New Unifying Principle". *Science* 325.5941, pp. 756–760. DOI: `10.1126/science.1171958`.

Larkum, M. E., Zhu, J. J., and Sakmann, B. (1999b). "A New Cellular Mechanism for Coupling Inputs Arriving at Different Cortical Layers". *Nature* 398.6725, pp. 338–341. DOI: `10.1038/18686`.

— (2001). "Dendritic Mechanisms Underlying the Coupling of the Dendritic with the Axonal Action Potential Initiation Zone of Adult Rat Layer 5 Pyramidal Neurons". *The Journal of Physiology* 533.2, pp. 447–466. DOI: `10.1111/j.1469-7793.2001.0447a.x`.

Latorre, R., Castillo, K., Carrasquel-Ursulaez, W., Sepulveda, R. V., Gonzalez-Nilo, F., Gonzalez, C., and Alvarez, O. (2017). "Molecular Determinants of BK Channel

Functional Diversity and Functioning". *Physiological Reviews* 97.1, pp. 39–87. DOI: `10.1152/physrev.00001.2016`.

Léna, I. and Mantegazza, M. (2019). "NaV1.2 Haploinsufficiency in Scn2a Knock-out Mice Causes an Autistic-like Phenotype Attenuated with Age". *Scientific Reports* 9.1, p. 12886. DOI: `10.1038/s41598-019-49392-7`.

Leterrier, C. (2016). "The Axon Initial Segment, 50Years Later". *Current Topics in Membranes*. Vol. 77. Elsevier, pp. 185–233. DOI: `10.1016/bs.ctm.2015.10.005`.

— (2018). "The Axon Initial Segment: An Updated Viewpoint". *The Journal of Neuroscience* 38.9, pp. 2135–2145. DOI: `10.1523/JNEUROSCI.1922-17.2018`.

Lévêque, C., el Far, O., Martin-Moutot, N., Sato, K., Kato, R., Takahashi, M., and Seagar, M. J. (1994). "Purification of the N-type Calcium Channel Associated with Syntaxin and Synaptotagmin. A Complex Implicated in Synaptic Vesicle Exocytosis". *The Journal of Biological Chemistry* 269.9, pp. 6306–6312.

Lilliefors, H. W. (1967). "On the Kolmogorov-Smirnov Test for Normality with Mean and Variance Unknown". *Journal of the American Statistical Association* 62.318, pp. 399–402. DOI: `10.1080/01621459.1967.10482916`.

Lim, H.-H. and Park, C.-S. (2005). "Identification and Functional Characterization of Ankyrin-Repeat Family Protein ANKRA as a Protein Interacting with BKCa Channel". *Molecular Biology of the Cell* 16.3, pp. 1013–1025. DOI: `10.1091/mbc.e04-06-0537`.

Lipkin, A. M., Cunniff, M. M., Spratt, P. W. E., Lemke, S. M., and Bender, K. J. (2021). "Functional Microstructure of Ca $_V$ -Mediated Calcium Signaling in the Axon Initial Segment". *The Journal of Neuroscience* 41.17, pp. 3764–3776. DOI: `10.1523/JNEUROSCI.2843-20.2021`.

Llinás, R. and Sugimori, M. (1980). "Electrophysiological Properties of in Vitro Purkinje Cell Dendrites in Mammalian Cerebellar Slices." *The Journal of Physiology* 305.1, pp. 197–213. DOI: `10.1113/jphysiol.1980.sp013358`.

Loane, D. J., Lima, P. A., and Marrion, N. V. (2007). "Co-Assembly of N-type Ca2+ and BK Channels Underlies Functional Coupling in Rat Brain". *Journal of Cell Science* 120.6, pp. 985–995. DOI: `10.1242/jcs.03399`.

Lorente de Nó, R. and Davis, L. (1947). *A Study of Nerve Physiology*. Studies from The Rockefeller Institute for Medical Research. University of Minnesota: Rockefeller Institute for Medical Research.

Lorenzon, N. M. and Foehring, R. C. (1995). "Characterization of Pharmacologically Identified Voltage-Gated Calcium Channel Currents in Acutely Isolated Rat Neocortical Neurons. I. Adult Neurons". *Journal of Neurophysiology* 73.4, pp. 1430–1442. DOI: `10.1152/jn.1995.73.4.1430`.

Lorenzon, N. M. and Beam, K. G. (2005). "Calcium Channelopathies". *Voltage-Gated Calcium Channels*. Molecular Biology Intelligence Unit. Boston, MA: Springer US, pp. 240–261. DOI: `10.1007/0-387-27526-6_16`.

Lörincz, A., Notomi, T., Tamás, G., Shigemoto, R., and Nusser, Z. (2002). "Polarized and Compartment-Dependent Distribution of HCN1 in Pyramidal Cell Dendrites". *Nature Neuroscience* 5.11, pp. 1185–1193. DOI: `10.1038/nn962`.

Mahapatra, C., Brain, K. L., and Manchanda, R. (2018). "A Biophysically Constrained Computational Model of the Action Potential of Mouse Urinary Bladder Smooth Muscle". *PLOS ONE* 13.7. Ed. by A. Guerrero-Hernandez, e0200712. DOI: `10.1371/journal.pone.0200712`.

Mainen, Z. F., Joerges, J., Huguenard, J. R., and Sejnowski, T. J. (1995). “A Model of Spike Initiation in Neocortical Pyramidal Neurons”. *Neuron* 15.6, pp. 1427–1439. DOI: `10.1016/0896-6273(95)90020-9`.

Mandge, D. and Manchanda, R. (2018). “A Biophysically Detailed Computational Model of Urinary Bladder Small DRG Neuron Soma”. *PLOS Computational Biology* 14.7. Ed. by W. W. Lytton, e1006293. DOI: `10.1371/journal.pcbi.1006293`.

Mantegazza, M., Cestèle, S., and Catterall, W. A. (2021). “Sodium Channelopathies of Skeletal Muscle and Brain”. *Physiological Reviews* 101.4, pp. 1633–1689. DOI: `10.1152/physrev.00025.2020`.

Markram, H., Helm, P. J., and Sakmann, B. (1995). “Dendritic Calcium Transients Evoked by Single Back-Propagating Action Potentials in Rat Neocortical Pyramidal Neurons.” *The Journal of Physiology* 485.1, pp. 1–20. DOI: `10.1113/jphysiol.1995.sp020708`.

Markram, H. and Sakmann, B. (1994). “Calcium Transients in Dendrites of Neocortical Neurons Evoked by Single Subthreshold Excitatory Postsynaptic Potentials via Low-Voltage-Activated Calcium Channels.” *Proceedings of the National Academy of Sciences* 91.11, pp. 5207–5211. DOI: `10.1073/pnas.91.11.5207`.

Marrion, N. V. and Tavalin, S. J. (1998). “Selective Activation of Ca2+- Activated K+ Channels by Co-Localized Ca2+ Channels in Hippocampal Neurons”. 395, p. 6.

Maximov, A. and Bezprozvanny, I. (2002). “Synaptic Targeting of N-type Calcium Channels in Hippocampal Neurons”. *The Journal of Neuroscience: The Official Journal of the Society for Neuroscience* 22.16, pp. 6939–6952. DOI: `20026688`.

McManus, O. B., Helms, L. M., Pallanck, L., Ganetzky, B., Swanson, R., and Leonard, R. J. (1995). “Functional Role of the Beta Subunit of High Conductance Calcium-Activated Potassium Channels”. *Neuron* 14.3, pp. 645–650. DOI: `10.1016/0896-6273(95)90321-6`.

Migliore, M., Novara, G., and Tegolo, D. (2008). “Single Neuron Binding Properties and the Magical Number 7”. *Hippocampus* 18.11, pp. 1122–1130. DOI: `10.1002/hipo.20480`.

Migliore, M. and Shepherd, G. M. (2002). “Emerging Rules for the Distributions of Active Dendritic Conductances”. *Nature Reviews Neuroscience* 3.5, pp. 362–370. DOI: `10.1038/nrn810`.

Miyamoto, H. et al. (2019). “Impaired Cortico-Striatal Excitatory Transmission Triggers Epilepsy”. *Nature Communications* 10.1, p. 1917. DOI: `10.1038/s41467-019-09954-9`.

Montnach, J. et al. (2022). “In Vivo Spatiotemporal Control of Voltage-Gated Ion Channels by Using Photoactivatable Peptidic Toxins”. *Nature Communications* 13.1, p. 417. DOI: `10.1038/s41467-022-27974-w`.

Müller, C. S. et al. (2010). “Quantitative Proteomics of the Cav2 Channel Nano-Environments in the Mammalian Brain”. *Proceedings of the National Academy of Sciences* 107.34, pp. 14950–14957. DOI: `10.1073/pnas.1005940107`.

Neher, E. and Sakmann, B. (1976a). “Noise Analysis of Drug Induced Voltage Clamp Currents in Denervated Frog Muscle Fibres”. *The Journal of Physiology* 258.3, pp. 705–729. DOI: `10.1113/jphysiol.1976.sp011442`.

— (1976b). “Single-Channel Currents Recorded from Membrane of Denervated Frog Muscle Fibres”. *Nature* 260.5554, pp. 799–802. DOI: `10.1038/260799a0`.

Neher, E., Sakmann, B., and Steinbach, J. H. (1978). “The Extracellular Patch Clamp: A Method for Resolving Currents through Individual Open Channels in Biological

Membranes". *Pflugers Archiv: European Journal of Physiology* 375.2, pp. 219–228. DOI: `10.1007/BF00584247`.

Nevian, T., Larkum, M. E., Polsky, A., and Schiller, J. (2007). "Properties of Basal Dendrites of Layer 5 Pyramidal Neurons: A Direct Patch-Clamp Recording Study". *Nature Neuroscience* 10.2, pp. 206–214. DOI: `10.1038/nn1826`.

Nevian, T. and Sakmann, B. (2006). "Spine Ca2+ Signaling in Spike-Timing-Dependent Plasticity". *The Journal of Neuroscience: The Official Journal of the Society for Neuroscience* 26.43, pp. 11001–11013. DOI: `10.1523/JNEUROSCI.1749-06.2006`.

Newcomb, R. et al. (1998). "Selective Peptide Antagonist of the Class E Calcium Channel from the Venom of the Tarantula Hysterocrates Gigas". *Biochemistry* 37.44, pp. 15353–15362. DOI: `10.1021/bi981255g`.

Newman, E. A., Araque, A., Dubinsky, J. M., Swanson, L. W., King, L. S., and Himmel, E., eds. (2017). *The Beautiful Brain: The Drawings of Santiago Ramón y Cajal*. New York: Abrams. 207 pp.

Ngo-Anh, T. J., Bloodgood, B. L., Lin, M., Sabatini, B. L., Maylie, J., and Adelman, J. P. (2005). "SK Channels and NMDA Receptors Form a Ca2+-Mediated Feedback Loop in Dendritic Spines". *Nature Neuroscience* 8.5, pp. 642–649. DOI: `10.1038/nn1449`.

Nicholls, J. G., ed. (2012). *From Neuron to Brain*. 5th ed. Sunderland, Mass: Sinauer Associates. 621 pp.

Noda, M., Ikeda, T., Suzuki, H., Takeshima, H., Takahashi, T., Kuno, M., and Numa, S. (1986). "Expression of Functional Sodium Channels from Cloned cDNA". *Nature* 322.6082, pp. 826–828. DOI: `10.1038/322826a0`.

Nowycky, M. C., Fox, A. P., and Tsien, R. W. (1985). "Three Types of Neuronal Calcium Channel with Different Calcium Agonist Sensitivity". *Nature* 316.6027, pp. 440–443. DOI: `10.1038/316440a0`.

Offner, F. F. (1991). "Ion Flow through Membranes and the Resting Potential of Cells". *The Journal of Membrane Biology* 123.2, pp. 171–182. DOI: `10.1007/BF01998087`.

Ogiwara, I. et al. (2018). "Nav1.2 Haplodeficiency in Excitatory Neurons Causes Absence-like Seizures in Mice". *Communications Biology* 1, p. 96. DOI: `10.1038/s42003-018-0099-2`.

Olivera, B. M., Miljanich, G. P., Ramachandran, J., and Adams, M. E. (1994). "Calcium Channel Diversity and Neurotransmitter Release: The Omega-Conotoxins and Omega-Agatoxins". *Annual Review of Biochemistry* 63, pp. 823–867. DOI: `10.1146/annurev.bi.63.070194.004135`.

Pallone, T. L., Khurana, S., and Cao, C. (2018). "Voltage-Gated Calcium Channels: Structure and Function (CACNA)". *Encyclopedia of Signaling Molecules*. Ed. by S. Choi. Cham: Springer International Publishing, pp. 5942–5949. DOI: `10.1007/978-3-319-67199-4_145`.

Papazian, D. M., Schwarz, T. L., Tempel, B. L., Jan, Y. N., and Jan, L. Y. (1987). "Cloning of Genomic and Complementary DNA from *Shaker* , a Putative Potassium Channel Gene from *Drosophila*". *Science* 237.4816, pp. 749–753. DOI: `10.1126/science.2441470`.

Pedarzani, P. and Stocker, M. (2008). "Molecular and Cellular Basis of Small- and Intermediate-Conductance, Calcium-Activated Potassium Channel Function in the Brain". *Cellular and Molecular Life Sciences* 65.20, pp. 3196–3217. DOI: `10.1007/s00018-008-8216-x`.

Peng, K., Shu, Q., Liu, Z., and Liang, S. (2002). "Function and Solution Structure of Huwentoxin-IV, a Potent Neuronal Tetrodotoxin (TTX)-Sensitive Sodium Channel

Antagonist from Chinese Bird Spider *Selenocosmia Huwena*". *Journal of Biological Chemistry* 277.49, pp. 47564–47571. DOI: `10.1074/jbc.M204063200`.

Pérez-García, M. T., Chiamvimonvat, N., Marban, E., and Tomaselli, G. F. (1996). "Structure of the Sodium Channel Pore Revealed by Serial Cysteine Mutagenesis." *Proceedings of the National Academy of Sciences* 93.1, pp. 300–304. DOI: `10.1073/pnas.93.1.300`.

Perez-Reyes, E. (2003). "Molecular Physiology of Low-Voltage-Activated t-Type Calcium Channels". *Physiological Reviews* 83.1, pp. 117–161. DOI: `10.1152/physrev.00018.2002`.

Pineda, J. C., Galarraga, E., Bargas, J., Cristancho, M., and Aceves, J. (1992). "Charybdotoxin and Apamin Sensitivity of the Calcium-Dependent Repolarization and the Afterhyperpolarization in Neostriatal Neurons". *Journal of Neurophysiology* 68.1, pp. 287–294. DOI: `10.1152/jn.1992.68.1.287`.

Popovic, M., Vogt, K., Holthoff, K., Konnerth, A., Salzberg, B. M., Grinvald, A., Antic, S. D., Canepari, M., and Zecevic, D. (2015). "Imaging Submillisecond Membrane Potential Changes from Individual Regions of Single Axons, Dendrites and Spines". *Membrane Potential Imaging in the Nervous System and Heart.* Ed. by M. Canepari, D. Zecevic, and O. Bernus. Vol. 859. Advances in Experimental Medicine and Biology. Cham: Springer International Publishing, pp. 57–101. DOI: `10.1007/978-3-319-17641-3_3`.

Rama, S., Zbili, M., Bialowas, A., Fronzaroli-Molinieres, L., Ankri, N., Carlier, E., Marra, V., and Debanne, D. (2015). "Presynaptic Hyperpolarization Induces a Fast Analogue Modulation of Spike-Evoked Transmission Mediated by Axonal Sodium Channels". *Nature Communications* 6.10163, pp. 1–12. DOI: `10.1038/ncomms10163`.

Rama, S., Zbili, M., and Debanne, D. (2018). "Signal Propagation along the Axon". *Current Opinion in Neurobiology* 51, pp. 37–44. DOI: `10.1016/j.conb.2018.02.017`.

Ramaswamy, S. and Markram, H. (2015). "Anatomy and Physiology of the Thick-Tufted Layer 5 Pyramidal Neuron". *Frontiers in Cellular Neuroscience* 9. DOI: `10.3389/fncel.2015.00233`.

Randall, A. and Tsien, R. W. (1995). "Pharmacological Dissection of Multiple Types of Ca2+ Channel Currents in Rat Cerebellar Granule Neurons". *The Journal of Neuroscience: The Official Journal of the Society for Neuroscience* 15.4, pp. 2995–3012.

Regan, L. J., Sah, D. W., and Bean, B. P. (1991). "Ca2+ Channels in Rat Central and Peripheral Neurons: High-Threshold Current Resistant to Dihydropyridine Blockers and Omega-Conotoxin". *Neuron* 6.2, pp. 269–280. DOI: `10.1016/0896-6273(91)90362-4`.

Rohl, C. A., Boeckman, F. A., Baker, C., Scheuer, T., Catterall, W. A., and Klevit, R. E. (1999). "Solution Structure of the Sodium Channel Inactivation Gate ". *Biochemistry* 38.3, pp. 855–861. DOI: `10.1021/bi9823380`.

Royeck, M., Horstmann, M.-T., Remy, S., Reitze, M., Yaari, Y., and Beck, H. (2008). "Role of Axonal Na $_V$ 1.6 Sodium Channels in Action Potential Initiation of CA1 Pyramidal Neurons". *Journal of Neurophysiology* 100.4, pp. 2361–2380. DOI: `10.1152/jn.90332.2008`.

Rush, A. M., Dib-Hajj, S. D., and Waxman, S. G. (2005). "Electrophysiological Properties of Two Axonal Sodium Channels, Na $_v$ 1.2 and Na $_v$ 1.6, Expressed in Mouse Spinal Sensory Neurones: Sodium Channels in Sensory Neurones". *The Journal of Physiology* 564.3, pp. 803–815. DOI: `10.1113/jphysiol.2005.083089`.

Al-Sabi, A., McArthur, J., Ostroumov, V., and French, R. (2006). “Marine Toxins That Target Voltage-gated Sodium Channels”. *Marine Drugs* 4.3, pp. 157–192. DOI: `10.3390/md403157`.

Sah, P. (1996). “Ca2+-Activated K+ Currents in Neurones: Types, Physiological Roles and Modulation”. *Trends in Neurosciences* 19.4, pp. 150–154. DOI: `10.1016/S0166-2236(96)80026-9`.

Sah, P. and Davies, P. (2000). “Calcium-Activated Potassium Currents In Mammalian Neurons”. *Clinical and Experimental Pharmacology and Physiology* 27.9, pp. 657–663. DOI: `10.1046/j.1440-1681.2000.03317.x`.

Sato, C., Ueno, Y., Asai, K., Takahashi, K., Sato, M., Engel, A., and Fujiyoshi, Y. (2001). “The Voltage-Sensitive Sodium Channel Is a Bell-Shaped Molecule with Several Cavities”. *Nature* 409.6823, pp. 1047–1051. DOI: `10.1038/35059098`.

Savio-Galimberti, E., Gollob, M. H., and Darbar, D. (2012). “Voltage-Gated Sodium Channels: Biophysics, Pharmacology, and Related Channelopathies”. *Frontiers in Pharmacology* 3. DOI: `10.3389/fphar.2012.00124`.

Schmidt, H., Stiefel, K. M., Racay, P., Schwaller, B., and Eilers, J. (2003). “Mutational Analysis of Dendritic Ca2+ Kinetics in Rodent Purkinje Cells: Role of Parvalbumin and Calbindin D28k”. *The Journal of Physiology* 551.1, pp. 13–32. DOI: `10.1113/jphysiol.2002.035824`.

Schumacher, M. A., Rivard, A. F., Bächinger, H. P., and Adelman, J. P. (2001). “Structure of the Gating Domain of a Ca2+-Activated K+ Channel Complexed with Ca2+/Calmodulin”. *Nature* 410.6832, pp. 1120–1124. DOI: `10.1038/35074145`.

Schwindt, P. C., Spain, W. J., Foehring, R. C., Stafstrom, C. E., Chubb, M. C., and Crill, W. E. (1988). “Multiple Potassium Conductances and Their Functions in Neurons from Cat Sensorimotor Cortex in Vitro”. *Journal of Neurophysiology* 59.2, pp. 424–449. DOI: `10.1152/jn.1988.59.2.424`.

Scott, R. H., Pearson, H. A., and Dolphin, A. C. (1991). “Aspects of Vertebrate Neuronal Voltage-Activated Calcium Currents and Their Regulation”. *Progress in Neurobiology* 36.6, pp. 485–520. DOI: `10.1016/0301-0082(91)90014-r`.

Shah, K. R., Guan, X., and Yan, J. (2022). “Structural and Functional Coupling of Calcium-Activated BK Channels and Calcium-Permeable Channels Within Nanodomain Signaling Complexes”. *Frontiers in Physiology* 12, p. 796540. DOI: `10.3389/fphys.2021.796540`.

Sheng, Z. H., Rettig, J., Takahashi, M., and Catterall, W. A. (1994). “Identification of a Syntaxin-Binding Site on N-type Calcium Channels”. *Neuron* 13.6, pp. 1303–1313. DOI: `10.1016/0896-6273(94)90417-0`.

Shibasaki, K., Nakahira, K., Trimmer, J. S., Shibata, R., Akita, M., Watanabe, S.-I., and Ikenaka, K. (2004). “Mossy Fibre Contact Triggers the Targeting of Kv4.2 Potassium Channels to Dendrites and Synapses in Developing Cerebellar Granule Neurons”. *Journal of Neurochemistry* 89.4, pp. 897–907. DOI: `10.1111/j.1471-4159.2004.02368.x`.

Shruti, S., Clem, R. L., and Barth, A. L. (2008). “A Seizure-Induced Gain-of-Function in BK Channels Is Associated with Elevated Firing Activity in Neocortical Pyramidal Neurons”. *Neurobiology of Disease* 30.3, pp. 323–330. DOI: `10.1016/j.nbd.2008.02.002`.

Sinnegger-Brauns, M. J., Huber, I. G., Koschak, A., Wild, C., Obermair, G. J., Einzinger, U., Hoda, J.-C., Sartori, S. B., and Striessnig, J. (2009). “Expression and

1,4-Dihydropyridine-Binding Properties of Brain L-type Calcium Channel Isoforms". *Molecular Pharmacology* 75.2, pp. 407–414. DOI: `10.1124/mol.108.049981`.

Sjöström, P. J., Turrigiano, G. G., and Nelson, S. B. (2003). "Neocortical LTD via Coincident Activation of Presynaptic NMDA and Cannabinoid Receptors". *Neuron* 39.4, pp. 641–654. DOI: `10.1016/s0896-6273(03)00476-8`.

— (2004). "Endocannabinoid-Dependent Neocortical Layer-5 LTD in the Absence of Postsynaptic Spiking". *Journal of Neurophysiology* 92.6, pp. 3338–3343. DOI: `10.1152/jn.00376.2004`.

Spratt, P. W. E., Alexander, R. P. D., Ben-Shalom, R., Sahagun, A., Kyoung, H., Keeshen, C. M., Sanders, S. J., and Bender, K. J. (2021). "Paradoxical Hyperexcitability from NaV1.2 Sodium Channel Loss in Neocortical Pyramidal Cells". *Cell Reports* 36.5, p. 109483. DOI: `10.1016/j.celrep.2021.109483`.

Spratt, P. W., Ben-Shalom, R., Keeshen, C. M., Burke, K. J., Clarkson, R. L., Sanders, S. J., and Bender, K. J. (2019). "The Autism-Associated Gene Scn2a Contributes to Dendritic Excitability and Synaptic Function in the Prefrontal Cortex". *Neuron* 103.4, 673–685.e5. DOI: `10.1016/j.neuron.2019.05.037`.

Spruston, N. (2008). "Pyramidal Neurons: Dendritic Structure and Synaptic Integration". *Nature Reviews Neuroscience* 9.3, pp. 206–221. DOI: `10.1038/nrn2286`.

Stewart, A. and Foehring, R. C. (2000). "Calcium Currents in Retrogradely Labeled Pyramidal Cells From Rat Sensorimotor Cortex". *Journal of Neurophysiology* 83.4, pp. 2349–2354. DOI: `10.1152/jn.2000.83.4.2349`.

Stuart, G. J. and Sakmann, B. (1994). "Active Propagation of Somatic Action Potentials into Neocortical Pyramidal Cell Dendrites". *Nature* 367.6458, pp. 69–72. DOI: `10.1038/367069a0`.

Stuart, G. J., Schiller, J., and Sakmann, B. (1997a). "Action Potential Initiation and Propagation in Rat Neocortical Pyramidal Neurons". *The Journal of Physiology* 505.3, pp. 617–632. DOI: `10.1111/j.1469-7793.1997.617ba.x`.

Stuart, G. J., Spruston, N., Sakmann, B., and Häusser, M. (1997b). "Action Potential Initiation and Backpropagation in Neurons of the Mammalian CNS". *Trends in Neurosciences* 20.3, pp. 125–131. DOI: `10.1016/S0166-2236(96)10075-8`.

Stühmer, W., Conti, F., Suzuki, H., Wang, X., Noda, M., Yahagi, N., Kubo, H., and Numa, S. (1989). "Structural Parts Involved in Activation and Inactivation of the Sodium Channel". *Nature* 339.6226, pp. 597–603. DOI: `10.1038/339597a0`.

Sun, X., Gu, X. Q., and Haddad, G. G. (2003). "Calcium Influx via L- and N-Type Calcium Channels Activates a Transient Large-Conductance Ca2+-Activated K+ Current in Mouse Neocortical Pyramidal Neurons". *The Journal of Neuroscience* 23.9, pp. 3639–3648.

Talley, E. M., Cribbs, L. L., Lee, J.-H., Daud, A., Perez-Reyes, E., and Bayliss, D. A. (1999). "Differential Distribution of Three Members of a Gene Family Encoding Low Voltage-Activated (T-Type) Calcium Channels". *The Journal of Neuroscience* 19.6, pp. 1895–1911. DOI: `10.1523/JNEUROSCI.19-06-01895.1999`.

Tazerart, S., Blanchard, M. G., Miranda-Rottmann, S., Mitchell, D. E., Navea Pina, B., Thomas, C. I., Kamasawa, N., and Araya, R. (2022). "Selective Activation of BK Channels in Small-Headed Dendritic Spines Suppresses Excitatory Postsynaptic Potentials". *The Journal of Physiology* 600.9, pp. 2165–2187. DOI: `10.1113/JP282303`.

Tazerart, S., Mitchell, D. E., Miranda-Rottmann, S., and Araya, R. (2020). "A Spike-Timing-Dependent Plasticity Rule for Dendritic Spines". *Nature Communications* 11.1, p. 4276. DOI: `10.1038/s41467-020-17861-7`.

Tian, C., Wang, K., Ke, W., Guo, H., and Shu, Y. (2014). "Molecular Identity of Axonal Sodium Channels in Human Cortical Pyramidal Cells". *Frontiers in Cellular Neuroscience* 8. DOI: `10.3389/fncel.2014.00297`.

Trimmer, J. S. (2015). "Subcellular Localization of K+ Channels in Mammalian Brain Neurons: Remarkable Precision in the Midst of Extraordinary Complexity". *Neuron* 85.2, pp. 238–256. DOI: `10.1016/j.neuron.2014.12.042`.

Tsien, R. W., Ellinor, P. T., and Horne, W. A. (1991). "Molecular Diversity of Voltage-Dependent Ca2+ Channels". *Trends in Pharmacological Sciences* 12.9, pp. 349–354. DOI: `10.1016/0165-6147(91)90595-j`.

Typlt, M., Mirkowski, M., Azzopardi, E., Ruettiger, L., Ruth, P., and Schmid, S. (2013). "Mice with Deficient BK Channel Function Show Impaired Prepulse Inhibition and Spatial Learning, but Normal Working and Spatial Reference Memory". *PLoS ONE* 8.11. Ed. by V. Ceña, e81270. DOI: `10.1371/journal.pone.0081270`.

Vierra, N. C. and Trimmer, J. S. (2022). "Ion Channel Partnerships: Odd and Not-So-Odd Couples Controlling Neuronal Ion Channel Function". *International Journal of Molecular Sciences* 23.4, p. 1953. DOI: `10.3390/ijms23041953`.

Vogt, K. E., Gerharz, S., Graham, J., and Canepari, M. (2011). "Combining Membrane Potential Imaging with L-Glutamate or GABA Photorelease". *PLoS ONE* 6.10. Ed. by O. J. Manzoni, e24911. DOI: `10.1371/journal.pone.0024911`.

Waters, J., Schaefer, A., and Sakmann, B. (2005). "Backpropagating Action Potentials in Neurones: Measurement, Mechanisms and Potential Functions". *Progress in Biophysics and Molecular Biology* 87 (1 SPEC. ISS.), pp. 145–170. DOI: `10.1016/j.pbiomolbio.2004.06.009`.

Wessler, I., Dooley, D. J., Werhand, J., and Schlemmer, F. (1990). "Differential Effects of Calcium Channel Antagonists (Omega-Conotoxin GVIA, Nifedipine, Verapamil) on the Electrically-Evoked Release of [3H]Acetylcholine from the Myenteric Plexus, Phrenic Nerve and Neocortex of Rats". *Naunyn-Schmiedeberg's Archives of Pharmacology* 341.4, pp. 288–294. DOI: `10.1007/BF00180653`.

Westenbroek, R. E., Sakurai, T., Elliott, E., Hell, J., Starr, T., Snutch, T., and Catterall, W. A. (1995). "Immunochemical Identification and Subcellular Distribution of the Alpha 1A Subunits of Brain Calcium Channels". *The Journal of Neuroscience* 15.10, pp. 6403–6418. DOI: `10.1523/JNEUROSCI.15-10-06403.1995`.

Williams, M. E., Washburn, M. S., Hans, M., Urrutia, A., Brust, P. F., Prodanovich, P., Harpold, M. M., and Stauderman, K. A. (1999). "Structure and Functional Characterization of a Novel Human Low-Voltage Activated Calcium Channel". *Journal of Neurochemistry* 72.2, pp. 791–799. DOI: `10.1046/j.1471-4159.1999.0720791.x`.

Williams, S. R. and Stuart, G. J. (2000). "Backpropagation of Physiological Spike Trains in Neocortical Pyramidal Neurons: Implications for Temporal Coding in Dendrites". *The Journal of Neuroscience* 20.22, pp. 8238–8246. DOI: `10.1523/JNEUROSCI.20-22-08238.2000`.

Wimmer, V. C. et al. (2010). "Axon Initial Segment Dysfunction in a Mouse Model of Genetic Epilepsy with Febrile Seizures Plus". *Journal of Clinical Investigation* 120.8, pp. 2661–2671. DOI: `10.1172/JCI42219`.

Wolfart, J. and Roeper, J. (2002). "Selective Coupling of T-Type Calcium Channels to SK Potassium Channels Prevents Intrinsic Bursting in Dopaminergic Midbrain Neurons". *The Journal of Neuroscience* 22.9, pp. 3404–3413. DOI: `10.1523/JNEUROSCI.22-09-03404.2002`.

Wu, S.-Y., Shen, Y., Shkolnikov, I., and Campbell, R. E. (2022). "Fluorescent Indicators For Biological Imaging of Monatomic Ions". *Frontiers in Cell and Developmental Biology* 10, p. 885440. DOI: `10.3389/fcell.2022.885440`.

Xiao, Y., Jackson, J. O., Liang, S., and Cummins, T. R. (2011). "Common Molecular Determinants of Tarantula Huwentoxin-IV Inhibition of Na $^+$ Channel Voltage Sensors in Domains II and IV". *Journal of Biological Chemistry* 286.31, pp. 27301–27310. DOI: `10.1074/jbc.M111.246876`.

Yang, H., Zhang, G., and Cui, J. (2015). "BK Channels: Multiple Sensors, One Activation Gate". *Frontiers in Physiology* 6. DOI: `10.3389/fphys.2015.00029`.

Yang, S., Ben-Shalom, R., Ahn, M., Liptak, A. T., van Rijn, R. M., Whistler, J. L., and Bender, K. J. (2016). "Beta-Arrestin-Dependent Dopaminergic Regulation of Calcium Channel Activity in the Axon Initial Segment". *Cell Reports* 16.6, pp. 1518–1526. DOI: `10.1016/j.celrep.2016.06.098`.

Yarov-Yarovoy, V., DeCaen, P. G., Westenbroek, R. E., Pan, C.-Y., Scheuer, T., Baker, D., and Catterall, W. A. (2012). "Structural Basis for Gating Charge Movement in the Voltage Sensor of a Sodium Channel". *Proceedings of the National Academy of Sciences* 109.2. DOI: `10.1073/pnas.1118434109`.

Yokoyama, C. T., Westenbroek, R. E., Hell, J. W., Soong, T. W., Snutch, T. P., and Catterall, W. A. (1995). "Biochemical Properties and Subcellular Distribution of the Neuronal Class E Calcium Channel Alpha 1 Subunit". *The Journal of Neuroscience* 15.10, pp. 6419–6432.

Young, J. Z. (1938). "The Functioning of the Giant Nerve Fibres of the Squid". *Journal of Experimental Biology* 15.2, pp. 170–185. DOI: `10.1242/jeb.15.2.170`.

Yu, F. H. and Catterall, W. A. (2004). "The VGL-Chanome: A Protein Superfamily Specialized for Electrical Signaling and Ionic Homeostasis". *Science's STKE* 2004.253. DOI: `10.1126/stke.2532004re15`.

Yu, Y., Maureira, C., Liu, X., and McCormick, D. (2010). "P/Q and N Channels Control Baseline and Spike-Triggered Calcium Levels in Neocortical Axons and Synaptic Boutons". *Journal of Neuroscience* 30.35, pp. 11858–11869. DOI: `10.1523/JNEUROSCI.2651-10.2010`.

Zhong, Y.-S., Wang, J., Liu, W.-M., and Zhu, Y.-H. (2013). "Potassium Ion Channels in Retinal Ganglion Cells (Review)". *Molecular Medicine Reports* 8.2, pp. 311–319. DOI: `10.3892/mmr.2013.1508`.

Zilberter, Y., Harkany, T., and Holmgren, C. D. (2005). "Dendritic Release of Retrograde Messengers Controls Synaptic Transmission in Local Neocortical Networks". *The Neuroscientist* 11.4, pp. 334–344. DOI: `10.1177/1073858405275827`.

Zilberter, Y., Kaiser, K. M., and Sakmann, B. (1999). "Dendritic GABA Release Depresses Excitatory Transmission between Layer 2/3 Pyramidal and Bitufted Neurons in Rat Neocortex". *Neuron* 24.4, pp. 979–988. DOI: `10.1016/S0896-6273(00)81044-2`.